# Understanding the Roles of Metal Ions in the Fate of Reactive Oxygen Species and in Alzheimer's Disease

**by**

**Joseph J. Braymer**

**A dissertation submitted in partial fulfillment**
**of the requirements for the degree of**
**Doctor of Philosophy**
**(Chemistry)**
**in the University of Michigan**
**2012**

**Doctoral Committee:**

**Assistant Professor Mi Hee Lim, Co-Chair**
**Professor Melanie Sanford, Co-Chair**
**Professor David Ballou**
**Associate Professor Nicolai Lehnert**

---

**To my undergraduate organic chemistry professor, Dr. Naod Kebede, and my parents. Without their support, I would not be where I am today.**

**Acknowledgement**

I would first like to thank the many Professors responsible for my PhD education at the University of Michigan. In particular, my thesis committee has been very important for my progress (Professor Mi Hee Lim, Professor Melanie Sanford, Professor Nicolai Lehnert, and Professor David Ballou). I thank Professor Lim for the valuable time spent in her lab and the knowledge and skills that I acquired in her lab. Professor Sanford has always been willing to help me and I greatly appreciate her support. Professors Lehnert, Sanford, and Ballou have always given critical and thoughtful feedback in my candidacy meeting, data presentation at the big bioinorganic group meeting, thesis data meeting, and I'm sure to come in my thesis defense. I also had the opportunity to acquire new skills and techniques in both Professor Sanford's and Lehnert's lab during my first year rotations. I have been lucky to have such a great committee for overseeing my thesis.

The reason I was able to pursue a PhD at the University of Michigan was because my undergraduate professors at Edinboro University of Pennsylvania provided me with a well-rounded background in the varying disciplines of chemistry. I must thank all the professors and in particular, Professor Naod Kebede, Professor Lisa Unico, Professor Joanne Smith, Professor Janet Rodgers, Professor Gerald Hoffmann, and Professor Paul Edwards.

Friends and colleagues at the University of Michigan were very important for surviving my PhD. I would like to thank all the members of the Lim lab that I have worked with, past and present. In particular, I must give all thanks and gratitude to Alaina S. DeToma and will be forever indebted for her support. She was my most dependable friend and without her, I would not have made it through. I still owe her somewhere around 2 billion dollars and several beverages. Amit Pithadia could always put a smile on my face and I also greatly appreciate his friendship.

I must also thank the Sanford lab where I spent a small portion of my PhD, especially Dr. Douglas Genna, Ansis Maleckis, and Dr. Monica Helvia Perez-Temprano. I thank them for the many thought-provoking scientific and nonscientific discussions that we had during my time there. Dr. Genna and Ansis provided valuable insight into my ORP, which was greatly appreciated. I'm also indebted to Dr. Genna for his time and willingness to proof read my drafts for my thesis.

To all my other friends in the chemistry department, thank you for taking my mind of things when times were tough or I needed a break from the lab. The disc golf with Tim, Lauren, Melissa, and Gary always made my day. The many instances we grabbed dinner at the Jolly pumpkin were always a blast. Thank you also to Tanya Breault and Allison Knauff for our many coffee dates, especially during thesis writing. Many thanks

to Andrea for our lively chats and to Nathan for taking me golfing. To the many acquaintances in the chemistry department, thank you to those who have come to my presentations and discussed science with me at poster sessions.

My chance to go to college and graduate school would not have happened if it were not for the undying support of my parents. Thank you for always supporting me even during the many times I was in the thick of trouble. I have to thank my sisters, Krista, Alaina, Jenna, and Alesha along with their families for checking up on me now and again and always asking when I would be coming home. Also, to my extended family who have always been supportive. Especially to my passed and surviving grandparents who have given nothing but unconditional love and care throughout my life.

My close friends have been my other backbone, always providing support. Thank you Jermo, Matty, Jaybird, Miki, Brady and Austin. I'm also very grateful to Melissa and Vincent who have become very dear friends in only a year. They have brightened my last year of graduate school in so many ways. Thank you to my long-standing roommate at Michigan, Matt, for putting up with me for over 4 years.

I would also like to thank Mary Jo Desprez and Ilona Phillips for all their support in my pursuit to finish a strong and healthy last year of my PhD.

During my PhD, I was very fortunate to have the opportunity to work in the lab of Professor Wonwoo Nam at Ewha Women's University in Seoul, South Korea. Although my work in his lab does not directly show up in my thesis, I learned a tremendous amount about nonheme intermediates in his lab. Thank you for the privilege to work in the lab and also to Dr. Jaeheung Cho and all the girls for all the help and kindness.

## Table of Contents

## List of Tables

## List of Figures

## List of Abbreviations

8-HQ – 8-hydroxyquinoline

12h – (*S,E*)-*N*-((1-(2-amino-3-(1H-indol-3-yl)propyl)-1H-1,2,3-triazol-4-yl)methyl)-3-(3,4-dihydroxy-phenyl) acrylamide

Aβ − amyloid β

AD – Alzheimer's disease

APP – amyloid precursor protein

BACE – β-secretase 1

BBB – blood brain barrier

BDE – bond dissociation energy

BM – 2-(2-aminophenyl)benzimidazole)

bpy – bipyridine

CNS – central nervous system

CP-Cu – copper bound chelator peptide ($H_2N$-DAHFWADR-$NH_2$)

CQ – clioquinol

CSF – cerebralspinal fluid

DFO – desferrioxamine

DMF – dimethylformamide

DMSO – dimethylsulfoxide

DNA – deoxyribonucleic acid

EDTA – ethlyenediaminetetraacetic acid

ELISA – enzyme-linked immunosorbent assay

EPR – electron paramagnetic resonance spectroscopy

ESI-MS – electrospray ionization mass spectrometry

$Et_2O$ – diethyl ether

ETC – electron transport chain

EtOH – ethanol

fAD – familial Alzheimer's disease

$^{18}$F-AV-45 – (*E*)-4-(2-(6-(2-(2-(2-$^{18}$F-fluoroethoxy)ethoxy)ethoxy)pyridin-3-yl)vinyl)-*N*-methyl benzenamine

FDA – federal drug administration

GL – 1-[4-(Dimethylamino)phenyl]-3-hydroxy-2-methyl-4(1H)-pyridinone

HAT – hydrogen atom transfer

HBA – hydrogen bond acceptor

HBD – hydrogen bond donor

HBT – 2-(2-hydroxyphenyl)benzothiazole

HBX – 2-(2-hydroxyphenyl)benzoxazole

HEPES – 4-(2-hydroxyethyl)-1-piperazineethanesulfonic acid

HOTf – trifluoromethanesulfonic acid

HSQC – heteronuclear single quantum correlation spectroscopy

*I* – ionic strength

ICP-MS – induced coupled plasma mass spectrometry

I-IMPY – 4-(7-iodoimidazo[1,2-a]pyridin-2-yl)-N,N-dimethylaniline

IR – infrared spectroscopy

KIE – kinetic isotope effect

**K0** – 2-[4-(dimethylamino)phenyl]imidazo[1,2-a]pyridine-8-ol

**K1** – 6-(imidazo-[1,2-a]pyridin-2-yl)-*N*,*N*-dimethylpyridin-3-amine

**K2** – 6-(6-iodo-imidazo[1,2-a]pyridin-2-yl)-*N*,*N*-dimethylpyridin-3-amine

$k' - k' = k_{obs}/[H_2O_2]$

$k_2$ – bimolecular rate constant

$k_2' - k_2' = k_2/n$, where *n* is the number of available protons for hydrogen atom transfer

$K_a$ – acid dissociation constant

$K_d$ – dissociation constant

$k_{obs}$ – observed rate constant

**L1-a** – *N*-(pyridin-2-ylmethylene)aniline

**L1-b** – $N^1$,$N^1$-dimethyl-$N^4$-(pyridin-2-ylmethylene)-benzene-1,4-diamine

**L2-a** – *N*-(pyridin-2-ylmethyl)aniline

**L2-b** – $N^1$,$N^1$-dimethyl-$N^4$-(pyridin-2-ylmethyl)benzene-1,4-diamine

log $\beta$ – metal complex stability constant

*m*-CPBA – *meta*-chloroperbenzoic acid

metal-Aβ – metal-associated amyloid β

MS – mass spectrometry

MW – molecular weight

N4Py – *N*,*N*-bis(2-pyridylmethyl)-*N*-[bis(2-pyridyl)methyl]amine

NHE – normal hydrogen electrode

NMR – nuclear magnetic resonance spectroscopy

OTf – trifluoromethanesulfonate

ORTEP – Oak Ridge Thermal-Ellipsoid Plot

PAMPA – parallel artificial membrane permeability assay

PET – positron emission tomography

PhI – iodobenzene

PhIO – iodosobenzene

PiB – Pittsburgh compound B

p-*I*-stilbene – N,N-dimethyl-4-[(1E)-2-(4-iodophenyl)ethenyl]benzenamine)

PIXE – particle induced X-ray emission

PS1 – presenilin 1

PSA – polar surface area

py – pyridine

ROS – reactive oxygen species

RNA – ribonucleic acid

RNS – reactive nitrogen species

rt – room temperature

**S0** – (*E*)-1,2-diphenylethene

**S1** – *N*,*N*-dimethyl-4-(2-phenylethenyl)benzamine

sAPP$\alpha$ – soluble amyloid precursor protein

SDS-$d_{25}$ – sodium dodecyl-$d_{25}$ sulfate

SPECT – single photon emission computed tomography

TauD – taurine $\alpha$-ketoglutarate dioxygenase

TDCPP − *meso-tetrakis* (dichlorophenyl)porphyrinate dianion

TEM – transmission electron microscopy

THF – tetrahydrofuran

ThT − 2-[4-(dimethylamino)phenyl]-3,6-dimethylbenzothiazolium chloride

tmc − 1,4,8,11-tetra-methyl-1,4,8,11-tetraazacyclotetradecane

tmc-Py − 1-(2'-pyridylmethyl)-4,8,11-tri-methyl-1,4,8,11-tetraazacyclotetradecane

TPEN − *N, N, N',* N'-tetrakis(2-pyridyl-methyl)ethylene diamine

TPFPP − *meso-tetrakis* (pentafluorophenyl)porphyrinate dianion

TROSY – transverse relaxation optimized spectroscopy

UV-Vis – UV-Visible spectroscopy

XAS – X-ray absorption spectroscopy

XH1 – *N*,*N*-bis[2-[[2-[[4-(2-benzothiazolyl)phenyl]amino]-2-oxoethyl](carboxymethyl) amino]ethyl]glycine

XRF – X-ray fluorescence spectroscopy

## Abstract

Biologically relevant metal ions play crucial roles in metabolic regulation and cellular function throughout nature and in the human body. An important regulatory mechanism is control of reactive oxygen species (ROS). The most abundant ROS molecule is hydrogen peroxide ($H_2O_2$), which is detoxified by heme enzymes called catalases. The breakdown of $H_2O_2$ by catalases has been proposed to involve a high-valent oxoiron(IV) porphyrin $\pi$-cation radical. While the mechanism is not fully understood, high-valent oxoiron(IV) species from other enzymes that possess different coordination to the metal center (nonheme) have not been previously reported to react with $H_2O_2$. Work carried out in this thesis project has shown that both synthetic heme and nonheme high-valent oxoiron(IV) complexes can react with $H_2O_2$ directly, which gives potential insight into ROS production and detoxification *in vivo*.

When metal and ROS homeostasis is disrupted, especially in the brain, it is believed to have severe consequences resulting in various diseases, such as Alzheimer's disease (AD). AD is the most prevalent form of dementia and is characterized by the build up of amyloid-$\beta$ (A$\beta$) peptide aggregates that are believed to contribute to AD pathology. These aggregates have also been shown to be co-localized with metals, which can facilitate aggregation of A$\beta$ and neurotoxicity through production of ROS *in vitro*. Although tremendous effort has been put forth to uncover the etiology of AD, it is still unknown what factors promote neurodegeneration in the brain, in addition

to how metal-amyloid-β (metal-Aβ) species contribute to AD. To provide a handle on studying metal-associated Aβ, bifunctional small molecules that can probe the relationship between metal ions and Aβ have been developed and studied *via* various spectroscopic methods. These compounds are capable of modulating several modes of metal-Aβ reactivity and show promise for the continued development of new chemical reagents for investigating metal-Aβ chemistry and biology in AD.

## Chapter 1: The Roles of Metal Ions and Reactive Oxygen Species in Biology

### 1.1 Metals in Biology

Metal ions contribute little to the overall mass of biological systems, yet are essential nutrients involved in the normal functioning of all types of cells.[1] It is estimated that approximately a third of known proteins are metalloproteins (*i.e.*, they bind metal ions).[2,3] The predominant transition metals in the human body are iron (Fe), copper (Cu), and zinc (Zn). These are distributed throughout the body in relatively small amounts (Table 1.1); however, they play critical roles in biology including structural support, storage, electron transfer, dioxygen ($O_2$) binding, and catalytic function (Figure 1.1).[3,4,5,6]

**Table 1.1. Total amounts in the body and concentrations in human plasma of the most abundant transition metal ions in healthy adults.[a]**

| Element | Total Amount (g) | Human Plasma (μM) |
|---|---|---|
| Fe | 3−5 | 22.3 |
| Zn | 2−4 | 17.2 |
| Cu | < 0.110 | 16.5 |

[a] Values from References 1, 5, and 6.

Take for example the role of these metal ions in the respiration and energy metabolism processes in humans.[1] Iron is essential for binding $O_2$ in the protein hemoglobin that transports $O_2$ throughout the body. Once delivered to the mitochondria, the energy-harvesting hub of the cell, $O_2$ accepts the excess electrons generated from

the consumption of glucose and fats in the energy-producing Krebs cycle. This transfer of electrons takes place in the electron transport chain (ETC) and is facilitated by the copper and heme-containing, enzyme cytochrome c oxidase.[17] This reaction neutralizes the potentially damaging electron equivalents and converts them into benign $H_2O$. In order to control the other byproduct of sugar metabolism, $CO_2$, the zinc-binding metalloprotein carbonic anhydrase regulates its conversion to bicarbonate.[1] These examples exemplify the importance of metal ions in human health and are only a small subset of the essential functions that metalloproteins provide within the human body.

The knowledge of how these systems work has been possible due to the contributions from the field of bioinorganic chemistry, which is the study of how metal ions behave in biological systems.[1] Confirming how metals bind to proteins leads to the understanding of how they function, whether it is in regulating metal ion homeostasis, carrying out catalytic manipulations of organic and inorganic molecules, or participating in electron transfer reactions.[3,4,8] A major topic in this field involves the study of synthetic biomimetic compounds, which can provide structural and catalytic insights into highly complex biological systems.[9,10,11] Understanding how metal ions behave under biological conditions has further led to their use as imaging agents and therapeutics in human disease as well as to the development of methods for manipulating endogenous metal concentrations for therapeutic purposes.[9,10,12,13]

**Figure 1.1. Schematic illustration showing the roles of metal ions and ROS.**

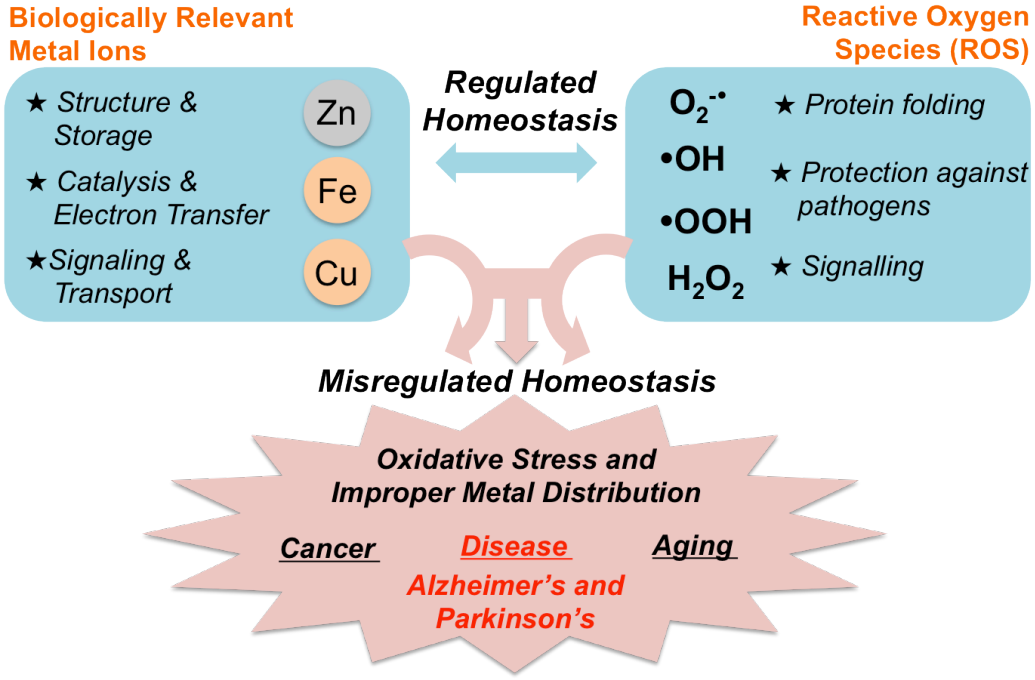


## 1.2 Reactive Oxygen Species in Biology

Intricately associated with metal ions in biology, in particular Cu and Fe, is the regulation of reactive oxygen species (ROS).[14] These species are versatile small molecules that are essential for physiological signaling, proper protein folding, and protection against pathogens (Figure 1.1).[14,15,16] Common ROS, which contribute to the estimated $10^{11}$ free radicals produced daily within the brain alone, are superoxide ($O_2^{\bullet-}$), hydroperoxyl radical (•OOH), hydrogen peroxide ($H_2O_2$), and hydroxyl radical (•OH).[5,17] Due to the highly reactive nature of these compounds, nature has evolved many protective mechanisms for their cellular control, and many of them include metalloenzymes.[1,5,17] Continuing from the example involving metal-binding proteins above, the normal metabolism of $O_2$ in the ETC is a common source of ROS.[18] Due to the ETC not being 100% efficient, electrons can leak out from this system and reduce $O_2$, forming superoxide radicals. The catalytic conversion of $O_2^{\bullet-}$ to $H_2O_2$ is carried out at

a copper-binding site in the enzyme superoxide dismutase.[18] This ROS cycle is then quenched by the dismutation of $H_2O_2$ into $O_2$ and two molecules of $H_2O$ by iron-containing enzymes called catalases.[19,20] The efficient activity of these metalloproteins is essential for keeping these reactive small molecules under control.

### 1.3 Relationships of Metal Ions and ROS in Health and Disease

It is remarkable that these enzymes utilize metals such as Fe, Cu, and Zn *via* metal dependent mechanisms to control the flux of ROS in the cell. Without the controlled and protected metal coordination environment provided by protein frameworks, the production of ROS *via* Fenton chemistry involving $M^{n+}$ and $M^{(n+1)+}$ (M = Cu or Fe) redox cycles becomes highly damaging (Eq. 1).[5,17] In particular, the aberrant production of ROS generates the highly reactive hydroxyl radical, which causes the greatest oxidative damage to proteins, DNA/RNA, and lipids (Eqs. 1 and 2).[16,17] Disruptions in the balance of proteins modulating ROS reactions as well as mutations of protein sequences of these proteins can also lead to the improper release and functioning of ROS.[5,21,22]

$$M^{n+} + H_2O_2 \rightarrow M^{(n+1)+} + {}^{-}OH + {\bullet}OH \quad (1)$$

$$O_2^{-} + H_2O_2 \rightarrow O_2 + {}^{-}OH + {\bullet}OH \quad (2)$$

Although the brain only accounts for 2% of the total body weight of a human, it metabolizes 25% of the body's glucose supply and 20% of consumed $O_2$.[23] This high activity leaves it particularly vulnerable to ROS, which are proposed to be involved in the natural process of aging through the slow yet steady accumulation of oxidative damage.[24] The concentration and regulation of metal ions are believed to fluctuate with increased age, in particular, copper levels in the brain decrease while iron increases,

which could be related to age-associated breakdown of ROS control.[25] The intertwined homeostasis of ROS and metal ions are additionally believed to be main contributors in the development of cancer and neurodegenerative diseases like Alzheimer's and Parkinson's (Figure 1.1).[25] Therefore, understanding the roles of metal ions, ROS, and their relationship in biological systems is important for understanding their control in healthy cells and how they could potentially contribute to aging and disease when they are mis-regulated.

### 1.4 Contributions of this Thesis

Two specific research projects related to the discussion above were undertaken in this thesis. Due to the importance of catalase in detoxifying $H_2O_2$, Chapter 2 entails studying biomimetic complexes that were used to probe how key intermediates in both nonheme and heme systems react with $H_2O_2$. The main contribution of this work has been published on nonheme high-valent complexes reacting with $H_2O_2$ (Braymer, J. J. *et al. Angew. Chem. Int. Ed.* **2012**, *51*, 5376). Preliminary work on heme complexes, that is unpublished, is also discussed.

With the aim of better understanding the contribution of metal ions in neurodegenerative disease, the project in Chapter 3 discusses the development of bifunctional molecules that target metal ions and peptides that are proposed to be central to the pathogenesis of Alzheimer's disease. The work presented here is all published and involves two families of the first generation of small molecules (Hindo, S. S. *et al. J. Am. Chem. Soc.* **2009**, *131,* 16663; Braymer, J. J.; *et al*. *Inorg. Chem.* **2011**, *50*, 10724; Braymer, J. J. *et al. Inorg. Chim. Acta.* **2011**, *380*, 261) as well as the second generation of compounds (Choi, J.-S., Braymer, J. J. *et al*. *Proc. Natl. Acad. Sci.*

*USA* **2010**, *107*, 21990; Choi, J.-S. *et al*. *Metallomics*, **2011**, *3*, 284). Due to the characterization and study of the two families of compounds being all related, they are all discussed together in one full, comprehensive chapter.

Progress in both projects has shown exciting new chemistry with respect to the biologically relevant reactivity of ROS and metal ions and is presented in this thesis.

### 1.5 References


[1] *Bioinorganic Chemistry*; Bertini, I.; Gray, H. B.; Lippard, S. J.; Valentine, J. S., Eds.; University Science Books: Mill Valley, CA, 1994.
[2] Yannone, S. M.; Hartung, S.; Menon, A. L.; Adams, M. W. W.; Tainer, J. A. *Curr. Opin. Biotech.* **2012**, *23*, 89.
[3] Ragsdale, S. W. *Chem. Rev.* **2006**, *106*, 3317.
[4] Holm, R. H.; Kennepohl, P.; Solomon, E. I. *Chem. Rev.* **1996**, *96*, 2239.
[5] Gaggelli, E.; Kozlowksi, H.; Valensin, D.; Valensin, G. *Chem. Rev.* **2006**, *106*, 1995.
[6] Rink, L.; Gabriel, P. *Proc. Nutr. Soc.* **2000**, *59*, 541.
[7] Kaila, V. R. I.; Verkhovsky, M. I.; Wikström, M. *Chem. Rev.* **2010**, *110*, 7062.
[8] Thiele, D. J.; Gitlin, J. D. *Nat. Chem. Biol.* **2008**, *4*, 145.
[9] Gray, H. *Proc. Natl. Acad. Sci. USA* **2003**, *100*, 3563.
[10] Lippard, S. J. *Nat. Chem. Biol*. **2006**, *2*, 504.
[11] David, S. S.; Meggers, E. *Curr. Opin. Chem. Biol.* **2008**, *12*, 194.
[12] Haass, K. L.; Franz, K. J. *Chem. Rev.* **2009**, *109*, 4921.
[13] Scott, L. E.; Orvig, C. *Chem. Rev.* **2009**, *109*, 4885.
[14] D'Autreaux, B.; Toledano, M. B. *Nat. Rev. Mol. Cell Biol.* **2007**, *8*, 813.
[15] Dickinson, B. C.; Chang, C. J. *Nat. Chem. Biol.* **2011**, *7*, 504.
[16] Winterbourn, C. C. *Nat. Chem. Biol.* **2008**, *4*, 278.
[17] Giorgio, M.; Trinei, M.; Migliaccio, E.; Pelicci, P. G. *Nat. Rev. Mol. Cell Biol.* **2007**, *8*, 722.
[18] Murphy, M. P. *Biochem. J.* **2009**, *417*, 1.
[19] Deisseroth, A.; Dounce, A. L. *Physiol. Rev.* **1970**, *50*, 319.
[20] Putnam, C. D.; Arvai, A. S.; Bourne, Y.; Tainer, J. A. *J. Mol. Biol.* **2000**, *296*, 295.
[21] Roberts, B. R.; Ryan, T. M.; Bush, A. I.; Masters, C. L.; Duce, J. A. *J. Neurochem*. **2012**, *120*, 149.
[22] von Bernhardi, R.; Eugenín, J. *Antioxid. Redox Signaling* **2012**, *16*, 974.
[23] Clark, D. D.; Sokoloff, L. *Basic Neurochemistry: Molecular, Cellular, and Medicinal Aspects.*; Siegel, G. J.; Agranoff, B. W.; Albers, R. W.; Fisher, S. K.; Uhler, M. D., Eds. Lippincott, Philadelphia, PA, 1999.
[24] Finkel, T.; Holbrook, N. J. *Nature*, **2000**, *408*, 239.
[25] Barnham, K. J.; Masters, C. L.; Bush, A. I. *Nat. Rev. Drug Discovery* **2004**, *3*, 205.

# Chapter 2: Elucidating the Reactivity of High-Valent Oxoiron(IV) Intermediates with Reactive Oxygen Species

## 2.1 Introduction

### 2.1.1 Collaboration in the $H_2O_2$ Project

The work presented in this chapter has been accomplished with the help of several colleagues, whom I wish to acknowledge. Aireen Romu tested initial conditions for heme reactivity studies with $H_2O_2$. Chun Chow assisted in preliminary reactivity screens for conditions of the nonheme complexes with $H_2O_2$. Dr. Xiaoming He synthesized $[Fe^{II}(tmc\text{-}Py)](OTf)_2$. Kevin O'Neill, an undergraduate working under my supervision, helped maintain our stock supply of $[Fe^{II}(N4Py)(NCCH_3](OTf)_2$ and repeated experiments regarding $[Fe^{IV}O(tmc)(NCCH_3)]^{2+}$. He additionally carried out the reactivity studies of $[Fe^{IV}O(tmc\text{-}Py)]^{2+}$ and $[Fe^{IV}O(tmc)(NCCH_3]^{2+}$ in acetone (Section 2.3). Jin Hoon Kim helped acquire data for the reactions of $Fe^{IV}$OTPFPP with $H_2O_2$ by UV-Vis. Our collaborator Professor Jan-Uwe Rohde from the University of Iowa also provided tremendous help on project directions, data analysis/interpretation, and writing of the manuscript published in *Angewandte Chemie International Edition*. I would like to also thank Lauren Goodrich for providing assistance in simulating EPR spectra and helping with setting up the EPR instrument for data collection at liquid helium temperature.

### 2.1.2 $H_2O_2$ and High-Valent Iron in Biology

Maintaining the concentration of $H_2O_2$ in biological systems is important because it is the most abundant ROS molecule and can lead to the formation of the very reactive hydroxyl radical through the Fenton reaction if not regulated properly (Eq. 1).[1,2] Iron homeostasis plays a key role in this balance as well.[3] If iron is properly stored in heme and nonheme metalloproteins, uncontrolled oxidation induced by iron and $H_2O_2$ is minimal. However, if labile pools of iron are present or regulation of ROS is imbalanced, this reaction can be very detrimental and is believed to be involved in neurodegenerative diseases.[1,2,3] Not only do iron-binding proteins protect against uncontrolled Fenton chemistry (Eq. 1), they specifically utilize the oxidizing potential of $H_2O_2$ to carry out essential oxidation reactions. For example, catalases are highly efficient metalloenzymes that are responsible for depleting $H_2O_2$ levels by dismuting two molecules of $H_2O_2$ *via* the proposed reaction pathways shown in Equations 2 and 3.[4,5,6,7] Initial oxidation of the $Fe^{III}$ resting state with $H_2O_2$ generates a high-valent oxoiron(IV) porphyrin $\pi$-cation radical, also known as compound I, $[(P^{\bullet+})Fe^{IV}=O]^+$, where P = porphyrinate dianion [Eq. 2] . The reaction of compound I with a second molecule of $H_2O_2$ results in the return to the resting state of the enzyme with the release of water and $O_2$ [Eq. 3]. Due to the rates of Equations 2 and 3 being comparable, the reaction mechanism involving the direct interaction of $H_2O_2$ with the oxo ligand of compound I in catalase still remains unclear.[6]

$$Fe^{II} + H_2O_2 \rightarrow Fe^{III} + {}^{-}OH + \bullet OH \quad (1)$$

$$[(P)Fe^{III}]^+ + H_2O_2 \rightarrow [(P^{\bullet+})Fe^{IV}=O]^+ + H_2O \quad (2)$$

$$[(P^{\bullet+})Fe^{IV}=O]^+ + H_2O_2 \rightarrow [(P)Fe^{III}]^+ + O_2 + H_2O \quad (3)$$

Two possible mechanisms could account for the observed catalytic reaction.[6] The first is a general acid-base mechanism that involves a distal histidine residue that deprotonates $H_2O_2$, leading to a hydride transfer from the peroxide molecule to the oxoiron(IV) center (Figure 2.1a).[6,8] This mechanism is supported by a low kinetic isotope effect (KIE = 2.1) in *Micrococcus lysodeikticus* catalase that is consistent with deprotonation as an important step in the catalytic cycle.[8] The second proposed mechanism derives from studies of a compound I species in myoglobin mutants that do not have a histidine residue but yet reduction of $H_2O_2$ still occurs (Figure 2.1c).[8] Based on very large KIE values (10-29), a hydrogen atom transfer (HAT) mechanism was proposed.[6,9]

Computational studies on the mechanism of catalase are in general agreement, showing that both the acid-base and HAT mechanisms are feasible.[7] However, the calculations suggest that the acid-base mechanism involves two one-electron reactions instead of a two-electron hydride transfer step (Figure 2.1b). These calculations also implicate slight differences in mechanism between catalases from different organisms, depending on the position of a histidine residue.[7] Thus, one unified mechanism may not be applicable for all catalases.

**Figure 2.1. Possible mechanisms for decomposition of $H_2O_2$ by compound I, a) acid-base hydride transfer, b) acid-base two one-electron transfers, and c) two one-electron transfers only.**

**a) acid-base hydride mechanism**

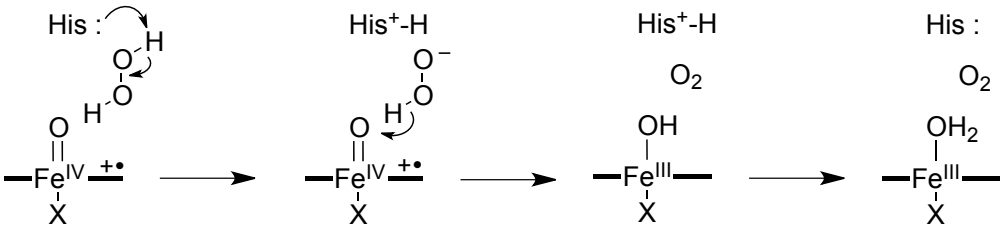


**b) acid-base HAT mechanism**

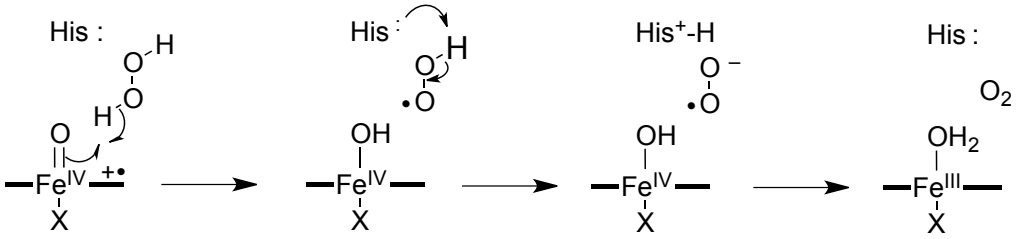


**c) HAT mechanism**

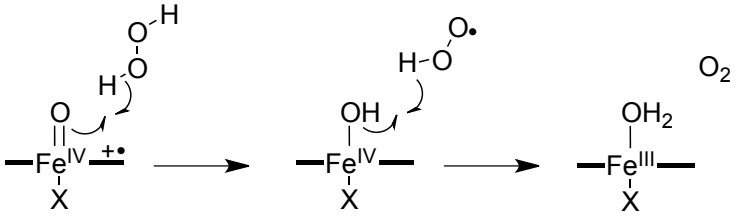


Other heme enzymes found throughout nature (peroxidases and catalase-peroxidases) can also form compound I species that exhibit catalase-like behavior under certain conditions.[10] For example, high concentrations of $H_2O_2$ can lead to catalase activity of peroxidases. The reactivity of the oxoiron(IV) moiety is typically dictated by amino acid side chains that surround the heme pocket along with the distal ligand trans to the oxo ligand.[11] Reactivity of heme proteins is tightly controlled based on the evolved reaction mechanisms with specific substrates.[6,10,11] For example, myleoperoxidases only promote the first HAT reaction between compound I and $H_2O_2$ producing the one electron reduced compound II species [$(P)Fe^{IV}-OH$ or $(P)Fe^{IV}=O$]

and superoxide (Figure 2.2).[12] Depending on the enzyme, this compound II species can be either catalytically competent (peroxidases, C−H oxidation) or an undesired reduced state of compound I that does not participate in the catalytic cycle (catalases).[5,10] Compound II species can be formed by either a one electron reducing substrate (peroxidase activity) or by 1 $e^-$ oxidation of a nearby amino acid residue by the heme system.

**Figure 2.2. Reactive iron-oxygen species from heme and nonheme enzymes. X = axial ligand and L = a general ligand.**

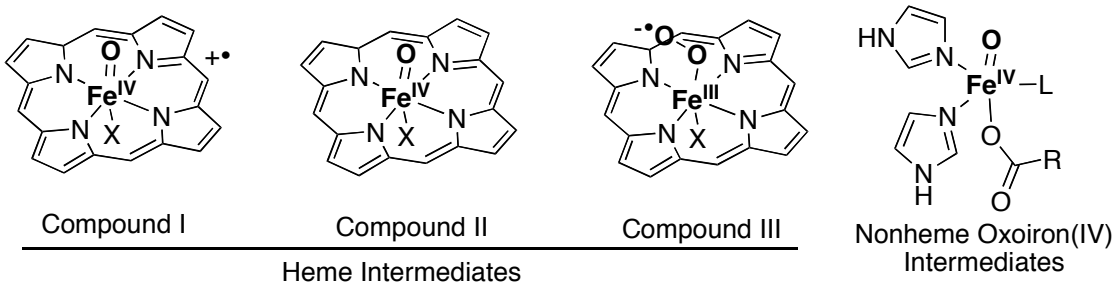


Compound II intermediates can also interact with $H_2O_2$ yielding compound III species ([(P)$Fe^{III}$−$OO^{-\bullet}$] ⇆ [(P)$Fe^{II}$−OO]).[10,13,14] Compound III is most likely formed by compound II abstracting a hydrogen atom from $H_2O_2$ to produce the hydroperoxyl radical (•OOH). This radical can then be deprotonated (p$K_a$ in water = 4.7), which leaves superoxide free to bind to the metal center. Alternatively, the hydroperoxyl radical can directly bind to the metal center to generate an iron(III) hydroperoxyl intermediate ([(P)$Fe^{III}$OOH]).[6,13,14] This is an important reaction because the reactivity of compound II with $H_2O_2$ is believed to be responsible for the suicide inactivation of heme enzymes *via* compound III.[13,14] Based on this chemistry, heme oxoiron(IV) intermediates should show rich reactivity with ROS ($H_2O_2$, •OOH, and/or $O_2^{\bullet-}$) due to the wide variety of heme enzymes and active sites.

Understanding the relationship between ROS and iron intermediates is important

for deciphering how these powerful redox active species are controlled in nature. This knowledge, in turn, could provide insights into to their roles in disease progression through uncontrolled or mis-regulated oxidation reactions. Considering the known reactivity of compound I and compound II species toward $H_2O_2$ in heme enzymes, it is interesting that a similar interaction with $H_2O_2$ has not been reported for oxoiron(IV) intermediates involved in the catalytic cycles of mononuclear nonheme iron enzymes.[15,16,17] Such reactivity though has been suggested in the nonheme enzyme phthalate dioxygenase. [18] The presence of either non-native substrate analogs, which result in various degrees of uncoupled oxidations and the consequent production of $H_2O_2$ or addition of $H_2O_2$ during turnover led to ROS production and enzyme inactivation. When the resting enzyme was incubated with $H_2O_2$, no generation of ROS was observed. These results suggest that an intermediate involved in the catalytic cycle could be reacting with $H_2O_2$ generating ROS. A proposed pathway involving a nonheme high-valent intermediate reacting with $H_2O_2$ may explain the production of ROS and indicates that this reaction could be of great interest in the deactivation of nonheme enzymes.[19]

Different from the iron coordination in heme enzymes, nonheme oxoiron(IV) complexes can be found in nature supported by the 2-His-1-carboxylate facial triad (Figure 2.2). There has been significant recent progress in understanding the molecular structure of mononuclear nonheme proteins by structural and spectroscopic methods, and these enzymes have been shown to carry out a wide variety of important oxidation reactions.[15, 20] Although the different iron coordination spheres, distal pocket environments, and spin states of the oxoiron(IV) intermediates found in heme and

nonheme iron enzymes afford specific oxidative reactivities, similar reactions can occur in both enzyme families.[15,16,17,20,21,22,23,24,25] For example, both the nonheme iron enzyme taurine α-ketoglutarate dioxygenase (TauD) and the heme-based cytochrome P450 enzymes promote C−H bond oxidation. These comparable reactions lead us to wonder whether nonheme oxoiron(IV) species play a role similar to that of catalases and other heme enzymes in modulating the fate of $H_2O_2$ and if so, how? We sought to first determine if nonheme oxoiron(IV) species could react with $H_2O_2$, and to secondly, compare their reactivity with heme oxoiron(IV) species to better understand the reactivity of the oxoiron(IV) unit with $H_2O_2$.

### 2.1.3 Biomimetic Iron Compounds

The feasibility of nonheme oxoiron(IV) species reacting with $H_2O_2$ may first be validated through the use of biomimetic model complexes.[24] The first X-ray crystallographic evidence supporting the structures of these model compounds was obtained in 2003 for $[Fe^{IV}O(tmc)(NCCH_3)](OTf)$ (**1**, tmc = 1,4,8,11-tetra-methyl-1,4,8,11-tetraazacyclotetradecane).[26] The X-ray structure of this complex shows iron-oxygen double bond character supported by the nonheme ligand (Figure 2.3). Spectroscopic characterization of **1,** along with another model complex $[Fe^{IV}O(N4Py)](OTf)_2$ (**2**, N4Py = N,N-bis(2-pyridylmethyl)-N-[bis(2-pyridyl)methyl]amine), provided strong support for the presence of a nonheme oxoiron(IV) moiety (Figure 2.3).[27,28] These initial two examples have provided vast insights into the mechanisms of chemical reactions underlying biological functions of oxoiron(IV) and other nonheme iron–oxygen intermediates.[24,29] These complexes have been utilized to isolate and characterize iron-oxygen adducts important in iron-containing metalloenzymes as well as to mimic their oxidative activity

towards organic substrates (C−H bond activation and oxygen atom transfer reactions).[21,24,29,30,31] Additionally, these complexes have been used to gain important insight into fundamental electron transfer chemistry involving the oxoiron(IV) group[32] as well as into its reactivity towards reactive nitrogen species (RNS). [33]

**Figure 2.3. Structures of 1 and 2.**

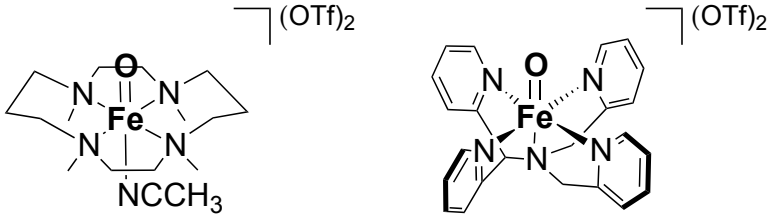


**1** **2**

### 2.1.4 Reactivity of $H_2O_2$ with Oxometal Compounds

Inorganic chemistry has provided many examples of $H_2O_2$ interacting with oxometal complexes for a variety of metals. The mechanisms of these transformations mainly involve coordination of peroxide to the metal center and exchange of the oxo ligand with peroxide (Figure 2.4a).[34,35,36,37,38] In contrast, relatively few examples of direct reaction of $H_2O_2$ with terminal or bridging oxo ligands through hydrogen atom transfer leading to $O_2$ generation have been observed with V, Cr, Mn, or Ru (Figure 2.4b).[34,38,39,40,41,42,43] The latter mechanism is related to the HAT mechanism of catalases described above (Figure 2.1b,c).

**Figure 2.4. General interaction modes for $H_2O_2$ and oxometal complexes.**

**a) $H_2O_2$ Metal Coordination and Exchange**

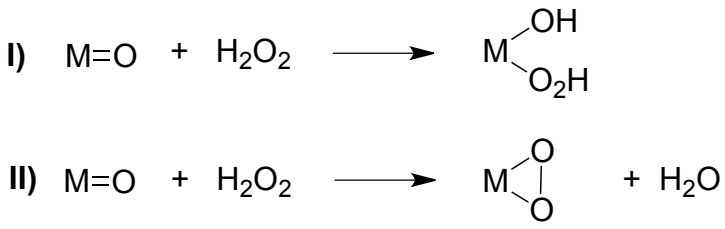


**b) $H_2O_2$ Interaction with Oxo Ligand**

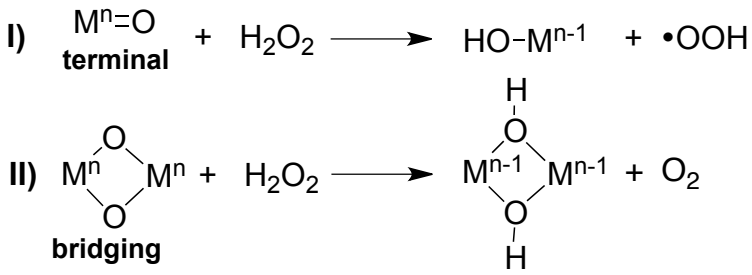


In iron chemistry, several studies involving the Fenton reaction ($Fe^{II}$ or $Fe^{III}$ salts and $H_2O_2$ or $O_3$) have proposed the interaction of aqueous oxoiron(IV) species with $H_2O_2$ at intermediate steps under acidic conditions.[44,45,46,47,48,49] $Fe^{II}$ and $Fe^{III}$ metal complexes have also been developed as catalase or peroxidase mimics where high-valent species were suggested to be involved in the dismutation of $H_2O_2$.[50,51] Other studies utilizing heme model compounds as oxidants of organic molecules have suggested that compound I analogs undergo competing reactions with $H_2O_2$ and organic peroxides against the oxidation of organic substrates by compound I analogs.[52,53,54,55] One recent study has shown this reaction to be possible in the absence of organic substrates indicating that a porphyrin compound I analog can react with $H_2O_2$.[56] These studies suggest the reactivity of high-valent oxoiron compounds with $H_2O_2$; however, detailed investigations have not been carried out to determine the reaction mechanisms. Most of these cases entail complicated reaction kinetics due to

the existence of multiple pathways involving different iron and oxygen species. Like the challenges with the catalase mechanism, $H_2O_2$ acting as both an oxidant and reductant in some of these examples complicates the observation of interactions between $H_2O_2$ and the high-valent intermediates. In summary, previous literature reports support the feasibility of interactions between $H_2O_2$ and heme and nonheme oxoiron(IV) complexes; however, neither direct observation of this reactivity nor mechanistic understanding of this transformation have been obtained.

The generation of both heme and nonheme oxoiron(IV) complexes can be carried out independent of $H_2O_2$ using alternative oxidants such as iodosobenzene (PhIO) and *m*-chloroperbenzoic acid (*m*-CPBA).[24,57] This provides an experimental system where the interference of $H_2O_2$ reacting with $Fe^{II}$ or $Fe^{III}$ starting material is minimized, thereby providing an opportunity to investigate the direct reactivity of the oxoiron(IV) group with $H_2O_2$. Using this approach, we have expanded upon investigations of the chemistry between high-valent oxoiron(IV) intermediates and $H_2O_2$.[6,10,58,59,60,61] This thesis chapter presents evidence for the direct and relatively rapid reaction of the mononuclear nonheme oxoiron(IV) complex **2** with $H_2O_2$.[62] To the best of our knowledge, this reaction demonstrates for the first time direct $H_2O_2$ reactivity of a terminal $Fe^{IV}$=O group of a nonheme iron complex. Additionally, studies on the less reactive nonheme complex **1** and heme oxoiron(IV) complexes are compared to the reactivity of **2** and $H_2O_2$ to gain insight into how these ligand frameworks affect this transformation in metalloenzymes. These studies indicate that in addition to heme-containing proteins, it may also be possible for high-valent nonheme species to be involved in ROS mechanisms in biological systems.

## 2.2 Nonheme Oxoiron(IV) Reactivity with $H_2O_2$

### 2.2.1 Studies with Fe(N4Py)

**Figure 2.5. Generation of 2.**

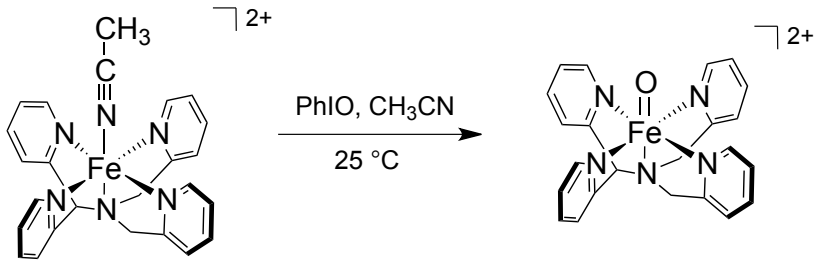


**3** **2**

Complex **2** was generated by treating $[Fe^{II}(N4Py)(CH_3CN)]^{2+}$ (**3**; Figure 2.5) with PhIO,[27,28] which resulted in oxidation of the $Fe^{II}$ center independent of $H_2O_2$. As shown in Figure 2.6a, the characteristic absorption band of **2** ($\lambda_{max}$ = 692 nm) disappeared upon the addition of $H_2O_2$ to a $CH_3CN$ solution of **2** at −20 °C, indicating its direct reaction with $H_2O_2$. The nearly full decay (*ca.* 94%) of **2** required 0.5 equiv of $H_2O_2$ with a half-life of about 20 min, suggesting a 2:1 stoichiometry for the reaction (Figure 2.6b). After the decay of **2**, the reaction ultimately produced **3** in fairly high yield (*ca.* 85%, after 250 min) as determined from the absorption bands at 380 and 454 nm (Figure 2.6c). No spectral bands of intermediates were evident in the UV-Vis spectra, even at $t_{1/2}$ (*ca.* 30 min, green line, Figure 2.6c). Small changes were evident at 380 and 454 nm after the decay of **2** suggesting the presence of iron species preceding the formation of **3** (black and red lines, Figure 2.6c).

**Figure 2.6. UV-Vis studies on the reaction of 2 with 0.5 equiv of $H_2O_2$.**

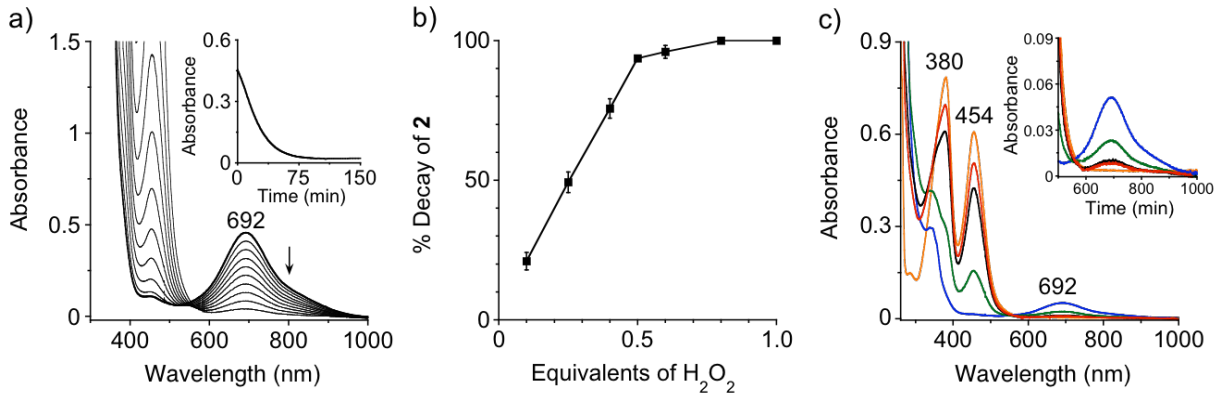


Conditions: Left: Reaction of 1.0 mM **2** (bold line) in $CH_3CN$ with 0.5 equiv of $H_2O_2$ at −20 °C (path length, 1.0 cm) Inset: Time course of the decay of **2** (692 nm). Middle: Percent decay of **2** (1 mM) with $H_2O_2$ (0.1−1.0 equiv) based on absorbance at 692 nm at the end of the reaction. Right: Reaction carried out with a 0.1 cm pathlength. Spectra indicate **2** (1 mM, blue, 692 nm), **3** (1 mM, orange, 380 and 454 nm), $t_{1/2}$ (green, 30 min), near full consumption of **2** (black, 100 min), and after no further spectral changes (red, 250 min).

The decomposition of **2** and formation of **3** were confirmed by electrospray ionization mass spectrometry (ESI-MS) and $^1$H NMR spectroscopy (Figure 2.7 and Figure 2.8). The signals corresponding to $[Fe^{IV}O(N4Py)]^{2+}$ and $\{[Fe^{IV}O(N4Py)] + OTf\}^+$ at 219.5 and 588.0 m/z were replaced by $[Fe^{II}(N4Py)]^{2+}$ and $\{[Fe^{II}(N4Py) + OTf\}^+$ at 211.5 and 572.0 m/z as the major species after the reaction went to completion with 0.5 equiv of $H_2O_2$ (Table 2.1). Likewise, the broad signals in the $^1$H NMR spectrum extending from −20 – 50 Hz due to the paramagnetic nature of **2** returned to the normal diamagnetic region (0 – 10 Hz, Figure 2.8, inset), indicating the formation of **3** as compared to the starting material. No intermediates were observed for either method but both are consistent with the UV-Vis data indicating the overall conversion of **2** to **3** upon reaction with 0.5 equiv of $H_2O_2$.

**Figure 2.7. ESI(+)MS mass spectra of 2, 3, and the products of the reaction of 2 with 0.5 equiv $H_2O_2$.**

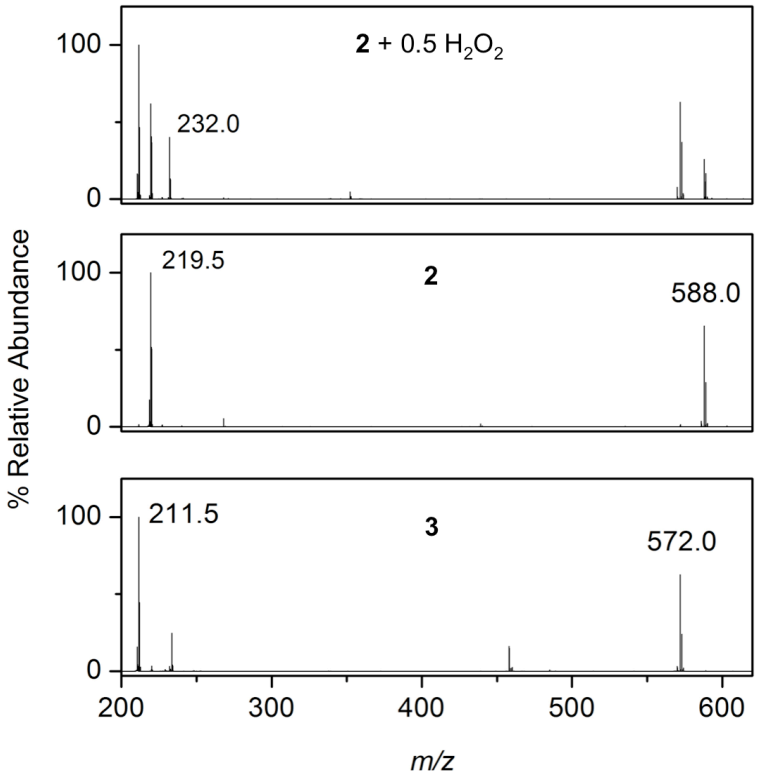


Conditions: Reaction of 1.0 mM **2** in $CH_3CN$ with 0.5 equiv of $H_2O_2$ carried out at −20 °C.

**Table 2.1. Observed and calculated *m/z* values from reaction of 2 with $H_2O_2$.**

| Species | Observed (*m/z*) | Calculated (*m/z*) |
|---|---|---|
| $[Fe^{II}(N4Py)]^{2+}$ | 211.5 | 211.6 |
| $\{[Fe^{II}(N4Py)] + CH_3CN\}^{2+}$ | 232.0 | 232.1 |
| $\{[Fe^{II}(N4Py)] + OTf\}^{+}$ | 572.0 | 572.1 |
| $[Fe^{IV}O(N4Py)]^{2+}$ | 219.5 | 219.5 |
| $\{[Fe^{IV}O(N4Py)] + OTf\}^{+}$ | 588.0 | 588.1 |

**Figure 2.8. $^1$H NMR spectra of 2, 3, and the products of the reaction of 2 and 0.5 equiv of $H_2O_2$.**

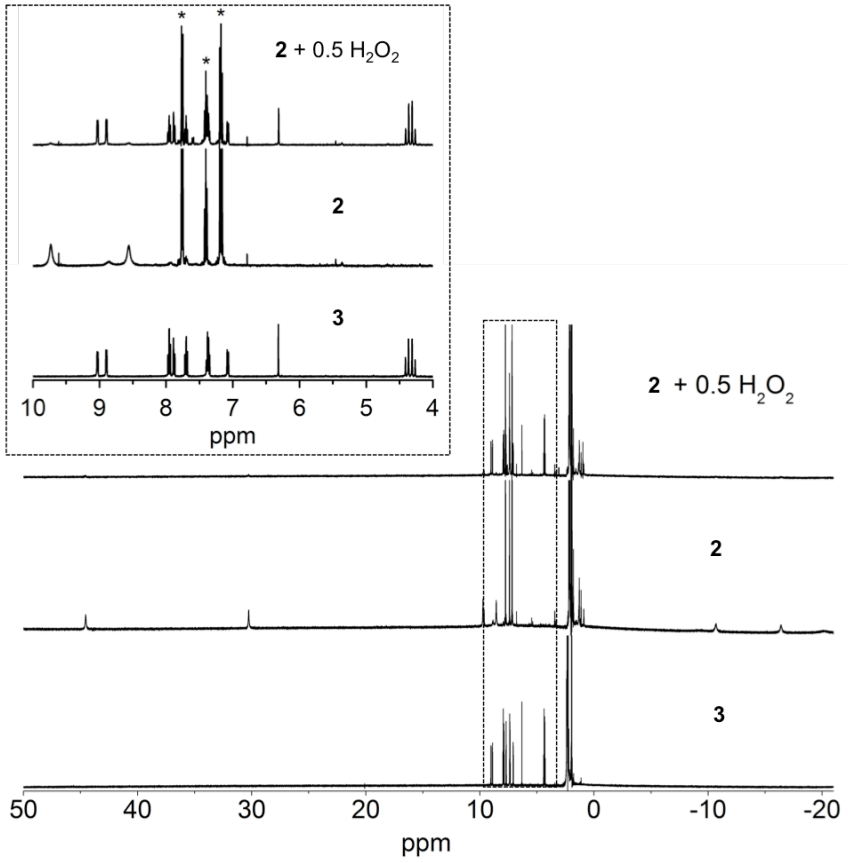


Conditions: Reaction of 1.0 mM **2** with 0.5 equiv $H_2O_2$ carried out at −20 °C in $CD_3CN$. Spectra acquired at rt. * indicate iodobenzene (PhI).

On the basis of the 2:1 stoichiometry of **2** to $H_2O_2$, a plausible mechanism for the initial phase of the reaction involves two hydrogen atom transfers (HAT) from $H_2O_2$ to **2** to produce 0.5 equiv of $O_2$ with respect to **2** [Eqs. 4 and 5, L = N4Py].[63,64] To verify $O_2$ generation, the concentration of dioxygen was measured by an optical probe throughout the reaction of 1 mM **2** with 0.5 equiv of $H_2O_2$ (Figure 2.9). Indeed, 19 ± 1 ppm of $O_2$ was detected upon decay of **2** (0.47 mM $O_2$, *ca.* 95% yield based on two HATs from $H_2O_2$). Control reactions of **2** only, $CH_3CN$ only, $H_2O_2$ only, and **3** + $H_2O_2$ indicated no significant generation of $O_2$ under the experimental conditions (Figure 2.9b). Both the

stoichiometric production of $O_2$ and the 2:1 ratio of the reactants (Figure 2.6b and Figure 2.9) support the mechanism described by Equations 4 and 5. The 2:1 ratio also implies that $O_2$ is not formed (or with only minimal contribution) from the reaction of the $Fe^{III}$ complex $[Fe^{III}(N4Py)(OH)]^{2+}$ (**4**) with the hydroperoxyl radical (•OOH) [Eq. 6], because this would require a 1:1 ratio.

**Figure 2.9. Determination of $O_2$ generation for 2 and $H_2O_2$.**

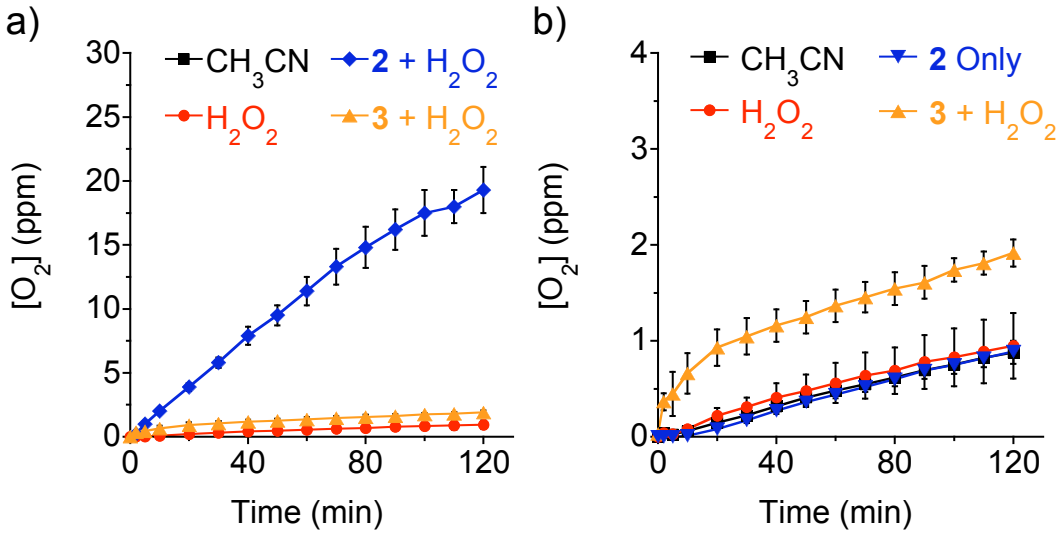


Conditions: a) Evolution of $O_2$ at −20 °C upon addition of 0.5 equiv of $H_2O_2$ to 1.0 mM solutions of **2** (blue) and **3** in $CH_3CN$ (orange) and upon introduction of the same amount of $H_2O_2$ into $CH_3CN$ (red). $CH_3CN$ only is shown in black. b) Expansion of a) showing results for control reactions in addition to monitoring $O_2$ evolution in the presence of **2** only.

$$\underset{\mathbf{2}}{[(L)Fe^{IV}{=}O]^{2+}} + H_2O_2 \longrightarrow \underset{\mathbf{4}}{[(L)Fe^{III}{-}OH]^{2+}} + {\bullet}OOH \quad (4)$$

$$\underset{\mathbf{2}}{[(L)Fe^{IV}{=}O]^{2+}} + {\bullet}OOH \longrightarrow \underset{\mathbf{4}}{[(L)Fe^{III}{-}OH]^{2+}} + O_2 \quad (5)$$

$$\underset{\mathbf{4}}{[(L)Fe^{III}{-}OH]^{2+}} + {\bullet}OOH \longrightarrow [(L)Fe^{II}{-}OH_2]^{2+} + O_2 \quad (6)$$

Complex **4** would then be the expected iron product from the reaction of **2** with $H_2O_2$ [Eqs. 4 and 5]. Although direct evidence for **4** was not obtained by UV-Vis

spectroscopy, the lag phase in the formation of **3** at 454 nm, along with an initial isosbestic point at 536 nm (Figure 2.10), suggest the formation of an intermediate that does not absorb light in this region.[65,66]

**Figure 2.10. Initial stage of reaction for 2 and $H_2O_2$.**

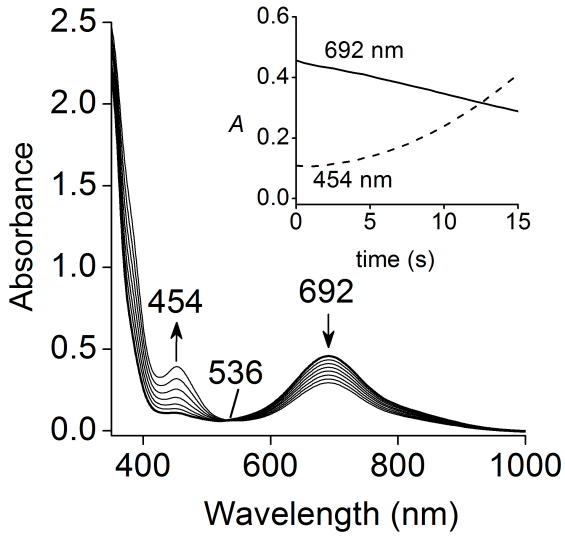


Conditions: Spectra of the first 15 min of the reaction of 1.0 mM **2** in $CH_3CN$ (bold line) with 0.5 equiv of $H_2O_2$ at −20 °C (path length, 1.0 cm). Inset: Time courses of the decay of **2** (λ = 692 nm, solid line) and the formation of **3** (λ = 454 nm, dashed line).

To probe potential iron-containing paramagnetic species prior to the production of **3**, the reaction of **2** with 0.5 equiv of $H_2O_2$ was investigated by electron paramagnetic resonance (EPR) spectroscopy (Figure 2.11). The spectrum of a sample of the reaction mixture frozen after the disappearance of **2** exhibited an EPR signal ($g$ = 2.40, 2.14, and 1.94) corresponding to **4** (Figure 2.11c).[65] However, in comparison to an authentic sample of **4** prepared in acetone, the signal was very weak, indicating that this complex was not present in a substantial amount. An EPR signal of an unidentified species was also observed throughout the reaction of **2** with 0.5 equiv of $H_2O_2$ ($g$ = 2.28, 2.13, and 1.96), which is possibly attributable to $[Fe^{III}(N4Py)(CH_3CN)]^{3+}$ (**5**) or $[Fe^{III}(N4Py)(H_2O)]^{3+}$

(Figure 2.11c).[67] Furthermore, an $Fe^{III}$ species present upon oxidation of **3** with PhIO ($g$ = 4.3) was also observed and is most likely attributable to incomplete formation of **2**.[68] The low accumulation of **4** in the reaction of **2** with 0.5 equiv of $H_2O_2$ could be due to its fast conversion to **5** and self-decay to **3** in $CH_3CN$ (Figure 2.13). An alternative route may also involve an equilibrium between **4** and the oxo-bridged dimer $[\{Fe^{III}(N4Py)\}_2(\mu\text{-}O)]^{4+}$ (**6**), which is EPR silent (X-band, perpendicular mode) and does not absorb light in the visible region (Figure 2.13).[65,66]

**Figure 2.11. EPR spectra of the reaction of 2 with $H_2O_2$.**

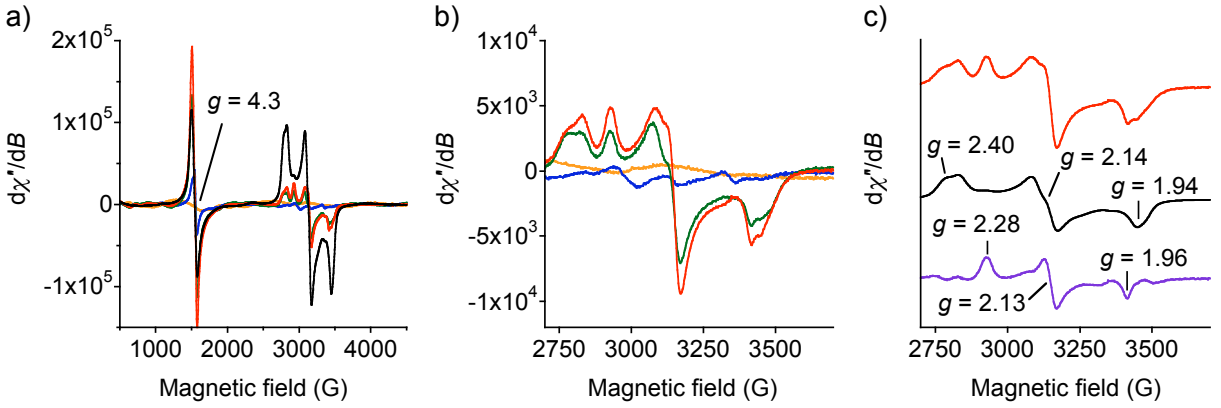


Conditions: Spectra of the reaction of 1.0 mM **2** in $CH_3CN$ at −20 °C with 0.5 equiv of $H_2O_2$. a) EPR spectra (recorded at 4 K) of frozen samples of 1.0 mM solutions of **2** (blue) and **3** (orange) in $CH_3CN$ and of samples of the reaction of 1.0 mM **2** with 0.5 equiv of $H_2O_2$ (in $CH_3CN$ at −20 °C) frozen at *ca.* 22 min (green) and at nearly complete decay of **2** (*ca.* 100 min, red). EPR spectrum of independently generated **4** (1.0 mM in acetone, black). Signals shown in a) were magnified by a factor of five except for that of **4.** b) Expanded view of the region from 2600 to 3800 G. c) Difference EPR spectrum (purple) generated by subtraction of the spectrum of **4** (reduced by a factor of 25, black) from that of the reaction mixture (*ca.* 100 min, red).

To determine kinetic parameters, the reaction of **2** with $H_2O_2$ was studied under pseudo-first-order conditions. The observed rate constant ($k_{obs}$) for the decomposition of **2** increased linearly with the concentration of $H_2O_2$ (Figure 2.12a), whereas no significant change in $k_{obs}$ was observed for varying concentrations of **2** (Figure 2.12b). This behavior indicates a bimolecular reaction with a $k_2$ value of 0.80 ± 0.02 L $mol^{-1}$ $s^{-1}$. Unexpectedly, no dependence on the concentration of deuterium peroxide ($D_2O_2$) was

observed upon varying its concentration (Figure 2.12c). Therefore, no kinetic isotope effect (KIE = $k_H/k_D$) could be determined for this reaction. However, the reaction of **2** with 0.5 equiv of $D_2O_2$ proceeded to only 75% completion, suggesting the possibility of a change in the reaction mechanism. Activation parameters for the reaction of **2** and $H_2O_2$ were also determined from an Eyring plot for experiments in the temperature range from −40 to −10 °C, affording an enthalpy of activation $\Delta H^{\ddagger}$ of 30.8 ± 0.7 kJ mol$^{-1}$ and an entropy of activation $\Delta S^{\ddagger}$ of −158 ± 2 J mol$^{-1}$ K$^{-1}$ (Figure 2.12).

**Figure 2.12. Kinetics and thermodynamics results for the reaction of 2 and $H_2O_2$.**

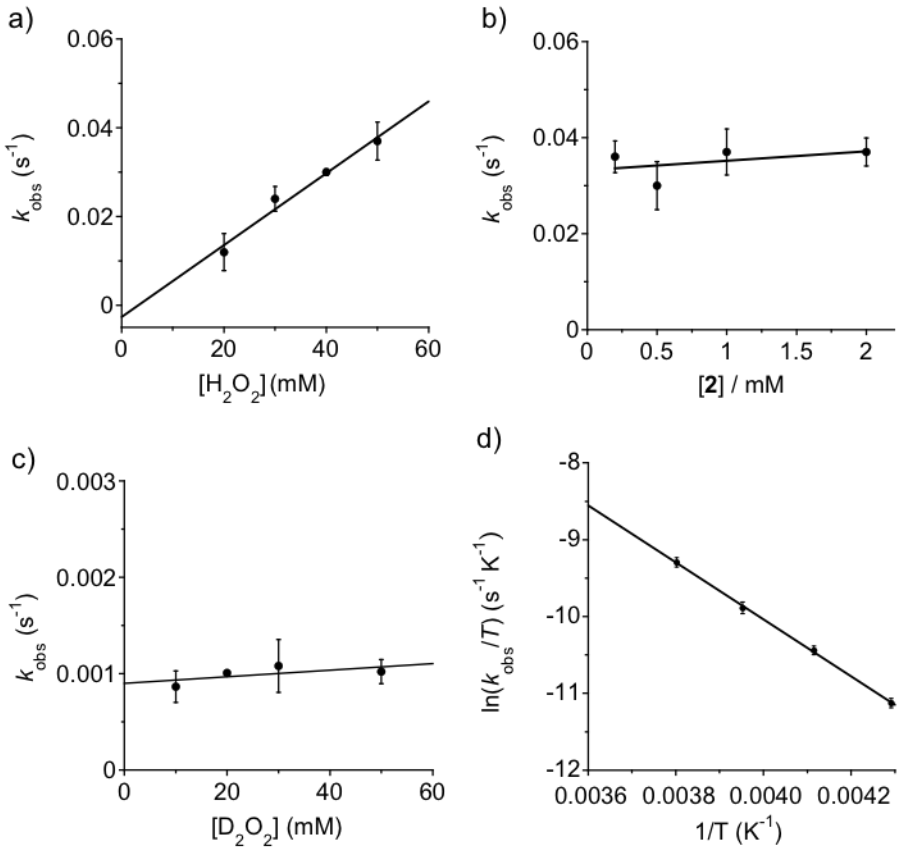


Conditions: a) Plot of the pseudo-first-order rate constant $k_{obs}$ versus [$H_2O_2$] (20–50 mM) to determine the second-order rate constant $k_2$ at −20 °C. b) Plot of the pseudo-first-order rate constant ($k_{obs}$) *versus* [**2**] (0.2 – 2.0 mM) for the reaction of **2** with 50 mM $H_2O_2$ in $CH_3CN$ at −20 °C. c) Plot of the pseudo-first-order rate constant $k_{obs}$ versus [$D_2O_2$] (10–50 mM) to determine the second-order rate constant $k_2$ at −20 °C. d) Eyring plot for the reaction of **2** with 20 equiv of $H_2O_2$ (T = 233–263 K).

### 2.2.2 Mechanistic Considerations (2:1 Stoichiometry)

**Figure 2.13. Proposed reaction mechanism.**

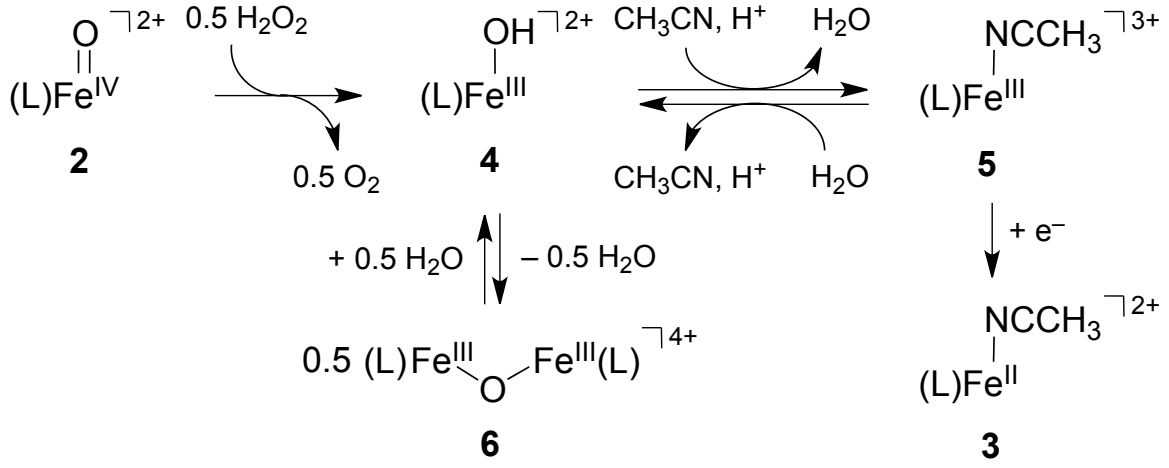


On the basis of these stoichiometric and kinetic studies we conclude that the oxoiron(IV) ligand of **2** directly interacts with $H_2O_2$ (Figure 2.13). At low concentrations of $H_2O_2$ (0.5 equiv), the oxidized product (•OOH) can also react with oxoiron(IV) to generate $O_2$ (Eq. 5). When the reaction is carried out with 0.5 equiv of $H_2O_2$, the decomposition of $H_2O_2$ appears to be dependent only on **2** (Figure 2.13). The interaction of **4** or **5** with $H_2O_2$ (Eqs. 7 and 8) under limiting $H_2O_2$ are not involved to an observable degree because no spectral features for $[Fe^{III}(N4Py)(OOH)]^{2+}$ (**7**) are seen in the EPR spectra.[65,73] Although these two $Fe^{III}$ complexes were not directly observed under our conditions, their formation and decay is reasonable based on previous electrochemical studies carried out in wet $CH_3CN$.[66] The identity of the one-electron source, which leads to the observed final product **3** from **5**, has not been identified. With a potential of 1.01 V (relative to NHE) for the reduction in $CH_3CN$, the reduction of **5** is expected to be facile.[66] The slow formation of **3** at the end of the reaction may be due to complex **6** being a relatively thermodynamic stable species under our conditions. Slow conversion of **6** to **3** *via* the pathway in Figure 2.13 may explain why small absorption changes are

observed by UV-Vis after the reaction of **2** and $H_2O_2$ has gone to completion (Figure 2.6c, *vide supra*). Overall, we propose the decomposition of $H_2O_2$ into $O_2$ under stoichiometric conditions is facilitated by the reaction with the high-valent oxoiron(IV) species **2** and the formation of **3** is independent of $H_2O_2$ or •OOH.

$$\underset{\mathbf{4}}{[(L)Fe^{III}\text{–}OH]^{2+}} + H_2O_2 \longrightarrow \underset{\mathbf{7}}{[(L)Fe^{III}\text{–}OOH]^{2+}} + H_2O \quad (7)$$

$$\underset{\mathbf{5}}{[(L)Fe^{III}\text{–}NCCH_3]^{3+}} + H_2O_2 \longrightarrow \underset{\mathbf{7}}{[(L)Fe^{III}\text{–}OOH]^{2+}} + CH_3CN + H^+ \quad (8)$$

$$\underset{\mathbf{2}}{[(L)Fe^{II}\text{–}NCCH_3]^{2+}} + 1.5\ H_2O_2 \longrightarrow \underset{\mathbf{7}}{[(L)Fe^{III}\text{–}OOH]^{2+}} + CH_3CN + H_2O \quad (9)$$

$$\underset{\mathbf{2}}{[(L)Fe^{II}\text{–}NCCH_3]^{2+}} + \text{•OOH} \longrightarrow \underset{\mathbf{7}}{[(L)Fe^{III}\text{–}OOH]^{2+}} + CH_3CN \quad (10)$$

It is also important to consider the possible decomposition pathways of •OOH. Studies have shown that •OOH (protonated superoxide, p$K_a$ = 4.7 in $H_2O$, p$K_a$ ≈ 12 in DMF, Eq. 11) does not react to a considerable degree with itself in nonpolar solvents like acetonitrile (Eq. 12).[69,70] The disproportionation of •OOH is proposed to occur through the one electron reduction by $O_2^{\bullet-}$ to give $^-$OOH and $O_2$ (Eq. 13). Since the p$K_a$ of •OOH is higher in aprotic solvent, the equilibrium in Equation 11 is expected to lie far to the right under our conditions. This greatly reduces the influence that Equation 13 would have under our conditions. Therefore, it is proposed that the main decomposition pathways for •OOH leading to $O_2$ generation under stoichiometric $H_2O_2$ (0.5 equiv) is *via* HAT to **2** (Eq. 5).

$$O_2^{\bullet-} + H^+ \leftrightarrows \text{•OOH} \quad (11)$$

$$\text{•OOH} + \text{•OOH} \rightarrow H_2O_2 + O_2 \quad (12)$$

$$\text{•OOH} + O_2^{\bullet-} \rightarrow {}^-OOH + O_2 \quad (13)$$

The second HAT reaction is expected to proceed at a much faster rate than the first (Eq. 4 versus Eq. 5) based on bond dissociation energies (H-OOH = 89 kcal $mol^{-1}$; H-OO• = 47 kcal $mol^{-1}$).[71] This is the case under aqueous conditions where •OOH reacts 200 times faster with oxoiron(IV) than $H_2O_2$ based on detailed kinetic modeling studies.[72] In a study by Jacobsen *et al*., pseudo first-order behavior for the reaction of aqueous oxoiron(IV) species with $H_2O_2$ was observed with no significant deviation due to the reaction with •OOH. Similar behavior is assumed under our conditions in $CH_3CN$ where we observed pseudo first-order kinetics for up to three half lives.

### 2.2.3 Mechanistic Considerations (Excess $H_2O_2$)

In contrast to the reaction of **2** with 0.5 equiv of $H_2O_2$, the absorption spectra of reactions with an excess of $H_2O_2$ showed an additional feature at 532 nm that is indicative of **7** (Figure 2.14a), which was confirmed by EPR spectroscopy (Figure 2.14b). These spectroscopic data were consistent with those previously reported for **7** in addition to the independent generation of **7** in $CH_3CN$ by the addition of a large excess of $H_2O_2$ to **3** (Figure 2.14c,d).[65,73] Complex **7** forms from the reaction of **4** with $H_2O_2$ [Eq. 7] in addition to other possible pathways involving $Fe^{III}$ or $Fe^{II}$ species and •OOH or excess $H_2O_2$ (Eqs. 8-10).[65] The reaction is still initiated by the interaction of **2** with $H_2O_2$, although a competition between the H−OOH and •OO−H bonds is expected.

**Figure 2.14. Formation of 7 in the reaction of excess $H_2O_2$ with 2 and 3.**

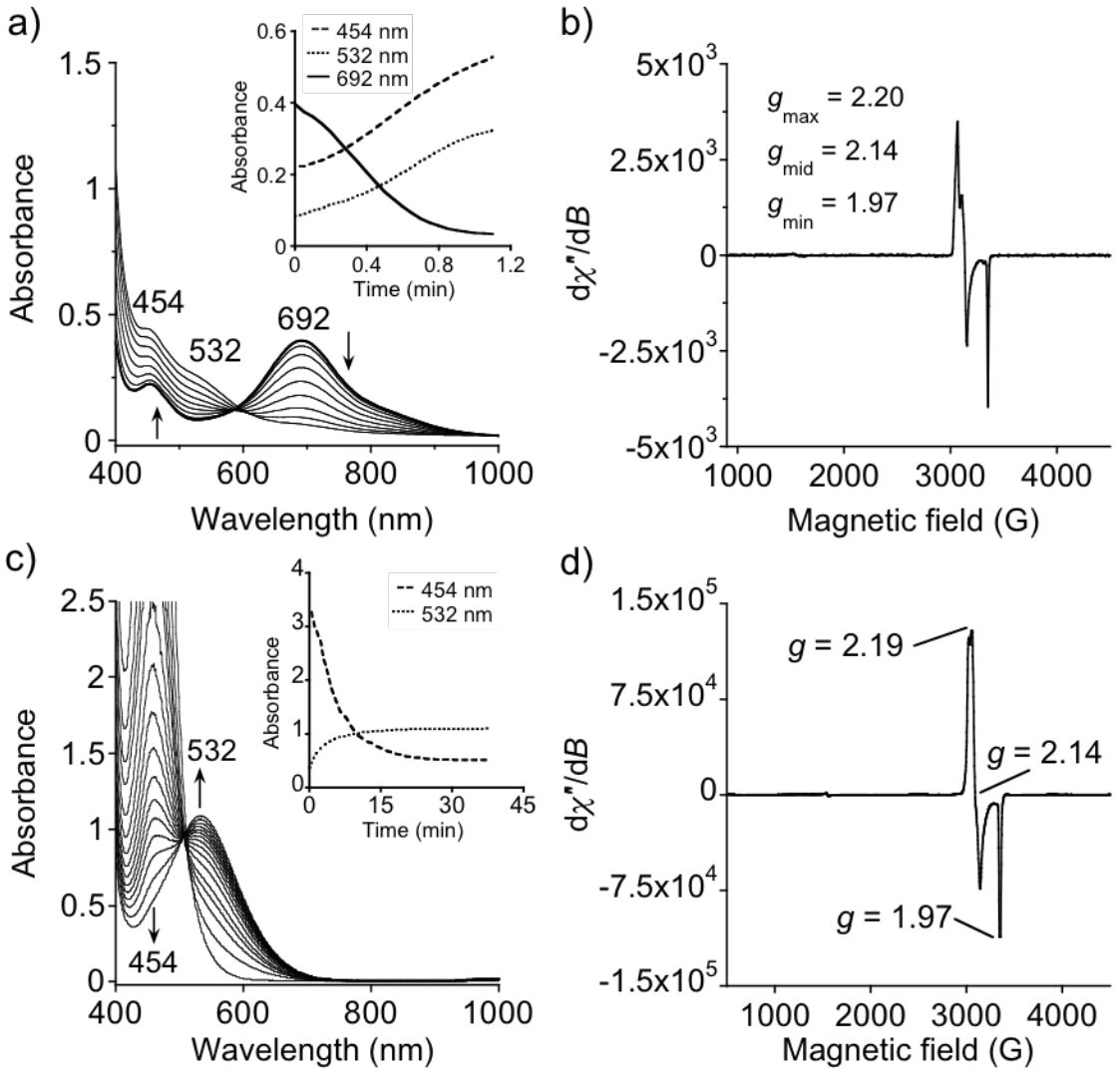


Conditions: a) Spectra of the first 1 min of the reaction of 1.0 mM **2** in $CH_3CN$ (bold line) with 50 equiv of $H_2O_2$ at −20 °C (path length, 1.0 cm). Inset: Time courses of the decay of **2** (λ = 692 nm, solid line), formation of **3** (λ = 454 nm, dashed line), and formation of **7** (λ = 532 nm, dotted line). b) EPR spectrum of a sample obtained upon consumption of **2** in the reaction of 1.0 mM **1** with 20 equiv of $H_2O_2$ (in $CH_3CN$ at −20 °C). c) UV-Vis spectra of the formation of **7** ($\lambda_{max}$ = 532 nm) upon the addition of 700 equiv of $H_2O_2$ to 1.0 mM **3** in $CH_3CN$ at −20 °C (path length, 1.0 cm). Inset: Time courses of the decay of **3** (λ = 454 nm, dashed line) and formation of **7** (λ = 532 nm, dotted line). d) EPR spectrum of **7** from Independent generation in c).

### 2.2.4 Reactivity Comparisons

For comparison, the reaction of another nonheme oxoiron(IV) complex, $[Fe^{IV}O(tmc)(NCCH_3)]^{2+}$ (**1**, Figure 2.15a), with $H_2O_2$ was investigated. The generation of **1** is carried out in a similar fashion to **2** with PhIO (Figure 2.5), except 1.0 equiv of PhIO is added from a methanol ($CH_3OH$) solution. The reactivity of this complex in the similar solvent system ($CH_3CN$, 1.3% $CH_3OH$) was significantly slower than that of **2**, yielding a $k_2$ value of $(3.5 \pm 0.2) \times 10^{-2}$ L mol$^{-1}$ s$^{-1}$ at 25 °C (Figure 2.15b). No dependence on the concentration of **1** was observed, in agreement with pseudo first-order conditions (Figure 2.15d). This result is consistent with the lower reactivity of **1** (compared to **2**) previously observed in oxidation reactions of organic substrates.[24,27] Analysis of the reaction by ESI-MS indicated that the metal-free ligand predominated after the reaction. This is different from **2**, where 85% of the $Fe^{II}$ UV-Vis spectral feature could be observed. Possible instability of the $Fe^{III}$−OH species formed upon HAT from $H_2O_2$ by **1** may lead to demetallation of the complex. Although complex **1** decomposes after the reaction, the dependence of $H_2O_2$ on the rate of decay of the oxoiron(IV) species suggests direct interaction.

**Figure 2.15. Structure of 1 and kinetics studies with $H_2O_2$.**

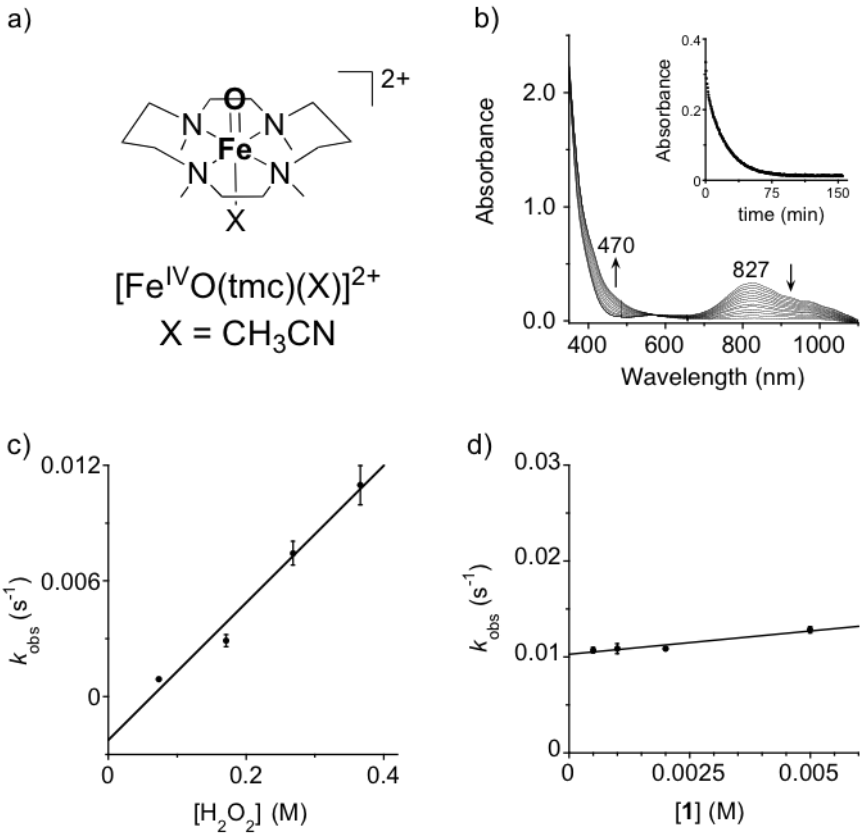


Conditions: b) Spectra of the reaction of 1.0 mM **1** ($\lambda_{max}$ = 827 nm) with 75 equiv of $H_2O_2$ (path length, 1.0 cm). Inset: Time course of the reaction ($\lambda$ = 827 nm). c) Plot of $k_{obs}$ *versus* [$H_2O_2$] (73 – 366 mM) for the reaction of 1.0 mM **1** with $H_2O_2$. d) Plot of $k_{obs}$ *versus* [**1**] (0.5 – 5.0 mM) for the reaction of **1** with 366 mM $H_2O_2$. All reactions carried out in $CH_3CN$ at 25 °C.

On the other hand, the $H_2O_2$ reactivity of **2** is comparable to that of the oxoruthenium(IV) complex $[Ru^{IV}O(bpy)_2(py)]^{2+}$ (**8**, Eqs 14 and 15, Figure 2.16). When the reaction of **2** with an excess of $H_2O_2$ was carried out at 25 °C, a *k*' value of *ca.* 8 L $mol^{-1}$ $s^{-1}$ was obtained (*k*' = $k_{obs}$/[$H_2O_2$]), while a similar value had been reported for the Ru complex, albeit in a different solvent [*k*' = 12.7 ± 1.3 L $mol^{-1}$ $s^{-1}$ (25 °C, $H_2O$, pH 7.92)].[40] Additionally, the stoichiometry for the Ru case was shown to be 1:1, which differs from the Fe case shown here. One main difference between Ru and Fe is the

involvement of the one electron reduced product $M^{III}$−OH (M = Fe or Ru) reacting with $H_2O_2$. Instead of oxidation, acid-base chemistry is observed for **4** and $H_2O_2$ producing **7** (Eq. 7)[65] while the $Ru^{III}$-OH case can oxidize both $H_2O_2$ and •OOH substrates, the latter being faster (Eqs. 16 and 17).[40]

**Figure 2.16. Structure of 8.**

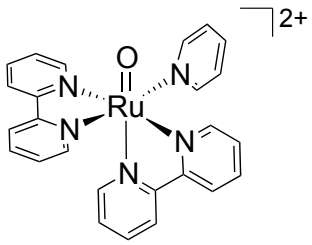


**8**

$$Ru^{IV}O + H_2O_2 \rightarrow Ru^{III}\text{−}OH + \bullet OOH \quad (14)$$

$$Ru^{IV}O + \bullet OOH \rightarrow Ru^{III}\text{−}OH + O_2 \quad (15)$$

$$Ru^{III}\text{−}OH + H_2O_2 \rightarrow Ru^{II}\text{−}OH_2 + \bullet OOH \quad (16)$$

$$Ru^{III}\text{−}OH + \bullet OOH \rightarrow Ru^{II}\text{−}OH_2 + O_2 \quad (17)$$

Previous reactivity studies of nonheme oxoiron(IV) complexes have largely been focused on organic substrates. For C−H bond activation mediated by nonheme oxoiron(IV) complexes (including **2**), the bond dissociation energy (BDE) and $k_2$' typically are inversely correlated ($k_2' = k_2/n$, where $n$ is the number of available protons for hydrogen atom transfer).[24] Complex **2** showed a higher reactivity toward $H_2O_2$ ($k_2'$ = 0.40 ± 0.01 L $mol^{-1}$ $s^{-1}$, −20 °C) than in C−H bond activation reactions ($k_2'$ = 4.6 ± $10^{-6}$–0.037 L $mol^{-1}$ $s^{-1}$, 25 °C, BDE = 81–99 kcal $mol^{-1}$),[27] even though the BDE of the O−H bond in $H_2O_2$ (89.5 kcal $mol^{-1}$)[71] falls in the range of the C−H BDEs of the hydrocarbon substrates used. The divergence from the correlation of BDE and $k_2$' is consistent with the greater reactivity of O−H bonds over C−H bonds in HAT mechanisms.[64] Taken

together, complex **2** exhibits significantly greater $H_2O_2$ reactivity than **1** and is also more reactive toward $H_2O_2$ than toward hydrocarbon C−H bond activation.

### 2.2.5 Implications of Nonheme Reactivity

The nature of the reaction of the nonheme oxoiron(IV) complex **2** with $H_2O_2$ presents a new view of iron redox chemistry and potentially of ROS detoxification and/or production. In the context of reactive metal-oxygen intermediates and also the oxidation of organic substrates catalyzed by metalloenzymes or synthetic metal complexes, $H_2O_2$ is commonly an oxidant.[5,6,10,23,24] In our study with a nonheme iron model complex, we have demonstrated that $H_2O_2$ can also function as a reductant resulting in $O_2$ production. $H_2O_2$ can therefore be added to the list of possible substrates for biomimetic oxoiron(IV) complexes in addition to organic substrates and NO•. This is an important observation for oxidation chemistry, especially in catalysis, because the desired oxidation activity of high-valent oxoiron(IV) species may be hindered from reacting with desired C−H bonds if it is competing with H-OOH.[74,75] This type of competition has been observed in oxidation reactions involving high-valent heme compounds.[52,53,54] Our results show that when using Fe and $H_2O_2$ for the oxidation of organic substrates, the undesired reaction of high-valent species with $H_2O_2$ should be considered.

The reaction is also related to the HAT mechanism proposed for catalase compound I; however, both mechanisms differ in the ratio of oxoiron(IV) reactant to $O_2$ product; that is, 2:1 versus 1:1 [Figure 2.1, Eqs. 4 and 5].[4,5,6,7] Our results indicate that the reactivity of oxoiron(IV) species with $H_2O_2$ or •OOH within the active site of mononuclear nonheme iron enzymes may be feasible and could be involved in the detoxification or generation of ROS ($O_2$ versus •OOH/$O_2^{\bullet-}$ production) depending on the

environmental conditions. Although direct $H_2O_2$ reactivity has not been documented for oxoiron(IV) intermediates in nonheme iron enzymes, to the best of our knowledge, it is intriguing to consider this interaction as a possible mechanism in biological systems.

In conclusion, the direct reaction of $H_2O_2$ with a nonheme oxoiron(IV) complex, generated independently of $H_2O_2$, was investigated and found to be relatively rapid. Nearly full decay of **2** was achieved with 0.5 equiv of $H_2O_2$ (2:1) resulting in the formation of an $Fe^{II}$ complex, **3**, and $O_2$ (Figure 2.1). The 2:1 stoichiometry and $O_2$ generation are consistent with a mechanism involving two HAT steps from $H_2O_2$ to the $Fe^{IV}$=O group of **2**. Determination of the bimolecular rate constant under pseudo-first-order conditions revealed that the reaction of **2** with $H_2O_2$ was more facile than its previously reported reactions with hydrocarbon substrates. In the presence of an excess of $H_2O_2$, the hydroperoxoiron(III) complex **7** was formed in the course of the reaction, but this was not observed for low equivalents of $H_2O_2$. The overall observations described herein indicate that if $H_2O_2$ (and/or •OOH) can directly react with nonheme oxoiron(IV) intermediates in enzymes, it may be converted into the hydroperoxyl radical (protonated superoxide) or $O_2$ [Eqs. 4 and 5] and could thus either disrupt or contribute to ROS homeostasis. Therefore, our findings on the interaction of a nonheme oxoiron(IV) complex with $H_2O_2$ may provide new insight into the reactivity of ROS with high-valent iron centers in both biomimetic complexes and metalloenzymes.

**2.3 Further studies with Fe(tmc)**

Additional studies on the tmc framework were carried out to understand how various structural and solvent effects contribute to the reactivity of the oxoiron(IV) moiety with $H_2O_2$. A derivatized tmc ligand with the pyridyl arm generating a six

coordinate complex ($[Fe^{IV}O(tmc\text{-}Py)]^{2+}$ (**9**, tmc-Py = 1-(2'-pyridylmethyl)-4,8,11-trimethyl-1,4,8,11-tetraazacyclotetradecane, Figure 2.17) was synthesized to test influences of the axial ligand on reactivity of the oxo ligand with $H_2O_2$.[76] Coordinating and noncoordinating solvents were also compared to investigate their effects on the reactivity. Progress made to date is discussed.

**Figure 2.17. Structure of 9 and 10.**

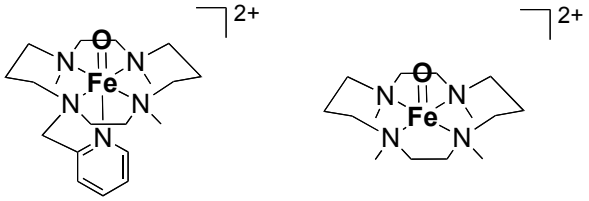


**9** **10**

The influences of solvent on the reaction of the oxoiron(IV) unit with $H_2O_2$ were preliminarily studied by carrying out the transformation in acetone, a very weakly coordinating solvent (as compared to $CH_3CN$). When oxidation of $[Fe^{II}(tmc)(OTf)](OTf)$ is carried out in acetone, no axial ligand is observed bound to the metal center (**10**, Figure 2.17), although under our conditions a small amount of $CH_3OH$ could be trans to the oxo ligand.[30] Upon varying the concentration of $H_2O_2$ in the presence of **10**, a linear dependence on the observed rate resulted in a $k_2$' value of 0.2 $M^{-1}$ $s^{-1}$ at 0 °C. This value is *ca.* 11 times faster than when the solvent is $CH_3CN$ at 25 °C (Table 2.2). This increase in rate could be due to solvent effects of the interaction of the oxo ligand with $H_2O_2$. Alternatively, $H_2O_2$ may bind trans to the oxo group and influence the decay of **10** under noncoordinating solvent conditions.

Performing the same reactions with **9** yielded overall slower reactivity of the oxoiron(IV) complex in both the coordinating and non-coordinating solvents (Table 2.2). Significant differences were not observed in second order rate constants ($k_2$' = 0.0071

and 0.005 $M^{-1}$ $s^{-1}$, in $CH_3CN$ and acetone, respectively). These results suggest that the oxoiron(IV) moiety supported by the tmc-Py framework reacts directly with $H_2O_2$ *via* the oxo ligand. Also, the solvent does not appear to greatly influence the mechanism for the oxo ligand abstracting an H atom from $H_2O_2$. This indicates that for **1** and **10** versus **9**, the main difference in the reactivity is due to $H_2O_2$ coordinating trans to the oxo ligand. $H_2O_2$ coordination may activate the oxo ligand for reaction with another molecule of $H_2O_2$ by the trans effect. Previous studies of **9** with different axial ligands have shown that electron donating groups greatly influence the reactivity of the oxo ligand.[77,78,79] A change in the proposed HAT mechanism of the reaction could also be possible for the decay of oxoiron(IV) considering the different reactivity modes of $H_2O_2$ with metals containing open coordination sites (Figure 2.4). Similar to the reactions of **1** and $H_2O_2$, no intermediates or the formation of $Fe^{II}$ species were observed for **9** or **10**. Comparing the tmc and tmc-PY frameworks, it is clear that the presence of an accessible coordination site can influence the reaction of oxiron(IV) complexes with $H_2O_2$. Overall, it was demonstrated that the oxo ligand in complex **9** reacts with $H_2O_2$ yet the pyridyl axial ligand does not provide substantial activation of the oxoiron(IV) unit.

**Table 2.2. Kinetic results for tmc complexes.**

| | $[Fe^{IV}O(tmc)(X)]^{2+}$ | | $[Fe^{IV}O(tmc\text{-}Py)]^{2+}$ (9) | | $[Fe^{IV}O(N4Py)]^{2+}$ (2) |
|---|---|---|---|---|---|
| | $CH_3CN$ (1) | acetone (10) | $CH_3CN$ | acetone | $CH_3CN$ |
| $k_2$' ($M^{-1}$ $s^{-1}$) $H_2O_2$ | 0.018 (25 °C) | 0.20 (0 °C) | 0.0071 (25 °C) | 0.005 (25 °C) | 0.40 (-20 C) |
| $t_{1/2}$ (h) (nat. decay) (25 °C) | 10[a] | 0.32 | 7[b] | 3.9 | 60[c] |

Conditions: Data from pseudo first-order studies with excess $H_2O_2$ and 1 mM oxoiron(IV) complexes. $k_2$' = $k_2/n$, $n$ = number of available protons for hydrogen atom transfer. [a] Reference 26. [b] Reference 76. [c] Reference 27.

## 2.4 Heme Oxoiron(IV) Reactivity with $H_2O_2$

To compare the $H_2O_2$ reactivity of nonheme with heme oxoiron(IV) complexes, studies with the compound I and compound II heme analogs $Fe^{IV}O$(TPFPP) [**12**, TPFPP = *meso-tetrakis*(pentafluorophenyl)porphyrinate dianion] and $Fe^{IV}O(TDCPP^{+\bullet})$ [**15**, TDCPP = *meso-tetrakis*(dichlorophenyl)porphyrinate dianion] were undertaken. The porphyrin complex with the pentafluorophenyl substituents was chosen based on previously reported work showing that either compound I or compound II could be generated by varying the solvent, temperature, and axial ligand.[80] Similar formation has also been reported for the ligand containing the dichlorophenyl substituents. The electron withdrawing nature of the fluoro porphyrin ligand increases the oxidative power of the oxoiron(IV) group compared to the chloro porphyrin.[24] These differences allow for the determination of how relative electron donation to the metal center effects reactivity.[24] Therefore, these complexes provide an ideal system for studying the reactivity of heme oxoiron(IV) species with $H_2O_2$.

In order to generate high-valent complexes independent of $H_2O_2$, the oxidant *m*-chloroperbenzoic acid (*m*-CPBA) was used to specifically monitor the reaction of the oxoiron(IV) species with $H_2O_2$.[81] This approach has been taken recently to identify the reaction of the compound I analog, $Fe^{IV}O(TPFPP^{+\bullet})$, with $H_2O_2$.[56] However, this report only qualitatively reported the reaction with excess $H_2O_2$ showing the formation of $Fe^{III}$(TPFPP)Cl. Our preliminary work on compound I and compound II complexes described below attempts to gain a more thorough mechanistic understanding of the reactivity of heme oxoiron(IV) species with $H_2O_2$.

### 2.4.1 Compound II and $H_2O_2$

**Figure 2.18. Formation of 12.**

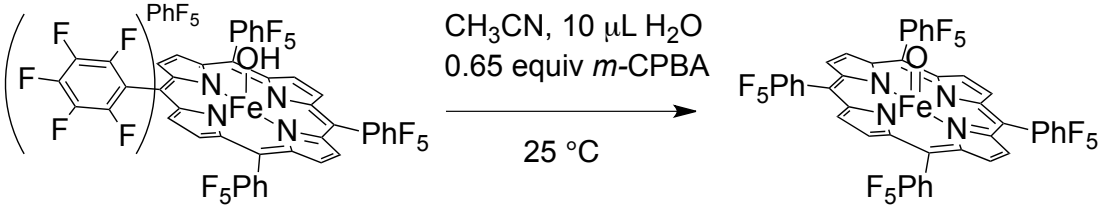


**11** **12**

We first attempted to observe the interaction of the compound II species with $H_2O_2$ because compound II reacts more slowly than compound I, making the study more tractable. $Fe^{III}$(TPFPP)OH (**11**) was synthesized from the chloro derivative (Fe(TPFPP)Cl) using a modified literature synthesis.[82] Fresh solutions of **11** in $CH_3CN$ were prepared by passing the chloro complex through basic alumina. In order to prevent the formation of the μ-oxo dimer ($[Fe(TPFPP)]_2O$), the solvent was not removed and the $CH_3CN$ solution was used directly in reactivity studies.[83,84,85,86] The observed absorption spectra of **11** ($\lambda_{max}$ = 395 and 558 nm) show small deviations from the literature values in $CH_3CN$ under similar conditions ($\lambda_{max}$ = 402 and 564 nm).[87] However, differences in

synthetic procedures are known to influence the absorption bands of **11**. For example, the formation of **11** with excess tetrabutylammonium hydroxide gives spectral features at 417 and 558 nm.[56] This indicates that different noncoordinating species in solution may result in variations of the spectra for **11**. Carrying out the oxidation of the solution of **11** generated by our method with *m*-CPBA resulted in the formation of **12** with the Soret band at 410 nm and Q-band at 546 nm. These values are more consistent with the literature values for compound II from several studies.[56,80,87] Therefore, although the starting material may be a mixture of the hydroxo complex with other species, **12** could still be generated and, thus its reactivity was preliminarily tested.

It should also be noted that attempts to produce **11** in $CH_2Cl_2$ based on the literature method gave reasonable spectra but the reaction of **12** with $H_2O_2$ showed contamination of chloride in the axial ligand position ($\lambda_{max}$ = 504 and 603 nm). Furthermore, the reactivity of compound II with $H_2O_2$ starting from Fe(TPFPP)Cl was not performed because excess oxidant is required to generate **12** with a chloride axial ligand.[87] The chloride complex was also not preferred because the presence of chloride anion would complicate the reaction mechanism due to competition as an axial ligand.

The oxidation of **12** was carried out in $CH_3CN$ in the presence of 10 μL of $H_2O$ (Figure 2.18). It was found that with this amount of water, the oxidation was most efficient requiring lower equivalents of oxidant. Compound II was generated to 90% conversion with 0.65 equiv of *m*-CPBA. The generation of **12** was limited to 90% formation because adding more *m*-CPBA caused an initial lag phase in the reaction with $H_2O_2$ indicating a side reaction independent of the decay of **12**. Also, more than 1 equiv of $H_2O_2$ could not be added to **12** because it resulted in significant decomposition of the

porphyrin ligand, which was observed by decay of the Soret band absorption. Initial work on compound II reactivity with $H_2O_2$ was carried out only with **12** in order to first optimize the reaction conditions.

**Figure 2.19. UV-Vis studies of the reaction of 12 and $H_2O_2$.**

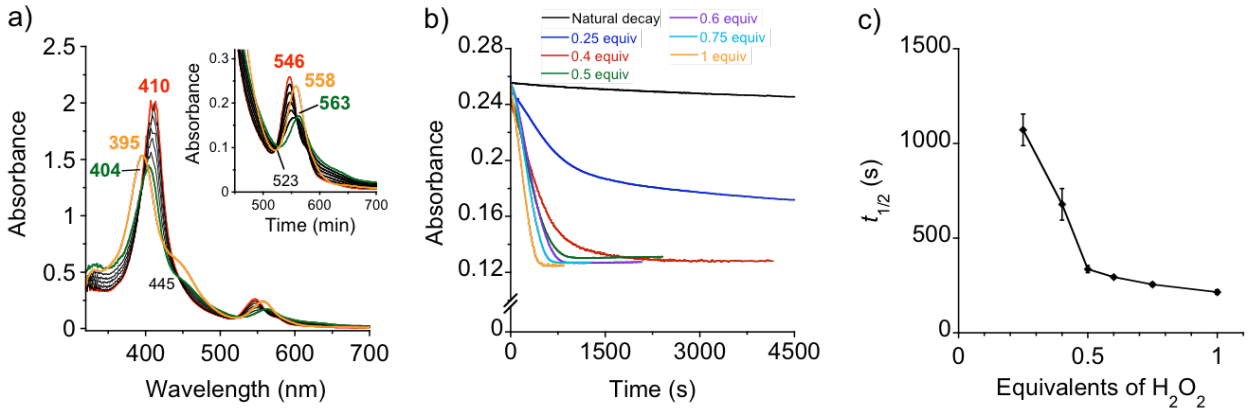


Conditions: a) Spectra of 0.2 mM **11** in $CH_3CN$ and 10 μL of $H_2O$ at 25 °C (0.1 cm path length, orange) and the oxidation of **11** with 0.65 equiv of m-CPBA resulting in 90% generation of **12** (red). Black spectra show decay of **12** upon addition of 0.5 equiv of $H_2O_2$ resulting in **11** (green). b) Decay curves for the addition of various equivalents of $H_2O_2$ to **12**. c) Plot of half lives versus equiv of $H_2O_2$ from experimental data shown in b).

Similar to the nonheme iron reactivity studies, changes in the absorption features were observed upon the addition of $H_2O_2$ to a solution of **12**. With 0.5 equiv of $H_2O_2$, the Soret and Q-bands at 410 and 546 nm for compound II shifted to 404 and 563 nm, respectively (Figure 2.19a). The latter absorption bands indicate the formation of **11** in the reaction. Additionally, isosbestic points were observed at 445 and 523 nm suggesting direct conversion from **12** to **11** (Figure 2.19a). Increasing the concentration from 0.25 to 1.0 equiv of $H_2O_2$ showed decreased reaction times for the decay of **12** (Figure 2.19b). A plot of the half lives against equiv of $H_2O_2$ indicated a break at 0.5 equiv of $H_2O_2$, suggesting a minimum of 0.5 equiv of $H_2O_2$ for the decomposition of **12** with a half life of *ca.* 5 min (Figure 2.19c). Compared to the natural decay of **12** ($t_{1/2}$ ≈ 20

h), the reaction with 0.5 equiv of $H_2O_2$ dramatically increased the rate of decay by a factor of *ca.* 240 (Figure 2.19b). The stoichiometry (2:1) is in agreement with two HAT mechanisms producing **11** analogous to the nonheme iron reactions shown in Equations 4 and 5. After the reaction with 0.5 equiv of $H_2O_2$, the absorption features at 402 and 563 compare well with literature values for the hydroxo complex **11**, which would be expected from the HAT mechanism.[80] Throughout the course of the reaction, no spectral indications of the $Fe^{III}$ superoxo species ($Fe^{III}(TPFPP)O_2^-$, $\lambda_{max}$ = 430 and 559 nm in $CH_3CN$)[88] or hydroperoxy species ($Fe^{III}(TPFPP)OOH$, $\lambda_{max}$ = 419 and 551 nm in $CH_3CN$)[56] were observed.

Based on two consecutive HAT mechanisms for the reaction of **12** and 0.5 equiv of $H_2O_2$, $O_2$ is the expected product from $H_2O_2$ decomposition. Following the addition of 0.5 equiv of $H_2O_2$ to **12**, $O_2$ concentrations were observed to increase over a 10-minute period, which is consistent with the reaction kinetics in Figure 2.19b. The generation of $O_2$ reached a maximum at *ca.* 78% yield relative to $H_2O_2$ (Figure 2.20). The formation of $O_2$ is consistent with two consecutive HAT mechanisms; however, side reactions involving •OOH may be occurring reducing the yield of $O_2$. The porphyrin ligand is well known to be susceptible to oxidation and may account for this observation.[55,56] Interference by the reaction of **11** with $H_2O_2$ most likely does not contribute to the lower yield because the addition of 10 equiv of $H_2O_2$ to **11** does not result in any spectral changes in the UV-vis spectra. Additionally, no $O_2$ is generated when 0.5 equiv of $H_2O_2$ is added to **11** (Figure 2.20). Reaction of •OOH with **11** produced with from the reaction of **12** with $H_2O_2$ or with the 10% remaining from the initial oxidation to **12**, however, could decrease the yield of $O_2$.

**Figure 2.20. Determination of $O_2$ generation for 12 and $H_2O_2$.**

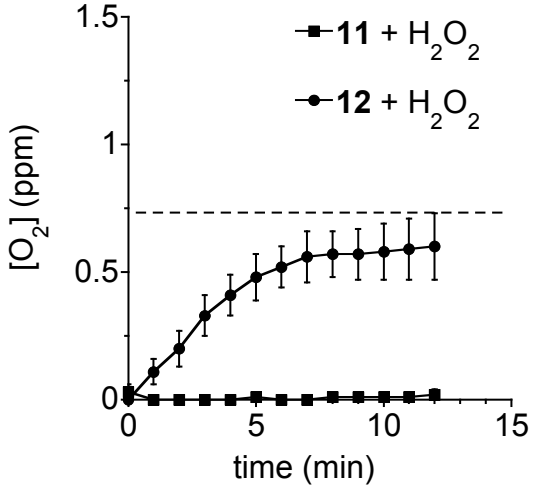


Conditions: Evolution of $O_2$ at 25 °C upon addition of 0.5 equiv of $H_2O_2$ to 4.0 mL of 0.2 mM solutions of **11** (squares) and **12** (circles) in $CH_3CN$ with 100 μL of $H_2O$ added. The dotted line indicates theoretical yield expected for two HAT reactions.

The reaction of **12** and 0.5 equiv of $H_2O_2$ was further characterized by EPR spectroscopy. The EPR spectrum of **11** showed a broad feature that consists of potential rhombic and axial signatures (Figure 2.21a). Fitting the spectrum showed a rhombic signal with $g$ = 7.5, 4.5, and 1.87 (Figure 2.21b). This feature most likely covers the expected spectrum of **11**, which should be an axial signal at $g$ = 5.6 based on the five-coordinate ligation of iron.[83,86] Like UV-Vis, the existence of other species in the starting material is apparent, which has been observed in previous EPR studies of this complex.[86] The unknown species do not prevent the formation of compound II, however. The decrease in the EPR signal upon the oxidation of **11** with *m*-CPBA indicates the formation of an iron complex with integer spin, in agreement with the formation of **12**. Based on the 90% formation of **12**, a signal of lower intensity is still

observed in the EPR spectrum due to the remaining concentration of $Fe^{III}$ in the solution. After the addition of 0.5 equiv of $H_2O_2$ to a sample of **12**, an axial signal at $g$ = 5.6 was observed. In agreement with UV-Vis, this indicates the formation of **11**, which would be expected based on the hydrogen atom transfer from $H_2O_2$ to **12**. Overall, EPR studies are in agreement with UV-Vis showing the decay of **12** to **11** in the presence of $H_2O_2$.

**Figure 2.21. EPR of reaction of 12 and $H_2O_2$ (a) and simulation of the spectrum for 11 (b).**

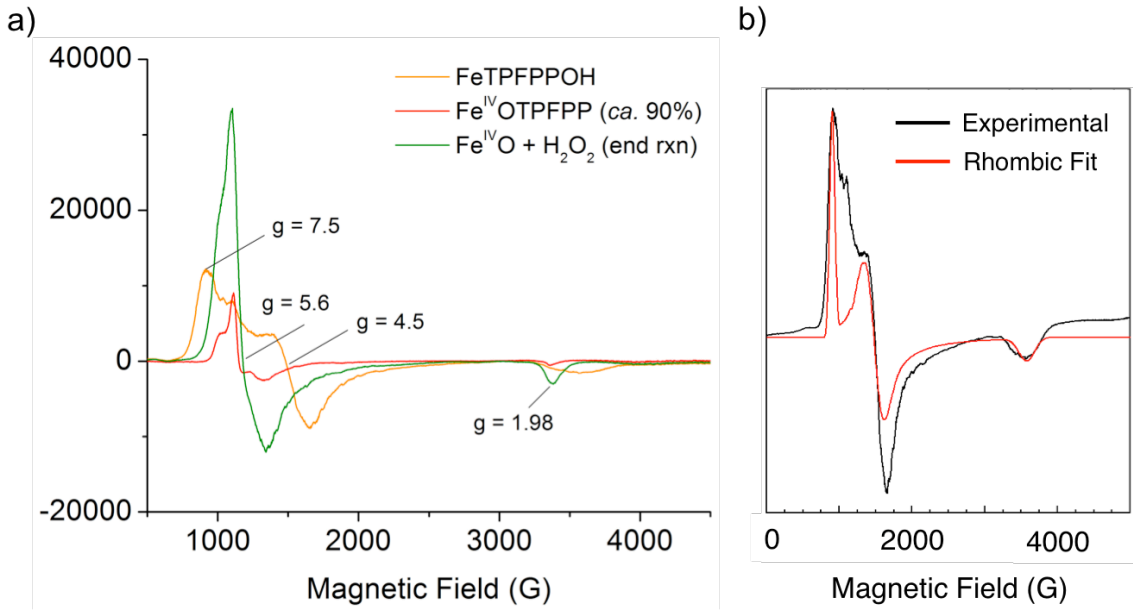


Conditions: Spectra of the reaction of 1.0 mM **12** in $CH_3CN/H_2O$ at 25 °C with 0.5 equiv of $H_2O_2$. a) EPR spectra (recorded at 4 K) of frozen samples of 1.0 mM solutions of **11** (orange) and **12** (red) in $CH_3CN$ and of samples of the reaction of 1.0 mM **12** with 0.5 equiv of $H_2O_2$ frozen at complete decay of **12** (green). b) Experimental data of **11** in black and rhombic fit using the SpinCount Program[89] in red with the following fit parameters: $g_x$, $g_y$, $g_z$ = 2.0; D1 = 10; and E/D1 = 0.065.

These preliminary studies with the heme system involving compound II suggest a relatively rapid, direct reaction of the oxo ligand of **12** with $H_2O_2$ with 2:1 stoichiometry. Monitoring the reaction of **12** and 0.5 equiv of $H_2O_2$ for the production of $O_2$ showed 78% generation supporting that two HAT from $H_2O_2$ could be occurring. In agreement

with UV-Vis reactivity studies, EPR studies showed the formation of **11** upon the reaction of **12** with $H_2O_2$. Further studies on compound II reactivity with $H_2O_2$ will be important for confirming this interaction and are outlined in the future directions.

### 2.4.2 Compound I and $H_2O_2$

Initial screening of reaction conditions with both heme complexes indicated that **15** was more stable under our conditions than the complex with the TPFPP ligand. Therefore, the reactivity of compound I with $H_2O_2$ was preliminarily explored with **15**. The iron(III) precursor ($Fe^{III}$(TDCPP)OH, **13**) was synthesized from the chloro derivative based on literature preparation.[83] In order to generate **15** from an iron(III) precursor, a weakly coordinating axial ligand is needed to facilitate O−O bond heterolysis of *m*-CPBA instead of homolysis, which results in compound II.[24] Triflate anion (OTf) is an ideal axial ligand for the former type of reaction. Complex **13** was converted to $Fe^{III}$(TDCPP)OTf (**14**) by the addition of 1.0 equiv of triflic acid (HOTf) diluted in $CH_3CN$ (Figure 2.22). With the *in situ* formation of **14**, the compound I analog **15** could be generated with 2.0 equiv of *m*-CPBA at −20 °C ($\lambda_{max}$ = 393 and 676 nm for Soret and Q-band, respectively).[90] Preliminary testing of the reaction conditions of **14** with of *m*-CPBA indicated that if 10 μL of $H_2O$ is present, similar to the generation of compound II, that a mixture of compound I and compound II results ($Fe^{IV}$O(TDCPP), **16**, $\lambda_{max}$ = 418 and 558 nm). Therefore, no $H_2O$ was added for the reactivity studies of **15** with $H_2O_2$ (Figure 2.22).

**Figure 2.22. Generation of 15.**

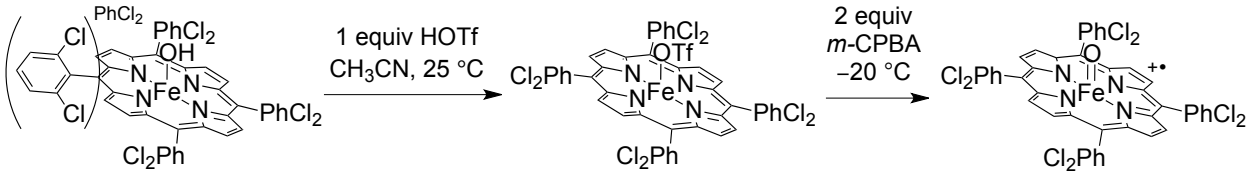


**13** **14** **15**

The reactivity of **15** with $H_2O_2$ was initially tested with various amounts of $H_2O_2$. Increasing the concentration from 0.2 – 1.0 equiv of $H_2O_2$ resulted in an increased rate of decay of **15** (Figure 2.23a). Initiating the reaction with 0.5 or 1.0 equiv of $H_2O_2$ led to a 10 or 25 times faster decay than the decomposition of **15** only ($t_{1/2}$ for **15** ≈ 134 s, $CH_3CN$, −20 °C). Complex **14** was observed at the end of all reactions. Monitoring the reaction of 0.5 equiv of $H_2O_2$ with **15** revealed isosbestic points at 377, 446, 490, and 538 nm suggesting no observable intermediates in the conversion to **14** (Figure 2.23b).

**Figure 2.23. UV-Vis studies for the reaction of 15 with $H_2O_2$.**

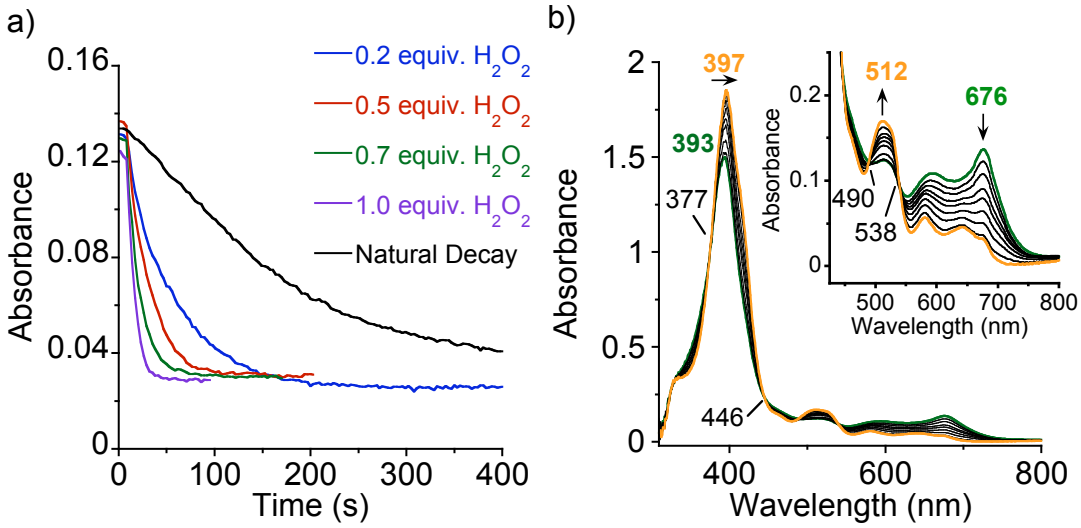


Conditions: a) Decay curves for the addition of various equiv of $H_2O_2$ (0 – 1.0 equiv) to 0.2 mM **15** in $CH_3CN$ at −20 °C. b) Spectra of 0.2 mM **15** in $CH_3CN$ at −20 °C generated with 2 equiv of *m*-CPBA (0.1 cm path length, green) and upon the reaction with 0.5 equiv of $H_2O_2$ leading to the formation of **14** (orange).

Since the reaction of **15** with various concentrations of $H_2O_2$ all yielded **14** at the end of the reaction, it was possible that the reaction could be cycled using the same reaction solution. The spectrum of **14** produced after the reaction of **15** with $H_2O_2$ agrees with the literature indicating that coordination of *m*-CBA (*m*-chlorobenzoate) produced from the oxidation of **14** by *m*-CPBA does not appear to compete with triflate as an axial ligand at the metal center (Figure 2.23).[80] To gain an understanding into the stoichiometry of the reaction of compound I with $H_2O_2$, the reaction of **15** with either 0.5 equiv or 1.0 equiv of $H_2O_2$ was monitored over several reaction cycles (Figure 2.24). Starting with 0.5 equiv of $H_2O_2$, the first reaction cycle indicated the decay of **15** to **14** with minimal changes in the Soret and Q-band of **14** (Figure 2.24a). Subjecting the reaction solution to a further 2.0 equiv of *m*-CPBA, **15** could be nearly fully regenerated (*ca.* 86% based on absorption at 676 nm, doted line, Figure 2.24a). Adding 0.5 equiv of $H_2O_2$ a second time resulted in the formation of **14** with a small amount of complex decay observed in the Soret band at 397 nm.

**Figure 2.24. Reaction of 15 with 0.5 and 1.0 equiv of $H_2O_2$ through several reaction cycles.**

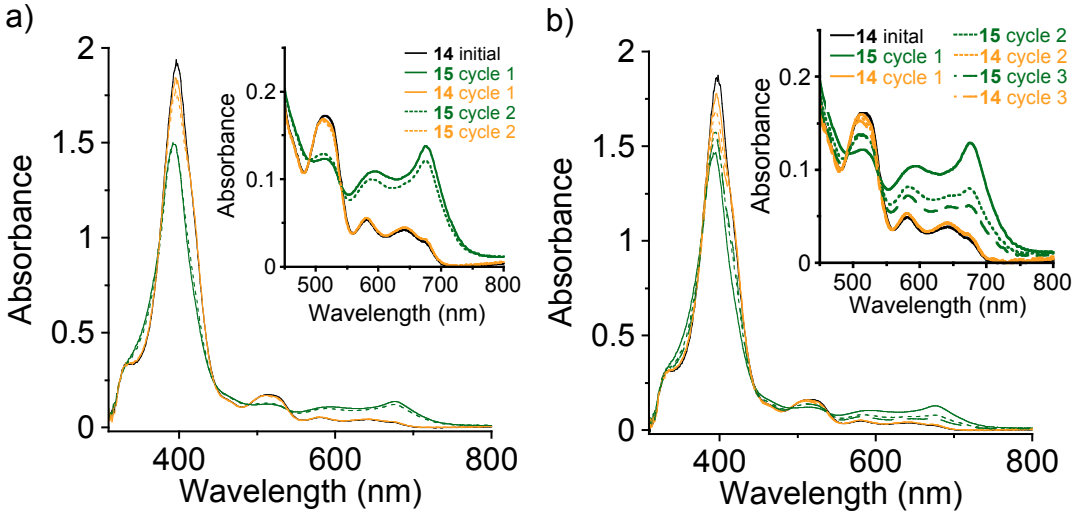


Conditions: a) Spectra of 0.2 mM **15** in $CH_3CN$ at −20 °C generated with 2 equiv of *m*-CPBA (0.1 cm path length, green) and upon the reaction with a) 0.5 equiv or b) 1.0 equiv of $H_2O_2$ leading to the formation of **14** (orange) through 2 or 3 cycles, respectively. Cycle 1 (solid lines), cycle 2 (dotted lines), cycle 3 (dashed lines).

Repeating the same set of reaction cycles with 1.0 equiv of $H_2O_2$ exhibited different behavior. After the first reaction cycle (generation of **15** and reaction with $H_2O_2$), **15** could only be regenerated to *ca.* 50% with 2 equiv of *m*-CPBA based on the initial spectrum of **15** (Figure 2.24b). The solution was treated with a further 1.0 equiv of $H_2O_2$ and **14** was produced a second time with decreased intensity of the Soret band. The cycle was repeated once more and showed even a smaller amount of **15** generation (*ca.* 36%).

The cycling experiments described above present confusing results in regards to stoichiometry for the reaction of **15** with $H_2O_2$. When the cycle is carried out with 0.5 equiv of $H_2O_2$, nearly full generation of **15** can be observed after the first cycle indicating that no $H_2O_2$ remained after the first cycle. With 1.0 equiv of $H_2O_2$, regeneration of **15** is not complete. This may be due to $H_2O_2$ left over from the first cycle reacting with **15**

generated in the second cycle. These observations would suggest that only 0.5 equiv of $H_2O_2$ is required for the full decomposition of **15**. Assuming two HAT reactions from $H_2O_2$ producing $O_2$, the first product of **15** and $H_2O_2$ should be **16** (the compound II analog). Proceeding from this reaction, compound I or compound II can react with either substrate, $H_2O_2$ or •OOH. Therefore, with 0.5 equiv of $H_2O_2$, it would be expected that compound II would remain in solution after the reaction went to completion. Based on this rational, 1.0 equiv. should provide full decay of **15** and/or **16** in the reaction to give **14**. However, this is not the case, and the experiments with 1.0 equiv. of $H_2O_2$ suggest remaining peroxide in solution after the first cycle.

Considering the proposed reaction mechanisms for compound I of catalase (Figure 2.1), a hydride mechanism could also be possible. If the hydride mechanism were occurring, similar conclusions as the HAT mechanism would apply. With 0.5 equiv of $H_2O_2$, the reaction would only go to 50% completion by direct two-electron reduction of **15** to **14**. In this case, no compound II species **16** would be expected. Based on the preliminary results, however, the difference between the two mechanisms cannot be delineated.

A possible explanation for the unpredicted results may be that since the natural decay of **15** is fast even at −20 °C ($t_{1/2}$ ≈ 134 s), the decay of **15** is occurring by reactions involving both $H_2O_2$ and natural decay. This would explain why excess $H_2O_2$ may be left over after the reaction with 1.0 equiv of $H_2O_2$. The stoichiometry is inconclusive based on these preliminary results and remains to be discerned under these conditions. However, the data suggest the increased rate of decay for compound I

in the presence of $H_2O_2$ indicating that a reaction between the oxo ligand and $H_2O_2$ may be occurring.

### 2.5 Conclusions and Comments for Future Directions

#### 2.5.1 Conclusions on Nonheme and Heme Reactivity with $H_2O_2$

Based on high-valent oxoiron(IV) complexes being important and powerful biological oxidants, we sought to understand how heme and nonheme species interact with the important ROS molecule $H_2O_2$. Since such reactivity is not known for nonheme metalloenzymes, we wanted to first determine how feasible this reaction could be. Reactivity studies with the nonheme complex, $[Fe^{IV}O(N4Py)]^{2+}$ (**2**) indicated that a facile reaction of the oxo ligand with $H_2O_2$ is possible. The proposed mechanism involves two hydrogen atom transfer steps that result in the production of dioxygen. This $O_2$ evolution behavior is observed with 0.5 equiv of $H_2O_2$. At higher concentrations of $H_2O_2$, the decay of the oxoiron(IV) complex still occurs through HAT with a competition between $H_2O_2$ and •OOH. Kinetic studies of the reaction of **2** and $H_2O_2$ indicate that this reaction can be more facile than corresponding C−H HAT reactions supporting the possible involvement of nonheme oxoiron(IV) species reacting with $H_2O_2$ in nature.

We also observed that the ligand framework plays an important role in the reaction of the oxoiron(IV) species with $H_2O_2$. With the five-coordinate N4Py ligand, the reaction proceeds at a fast rate even at low temperature. Changing the ligand to the saturated amine-based tmc framework leads to a much slower interaction of the oxo ligand with $H_2O_2$. The presence of an open coordination site at the iron(IV) center increased the rate of decay under excess $H_2O_2$. Removing the open coordination site using a five-coordinate tmc derivative (tmc-Py) indicated that the oxoiron(IV) group does

react with $H_2O_2$ directly. It is difficult to directly compare the reactivity of **2** and the heme complex $Fe^{IV}$OTPFPP (**12**); however, it can be concluded that the heme oxoiron(IV) reacts much faster than the nonheme $[Fe^{IV}O(tmc)(NCCH_3)]^{2+}$ (**1**) species.

With complexes **2** and **12** reacting with $H_2O_2$ at stoichiometric concentrations, mechanistic investigations suggested that both reactions occur *via* HAT mechanisms. Although the stoichiometry for the compound I analog **13** ($Fe^{IV}OTDCPP^{+\bullet}$) could not be determined, reactivity of the oxoiron(IV) species with $H_2O_2$ is suggested due to the increased rates of decay for **13** in the presence of $H_2O_2$. In terms of redox chemistry, this reactivity shows interesting behavior of $H_2O_2$ having the ability to reduce the high-valent oxoiron(IV) species. Typically $H_2O_2$ is thought of as an oxidant in the presence of iron. In contrast to low concentrations of $H_2O_2$, high concentrations have differing effects on the oxoiron(IV) complexes studied here. An important observation was that the nonheme ligand N4Py provides substantial protection from oxidative decomposition of its iron complexes in the presence of excess $H_2O_2$. Although the tmc and porphyrin ligands support oxoiron(IV) species that react with $H_2O_2$, they are very susceptible to complex degradation by high equivalents of $H_2O_2$. This would suggest that catalytic use of iron and $H_2O_2$ would be most suitable with a coordination environment similar to that of N4Py.

In summary, it has been shown that nonheme oxoiron(IV) complexes can directly react with $H_2O_2$ in addition to heme high-valent complexes. This expands the substrate scope of nonheme oxoiron(IV) biomimetic complexes and further suggests that this reaction could be feasible in biological systems.

### 2.5.2 Future Directions

*Nonheme*. The work carried out for the nonheme reactivity, in particular for **2**, has shown very interesting chemistry. However, more study remains necessary in order to thoroughly understand the mechanism. One aspect that may yield further insight is testing solvent effects on the reaction of **2** with $H_2O_2$. Solvents such as acetone and dichloromethane may provide different results due to their noncoordinating nature. These solvents could also lead to different products due to differing stabilities of iron complexes in Figure 2.13. Additionally, reactivity in water could yield different results based on hydrogen bonding and polarity. Comparing the reactivity of oxoiron(IV) species in aqueous versus non-aqueous conditions could give insight into hydrophobic versus hydrophilic actives sites in nonheme enzymes. The use of these solvents may also provide more appropriate conditions for determining a KIE value for the reaction of **2** and $H_2O_2$**.**

Although the interaction of tmc complexes with $H_2O_2$ is slow compared to **2**, conditions may be developed for enhancing the reaction of this complex with $H_2O_2$. The use of different axial ligands may enable the pursuit of mechanistic studies with the tmc framework which could yield new insights into the overall mechanism of nonheme oxoiron(IV) species with $H_2O_2$.

*Heme*. Initial studies have indicated the direct reactivity of a heme oxoiron(IV) compound II analog **12** with $H_2O_2$, which is suggested to occur through HAT similar to the nonheme complexes. Further work should address identifying the unknown species in the starting material **11** or determining synthetic manipulations that will prevent its formation. Starting with pure **11** will be important for confirming the stoichiometry of the

reaction in addition to identifying the amount of **11** produced from the reaction of **12** and $H_2O_2$. This will provide more information on the yield of the reaction with various amounts of $H_2O_2$ and how much of the porphyrin complex decomposes during the reaction. Identifying if porphyrin decomposition occurs during the reaction of **12** with $H_2O_2$ will be important for understanding if this results in the lower than expected yield of $O_2$ in the preliminary experiments.

Many studies remain for the reactivity of the compound I analog **15** with $H_2O_2$. Instead of using the procedure shown in Figure 2.22 to generate **14** *in situ*, isolation of **14** may provide a better method for testing the reactivity of compound I. By starting from **14**, the presence of water would be reduced. Although completely removing water from the reaction is not possible due to the addition of $H_2O_2$, limiting its concentration in the reaction may yield different results. The detection of $O_2$ needs to be carried out, which may also provide clues into the stoichiometry and mechanism of the reaction.

Furthermore, developing conditions for testing and comparing the reactivity of compounds I and II under similar conditions as **2** will be important for direct comparisons between heme and nonheme reaction rates. Establishing the reactivity of the compound II analog with $H_2O_2$ and contrasting to the mechanism of compound I with $H_2O_2$ will also be an interesting aspect that can lead from the current work.

## 2.6. Experimental Section

### 2.6.1 General Methods and Procedures

*Materials.* All reagents were purchased from commercial suppliers and used as received unless stated otherwise. Acetonitrile ($CH_3CN$), tetrahydrofuran (THF),

dichloromethane ($CH_2Cl_2$), and diethyl ether ($Et_2O$) were deoxygenated by sparging with $N_2$ and purified by passage through two packed columns of molecular sieves under an $N_2$ pressure (MBraun solvent purification system). Preparation and handling of air- and moisture-sensitive materials were carried out in a glovebox under an inert atmosphere of $N_2$.

*Nonheme Procedures.* $Fe(OTf)_2 \bullet 2CH_3CN$ (OTf = trifluoromethanesulfonate) was synthesized by a modified literature method from anhydrous $FeCl_2$ and trimethylsilyl trifluoromethanesulfonate in $CH_3CN$ and recrystallized from $CH_3CN/Et_2O$.[91,92] The compound $[Fe^{II}(N4Py)(NCCH_3)](OTf)_2$ [**3**$(OTf)_2$, N4Py = *N,N*-bis(2-pyridylmethyl)-*N*-[bis(2-pyridyl)methyl]amine] was prepared following the previously reported procedure by addition of $Fe(OTf)_2 \bullet 2CH_3CN$ to a solution of N4Py in THF with a slightly modified work-up.[73,93] After stirring overnight, $Et_2O$ was used to precipitate the orange product, which was recrystallized from $CH_3CN/Et_2O$. The characterization of the Fe complex by $^1H$ NMR spectroscopy and electrospray ionization mass spectrometry (ESI-MS) was in agreement with the previous report of **3**$(ClO4)_2$.[73] The molar extinction coefficients for $[Fe^{II}(N4Py)(CH_3CN)]^{2+}$ (**3**) in $CH_3CN$ were $7.4 \times 10^3$ $M^{-1}$ $cm^{-1}$ ($\lambda_{max}$ = 380 nm) and $5.8 \times 10^3$ $M^{-1}$ $cm^{-1}$ ($\lambda_{max}$ = 454 nm) at 25 °C. $[Fe^{II}(tmc)(OTf)]OTf$, $[Fe^{II}(tmc\text{-}Py)](OTf)_2$, and iodosylbenzene (PhIO) were prepared by literature methods.[26,76,94] Oxidation of the iron(II) complexes (stored in $N_2$ atmosphere) to the oxoiron(IV) complexes $[Fe^{IV}O(N4Py)]^{2+}$ (**2**), $[Fe^{IV}O(tmc)(CH_3CN)]^{2+}$ (**1**), and $[Fe^{II}(tmc\text{-}Py)](OTf)_2$ (**9**) was carried out with PhIO as reported.[26,27,76]

*Heme Procedures.* The synthesis of FeTPFPPOH was carried out by a modified literature procedure.[82] 10 mg (9.4 μmol) of FeTPFPPCl was dissolved in a minimal

amount of reagent grade acetonitrile (~ 750 μL) and passed through a column of basic alumina (~ 5 g containing 10% $H_2O$ added directly before porphyrin solution). FeTPFPPOH eluted as a dark red band and was used directly for reactivity studies with $H_2O_2$. Removing the solvent was not carried out in order to avoid formation of $(FeTPFPP)_2O$.[83,84,85,86] The absoprtion band at 563 nm was used to determine the concentration of the solution of **11**.[80] *m*-chloroperbenzoic acid (m-CPBA) was purified to ≥ 95%[95] and used to generate **12** from **11** based on the previous report.[80] *Caution:* Purified mCPBA is potentially explosive and should be handled with care in small amounts. The synthesis of FeTDCPPOH was carried out based on the literature preparation.[83] Commerically available 77% *m*-CPBA was used for FeTDCPPOH reactivity studies.

*$H_2O_2$*. Diluted aqueous solutions of hydrogen peroxide ($H_2O_2$) were used for standardizing its 50% (w/w) stock solution (Sigma Aldrich, St Louis, MO, USA) by UV-Vis spectroscopy ($\lambda$ = 230 nm, $\varepsilon$ = 72.4 $M^{-1}$ $cm^{-1}$).[96] Deuterium peroxide ($D_2O_2$, 30% (w/w) in $D_2O$) was purchased from Icon Isotopes (Summit, NJ, USA) and standardized using solutions diluted with $D_2O$ in a similar manner to $H_2O_2$.

### 2.6.2 UV-Vis Spectroscopy

*General.* UV-Vis spectra were recorded on a Hewlett Packard 8453 diode array spectrophotometer with samples maintained at the desired temperature using a cryostat/heater from Unisoku Scientific Instruments (Japan). The fitting of kinetic data and determination of $k_{obs}$ values for oxoiron(IV) complexes were carried out using the ChemStation software (Agilent Technologies, Santa Clara, CA, USA). Values of $k_2'$ were determined by dividing the second-order rate constant ($k_2$) by the number ($n$) of

available protons for hydrogen atom transfer (for $H_2O_2$, $n$ = 2). Kinetic experiments were carried out in triplicate.

*Nonheme.* A typical reaction involved adding 50 μL of a pre-chilled solution of $H_2O_2$ (50% in $H_2O$) in $CH_3CN$ to a UV-Vis cuvette (path length, 1.0 cm) containing 2.0 mL of a solution of **1, 2, 9**, or **10** in $CH_3CN$ at −20, 0 or 25 °C. For experiments in a 0.1 cm UV-Vis cuvette, 10 μL of a solution of $H_2O_2$ in $CH_3CN$ was added to 400 μL of a solution of **2** in $CH_3CN$. Kinetic experiments for reactions of **2** with an excess of $H_2O_2$ were monitored at 800 nm to reduce interference from other optical signals [i.e., formation of **7**]. Analysis of pseudo-first-order decay traces of **2** by plotting ln A *versus t* indicated a linear trend for at least three half-lives. For the determination of the observed rate constant ($k_{obs}$) under pseudo-first-order conditions, data were used from at least three (for **2**) or four (for **1**, **9**, and **10**) experimentally determined half-lives.

*Heme compound II.* Reactions typically involved adding 10 μL of a solution of $H_2O_2$ (50% in $H_2O$) in $CH_3CN$ to a UV-Vis cuvette (path length, 0.1 cm) containing 400 μL solution (390 μL $CH_3CN$ and 10 μL $H_2O$) of **12** at 25 °C.

*Heme compound I.* To 400 μL of a 0.2 mM solution of FeTDCPPOH (**13**) in $CH_3CN$ was added 10 μL of *ca.* 1.0 equiv. of HOTf diluted in $CH_3CN$ at room temperature to produce FeTDCPPOTf (**14**). After *ca.* five minutes, 2.0 equiv. of mCPBA (77%) was added at low temperature (−20 °C). Reactions of **15** were initiated by adding 10 μL of various equivalents of $H_2O_2$ diluted in $CH_3CN$ to a 0.1 cm UV-Vis cuvette.

### 2.6.3 ESI(+)MS Measurements

ESI-MS measurements were performed with a Micromass LCT time-of-flight mass spectrometer operating in the positive ion mode. Into a septum-sealed 4.0 mL

vial, suspended in a cold bath at −20 °C and containing a 1.0 mM solution of **2** in $CH_3CN$, was injected a solution of 0.5 equiv of $H_2O_2$ in $CH_3CN$. Direct introduction of a sample from the reaction mixture into the mass spectrometer *via* a short transfer line was facilitated by applying slight pressure on the headspace of the solution with a syringe. Data were collected at a capillary voltage of 3100 V, a sample cone voltage of 17 V, a desolvation temperature of 100 °C, and a source temperature of 100 °C.

### 2.6.4 $^1$H NMR Spectroscopy

$^1$H nuclear magnetic resonance (NMR) spectra were acquired with a Varian 400 MHz instrument at ambient temperature. The reaction of 1.0 mM **2** in $CD_3CN$ with 0.5 equiv of $H_2O_2$ at −20 °C was monitored by UV-Vis spectroscopy. After no further spectral changes were observed at −20 °C (*ca*. 4 h), the reaction solution was warmed to room temperature (no significant changes were observed in the optical spectrum upon warming). The orange solution was then analyzed by $^1$H NMR spectroscopy. The NMR spectrum of **2** in $CD_3CN$ prior to the reaction with $H_2O_2$ was consistent with that previously reported.[28]

### 2.6.5 EPR Spectroscopy

*General.* Electron paramagnetic resonance (EPR) data were collected on a Bruker EMX electron spin resonance spectrometer equipped with an Oxford liquid helium cryostat or a Varian liquid nitrogen cryostat.

*Nonheme.* For the preparation of EPR samples at different reaction time points, the reaction of 1.0 mM **2** in $CH_3CN$ with 0.5 equiv of $H_2O_2$ at −20 °C was monitored by UV-Vis spectroscopy (path length = 1.0 cm). At various time points, an aliquot of the reaction mixture was quickly transferred with a chilled Pasteur pipette into an EPR tube

pre-cooled to −40 °C and immediately frozen in liquid nitrogen. The EPR sample of $[Fe^{III}(N4Py)(OH)]^{2+}$ (**4**) was prepared from the reaction of **3** (1.0 mM in acetone) with 0.5 equiv of $H_2O_2$ at room temperature.[65] The EPR spectra shown in Figure 2.11 were recorded at 4 K under non-saturating conditions with the instrument operating at 9.37 GHz, a power of 20.5 mW, a modulation frequency of 100 kHz, a modulation amplitude of 10 G, and a resolution in the X direction of 2048 points. The spectra in Figure 2.14 were recorded at 77 K under non-saturating conditions with the instrument operating at 9.26 GHz, a power of 20.5 mW, a modulation frequency of 100 kHz, a modulation amplitude of 10 G, and a resolution in the X direction of 1024 points.

*Heme.* For the preparation of EPR samples at different reaction time points, the reaction of 1.0 mM **11** in $CH_3CN/H_2O$ (390 and 10 μL, respectively) with 0.5 equiv of $H_2O_2$ at 25 °C was monitored by UV-Vis spectroscopy (path length = 1.0 cm). At various time points, an aliquot of the reaction mixture was quickly transferred into an EPR tube and immediately frozen in liquid nitrogen. The EPR spectra shown in Figure 2.21 were recorded at 4 K under non-saturating conditions with the instrument operating at 9.37 GHz, a power of 20.5 mW, a modulation frequency of 100 kHz, a modulation amplitude of 10 G, and a resolution in the X direction of 2048 points.

### 2.6.6 $O_2$ Detection

*General.* Concentrations of $O_2$ were measured using a borosilicate optical probe with 4.0 mm RedEyeTM patches from Ocean Optics (Dunedin, FL, USA; HIOXY coating, calibrated for −20 to 25 °C and 0.0 to 8.0 ppm (mass/mass) of $O_2$). The experiments were carried out in a threaded 1.0 cm cuvette (Starna Cells, Inc., Atascadero, CA, USA), containing 4.0 mL of solution to minimize headspace and sealed

with a septum cap, at a temperature of −20 °C (for nonheme) and 25 °C (for heme) maintained by a cryostat from Unisoku Scientific Instruments. The borosilicate fiber optic probe was positioned with the RedEye oxygen sensing patch within the cuvette, and the entire set-up was then purged with $N_2$ to remove $O_2$.

*Nonheme.* The $O_2$ concentrations were measured upon injection of 100 μL of a thoroughly $N_2$ purged 0.02 M solution of $H_2O_2$ in $CH_3CN$ *via* an air-tight syringe into either $CH_3CN$ only, 1.0 mM **2** in $CH_3CN$, or 1.0 mM **3** in $CH_3CN$. Concentrations were measured at various time points over 2 h at −20 °C. For experiments with 0.5 equiv of $H_2O_2$ and 1.0 mM **2** or **3** in $CH_3CN$, the reaction was continuously monitored by UV-Vis spectroscopy (path length = 1.0 cm). As a control experiment, the concentration of $O_2$ in $CH_3CN$ in this set-up was measured over 2 h [0.9 (± 0.1) ppm], verifying minimal $O_2$ leakage into the cuvette. The measurements for $O_2$ detection were conducted in triplicate. A calibration curve was created at −20 °C using various concentrations (4.0 – 20 ppm) of $O_2$ with solutions prepared by dilution of an $O_2$ saturated $CH_3CN$ solution (8.1 mM $O_2$ in $CH_3CN$ at 25 °C).[97] The theoretical yield of 20.3 ppm of $O_2$ for the reaction of **2** with $H_2O_2$ (based on a 2:1 stoichiometry between **2** and the produced $O_2$) was found to correspond to a sensor reading of 13.7 (±0.4) ppm.

*Heme.* The $O_2$ concentrations were measured upon injection of 100 μL of a thoroughly $N_2$ purged 8 mM solution of $H_2O_2$ in $CH_3CN$ *via* an air-tight syringe into either 0.4 mM **11** in $CH_3CN$ or 0.4 mM **12** in $CH_3CN/H_2O$ (3.9 mL/0.1 mL). Concentrations were measured every minute over 10 min at 25 °C. For experiments with 0.5 equiv of $H_2O_2$ and 0.4 mM **11** or 1**2** in $CH_3CN/H_2O$, the reaction was continuously monitored by UV-Vis spectroscopy (path length 1.0 cm). $O_2$ concentrations were corrected for

generating 90% of **12**. A calibration curve was created at 25 °C using various concentrations (0.0 – 9.0 ppm) of $O_2$ with solutions prepared by dilution of an $O_2$ saturated $CH_3CN$ solution (8.1 mM $O_2$ in $CH_3CN$ at 25 °C).[97]

## 2.7 References


[1] Giorgio, M.; Trinei, M.; Migliaccio, E.; Pelicci, P. G. *Nat. Rev. Mol. Cell Biol.* **2007**, *8*, 722.
[2] Winterbourn, C. C. *Nat. Chem. Biol.* **2008**, *4*, 278.
[3] Hentze, M. W.; Muckenthaler, M. U.; Andrews, N. C. *Cell* **2004**, *117*, 285.
[4] Deisseroth, A.; Dounce, A. L. *Physiol. Rev.* **1970**, *50*, 319.
[5] Putnam, C. D.; Arvai, A. S.; Bourne, Y.; Tainer, J. A. *J. Mol. Biol.* **2000**, *296*, 295.
[6] Watanabe, Y.; Nakajima, H.; Ueno, T. *Acc. Chem. Rev.* **2007**, *40*, 554.
[7] Alfonso-Prieto, M.; Biarnés, X.; Vidossich, P.; Rovira, C. *J. Am. Chem. Soc.* **2009**, *131*, 11751.
[8] Kato, S.; Ueno, T.; Fukuzumi, S.; Watanabe, Y. *J. Biol. Chem.* **2004**, *279*, 52376.
[9] Kwart, H. *Acc. Chem. Res.* **1982**, *15*, 401.
[10] Vlasits, J.; Jakopitsch, C.; Bernroitner, M.; Zamocky M.; Furtmüller, P. G.; Obinger, C. *Arch. Biochem. Biophys.* **2010**, *500*, 74.
[11] Hersleth, H.-P.; Ryde, U.; Rydberg, P.; Borbitz, C. H.; Andersson, K. K. *J. Inorg. Biochem*. **2006**, *100*, 460.
[12] Marquez, L. A.; Huang, J. T.; Dunford, H. B. *Biochemistry* **1994**, *33*, 1447.
[13] Valderrama, B.; Ayala, M.; Vazquez-Duhalt, R. *Chem. Biol.* **2002**, *9*, 555.
[14] Valderrama, B. Deactivation of Hemeperoxidases by Hydrogen Peroxide: Focus on Compound III. In *Biocatalysis Based on Heme Peroxidases*; Torres, E.; Ayala, M., (Eds.); Springer-Verlag, Berlin, **2010.**
[15] Krebs, C.; Galonic Fujimori, D.; Walsh, C. T.; Bollinger, J. M., Jr. *Acc. Chem. Res.* **2007**, *40*, 848.
[16] Bruijninex, P. C. A.; van Koten, G.; Klein Gebbink, R. J. M. *Chem. Soc. Rev.* **2008**, *37*, 2716.
[17] Kovaleva, E. G.; Lipscomb, J. D. *Nat. Chem. Biol.* **2008**, *4*, 186.
[18] Gassner, G. T. Mechanistic Studies of the Phthalate Dioxygenase System. PhD Thesis. The University of Michigan: Ann Arbor, MI, 1995.
[19] Moonen, M. J. H.; Synowsky, S. A.; van den Berg, W. A. M.; Westphal, A. H.; Heck, A. J. R.; van den Heuvel, R. H. H.; Fraaije, M. W.; van Berkel, W. J. H. *J. Bacteriol.* **2008**, *190*, 5199.
[20] Solomon, E. I.; Decker, A.; Lehnert, N. *Proc. Natl. Acad. Sci. USA* **2003**, *100*, 3589.
[21] Costas, M.; Mehn, M. P.; Jensen, M. P.; Que, L., Jr. *Chem. Rev.* **2004**, *104*, 939.
[22] De Visser, S. P. *Angew. Chem. Int. Ed.* **2006**, *45*, 1790.
[23] Groves, J. T. *J. Inorg. Biochem.* **2006**, *100*, 434.
[24] Nam, W. *Acc. Chem. Res.* **2007**, *40*, 522.
[25] Ortiz de Montellano, P. R. *Chem. Rev.* **2010**, *110*, 932.
[26] Rohde, J.-U.; In, J.-H.; Lim, M. H.; Brennessel, M. R.; Bukowski, A.; Stubna, A.; Münck, E.; Nam, W.; Que, L., Jr. *Science* **2003**, *299*, 1037.
[27] Kaizer, J.; Klinker, E. J.; Oh, N. Y.; Rohde, J.-U.; Song, W. J.; Stubna, A.; Kim, J.; Münck, E.; Nam, W.; Que, L., Jr. *J. Am. Chem. Soc.* **2004**, *126*, 472.
[28] Klinker, E. J.; Kaizer, J.; Brennessel, W. W.; Woodrum, N. L.; Cramer, C. J.; Que, L., Jr. *Angew. Chem. Int. Ed.* **2005**, *44*, 3690.

[29] Que, L., Jr. *Acc. Chem. Res.* **2007**, *40*, 493.
[30] Cho, J.; Jeon, S.; Wilson, S. A.; Liu. L. V.; Kang, E. A.; Braymer, J. J.; Lim, M. H.; Hedman, B.; Hodgson, K. O.; Valentine, J. S.; Solomon, E. I.; Nam, W. *Nature* **2011**, *478*, 502.
[31] Abouelatta, A. I.; Campanali, A. A.; Ekkati, A. R.; Shamoun, M.; Kalapugama, S.; Kodanko, J. J. *Inorg. Chem.* **2009**, *48*, 7729.
[32] Fukuzumi, S.; Morimoto, Y.; Kotani, H.; Naumov, P.; Lee, L.-M.; Nam, W. *Nat. Chem*. **2010**, *2*, 756.
[33] Owen, T. M.; Rohde, J.-U. *Inorg. Chem*. **2011**, *50*, 5283.
[34] Dickman, M. H.; Pope, M. T. *Chem. Rev.* **1994**, *94*, 569.
[35] Butler, A.; Clague, M. J.; Meister, G. E. *Chem. Rev.* **1994**, *94*, 625.
[36] Salem, I. A.; El-Maazawi, M.; Zaki, A. B. *Int. J. Chem. Kinet.* **2000**, *32*, 643.
[37] Bayot, D.; Devillers, M. *Coord. Chem. Rev.* **2006**, *250*, 2610.
[38] Wu, A. J.; Penner-Hahn, J. E.; Pecoraro, V. L. *Chem. Rev.* **2004**, *104*, 903.
[39] Gilbert, J. A.; Gersten, S. W.; Meyer, T. J. *J. Am. Chem. Soc.* **1982**, *104*, 6872.
[40] Gilbert, J. A.; Roecker, L.; Meyer, T. J. *Inorg. Chem*. **1987**, *26*, 1126.
[41] Colpas, G. J.; Hamstra, B. J.; Kampf, J. W.; Pecoraro, V. L. *J. Am. Chem. Soc.* **1996**, *118*, 3469.
[42] Crans, D. C.; Smee, J. J.; Gaidamauskas, E.; Yang, L. *Chem. Rev.* **2004**, *104*, 849.
[43] Yang, J. Y.; Nocera, D. G. *J. Am. Chem. Soc.* **2007**, *129*, 8192.
[44] Melton, J. D.; Bielski, B. H. J. *Radiat. Phys. Chem*. **1990**, *36*, 725.
[45] Løgager, T.; Holcman, J.; Sehested, K.; Pederson, T. *Inorg. Chem.* **1992**, *31*, 3523.
[46] Jacobsen, F.; Holcman, J.; Sehested, K. *Int. J. Chem. Kinet.* **1997**, *29*, 17.
[47] Jacobsen, F.; Holcman, J.; Sehested, K. *Int. J. Chem. Kinet.* **1998**, *30*, 215.
[48] Kremer, M. L. *J. Phys. Chem. A* **2003**, *107*, 1734.
[49] Pestovsky, O.; Bakac, A. *J. Am. Chem. Soc.* **2004**, *126*, 13757.
[50] Sustmann, R.; Korth, H.-G.; Kobus, D.; Baute, J.; Seiffert, K.-H.; Verheggen, E.; Bill, E.; Kirsch, M.; de Groot, H. *Inorg. Chem.* **2007**, *46*, 11416.
[51] Ghosh, A.; Mitchell, D. A.; Chanda, A.; Ryabov, A. D.; Pepescu, D. L.; Upham, E. C.; Collins, T. J. *J. Am. Chem. Soc.* **2008**, *130*, 15116.
[52] Traylor, T. G.; Tsuchiya, S.; Byun, Y.-S.; Kim, C. *J. Am. Chem. Soc.* **1993**, *115*, 2775.
[53] Traylor, T. G.; Kim, C.; Fann, W.-P.; Perrin, C. L. *Tetrahedron* **1998**, *54*, 7977.
[54] Goh, Y. M.; Nam, W. *Inorg. Chem.* **1999**, *38*, 914.
[55] Stephenson, N. A.; Bell, A. T. *J. Am. Chem. Soc.* **2005**, *127*, 8635.
[56] Franke, A.; Fertinger, C.; van Eldik, R. *Chem. Eur. J.* **2012**, *18*, 6935.
[57] Groves, J. T.; Haushalter, R. C.; Nakamura, M.; Nemo, T. E.; Evans, B. J. *J. Am. Chem. Soc.* **1981**, *103*, 2884.
[58] Jakopitsch, C.; Vlasits, J.; Wiseman, B.; Loewen, P. C.; Obinger, C. *Biochemistry* **2007**, *46*, 1183.
[59] Hersleth, H.-P.; Hsiao, Y.-W.; Ryde, U.; Görbitz, C. H.; Andersson, K. K. *Biochem. J.* **2008**, *412*, 257.
[60] Suarez, J.; Ranguelova, K.; Jarzecki, A. A.; Manzerova, J.; Krymov, V.; Zhao, X.; Yu, S.; Metlitsky, L.; Gergen, G. J.; Magliozzo, R. S. *J. Biol. Chem*. **2009**, *284*, 7017.

[61] Zhao, X.; Yu, S.; Ranguelova, K.; Suarez, J.; Metlitsky, L.; Schelvis, J. P. M.; Magliozzo, R. S. *J. Biol. Chem.* **2009**, *284*, 7030.
[62] Braymer, J. J.; O'Neill, K. P.; Rohde, J.-U.; Lim, M. H. *Angew. Chem. Int. Ed.* **2012**, *51*, 5376.
[63] Meyer, T. J.; Huynh, M. H. V. *Inorg. Chem.* **2003**, *42*, 8140.
[64] Mayer, J. M. *Acc. Chem. Res.* **2011**, *44*, 36.
[65] Roelfes, G.; Lubben, M.; Chen, K.; Ho, R. Y. N.; Meetsma, A.; Genseberger, S.; Hermant, R. M.; Hage, R.; Mandal, S. K.; Young, V. G., Jr.; Zang, Y.; Kooijman, H.; Spek, A. L.; Que, L., Jr.; Feringa, B. L. *Inorg. Chem.* **1999**, *38*, 1929.
[66] Collins, M. J.; Ray, K.; Que, L., Jr. *Inorg. Chem.* **2006**, *45*, 8009.
[67] Kotani, H.; Suenobu, T.; Lee, Y.-M.; Nam, W.; Fukuzumi, S. *J. Am. Chem. Soc.* **2011**, *133*, 3249.
[68] Decker, A.; Rohde, J.-U.; Klinker, E. J.; Wong, S. D.; Que, L., Jr.; Solomon, E. I. *J. Am. Chem. Soc.* **2007**, *129*, 15983.
[69] Andrieux, C. P.; Hapiot, P.; Savéant, J.-M. *J. Am. Chem. Soc.* **1987**, *109*, 3768.
[70] Che, Y.; Tsushima, M.; Matsumoto, F.; Okajima, T.; Tokuda, K.; Ohsaka, T. *J. Phys. Chem.* **1996**, *100*, 20134.
[71] Darwent, B. d. Bond Dissociation Energies in Simple Molecules (NSRDS-NBS 31), National Bureau of Standards, Washington, DC, **1970**.
[72] Jacobsen, F.; Holcman, J.; Sehested, K. *Int. J. Chem. Kinet.* **1997**, *29*, 17.
[73] Lubben, M.; Meetsma, A.; Wilkinson, B.; Feringa, L.; Que, L., Jr. *Angew. Chem. Int. Ed.* **1995**, *34*, 1512.
[74] Gómez, L.; Garcia-Bosch, I.; Company, A.; Benet-Buchholz, Polo, A.; Sala, X.; Ribas, X. Costas, M. *Angew. Chem. Int. Ed.* **2009**, *48*, 5720.
[75] Chen, M. S.; White, M. C. *Science* **2010**, *327*, 566.
[76] Thibon, A.; England, J.; Martinho, M.; Young, V. G., Jr.; Frisch, J. R.; Guillot, R.; Girerd, J.-J.; Münck, E.; Que, L., Jr.; Banse, F. *Angew. Chem. Int. Ed.* **2008**, *47*, 7064.
[77] Rohde, J.-U.; Que, L., Jr. *Angew. Chem. Int. Ed.* **2005**, *44*, 2255.
[78] Jackson, T. A.; Rohde, J.-U.; Seo, M. S.; Sastri, C. V.; DeHont, R.; Stubna, A.; Ohta, T.; Kitagawa, T.; Münck, E.; Nam, W.; Que, L., Jr. *J. Am. Chem. Soc.* **2008**, *130*, 12394.
[79] Sastri, C. V.; Lee, J.; Oh, K.; Lee, Y. J.; Lee, J.; Jackson, T.; Ray, K.; Hirao, H.; Shin, W.; Halfen, J. A.; Kim, J.; Que, L., Jr.; Shaik, S.; Nam, W. *Proc. Natl. Acad. Sci. USA* **2007**, *104*, 19181.
[80] Nam, W.; Lim, M. H.; Oh, S.-Y.; Lee, J. H.; Lee, H. J.; Woo, K.; Kim, C.; Shin, W. *Angew. Chem. Int. Ed.* **2000**, *39*, 3646.
[81] Nam, W.; Park, S.-E.; Lim, I. K.; Lim, M. H.; Hong, J.; Kim, J. *J. Am. Chem. Soc.* **2003**, *125*, 14674.
[82] Wang, C. C.-Y.; Ho, D. M.; Groves, J. T. *Inorg. Chem.* **1999**, *121*, 12094.
[83] Cheng, R.-J.; Latos-Grazynksi, L.; Balch, A. L. *Inorg. Chem.* **1982**, *21*, 2412.
[84] Jayaraj, K.; Gold, A.; Toney, G. E.; Helms, J. H.; Hatfield, W. E. *Inorg. Chem.* **1986**, *25*, 3516.
[85] Gold, A.; Jayaraj, K. *Inorg. Chim. Acta* **1988**, *150*, 177.

[86] Manso, C. M. C. P.; Neri, C. R.; Vidoto, E. A.; Sacco, H. C.; Ciuffi, K. J.; Iwamoto, L. S.; Iamamoto, Y.; Nascimento, O. R.; Serra, O. A. *J. Inorg. Biochem.* **1999**, *73*, 85.
[87] Pan, Z.; Newcomb, M. *Inorg. Chem.* **2007**, *46*, 6767.
[88] Selke, M.; Sisemore, M. F.; Valentine, J. S. *J. Am. Chem. Soc.* **1996**, *118*, 2008.
[89] SpinCount (Version 3.1.2), written by Prof. Michael Hendrich, Carnegie Mellon University, 2008.
[90] Pan, Z. *Inorg. Chem. Commun*. **2011**, *14*, 968.
[91] Arnold, J.; Hoffman, C. G.; Dawson, D. Y; Hollander, F. J. *Organometallics* **1993**, *12*, 3645.
[92] Hagen, K. S. *Inorg. Chem.* **2000**, *39*, 5867.
[93] Rohde, J.-U.; Torelli, S.; Shan, X.; Lim, M. H.; Klinker, E. J.; Kaizer, J.; Chen, K.; Nam, W.; Que, L., Jr. *J. Am. Chem. Soc.* **2004**, *126*, 16750.
[94] Saltzman, H.; Sharefkin, J. G. *Org. Synth.* **1963**, *43*, 60.
[95] Armarego, W. L. F.; Chai, C. *Purification of Laboratory Chemicals*, 5th ed.; Butterworth-Heinemann: Oxford, U.K., 2003.
[96] George, P. *Biochem. J.* **1953**, *54*, 267.
[97] Kryatov, S. V.; Rybak-Akimova, E. V.; Schindler, S. *Chem. Rev.* **2005**, *105*, 2175.

# Chapter 3: The Development of Bifunctional Molecules for Understanding the Role of Metal-Amyloid-β Species in Alzheimer's Disease

## 3.1 Introduction

### 3.1.1 Collaboration in the Alzheimer's Project

The work presented in Chapter 3 is the result of a highly collaborative environment within the Lim Lab in addition to collaboration with other research groups at the University of Michigan and at other institutions. The progress made would not have been possible without the teamwork of all contributors to the project. I have the privilege of summarizing the initial work that has been produced by the Lim lab and must acknowledge the contributions from fellow colleagues that have either produced the data or helped in acquiring and interpreting the experimental results. Dr. Sarmad Hindo and Allana Mancino were the first to explore the reactivity of the first generation molecules (**K0** and **L1-b**) that resulted in our publication in the Journal of the American Chemical Society. Yihong Liu also provided the data for the cell studies for this publication. Chen Wang and Juno Yoo, undergraduate students, were involved in the synthesis and purification of the **K** and **L** families of compounds. The IR and $^{1}$H NMR data for the **L** series of compounds was acquired by Nathan Merrill, an undergraduate working under my supervision. Major contributions to further studies on the **L** series of compounds were from Dr. Jung-Suk Choi, Alaina S. DeToma, and myself. In particular,

Dr. Choi acquired all of the UV-Vis titration data of the **K** and **L** series while Alaina assisted me in working up the data and fitting the experimental results. Dr. Choi, Alaina, and I all worked together on acquiring metal binding data for the **L** series of molecules. Alaina and I also collaborated on 2D NMR and docking studies. Dr. Choi produced all of the biochemical data for the **L2** series that is summarized in Section 3.4.1 and 3.4.2 in addition to data for the **K1** and **K2** molecules not presented here. Dr. Choi and Alaina also carried out the PAMPA studies. I would like to thank Dr. Xiaoming He, Kisoo Nam, Nicole Schmidt, Kristin Ko, Akiko Kochi, and Amit Pithadia for experimental assistance, fruitful discussions, and insightful comments on manuscript drafts.

Outside of the Lim lab, Professor Ramamoorthy and his group were instrumental in helping us with the 900 MHz NMR. Dr. Subramanian Vivekanandan and Dr. Ravi P. R. Nanga initially helped in establishing the 2D pulse sequence so that we could acquire data of Aβ on our own and Kermit Johnson of Michigan State University assisted with any technical problems with the NMR instrument. Dr. Jeff Kampf collected X-ray crystallographic data and solved the crystal structures for the **L** series. Dr. Ted Huston acquired ICP-MS data on AD patient's brain tissue samples from the Neuropathology Core of the Michigan Alzheimer's Disease Research Center. Professor Gestwicki and lab members also provided a tremendous amount of insight into the biochemical experiments. I would like to thank Dr. Srikanth Patury for showing us how to setup docking studies.

Our international collaborators, Dr. Junghyun Chae and lab members Se Kyung Park and Shaik Mustafa of the Department of Chemistry and Research Institute of Basic

Sciences at Sungshin Women's University in Seoul, South Korea prepared the molecules **K1** and **K2**.

### 3.1.2 Alzheimer's Disease and the Amyloid Hypothesis

Alzheimer's disease (AD) is the leading form of dementia and causes deterioration of cognitive function in over 5.4 million people in the United States.[1] Although the disease has been known for over a century, no therapeutics exist to prevent intellectual decline or reverse brain dysfunction.[2] The only treatments available are drugs that provide temporary symptomatic relief.[3] Difficulty in determining the etiology of this disease has arisen from the myriad of neuropathological features that have been found in AD brains that may or may not be the causative events leading to neuronal death.[4,5] Further complicating the diagnosis of this disease is that it can only be identified with 100% certainty after death by carrying out an autopsy of the brain. Advances in brain imaging and the identification of biomarkers from cerebralspinal fluid (CSF) have made progress for detecting signs of AD in living brains. However, disease diagnosis remains at the 95% confidence level with these methods.[6] Estimates predict that the number of AD cases will double in the next 20 years.[7] Thus, continued efforts on all fronts of this devastating and incurable disease are needed to better understand its biological and biochemical origins.

The main hallmarks that distinguish AD in the post-mortem brain are the presence of extracellular plaques composed of the amyloid-β (Aβ) peptide, intracellular neurofibrillary tangles involving hyperphosphorylated tau protein, and extensive oxidative damage of biological tissues.[4,5,8,9,10] While it is still debated which of these pathologies leads to AD, genetics suggests the formation of Aβ aggregates to be the

root cause based on familial forms of AD that involve mutations in the genes producing Aβ.[11,12] Focus on Aβ has led to one of the most generally accepted hypotheses of AD, the amyloid-β hypothesis.[13,14,15] This hypothesis is centered on the aberrant production and reactivity of Aβ peptides ($A\beta_{39-43}$, Figure 3.1). These peptides are present in the normally functioning human brain; however, in AD they are believed to have imbalanced concentrations and/or are not properly cleared from the brain.[10,16] Cleavage of the transmembrane amyloid precursor protein (APP) by a series of secretases results in either amyloidogenic or nonamyloidogenic production of Aβ.[4,8,9] The nonamyloidogenic pathway produces a soluble fragment (sAPPα) that is nontoxic *via* α-sectretase. $A\beta_{1-40}$ and $A\beta_{1-42}$ peptides are formed in the amyloidogenic pathway through APP processing by β- and γ-secretases. These forms have been identified as the main components of amyloid plaques.

While $A\beta_{1-40}$ is 10 times more prevalent in the brain overall, $A\beta_{1-42}$ is more toxic due to two additional hydrophobic residues that alter aggregation properties of the peptide (Figure 3.1).[17] These peptides are rapidly degraded in the healthy brain by several proteases including neprilysin, insulin-degrading enzyme, angiotensin-converting enzyme, and matrix metalloprotease-2 and -9.[4,8,10] The development of AD may involve over-production of Aβ peptides, changes in ratios of various peptide monomers, and/or defects in the clearance mechanisms. Mutations in γ-secretase and APP genes induce altered production of Aβ that is associated with early onset familial AD (fAD), which accounts for 5% of cases.[4,8] The remaining AD population suffers from late stage onset (sporadic AD) with the main risk factor being age. It is generally accepted that mutations are the basis for fAD; however, how the secretases, APP, and

Aβ are involved in sporadic AD is not well understood.

**Figure 3.1. Sequence of amyloid-β peptide (up to 43 residues) with potential metal binding residues shown in red.**


Through mainly hydrophobic interactions of the C-terminal residues, Aβ monomers in solution can self-assemble to form aggregated states (*e.g.*, oligomers, protofibrils, and fibrils, Figure 3.2).[4, 18, 19, 20] The fibril-containing plaques were first identified in the brain tissue of AD patients and thought to be the origin of toxicity; however, continued study of Aβ species has suggested that low MW oligomers (in particular Aβ dimer) are the main source of neuronal toxicity.[20,21,22] Although Aβ fibrils are generally not considered the toxic source, they may provide stockpiles of Aβ that could be involved in the dissociation of oligomers that cause damage to the integrity of surrounding biological membranes and induce inflammation.[23] Current therapeutic developments for AD are predominately aimed at correcting the dysfunctional Aβ homeostasis by clearing Aβ from the brain *via* anti-Aβ antibodies, inhibiting Aβ aggregate formation, preventing amyloidogenic Aβ production by inhibiting β- and γ-secretase, or neutralizing the toxicity of Aβ.[3,24]

With the limited success to date of drugs based on the Aβ hypothesis alone, it has been suggested that an expanded or modified view of the disease is required.[24] Not only may an expansion be necessary but the disease may not be fully treatable until the full etiology is uncovered. This is a tremendous challenge that requires finding the sources of disease initiation and propagation throughout a multitude of malfunctioning

molecular and cellular machinery that has been identified in the AD brain.[4,5,10]

**Figure 3.2. Amyloid cascade events based on Aβ (top) and metal-Aβ aggregation (bottom).**

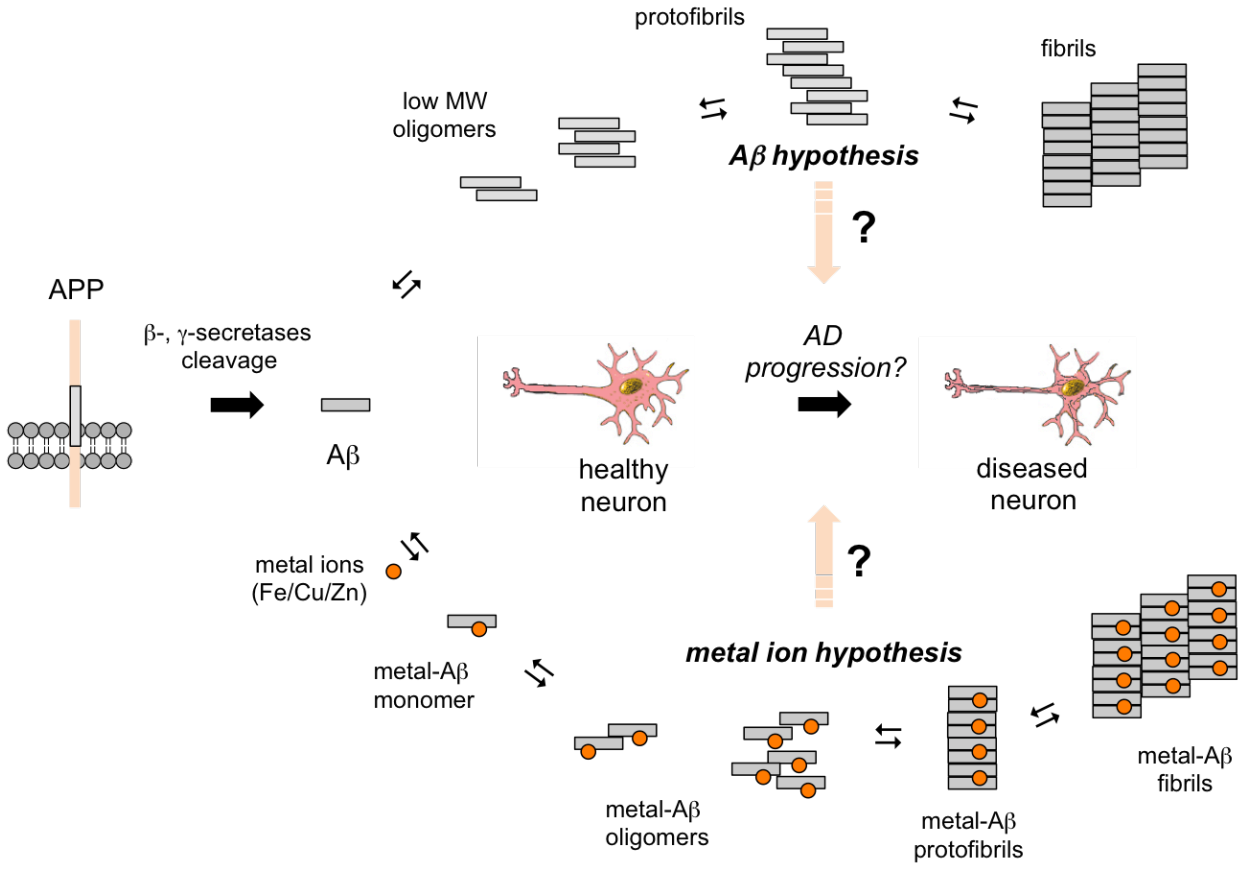


### 3.1.3 Metal Ions in AD

An alternative hypothesis of AD involves the dyshomeostasis of metal ions in the brain.[25,26,27] The metal ion hypothesis intertwines the improper regulation of metal ions that are required for normal neuronal function with imbalanced protein regulation.[10,28] A central tenet to this theory is that the binding of transition metal ions (Fe, Cu, and Zn) to Aβ causes increased aggregation rates and imparts toxicity to surrounding brain tissue (Figure 3.2). [4,10,29] Although a wealth of *in vitro* and *in vivo* literature exists supporting the metal ion hypothesis, the role of metal ions remains highly controversial.

Importantly, metal chelators have shown the ability to modulate metal-associated Aβ species (metal-Aβ) and the metal binding compound PBT2 is currently in clinical trials as a therapeutic for AD.[27] The recent progress and insight PBT2 has provided for the metal ion hypothesis has spurred the development of rationally designed bifunctional molecules as chemical tools for understanding the relevance of metal-Aβ species in AD.[30,31] Two families of bifunctional compounds have been established by the Lim group and their development will be discussed in this thesis. First, the current evidence supporting the metal ion theory in AD is presented below to establish the background and significance of the field.

*Effects of Metal Ions on Aβ Aggregation.* Based on observations that monomeric synthetic Aβ alone at concentrations of 3.7 mM in phosphate buffer above pH 7.2 does not lead to significant fibrillization,[32] Bush and coworkers sought neurochemical inducers of Aβ aggregation. They discovered that $Zn^{2+}$ could drastically enhance aggregation of $A\beta_{1\text{-}40}$.[33,34] Following the initial studies with $Zn^{2+}$, $Cu^{2+}$, and $Fe^{3+}$ were also identified to have this effect with exacerbated effects at low pH ranges similar to acidosis.[35] A lower degree of aggregation was observed for $Fe^{3+}$ suggesting that it does not interact as strongly as $Cu^{2+}$ and $Zn^{2+}$. This is a common trend observed in the literature and has led to a greater amount of detailed metal binding characterization for $Cu^{2+}$ and $Zn^{2+}$ to Aβ as compared to $Fe^{2+/3+}$.[36] This should not detract from the study of Fe though, because numerous studies implicate $Fe^{2+/3+}$ as a source of oxidative stress in AD (*vide infra*).[37,38,39] Available data for $Fe^{2+/3+}$ will be discussed although it is not considered for studies in this thesis project. It should be noted that $Al^{3+}$ was the first metal associated with AD, but continued studies have shown no clear pathogenic

mechanisms in AD.[10] Furthermore, exposure to exogenous metal ions ($Al^{3+}$, $Cd^{2+}$, and $Pb^{2+}$) may have roles in neurodegenerative disease, but they are most likely not the major contributors.[10,40] Endogenous transition metal ions ($Fe^{2+/3+}$, $Cu^{1+/2+}$, and $Zn^{2+}$) are believed to be the main metal ions involved in the progression of AD, and the initial studies above were instrumental in formulating their potential involvement in the pathogenesis of AD.[25,41]

Continued in depth analyses on the effects of metal ions on Aβ aggregation have shown the importance of stoichiometry of metal ions to Aβ and the corresponding influence on morphology.[42] $Fe^{3+}$, $Cu^{2+}$, and $Zn^{2+}$ induce changes in the secondary structure of Aβ in the submillisecond to millisecond time range upon metal binding.[43,44] Stoichiometric and suprastoichiometric amounts of these metal ions inhibit fibril formation and induce the formation of amorphous aggregates.[43] Toxicity of metal-Aβ species has been controversial with reports of both toxic and nontoxic aggregates.[42] Careful control of $Cu^{2+}$ concentrations indicated that at substoichiometric levels of $Cu^{2+}$ cytotoxic metal-Aβ aggregates are generated, whereas stoichiometric and suprastoichiometric amounts of $Cu^{2+}$ result in amorphous aggregates that are nontoxic.[45] As for $Zn^{2+}$, metastable neurotoxic $Zn^{2+}$-$Aβ_{1-40}$ oligomers have been observed that inhibit neuronal activity leading to death in hippocampal cell cultures.[46] Allowing the $Zn^{2+}$-Aβ aggregates to come to equilibrium results in nontoxic amorphous aggregates, indicating a dependence on aggregation state on toxicity. Different from $Cu^{2+}$, the oligomers in this case were prepared using suprastoichiometric amounts of $ZnCl_2$. Based on the observation that $Fe^{3+}$ inhibits fibril formation,[43] Crowhler *et al*. proposed that the smaller amorphous aggregates produced in the presence of iron lead

to neurotoxicity in a fly model.[47] These studies coincide with the toxicity proposed for oligomeric species in the Aβ hypothesis, although the metal ion hypothesis involves metal-associated low MW Aβ species that may lead to the greatest toxicity compared to metal-Aβ monomer and larger metal-incorporated aggregates.[42, 48, 49] However, the definitive forms of metal-Aβ species inducing toxicity are still contested and have yet to be fully agreed upon.

Contributing to the controversy of not only metal-Aβ species but also Aβ itself is the difficulty in working with the peptide due to its aggregation propensity. It is very important to consider how the preparation of Aβ, buffer used, pH, ionic strength, and techniques used to monitor Aβ reactivity affect metal-Aβ aggregation.[36] Differences in these conditions can lead to ambiguous and contradictory results. This ambiguity is exemplified by the range of binding constants reported for metal-Aβ species. For $Cu^{2+}$ binding to monomeric Aβ, reported binding affinities range from attomolar to micromolar.[36] Consensus suggests the actual binding affinity to be in the pico- to nanomolar range.[36,42] For $Zn^{2+}$, binding affinities are approximately in the micromolar range.[36] Concentrations of $Cu^{2+}$ and $Zn^{2+}$ released in the synapse have been suggested to reach 3 and 10-300 μM, respectively.[50] With the concentration of monomeric Aβ approximated at low nanomolar in the CSF[51], it is feasible for these metal ions to bind to Aβ in the synaptic cleft between neurons.

Indirect evidence supporting the activity of Cu and Zn-Aβ oligomeric species in neurons has been demonstrated in rat hippocampal cells and human cortical neurons.[52] Treatment with a metal chelator was able to reverse the formation of oligomers suggesting the involvement of metal-Aβ species at synapses. Overall, it is feasible

under physiological conditions for Aβ to bind metal ions, thereby promoting its aggregation into potentially neurotoxic agents.

*Metals in AD Brain Tissues.* The first indication of metal levels being disrupted in the AD brain were from a qualitative study identifying iron deposits by Prussian blue staining over half a century ago.[53] Many studies have been carried out since to try to understand how metal concentrations change in the AD brain. Fluctuations in bulk Fe, Cu, and Zn concentrations have been observed in different AD brain samples. Due to variation in the technique used, the sampling and tissue fixation method employed, and the care taken to avoid metal contamination, a consensus on concentrations being elevated or depleted has not been reached. Based on a meta-analysis carried out by Schrag and coworkers on reported bulk brain metal levels in AD brains, overall Zn levels appeared to be not significantly changed from age-matched brains except for possibly in the parietal lobe. Cu levels throughout the brain were depleted, and Fe concentrations were not too significantly altered except for possible elevation in the putamen.[54] The large heterogeneity in the bulk data in the numerous literature reports may be a result of differences from patient to patient and may not accurately illustrate focal disruption in metal concentrations (*i.e.,* localized pools of metals).

A recent study that involved numerous controls to account for metal contamination generally agrees with the above meta-analysis with Fe levels increased and Cu decreased.[55] Recent work in PSAPP and APP/V717I AD mouse models are in accord with Fe levels being elevated.[56,57] In contrast, a report by Wang et al. disagrees with the above analysis and shows higher Cu values in APP/V717I AD mouse models.[56] Results from mice models must be carefully considered, especially since mice do not

show complete human AD pathology.[11] On the other hand, mouse models are important for developing techniques that can be later used to study human tissue.[58] Continued improvement in sampling methods for understanding the normal distribution and changes in metal concentrations of healthy brains upon aging are required to help understand metal changes in diseased states like AD.[59,60] Overall, although it is believed that bulk metal concentrations change in the AD brain, consensus on how the levels differ from normal, age-matched brains is not well established.

Substantial support for the involvement of metal ions in human AD brains has come from the observation that localized concentrations of Fe, Cu, and Zn correlate spatially with Aβ senile plaques in AD brain tissue.[61,62] These results (obtained using X-ray fluorescence (XRF) and particle induced X-ray emission (PIXE) spectroscopic methods validate the co-association of Aβ and metal ions *in vivo*. Confirmation of Cu and Zn binding to the Aβ peptide has additionally been reinforced by Raman spectroscopic evidence, and appears to be retained even after purification of the Aβ aggregates.[63] Fe was not observed bound after purification, suggesting either that it does not interact directly with Aβ plaques or that the interaction is too weak to survive isolation by aqueous separation methods. Observing the relationship of metal ions and Aβ in AD brain tissue has provided further evidence to the metal ion hypothesis. These studies should be viewed with caution because the results have not been rigorously confirmed by large samples sizes; furthermore, metal contamination is always a concern during tissue fixation.

*Binding of Metal Ions to Aβ.* Following from the few reports exhibiting the colocalization of metals and Aβ in brain samples, a large amount of *in vitro* data has

accumulated showing the ability of $Cu^{2+}$ and $Zn^{2+}$ to directly bind to Aβ.[36,42,64] Metal coordination to Aβ drives the changes in aggregation rates and morphology discussed above. NMR and EPR techniques have been particularly powerful tools to study metal binding. These investigations often utilize isotope labeling to delineate the potential binding modes of $Fe^{2+/3+}$, $Cu^{1+/2+}$, and $Zn^{2+}$ (only NMR with $Fe^{2+/3+}$ and $Zn^{2+}$). Although coordination environments remain debated due to dynamic binding sites, the dependence on pH, and conditions used for analysis, interaction of transition metals at the N–terminal portion of the peptide *via* the involvement of H6, H13, and/or H14 is well accepted (Figure 3.3).[36,42,64] The length of Aβ can have an effect on aggregation kinetics but does not significantly alter metal coordination as long as the first 16 residues remain intact (Figure 3.1).[28,36] $Zn^{2+}$ coordinates with a 1:1 binding stoichiometry with typically 4 to 6 coordinated ligands being proposed. NMR supports binding of the three histidine residues along with the N-terminal amine (D1).[65] A combination of both the free amine and/or the carboxylate side chain of D1 have also been suggested to be bound to the metal center, dependent on pH.[36,65]

Mononuclear coordination modes for $Cu^{2+}$ are also dynamic based on pH; therefore, a discrete coordination environment is not possible.[36] Two main components have been described for $Cu^{2+}$ binding. At physiological pH (*i.e.*, 7.4), a four-coordinate, 3N1O coordination mode for component I involves either three histidine residues and the carboxylate of D1 (by NMR)[65] or two histidines and the amino terminus and carboxylate of D1 (by EPR, Figure 3.3)[66]. These two species may also be in equilibrium with one another, which would explain differences in the NMR and EPR results. However, this specific speciation has not been shown.[36] At pH values above 8, a

different 3N1O coordination environment is proposed (component II) based on EPR that is believed to involve the carbonyl of A2 along with the three histidine residues.[66] Other studies have proposed ligands for component II that involve carbonyl donors and 4N coordination modes (deprotonated amide backbone and N-terminus).[36]

As $Cu^{+/2+}$ is a biologically active redox agent, the binding of $Cu^{+}$ to Aβ is also an important consideration. $Cu^{+}$ coordination has been observed in a linear binding mode between two histidine residues.[67,68] Similar to $Cu^{2+}$ and $Zn^{2+}$ binding to Aβ, the $Cu^{+}$ interaction is believed to be dynamic as observed by NMR.[67] Metal binding to Aβ for the other redox active metal, Fe, has not been well established.[36] While $Fe^{3+}$ is suggested to not bind Aβ to any considerable degree,[69] $Fe^{2+}$ binds to Aβ as observed by shifts in the $^{1}H$ NMR signals of the peptide.[70] Computational studies are in agreement with the qualitative $Fe^{2+}$-Aβ NMR binding study, suggesting similar ligands involved in coordination as with $Cu^{2+}$ (histidines, carbonyls, N-terminus, and carboxylate side chains) although with a six coordinate binding geometry (Figure 3.3).[70, 71] This suggests that iron may play a larger role in metal-Aβ toxicity *in vivo* than previously thought. The fact that iron did not copurify in the previous Raman study[63] may be due to the fact that $Fe^{2+}$ was oxidized upon exposure to air. Differentiating oxidation states and what proteins iron is bound to in Aβ plaques (*i.e.*, Aβ *vs* ferritin)[36] is an area that needs to be further addressed.

The above summary on the studies involving metal binding to Aβ clearly indicates that metal ions, in particular $Cu^{2+}$ and $Zn^{2+}$, interact through several contact modes with the Aβ peptide. This interaction has yet to be shown *in vivo* where other biological ligands could play a factor in how metals bind to Aβ. Distinguishing the

binding modes under such conditions will be important for understanding how metal-Aβ species behave within the brain.

**Figure 3.3. Potential coordination modes of divalent metal-Aβ species.**

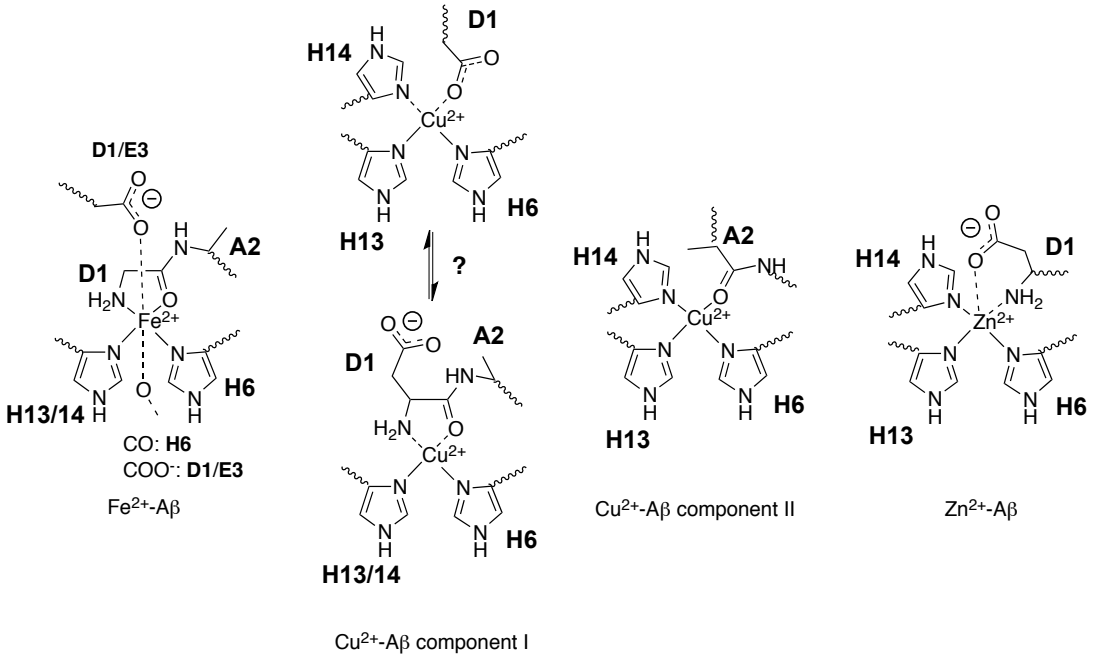


*Metal-Aβ and ROS in AD.* A further hallmark of AD, in addition to Aβ plaques, is the presence of increased oxidative stress.[5,23,72] The development of pathogenesis as a result of reactive oxygen species (ROS) has been proposed to occur early in the disease, even before Aβ plaques are formed.[73,74] Indications of oxidative damage can be observed colocalized with Aβ deposits in AD mouse brains.[75] It remains unclear whether oxidative stress and inflammation are a cause or an effect of neuropathology observed in AD.

While pools of loosely bound Cu and Fe have been observed in AD tissues that could contribute to Fenton chemistry[39,76], metal-bound Aβ species are also believed to contribute to neurotoxicity. *In vitro* data suggest that $H_2O_2$ can be produced upon

binding of $Cu^{2+}$ to Aβ in the presence of biological reducing agents such as ascorbate, pyruvate, and glutathione.[77,78] This redox chemistry may explain the reason why $H_2O_2$ levels were increased in PC12 cells and CNS primary cultures that were exposed to Aβ in a previous study.[79] Accurate redox potentials validating Cu-Aβ redox cycles have yet to be agreed upon[78,80], but a recent X-ray absorption study (XAS) study has shown that $Cu^{2+}$-Aβ can be reduced to $Cu^{+}$-Aβ by ascorbate.[81] Furthermore, this study found that $Cu^{+}$-Aβ oligomers are highly dioxygen sensitive, unlike the monomeric and fibril forms. This suggests that the metal coordination geometry imposed by oligomeric species is critical for Cu-Aβ redox processes.[81] Histochemical staining of AD brain slices has linked Fe to oxidative damage that is colocalized with Aβ plaques[37]; however, based on the small amount of evidence for Fe-Aβ species, the contribution of such complexes to AD remains unclear. In summary, studies indicate that ROS are produced from metal-Aβ species (predominately $Cu^{+}/Cu^{2+}$ cycles), but their relevance to disease progression remains uncertain.[78]

*Metal Ion Dyshomeostasis in AD.* With the current drawbacks in drug development for AD, some have suggested other approaches to AD treatment need to be considered, like the metal ion hypothesis.[10] Since metal ions can induce the aggregation and effects of Aβ toxicity *in vitro*, they may have the potential to influence the progression of AD. If and how metal-Aβ species are directly involved in neurotoxic pathways within the brain remains to be established. Metal ions have critical functions in the processing of Aβ (by the metalloenzymes responsible for APP cleavage) and for Aβ clearance mechanisms by metalloproteases, indicating a multi-faceted dilemma that can lead to a detrimental feedback cycle (Figure 3.4).[4,9,10] The point of initiation could be the

result of several factors (for example, elevated metal ion levels, elevated ROS, overproduction of Aβ, improper or slowed removal of Aβ, among many others). Upon formation of low MW metal-Aβ aggregates, metal ions could be deprived of the enzymes critical for their homeostatic balance. Furthermore, the metal-Aβ aggregates could be protease resistant and/or induce toxicity by generating ROS or causing membrane disruptive oligomers.[41,48,49] These could be possible early stages of AD, which eventually lead to the deposition of metal-Aβ plaques (Figure 3.4). This destructive cycle entails only a small fraction of the disturbed biochemical functions in the AD brain but could be central to the disease.[5,10] Continued study is warranted to determine possible factors that could initiate this hypothesized cycle as well as methods for shutting it down as a potential therapeutic strategy.

**Figure 3.4. Normal Aβ clearance on the left and dysfunctional clearance induced by metal-Aβ species on the right.**

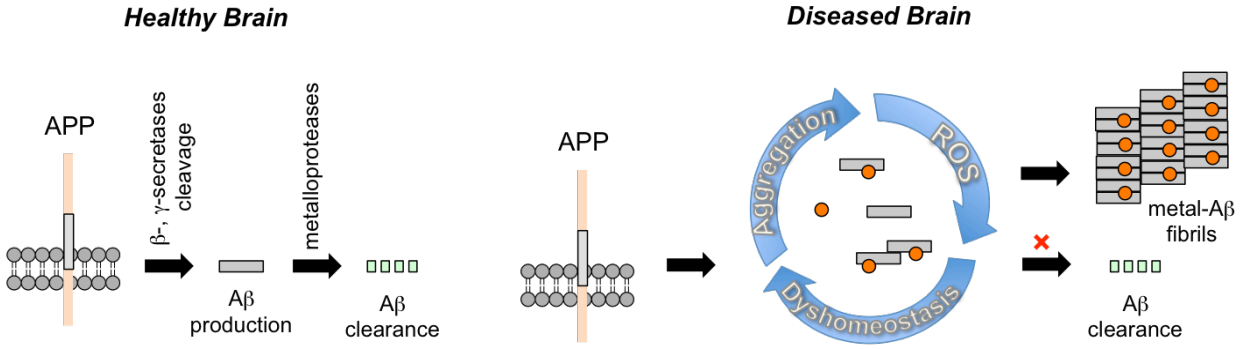


### 3.1.4 Metal Chelators in AD

*Traditional Metal Chelators.* If the presence or excess of metal ions leads to aggregation of Aβ, a simple remedy should be to use metal chelators to restore appropriate metal concentrations. Based on the observation that $Cu^{+/2+}$ and $Zn^{2+}$ induce rapid Aβ fibrillization, the traditional metal chelator EDTA (ethylenediaminetetraacetic

acid, Figure 3.5) was utilized to determine if metal removal from Aβ species or chelation of free zinc before the onset of aggregation had any effects on the size of Aβ species produced.[34,35,82] EDTA showed the ability to interfere and prevent the formation of large aggregates. A later study showed that other EDTA-like chelators (*N, N, N', N'*-tetrakis(2-pyridyl-methyl)ethylene diamine, TPEN) and the aromatic compound bathocuproine could resolubilize precipitated metal-Aβ from AD brains by abstracting metals from Aβ deposits (Figure 3.5).[83] It was suggested from these studies that chelators specific for $Cu^{2+}$ and $Zn^{2+}$ were necessary if metal chelation compounds were to be used as metal-Aβ inhibitors in AD. Additionally, the traditional metal chelators used are not blood brain barrier (BBB) penetrable, which needs to be addressed to achieve potential therapeutics. This led to the search for more selective metal chelators as potential therapeutic targets in AD.

It is worth mentioning here that the very first metal chelator therapeutic for AD was desferrioxamine (DFO, Figure 3.5), which was examined in a clinical trial to determine the effects of aluminum in AD.[84] The trial concluded that DFO leads to positive effects on cognition; however, no other metal ion levels were monitored in the study. Most likely, DFO had no direct influence on brain metal concentrations due to being BBB impenetrable. As mentioned before, this study provided no clear relationship of aluminum with AD.[40]

**Figure 3.5. Traditional metal chelators used for metal-Aβ studies.**

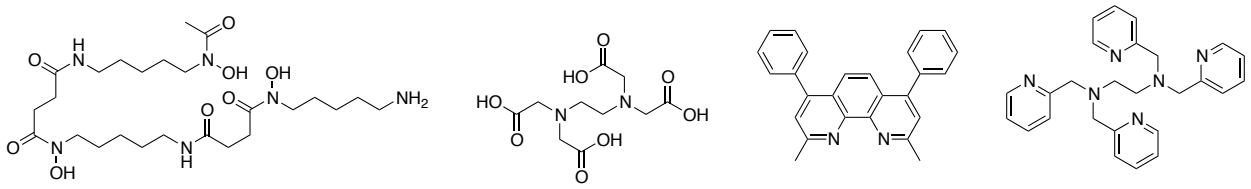

*Clioquinol and PBT2.* After searching for compounds with more favorable drug-like properties, Bush and colleagues reported on the success of a bidentate chelator with previously known BBB penetration and $Cu^{2+}/Zn^{2+}$ selectivity, clioquinol (CQ, Figure 3.7). In the Tg2576 transgenic AD mouse model, clioquinol was capable of reducing amyloid plaque burden after 9 weeks of administration, and it also improved the overall health of the mice.[85] The *in vivo* activity of CQ may be due to a combination of solubilization of Aβ aggregates by removal of $Cu^{2+}$ and $Zn^{2+}$ from amyloid aggregates followed by the up-regulation of metal-dependent metalloproteases responsible for Aβ degradation (Figure 3.6).[86] It is suggested that CQ acts as a small molecule metal chaperone capable of redistributing metal ions within cells, which accounts for the activation of metalloproteases.[87] It is important to point out that this is a different mechanism from the systemic metal chelation approach taken for Wilson's disease, where an abundance of Cu needs to be removed from the body.[9] The systemic approach has been targeted in AD for iron dyshomeostasis but is not discussed here.[88] Studies on CQ have provided a substantial basis for establishing the treatment of AD based on the metal ion hypothesis.[87] Therapeutic use of CQ, however, is limited in applicability due to difficulty in separating it from diiodo derivatives in the chemical synthesis. In addition, it was connected with subacute myelo-optic neuropathy observed in the Japanese population after being overprescribed as an amebicide for indigestion and diarrhea.[89]

**Figure 3.6. The use of metal chelators to disrupt effects of metal-Aβ species.**

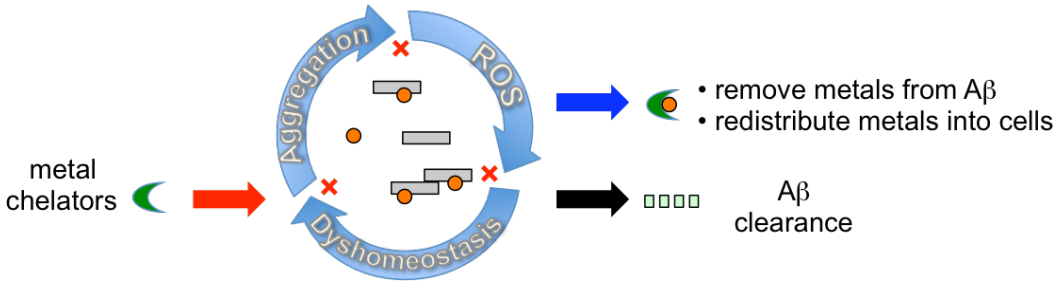


Expanding upon the success of CQ for understanding metal ions and Aβ in AD, Bush and coworkers developed the new hydroxyquinoline derivative, PBT2, as a potential therapeutic for AD. The structure of PBT2 has yet to be revealed. PBT2 has shown enhanced properties as compared to CQ and is currently in phase IIa clinical trials. Initial studies in two transgenic AD mouse models demonstrated the ability of PBT2 to reduce interstitial Aβ concentrations. It also resulted in improved cognition in the mice.[90] PBT2 is proposed to act in a similar fashion to CQ by removing metals from Aβ aggregates and redistributing metal ion concentrations within cells by transporting metal ions past the cell membrane (Figure 3.6).[91,92] This metal ion redistribution ability of PTB2 also shows beneficial up-regulating effects on signal cascades responsible for synaptic activity. Furthermore, PBT2 can inhibit the formation of $Zn^{2+}$-Aβ species that are resistant to Aβ degrading enzymes, further expanding its therapeutic profile. Studies utilizing CQ and PBT2 have provided additional evidence and insight into the metal ion hypothesis of AD and provided a proof of principle for the therapeutic approach that targets metal-Aβ species with metal chelators.

### 3.1.5 Bifunctional Molecules as Chemical Tools in AD

CQ and PBT2 are valuable compounds in understanding the role of metal ions and Aβ in AD. While these chelators are relatively specific for $Cu^{2+}$ and $Zn^{2+}$, they may not efficiently target metal-Aβ species in heterogeneous environments because they do not recognize metal-free Aβ.[85] This lack of functionality suggests a possible improvement in molecules designed to target metal-Aβ species in the brain. Progressing from traditional metal chelators, new bifunctional molecules that have both Aβ interaction functionality and metal chelation properties have been developed based on either linkage or incorporation approaches (Figure 3.7).[30,31]

**Figure 3.7. Design strategies for new bifunctional compounds for targeting metal-Aβ species.**

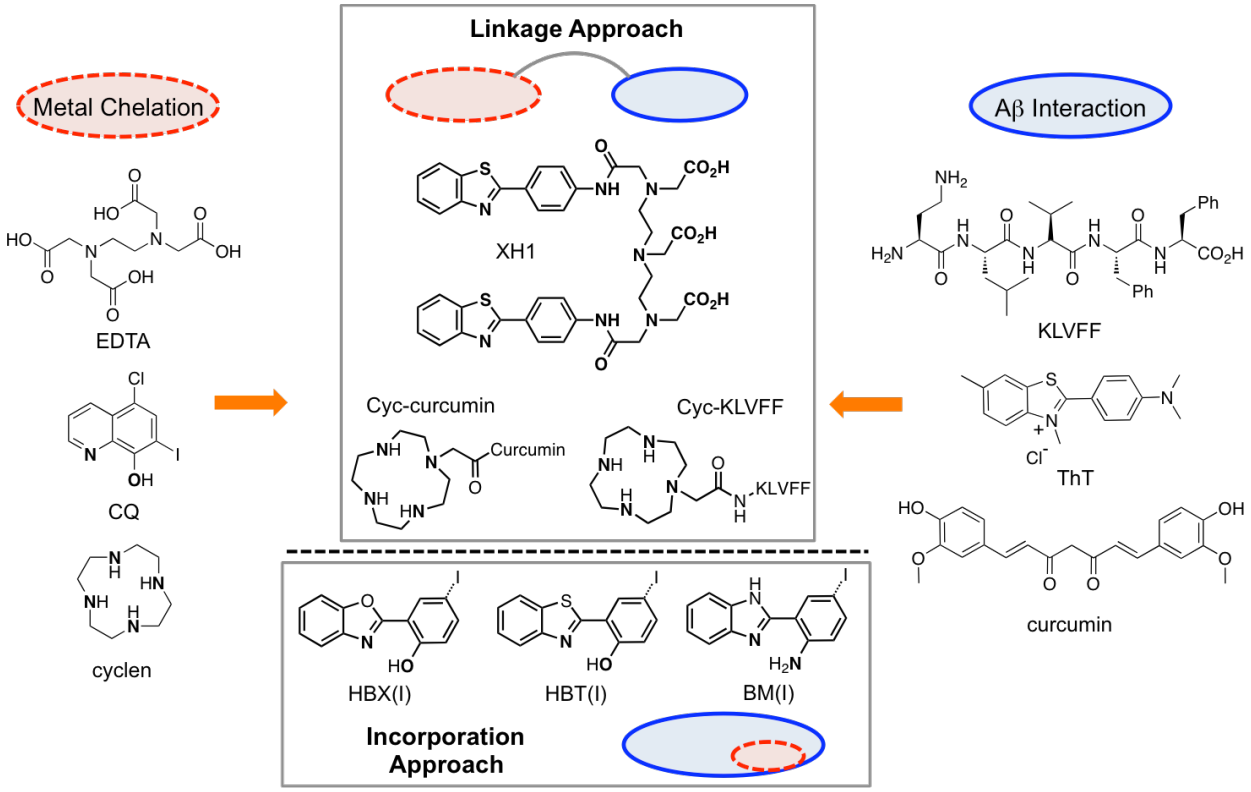

The first reported bifunctional molecule (XH1) combined the metal chelation properties of an EDTA-like moiety and the Aβ interaction of ThT (Thioflavin T, Figure 3.7).[93] ThT is perhaps the most well known indicator of amyloid plaques and has been used extensively for several decades because of its ability to bind specifically to Aβ aggregates.[94,95] XH1 was able to decrease $Zn^{2+}$-induced $A\beta_{1-40}$ aggregation as well as APP expression in human SH-SY5Y neuroblastoma cells, indicating the possible interference of metal-Aβ interactions. Given these positive results *in vitro* and no significant neurotoxicity at low micromolar concentrations in living cells, XH1 was tested further in the presenilin 1 (PS1)/APP transgenic mouse model. While no behavior differences were observed in mice treated with XH1 for four weeks compared to those left untreated, the deposition of Aβ plaques and the concentration of cortical Aβ were reduced in the treated mice. XH1 showed promising results as the first molecule designed using the bifunctional approach; however, no further developments have been reported.

The linkage approach has been further explored by using the macrocyclic metal chelator cyclen attached to peptides or small molecules capable of interacting with Aβ (Figure 3.7).[96] Cyc-KLVFF was effective in reducing metal-triggered Aβ aggregation and neurotoxicity including $Cu^{2+}$-induced ROS production *in vitro* and in neuronal cell culture. Aggregated forms of the peptide also were cleaved upon incubation with cyc($Cu^{2+}$)-KLVFF. Apo-cyc-KLVFF was nontoxic in primary mouse N2a neuroblastoma cells and could recover the toxicity of $A\beta_{1-42}$ in cells pretreated with $Cu^{2+}$. These results indicate the potential of apo-cyc-KLVFF to sequester $Cu^{2+}$ from heterogeneous environments to protect against metal-Aβ induced toxicity.

Another bifunctional small molecule containing cyclen, cyc-curcumin (Figure 3.7), was prepared to evaluate the ability of other recognition frameworks to function in this platform.[96] The corresponding metal complex, cyc($Cu^{2+}$)-curcumin, presented Aβ aggregation inhibition and Aβ cleavage activity similar to cyc($Cu^{2+}$)-KLVFF. The cyc($Cu^{2+}$)-curcumin complex showed modest rescue of Aβ-induced neurotoxicity. These compounds demonstrate that linking a peptide or non-peptide Aβ recognition/interaction molecule to a metal chelation framework may influence metal-induced Aβ aggregation pathways, introducing another avenue for development of bifunctional compounds for targeting metal-Aβ species using the linkage approach.

An alternative to the linkage approach involves directly incorporating metal binding sites into Aβ interaction molecules. The first example of this strategy was reported by Rodríguez-Rodríguez *et al*.[97] A virtual screening of commercially available neutral ThT derivatives containing a bidentate metal chelation site allowed this team to identify HBX, HBT, and BM as potential candidates for targeting metal ions surrounded by Aβ (Figure 3.7). The iodinated versions of these three compounds, HBXI, HBTI, and BMI, also were prepared and investigated due to their potential contribution to the development of new SPECT imaging agents (SPECT = single photon emission computed tomography). HBXI and HBTI were found to be primarily neutral at physiological pH (*e.g.*, 7.4), which indicates potential BBB permeability *in vivo*. In contrast, BMI exists in both the protonated and neutral forms at this pH. The solution speciation studies regarding the binding affinities of $Cu^{2+}$ and $Zn^{2+}$ to these compounds suggest their capability to sequester metal ions associated with soluble forms of Aβ.

Inhibition of both $Cu^{2+}$- and $Zn^{2+}$-induced Aβ aggregation was most significant for HBTI, while HBXI and BMI showed a similar effect only for $Cu^{2+}$-triggered Aβ aggregation.

In addition, fluorescence measurements were conducted to assess the possible use of HBX, HBT, and their iodinated analogues as potential *in vivo* biomarkers for amyloid aggregates. Promisingly, HBX and HBT exhibited stronger fluorescence responses with mature amyloid fibrils than Pittsburgh Compound B, used in clinical trials. This family of ThT-derived metal chelators demonstrated the potential for improving radioisotopic detection of Aβ aggregates in the human brain and a potential therapeutic approach to AD.

Due to the many discrepancies that persist in the metal ion hypothesis (*vide supra*), continued study is needed to determine the validity of the metal-ion hypothesis in AD. In addition to verification of metal binding effects on Aβ reactivity by spectroscopic and biochemical assays, the continued development of chemical tools could greatly assist in determining the neurotoxicity of metal-Aβ species *in vivo* and *in vitro*. As seen for CQ and PBT2, new metallobiochemistry was uncovered by perturbing cellular function and similar compounds could lead to additional discoveries. The molecules designed up to this point by either the linkage or incorporation approach mark the beginning of strategies to better understand the roles of metal ions associated with Aβ in AD.[30,31] However, several concerns in the design of these molecules may limit their applicability as *in vitro* and *in vivo* chemical tools and/or therapeutics. These include nonspecific metal binding properties, inability to cross the BBB due to size/hydrophilicity, and/or truncated Aβ-interaction moieties. These limitations suggested that improvements could be made to these approaches. The work described

in this thesis has sought to further advance strategies of rationally designed bifunctional compounds by minimally modifying compounds known to interact with Aβ aggregates.

### 3.2 Design Considerations and Rationale of Bifunctional Molecules

In order to design bifunctional molecules that target metal-Aβ species, molecular scaffolds were first chosen that are known to interact with Aβ fibrils. The first two families of bifunctional compounds developed in the Lim Lab were based on the SPECT imaging agents, $^{125}$I-IMPY and *p*-$^{125}$I-stilbene (Figure 3.8).[98,99,100] In addition to their strong binding affinity for Aβ plaques ($K_i$ ≤ 2 nM), both compounds are small, neutral, lipophilic, able to penetrate the BBB, and effectively removed from the body, making them valid candidates for in vivo applications.[101,102,103,104,105] Compared to the common amyloid-staining and amyloid-aggregation detecting molecule, ThT (Figure 3.7)[94,95], IMPY is an attractive molecular scaffold for developing bifunctional molecules due to its structural similarity in addition to its lack of charge. Neutral ThT derivatives facilitate greater BBB penetration and can improve binding affinity to Aβ as observed for the benchmark positron emission tomography (PET) imaging agent used for detecting amyloid deposits in the human AD brain, Pittsburgh Compound B (PiB, Figure 3.8).[101,106,107,108,109] Electron rich styrylbenzene derivatives similar to *p*-I-stilbene have also been extensively studied for their ability to bind to Aβ fibrils.[98,99,105] The utility of this framework has recently been displayed in the development of the only FDA approved PET imaging agent, $^{18}$F-AV-45, for AD (Figure 3.8). Therefore, these two molecular scaffolds present attractive targets for the design of bifunctional molecules that target both metal ions and Aβ.

**Figure 3.8. Aβ imaging agents (top) and rationally designed metal chelators for targeting metal-Aβ species (bottom). Metal binding sites are in bold.**

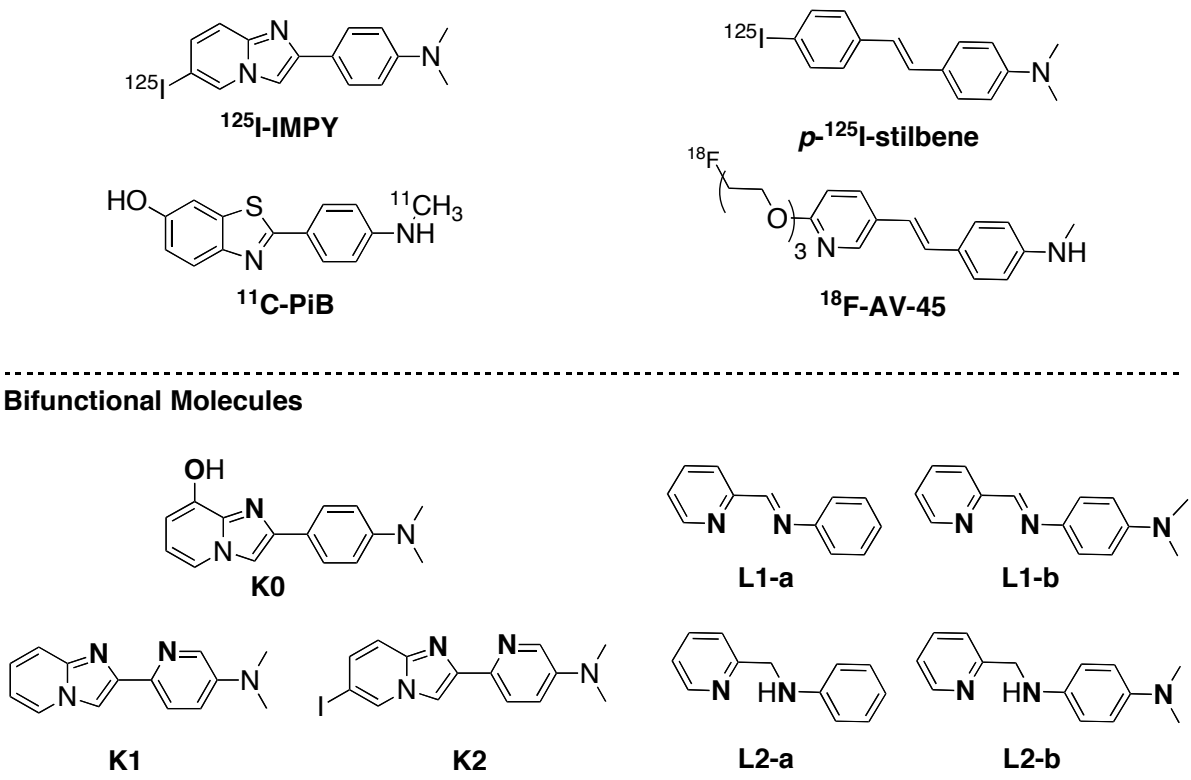


The incorporation strategy (Figure 3.7) for developing metal chelators as chemical tools for specifically targeting and modulating metal-Aβ species was undertaken with these two families of molecules. This approach is attractive because it requires minimal structure perturbation, thereby allowing for the greatest potential for retaining Aβ interaction ability.[30,31] The metal binding IMPY family was created by either installation of an OH group on the imidazopyridine ring (**K0**, first generation)[110] or an N atom on the aniline ring (**K1** and **K2**, second generation)[111] (Figure 3.8). Similarly, the pyridinylimines (**L1-a** and **L1-b**, first generation)[110,112,113] and pyridinylamines (**L2-a** and **L2-b**, second generation)[112,114] were devised by the installation of two N atoms into the stilbene scaffold). The second generation **K** series was inspired by searching for

molecules less toxic than **K0.** Furthermore, the **L2** series was developed due to the instability of the **L1** series under aqueous conditions.

One important feature that is common to the Aβ imaging molecules (Figure 3.8) as well as ThT (Figure 3.7) is the presence of either a mono- or dimethylaniline substituent. These groups are suggested to be critical for the binding of these molecules to Aβ aggregates.[109,115,116] In order to confirm the necessity of this substituent for targeting metal-Aβ species, the **L** series includes molecules with and without this group to probe the structure-interaction-reactivity relationship.[113,114]

Along with the requirement of binding metal ions and Aβ interaction capability, the designed molecules should have drug-like properties and must be able to penetrate the BBB if they are to be considered as potential chemical tools and/or therapeutics for use within the brain. Such molecules should adhere to the restrictive terms of Lipinski's rules for drug-likeness and have an agreeable BBB passive diffusion parameter (logBB, Table 3.1).[117,118] All of the compounds follow the five Lipinski rules defined in Table 3.1. **K2** and **L2-b** indicate the greatest potential to pass the BBB on the basis of their calculated logBB. Although the other compounds have logBB values in between good and poor, they are suggested to be potential BBB penetration candidates (CNS+) based on the Parallel Artificial Permeability assay (PAMPA). This assay predicts the ability of small molecules to penetrate the BBB by using a synthetic lipid membrane that mimics the composition of the BBB.[119,120] Results indicated that all the designed compounds show potential BBB passage as compared to known BBB permeable compounds (Table 3.1).[120]

**Table 3.1 Values for drug-likeness and BBB penetration properties.**

| Calculation | K0 | K1 | K2 | L1-a | L1-b | L2-a[114] | L2-b[114] | Lipinski's rules & others |
|---|---|---|---|---|---|---|---|---|
| **MW (g/mol)** | 253 | 238 | 364 | 182 | 225 | 184 | 227 | ≤450 |
| ***c*log P** | 3.86 | 3.04 | 4.16 | 1.61 | 1.77 | 1.59 | 1.76 | ≤5.0 |
| **HBA** | 4 | 4 | 4 | 2 | 3 | 2 | 3 | ≤10 |
| **HBD** | 1 | 0 | 0 | 0 | 0 | 1 | 1 | ≤5 |
| **PSA (Å$^2$)** | 40.8 | 31.2 | 31.2 | 24.7 | 28.5 | 24.9 | 28.2 | ≤90 |
| **logBB** | 0.12 | 0.13 | 0.30 | 0.0089 | -0.014 | 0.012 | 0.85 | >0.3(good)<br><-1.0(poor) |
| **$-\log P_e$** | 4.21(7) | 4.41(8) | 4.23(8) | 4.52(3) | 4.62(3) | 4.24(1) | 4.04(1) | <5.4(CNS+)<br>>5.7(CNS–) |

MW: molecular weight; *c*logP: calculated logarithm of the octanol-water partition coefficient; HBD: hydrogen-bond donor atoms; HBA: hydrogen-bond acceptor atoms; PSA: polar surface area; logBB = -0.0148 × PSA + 0.152 × *c*logP + 0.130; –log $P_e$: measured permeability, calculated by PAMPA software v. 3.5 ($n$ = 6). Error values are reported in parentheses. Controls (–log $P_e$): Verapamil 4.46(2), Quinidine 4.49(4), Theophyline 6.57(3).

The IMPY and stilbene-derived families (Figure 3.8) are potential candidates as chemical tools for studying metal-Aβ species based on the above discussion. Their desired properties as bifunctional molecules (metal chelation and Aβ interaction) were confirmed by spectroscopic and other studies that will be described in Section 3.3.

### 3.3 Characterization of Bifunctionality

In order to distinguish the **K** and **L** series as bifunctional molecules, their properties as metal chelators and as compounds that can interact with Aβ needed to be established. These properties are important for being able to distinguish our compounds from traditional metal chelators that may remove metals from Aβ species, yet are not able to differentiate metal ions associated with Aβ from other metalloproteins throughout the brain and rest of the body. Identifying ligands that have specificity for Cu and/or Zn and Aβ species is the main objective of the bifunctional compounds in order to study metal-Aβ reactivity and their relation to the neurotoxicity observed in AD. Based on the success of the stilbene framework, extensive metal binding of the designed molecules was verified by UV-Vis, X-ray crystallography, IR, MS, and $^{1}$H NMR. These detailed studies were conducted to understand how both the imine/amine and dimethylamino groups influence metal binding.

### 3.3.1 Metal Binding of First Generations

**Figure 3.9. First-generation of ligands and their corresponding 1:1 ligand to metal complexes.**

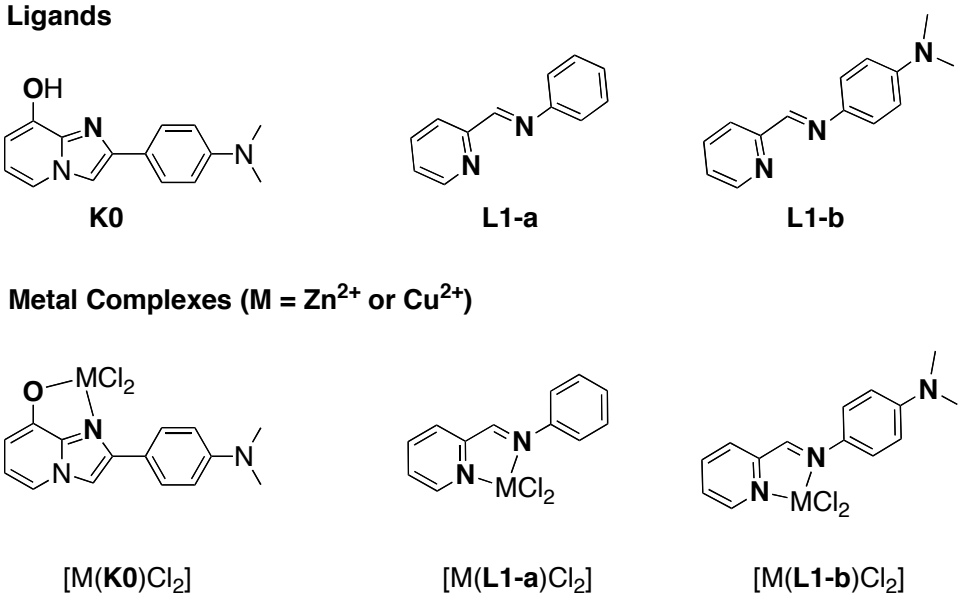


*UV-Vis of **K0**.* Changes in the absorption spectrum of **K0** (40 μM) upon the addition of 2 equiv of $CuCl_2$ in EtOH indicated metal binding (Figure 3.10a and Table 3.2). The binding stoichiometry was predicted based on UV-Vis spectra using Job's method of continuous variation. The data showed an inflection point between 0.33 and 0.5, suggesting a mixture of 1:2 and 1:1 metal to ligand complexes (Figure 3.9 and Figure 3.10b). Unlike the stilbene derivatives, comparison of isolated metal complexes and *in situ* complexes was not carried out due to the lack of crystals for the **K** series.

**Figure 3.10. Metal binding studies of K0, a) UV-vis and b) Job's plot.**

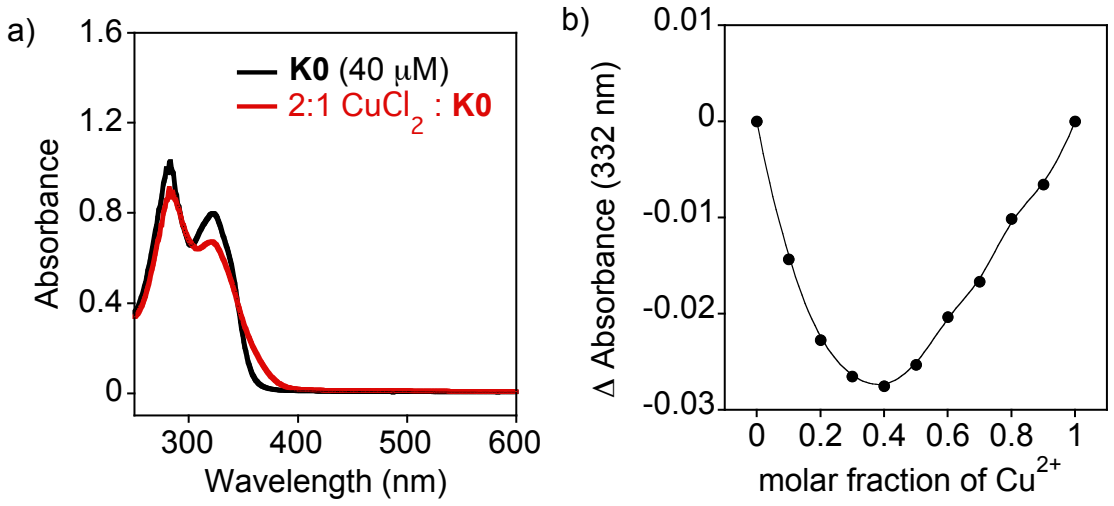


Conditions: Spectra acquired in EtOH at rt. a) [**K0**] = 40 μM, [$CuCl_2$] = 80 μM and b) [**K0**] = 15 μM.

*UV-vis **L1** Series.* The solution metal binding properties of **L1** series with metal chloride salts were initially evaluated using UV-vis spectroscopy.[113] Metal coordination was established based on shifts in the optical bands of **L1-a** and **L1-b** upon addition of $CuCl_2$ or $ZnCl_2$ in EtOH (Figure 3.11 and Table 3.2). Small intensity changes of absorption features at 280 and 323 nm were observed in the absorption spectra for **L1-a** (100 μM) upon the addition of 1 equiv of $CuCl_2$ or $ZnCl_2$. In contrast, clear red shifts of the absorption feature at 396 nm in the spectra of **L1-b** (40 μm) to *ca.* 450 nm and *ca.* 470-480 nm, for 1 equiv of $Cu^{2+}$ and $Zn^{2+}$, respectively, were indicated. Differentiating the absorption features of **L1-a** and **L1-b**, the absorption band for **L1-b** at 396 nm is due to the intramolecular charge transfer between the lone pairs of the nitrogen of the dimethylamino group and the aromatic ring (Figure 3.11).[121] Dimethylanilines are well known for their photochemistry, and the effects of pH, ionic strength, and presence of metal ions on their UV-Vis spectra.

Isolated crystals of [Zn(**L1-a**)$Cl_2$] and [Zn(**L1-b**)$Cl_2$] were obtained allowing for the comparison of discrete metal complexes with the *in situ* generated complexes (Figure 3.9 and Figure 3.13). The optical features of the $Zn^{2+}$-**L1-a** or $Zn^{2+}$-**L1-b** interaction in EtOH were in agreement with the isolated metal complexes acquired in $CH_3CN$ (Table 3.2). The EtOH solution of ligands and chloride salts indicated equilibria of metal free and metal bound ligands. With the addition of 10 equiv of **L1-b** in EtOH, the metal binding equilibrium could be further driven toward metal complexes, although not completely as compared to the isolated complexes (Figure 3.11b). In $CH_3CN$, no spectral changes were observed over time indicating no dissociation of the metal from the ligand for the preformed complexes. Overall, UV-Vis studies suggest metal binding of **L1-a** and **L1-b** in solution.

**Figure 3.11. Metal binding of L1 series as established by UV-Vis.**

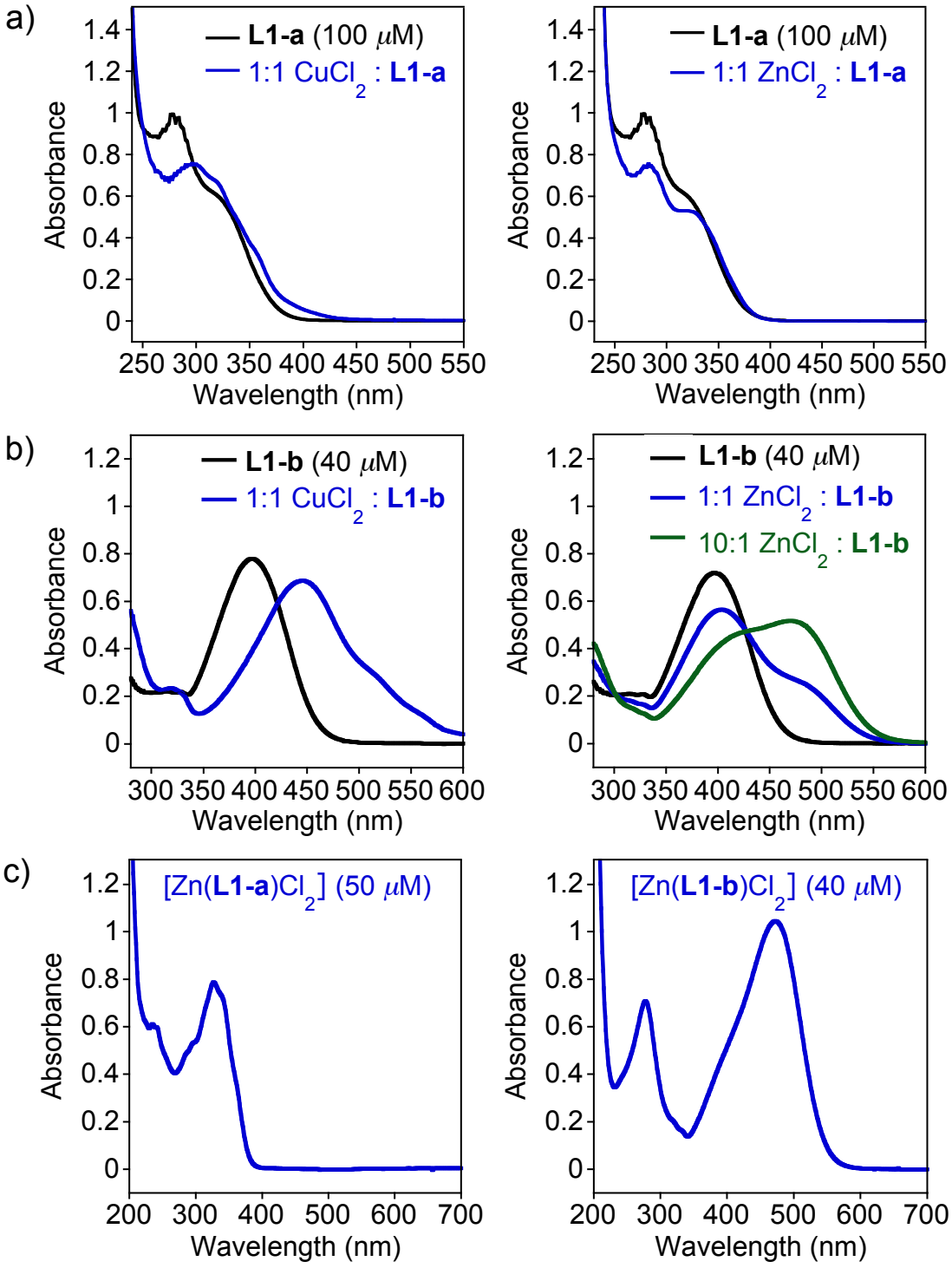


Conditions: UV-vis spectra of compounds (black, **L1-a** (a) and **L1-b** (b)) with $CuCl_2$ (blue) or $ZnCl_2$ (dark or light green) in EtOH at rt. (c) UV-vis spectra of [Zn(**L1-a**)$Cl_2$] and [Zn(**L1-b**)$Cl_2$] in $CH_3CN$ at rt.

**Table 3.2. Summary of optical results for K0 and L1 series[a].**

| | Spectral properties (nm) | | | |
|---|---|---|---|---|
| **Compound** | **Unbound** | **$CuCl_2$** | **$ZnCl_2$** | **crystals[b]** |
| **K0** | 280, 320 | 284, 322, 365 (sh) | - | - |
| **L1-a** | 280, 323 | 297 | 283, 325 | [Zn(**L1-a**)$Cl_2$] 235, 241, 328, 341 |
| **L1-b** | 316, 396 | 318, 450 | 403, 484 408[c], 473[c] | [Zn(**L1-b**)$Cl_2$] 277, 475 |

[a] Measurements carried out in EtOH at rt following 10 min incubation. Ratio of metal to ligand was 1:1 unless otherwise noted.
[b] Optical data were obtained in $CH_3CN$.
[c] [$ZnCl_2$]/[**L1-b**] = 10:1.

Attempts to study **L1-a** and **L1-b** under more biologically relevant conditions revealed that the ligands have limited stability in aqueous solution ($t_{1/2}$ = *ca.* 70 s and *ca.* 240 s, respectively, in 20 mM HEPES buffer (pH 7.4) containing 150 mM NaCl ([ligand] = 40 μM)) because of their hydrolysis, which was confirmed by ESI-MS. However, the stability of the imine functionality of the **L1** series was enhanced in the presence of metal ions (two- to three-fold increase in $t_{1/2}$ with $CuCl_2$ or $ZnCl_2$). This stability may help facilitate the compounds ability to survive long enough to interact with and modulate metal-Aβ species (refer to Section 3.4). Alternatively, the hydrolyzed products may contribute to metal-Aβ reactivity. Because of the limited stability of these imine compounds in aqueous solutions, further metal binding properties such as pH-variable solution speciation were not studied.

Although these compounds have limitations under aqueous conditions, their metal selectivity can still provide insight into how this framework may compete for metal ions. Investigation of the metal selectivity of **L1-b** (40 μM) using UV-Vis was

undertaken.[113] These experiments indicate that this ligand is relatively selective for $Cu^{2+}$ over other metal ions (*e.g.*, $Mg^{2+}$, $Ca^{2+}$, $Mn^{2+}$, $Fe^{2+}$, $Fe^{3+}$, $Co^{2+}$, $Ni^{2+}$, and $Zn^{2+}$) at stoichiometric ratios in EtOH. Figure 3.12 indicates that while the later, first row transition metal ions can bind to **L1-b** (black bars), $Cu^{2+}$ is capable of out-competing these ions as depicted by the grey bars returning near to the normalized value for **L1-b**-$Cu^{2+}$ (entry 9). These data suggest that it may be possible to make further modifications to this molecular framework (to enhance stability) and maintain metal selectivity.

**Figure 3.12. Metal selectivity of L1-b.**

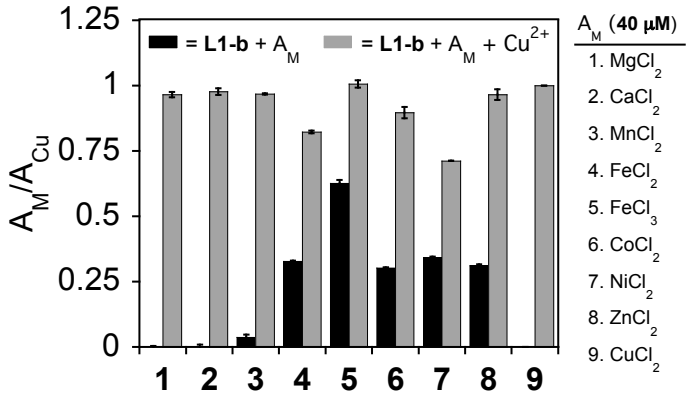


Conditions: Selectivity carried out in EtOH at rt, [**L1-b**] = 40 μM. Grey bars represent the addition of $CuCl_2$ (40 μM) to the solution containing other metal ions ($A_M$, black bars; 40 μM) followed by 5 min incubation at room temperature. The absorbance at 525 nm was used for the calculation of $A_M/A_{Cu}$ to minimize interference between the optical bands.

*X-ray crystallographic characterization of **L1** Series.* To further understand the metal binding properties in the solid state, X-ray quality single crystals of the metal complexes [Zn(**L1-a**)$Cl_2$] and [Zn(**L1-b**)$Cl_2$] were obtained and analyzed (Figure 3.13).[113] The complexes were grown by slow diffusion of $Et_2O$ into a solution of ligand and $ZnCl_2$ (1:1) in $CH_3CN$. Selected bond lengths and angles are summarized in Table 3.3. The structures show that the two desired nitrogen atoms of the ligands are

responsible for metal binding. The overall conformation of the imine ligands **L1-a** and **L1-b** of the Zn complexes is planar in the solid state, with a distorted tetrahedral geometry around the metal center. The bond lengths and angles for the Zn complexes do not vary significantly in the presence/absence of the dimethylamino group; however, slight differences in bond angles and the Zn−N1 bond length between [Zn(**L1-a**)$Cl_2$] and [Zn(**L1-b**)$Cl_2$] were observed (Table 3.3). A $Zn^{2+}$ complex with a structure similar to **L1-b** where the dimethylamino group is substituted with an iodine atom has been reported.[122] This molecule binds to $ZnCl_2$ in a 1:1 ratio to form a slightly distorted tetrahedral metal center with bond lengths and angles that are similar to those of [Zn(**L1-a**)$Cl_2$] and [Zn(**L1-b**)$Cl_2$]. This suggests that neither an electron withdrawing nor electron donating substituent in the para position of the phenyl ring significantly alters bond lengths or angles. Overall, the X-ray crystal structure determination confirmed the desired metal chelation by **L1-a** and **L1-b** *via* two nitrogen donor atoms.

**Figure 3.13. ORTEP diagrams showing 50% thermal ellipsoids for a) [Zn(L1-a)$Cl_2$] and b) [Zn(L1-b)$Cl_2$].**

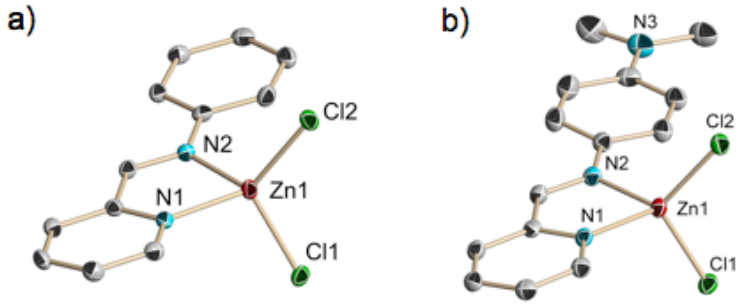

**Table 3.3. Selected bond lengths (Å) and angles (deg) of $Zn^{2+}$-L1 complexes.**

| | [Zn(**L1-a**)$Cl_2$] | [Zn(**L1-b**)$Cl_2$] |
|---|---|---|
| Zn1-N1 | 2.060(2) | 2.0446(17) |
| Zn1-N2 | 2.081(2) | 2.0828(18) |
| Zn1-Cl1 | 2.2280(6) | 2.2162(8) |
| Zn1-Cl2 | 2.1998(6) | 2.2056(8) |
| N1-Zn1-N2 | 81.20(8) | 82.24(7) |
| N1-Zn1-Cl1 | 107.72(6) | 110.16 |
| N1-Zn1-Cl2 | 119.14(6) | 117.42(6) |
| N2-Zn1-Cl1 | 111.40(6) | 110.06(5) |
| N2-Zn1-Cl2 | 117.10(6) | 120.03(6) |
| Cl1-Zn1-Cl2 | 115.48(2) | 113.18(2) |

*1D NMR of **L1** Series*. In order to elucidate differences in the structural and electronic environments of the **L1** ligands and their metal complexes, analysis of proton resonances by $^1$H NMR spectroscopy was executed (400 MHz, $CD_3CN$).[112] Focusing on the aromatic region of the spectrum first, an increase in shielding throughout the aromatic rings was observed upon moving from **L1-a** to **L1-b** in agreement with adding the electron-donating dimethylamino group (Figure 3.14a). For the isolated $Zn^{2+}$ complexes, [Zn(**L1-a**)$Cl_2$] and [Zn(**L1-b**)$Cl_2$], downfield shifting for all protons was observed upon $Zn^{2+}$ binding to the ligands, indicating that $Zn^{2+}$ withdraws electron density from the entire ligand framework (Figure 3.14). For $Zn^{2+}$ binding, the chemical shifts of protons in the $H_b$ and $H_c$ position of the pyridyl rings were moved downfield the most ($\Delta\delta$ > 0.40 ppm) while the resonances for $H_a$ and $H_d$ position did not shift significantly (Figure 3.14). This type of shifting is consistent with previous studies of

pyridyl-type metal complexes.[123] Overall, these $^{1}$H NMR studies revealed that the electronic environment of the whole scaffold was affected by $Zn^{2+}$ coordination.

**Figure 3.14. 1D $^{1}$H NMR metal binding studies of L1 series.**

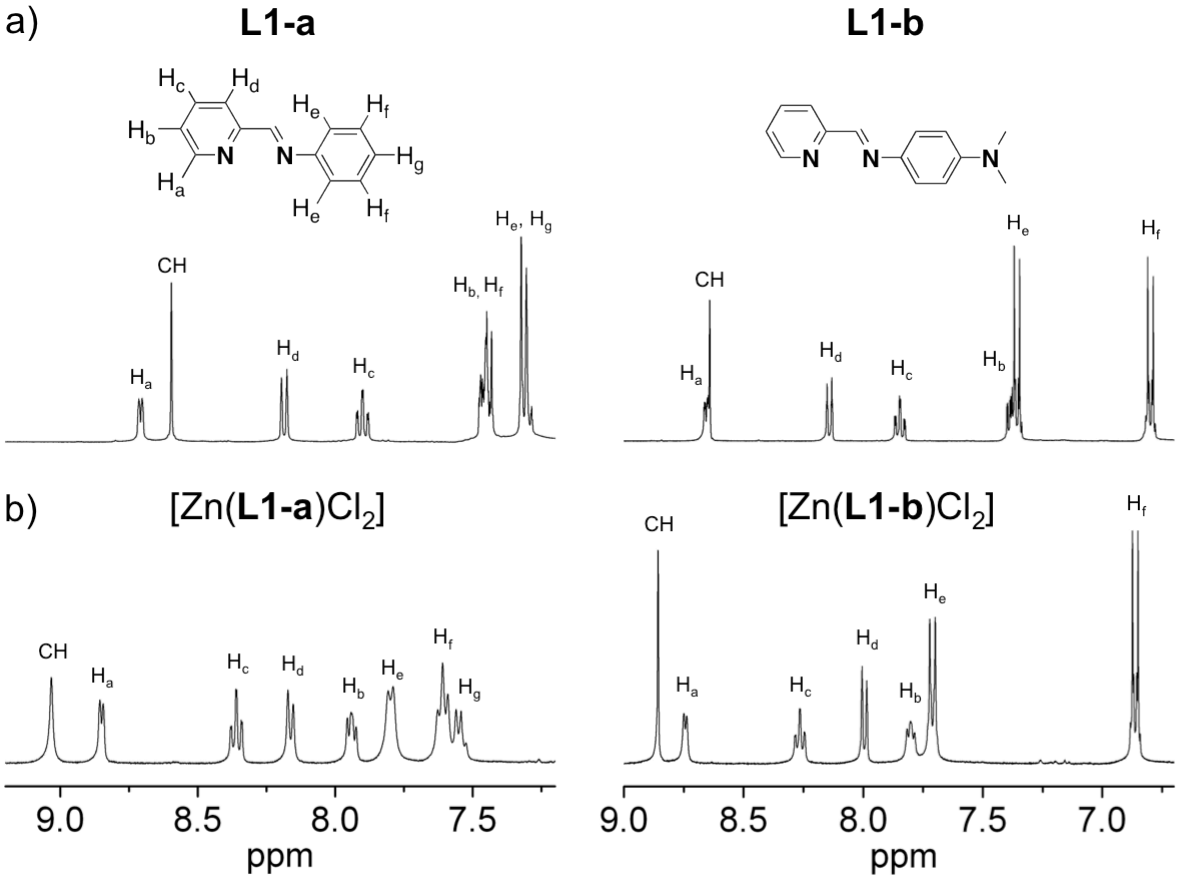


Conditions: Spectra recorded in $CD_3CN$ at rt (400 MHz).

*FT-IR of **L1** Series.* To investigate how structural alterations and metal binding can affect individual bond vibrations of the **L1** ligands, IR spectroscopy was carried out (Figure 3.15).[112] The Schiff base stretching bands at 1580 cm$^{-1}$ (**L1-a**) and 1572 cm$^{-1}$ (**L1-b**) were observed (Figure 3.15a). The appearance of the C–N stretching frequency at 1517 cm$^{-1}$ for **L1-b** is indicative of the *sp*$^{2}$ character of the dimethylamino moiety, which showed an effect mainly in the fingerprint region of the spectra. Additional

confirmation of metal binding effects in the solid state was obtained by FT-IR of the isolated metal complexes [Zn(**L1-a**)$Cl_2$] and [Zn(**L1-b**)$Cl_2$] and compared with the free ligands. Shifting of bond frequencies in the fingerprint region and particularly in the region between 1100 and 1700 $cm^{-1}$ of the IR spectrum are indicative of metal binding (Figure 3.15b). In the metal bound form, the imine (C=N) stretching frequency shifts to higher wavenumbers, from 1580 (**L1-a**) to 1594 $cm^{-1}$ and 1572 (**L1-b**) to 1598 $cm^{-1}$ for [Zn(**L1-a**)$Cl_2$] and [Zn(**L1-b**)$Cl_2$], respectively. A similar strengthening of the imine bond was also observed for previously reported $Zn^{2+}$–imine complexes and was attributed to the reorganization of the *s* character of the nitrogen lone pair.[124,125] From the IR analysis, effects of the dimethylamino group and metal chelation on the molecular structure were observed.

**Figure 3.15. IR metal binding studies of L1 series.**

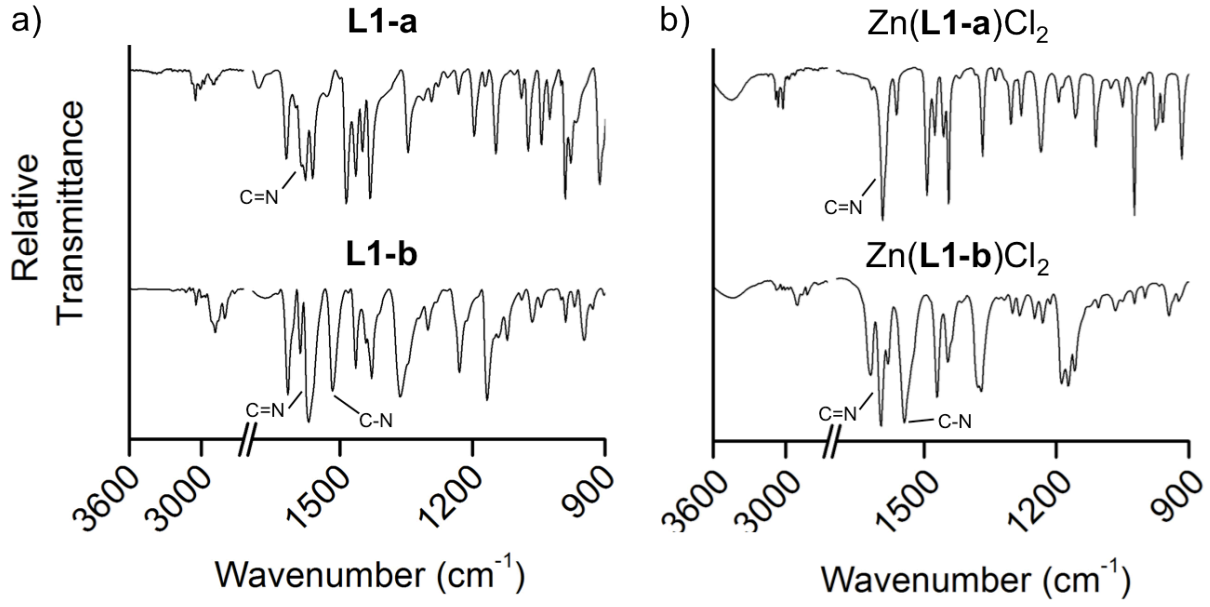


Conditions: FT-IR spectra of a) ligands **L1-a** and **L1-b** and b) their $Zn^{2+}$ complexes [Zn(**L1-a**)$Cl_2$] and [Zn(**L1-b**)$Cl_2$] in KBr.

From the above spectroscopic studies, the metal binding ability of the first-generation of **K** and **L** molecules was demonstrated. Crystallographic data also suggested that metal coordination occurs *via* the two N atoms for the stilbene derivatives and that **L1-b** is relatively selective for $Cu^{2+}$ over other divalent metal ions.

### 3.3.2 Metal Binding of Second Generations

**Figure 3.16. Second-generation of ligands and their corresponding 1:1 ligand to metal complexes.**

**Ligands**

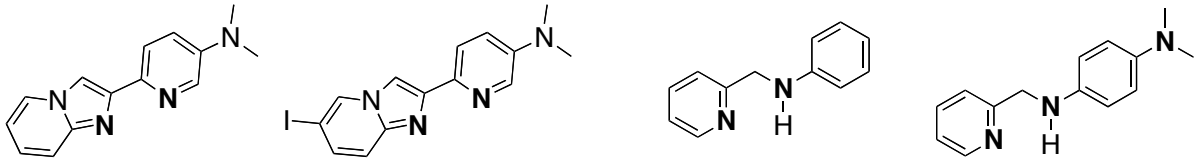

**K1** **K2** **L1-a** **L1-b**

**Metal Complexes (M = $Zn^{2+}$ or $Cu^{2+}$)**

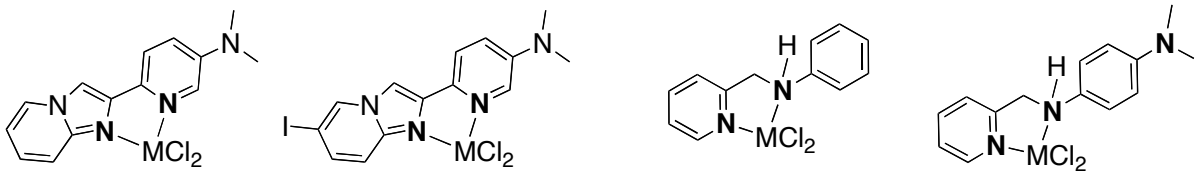

[M(**K1**)$Cl_2$] [M(**K2**)$Cl_2$] [M(**L2-a**)$Cl_2$] [M(**L2-b**)$Cl_2$]

Moving towards more biocompatible bifunctional molecules, both families of second-generation **K**[111] and **L**[114] molecules are stable in water, allowing for their metal binding properties to be studied under aqueous conditions. The ability of molecules to bind metal ions was investigated using UV-Vis spectroscopy at room temperature in 20 mM HEPES at pH 7.4 and 150 mM NaCl.

*UV-vis of **K1** and **K2***. Spectral features of the ligands only (**K1** and **K2**) showed two absorption bands similar to that of **K0** with the absorption feature above 300 nm

more red shifted in the second generation compounds (Table 3.2 and Table 3.4). The addition of two equiv of $CuCl_2$ or $ZnCl_2$ to a solution of **K1** or **K2** (50 and 25 μM, respectively) resulted in bathochromic shifts of the optical bands at *ca.* 275 and *ca.* 350 nm (Figure 3.17). The shifts due to metal binding in the absorption bands of the IMPY derivative with the iodine functionality (**K2**) were visualized to be more prominent as compared to **K1**. **K1** showed more of a decrease in absorption intensity rather than a band shift upon addition of $CuCl_2$ similar to results for **K0**. These changes in absorption spectra in the presence of metal salts indicate the ability of **K1** and **K2** to bind $Cu^{2+}$ and $Zn^{2+}$.

**Figure 3.17. UV-Vis spectra of a) K1 and b) K2 with metal chloride salts.**

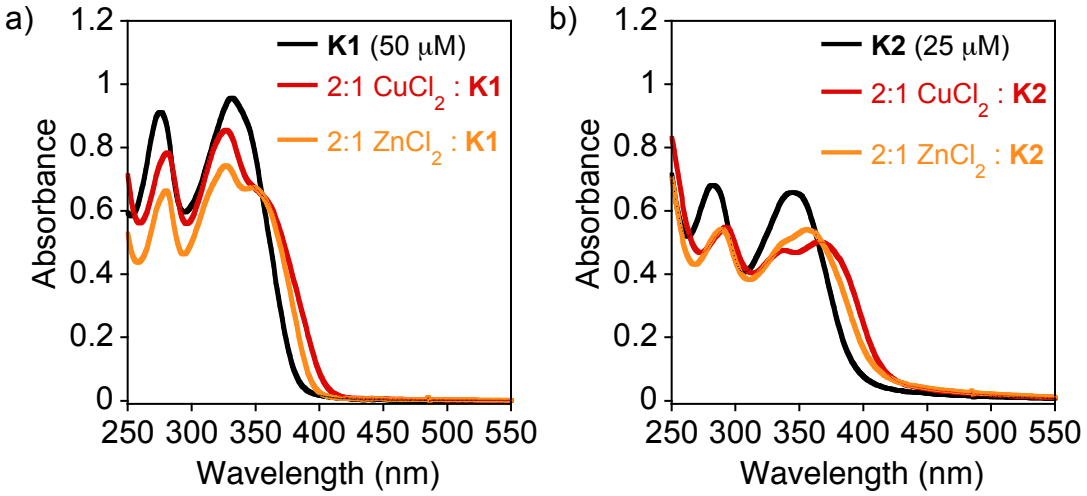


Conditions: IMPY derivatives **K1** and **K2** (50 μM, black) were incubated with metal ions (25 μM) for 5 min (20 mM HEPES, pH 7.4, 150 mM NaCl). Left: **K1**+$CuCl_2$ (red) or $ZnCl_2$ (orange). Right: **K2**+$CuCl_2$ (red) or $ZnCl_2$ (orange).

*UV-Vis of **L2** Series.* As a result of disrupting the conjugation by reduction to the secondary amine, the absorption feature at *ca.* 400 nm for **L1-b** was not present in the spectral window for **L2-b** (Figure 3.11 and Figure 3.18). For metal binding with the **L2** series, optical shifts were observed upon treatment with one equiv of the metal salts

(Figure 3.18).[114] For **L2-a**, significant spectral changes were not observed upon the addition of $ZnCl_2$ indicating weak metal interaction under these conditions; however, a new absorption band appeared at 388 nm in the presence of $CuCl_2$ indicating stronger binding for $Cu^{2+}$ (Figure 3.18a). Different from **L2-a**, both metal ions were suggested to bind to **L2-b** based on new absorption features (430 nm, $ZnCl_2$ and 450 nm, $CuCl_2$, (Figure 3.18b). It should be noted that unlike the **L1** series, the **L2** series was stable under these conditions and showed no decomposition over several hours.

Attempts to grow crystals were successful for [Cu(**L2-a**)$Cl_2$] and [Zn(**L2-b**)$Cl_2$]. Similar UV-vis absorption bands were observed in the *in situ* generated metal complexes in buffered solution as compared to the isolated complexes in $CH_3CN$ (Figure 3.18c). For both isolated compounds, the absorption bands are red-shifted compared to the complexes generated in aqueous conditions. Absorption spectra of the isolated complexes were acquired in $CH_3CN$ instead of water to maintain the 1:1 ligand to metal binding and prevent formation of other species (see speciation studies below).

**Figure 3.18. UV-Vis spectra of L2 series.**

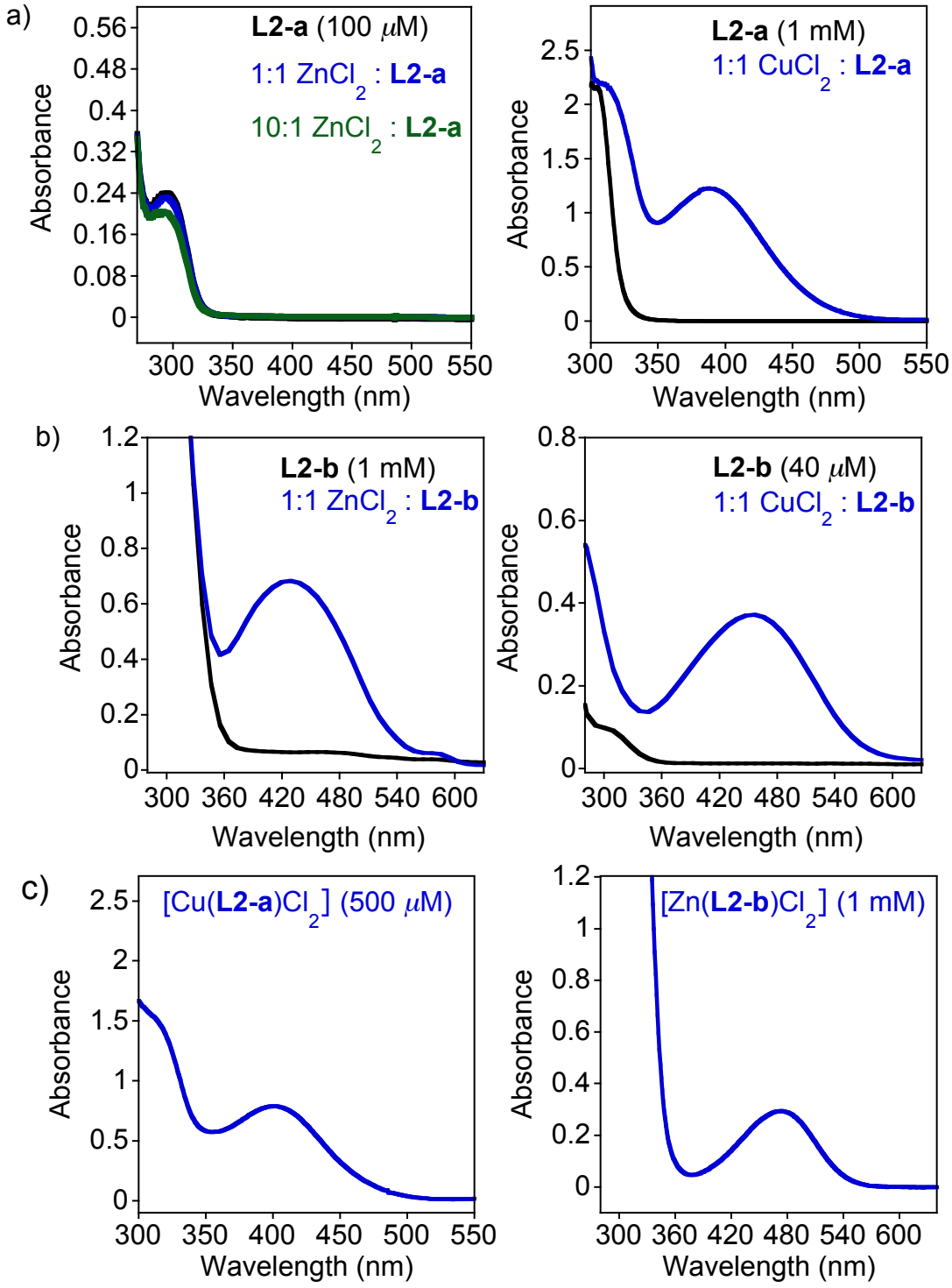


Conditions: Stilbene derivatives a) **L2-a** and b) **L2-b** with 1 equiv of $CuCl_2$ (incubation for 5 min) and 1 or 10 equiv $ZnCl_2$ (incubation for 30 min) in 20 mM HEPES, pH 7.4, 150 mM NaCl. c) Spectra of [Zn(**L1-a**)$Cl_2$] and [Zn(**L1- b**)$Cl_2$] in $CH_3CN$ at rt.

**Table 3.4. Summary of optical results for second-generation molecules[a].**

| Compound | Spectral properties (nm) | | | |
|---|---|---|---|---|
| | Unbound | $CuCl_2$ | $ZnCl_2$ | crystals[b] |
| **K1** | 274, 330 | 280, 326, 355 | 278, 327, 355 | - |
| **K2** | 282, 345 | 290, 337, 370 | 290, 338, 356 | - |
| **L2-a** | 304 | 304, 388 | 304 | [Cu(**L2-a**)$Cl_2$] 310, 400 |
| **L2-b** | 310 | 454 | 428 | [Zn(**L2-b**)$Cl_2$] 310, 473 |

[a] Measurements carried out in 20 mM HEPES, pH 7.4, 150 mM NaCl at rt. Ratio of metal to ligand was 1:1 and 1:2 for **L** and **K** series, respectively.
[b] Optical data were obtained in $CH_3CN$.

As mentioned in the introduction, the ability of metal chelators to be selective for certain metal ions is an important aspect in designing compounds for targeting metal-Aβ species under heterogeneous biological systems. The optical response of **L2-b** in the presence of other divalent metal ions was first examined ($Mg^{2+}$, $Ca^{2+}$, $Mn^{2+}$, $Fe^{2+}$, $Co^{2+}$, and $Ni^{2+}$, 20 mM HEPES, pH 7.4, 150 mM NaCl, Figure 3.19) in order to explore its ability to bind different metals. Only minor absorption changes were observed upon incubation of **L2-b** with biologically relevant alkaline earth metal salts, $CaCl_2$ and $MgCl_2$, and divalent transition metal salts, $MnCl_2$ and $FeCl_2$, even at high concentrations (ligand to metal ions, 1 mM/1 mM). On the other hand, treatment of **L2-b** (1 mM) with $CoCl_2$ and $NiCl_2$ (1 mM) resulted in distinct optical band shifts. These results indicate noticeable optical responses of **L2-b** with the divalent metal ions $Co^{2+}$, $Ni^{2+}$, $Cu^{2+}$, and $Zn^{2+}$.

**Figure 3.19. Metal binding of L2-b.**

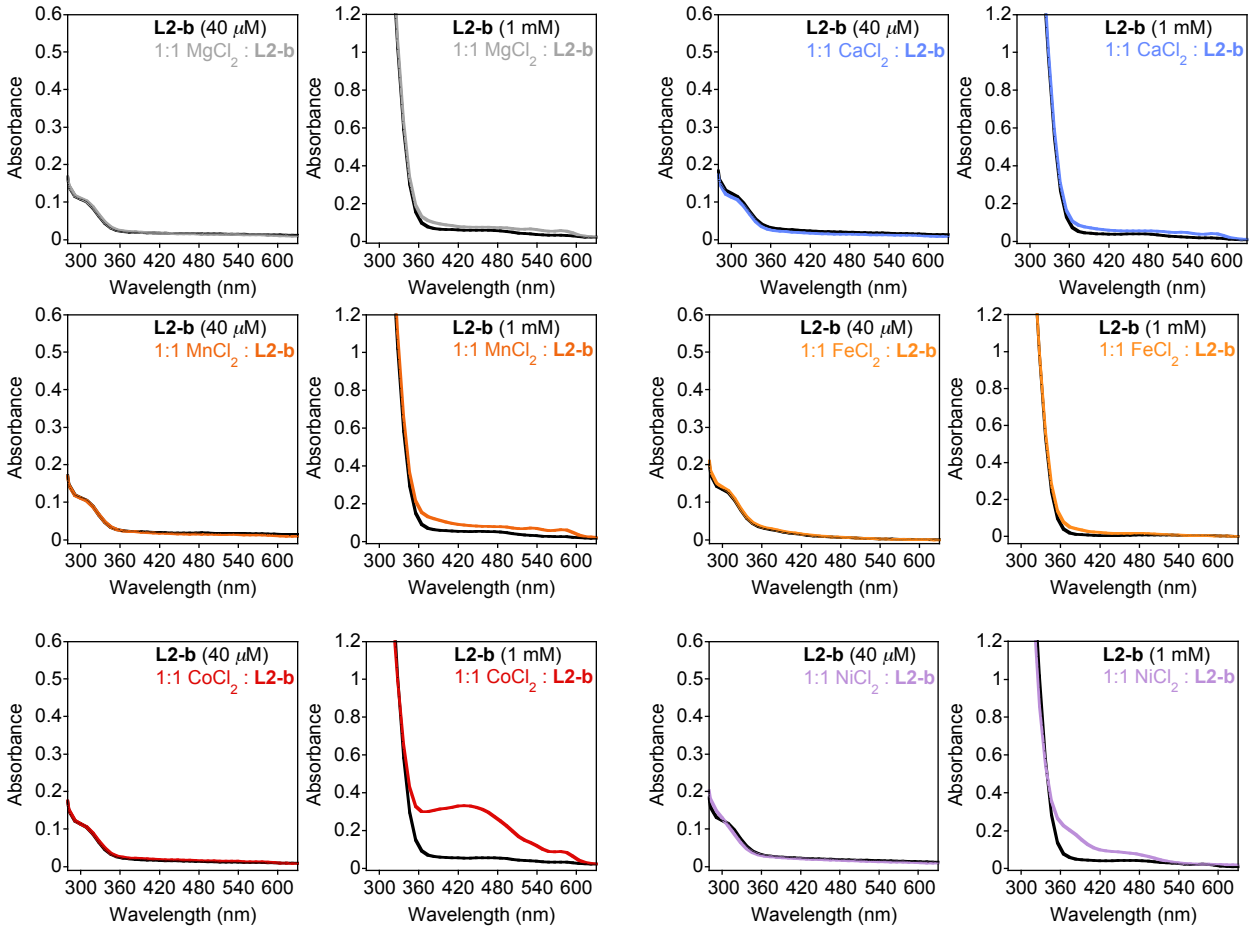


Conditions: Spectra of **L2-b** (40 μM) with 1 equiv of other divalent metal ions (either at 40 μM or 1 mM) in 20 mM HEPES, pH 7.4, 150 mM NaCl at room temperature (5 min incubation).

Secondly, the selectivity of **L2-b** for $Cu^{2+}$ in the presence of other divalent metal ions in 20 mM HEPES, pH 7.4, 150 mM NaCl was investigated by UV-vis (Figure 3.20). The optical intensity at 450 nm (absorption band for $Cu^{2+}$-treated **L2-b**, Figure 3.18b) was monitored when the appropriate metal ions (40 μM and 1 mM) were added to a 40-μM solution of **L2-b** followed by the subsequent treatment with 40 μM $Cu^{2+}$. Binding of $Cu^{2+}$ (40 μM) to **L2-b** (40 μM) was observed in the presence of other metal ions (40 μM and even 1 mM), which indicates that **L2-b** is selective for $Cu^{2+}$ at physiological pH.

Selectivity for $Cu^{2+}$ against $Fe^{3+}$ could not be determined at 1 mM due to precipitation upon the addition of $CuCl_2$ to the **L2-b**-$Fe^{3+}$ solution (denoted by * in Figure 3.20).

**Figure 3.20. Metal ion selectivity of L2-b.**

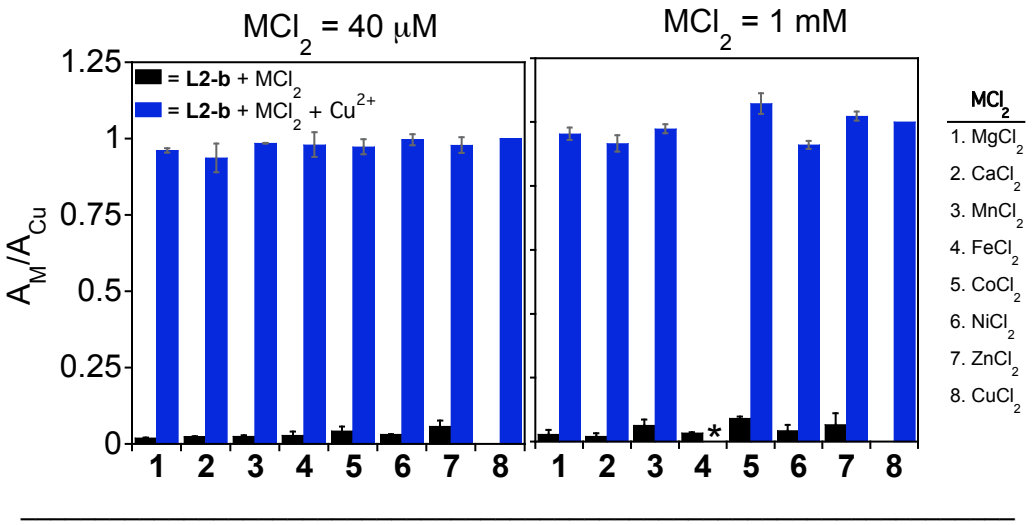


Conditions: Spectra were acquired in 20 mM HEPES, pH 7.4, 150 mM NaCl. Black bars represent the addition of the appropriate metal salts (40 μM (left); 1 mM (right);. Blue bars represent the subsequent addition of 40 μM $CuCl_2$ to the solution followed by 5 min incubation. [**L2-b**] = 40 μM. The absorbance at 450 nm was used for calculation of $A_M/A_{Cu}$. * Precipitation was observed in the reaction.

A further desired property of molecules designed for brain applications is their chemical neutrality, in order for more facile diffusion through the BBB as compared to charged compounds. To determine the species present as a function of pH, UV-vis variable pH titrations were carried out from pH 2.0 to 10.0 at room temperature with an ionic strength (*I*) of 0.10 M NaCl. Starting with an alkaline solution, small aliquots of an HCl solution were added, resulting in absorption changes. The resulting UV-Vis data were fitted with the HySPEC software to determine acid dissociation constants ($K_a$).

For **K1** (50 μM), absorption changes were observed in both the 274 and 330 nm absorption bands with two conversions of species defined by isosbestic points at 306 and 340 nm for the first conversion and 257 and 324 nm for the second (isosbestic

points shown as * in Figure 3.21a).[111] These observations indicate the presence of three different species (diprotonated, monoprotonated, and neutral forms) in the pH range 2.0–10 (Figure 3.21). Fitting the data for the protonated species LH and $LH_2$ (L = **K1**) gave two p$K_a$ values, 5.989(2) and 2.41(1), respectively (Figure 3.5). The first p$K_a$ is assigned to the pyridyl nitrogen and the second to the nitrogen of the dimethylamino group based on comparison with literature p$K_a$ values.[126] This result shows that at pH 7.4, greater than 95% of the neutral form of the ligand exists in solution. Attempts to carry out speciation studies on the **K2** species did not yield substantial enough changes in the absorption profile; therefore ligand speciation data was not completed.

**Figure 3.21. UV-Vis titration spectra (a) and ligand speciation (b) of K1.**

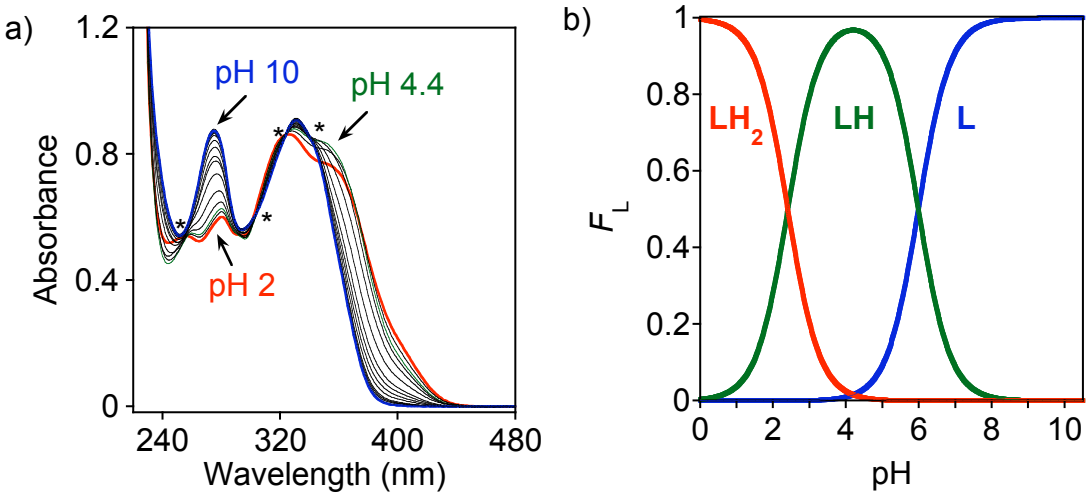


Conditions: UV-vis variable pH (pH 2.0–10) titration of **K1** (50 μM, rt, I = 0.1 M NaCl). Left: Spectra from pH titration with the three different species indicated in color corresponding to pH. Right: Speciation diagram calculated for **K1** showing the neutral and protonated states (L, LH, and $LH_2$; L = **K1**; charges are omitted for clarity). * indicate isosbestic points.

The acid dissociation constants were obtained in a similar manner for **L2-a** (500 μM) and **L2-b** (100 μM) under aqueous conditions.[112,114] Upon lowering the pH, spectral changes were observed for both ligands indicating the formation of protonated species

(Figure 3.22). For **L2-a**, a p$K_a$ value of 5.037(2) was determined with a corresponding isosbestic point at *ca.* 314 nm. Two p$K_a$ values of 4.844(4) and 6.684(5) were calculated for **L2-b** from the pH-variable titration data (Figure 3.5). Based on these results and literature values, p$K_{a1}$ for **L2-b** can be assigned to the pyridyl nitrogen ($LH_2 \leftrightarrows LH + H$, p$K_{a1}$ = 4.844(4)) with an isosbestic point at 241 nm and p$K_{a2}$ corresponding to protonation of the dimethylamino group ($LH \leftrightarrows L + H$, p$K_{a2}$ = 6.684(5)).[126] For **L2-a**, p$K_{a1}$ is assigned to protonation of the pyridyl nitrogen (Figure 3.5). Using the titration data, solution speciation diagrams were generated showing that at pH 7.4, the neutral forms of both compounds predominate in aqueous solution (Figure 3.22, *ca*. 100 and 85% for **L2-a** and **L2-b**, respectively). Overall, the solution studies of small molecules suggest that they could have neutral forms in biological systems, which are suitable as hydrogen bond acceptors/donors that may have the capability of interacting with Aβ species as well as for blood-brain barrier (BBB) penetration considering the required parameters (*e.g.,* a neutral form has better greater coefficient than an ionic one).

**Figure 3.22. UV-Vis titration data (left) and speciation diagrams (right) of a) L2-a and b) L2-b.**

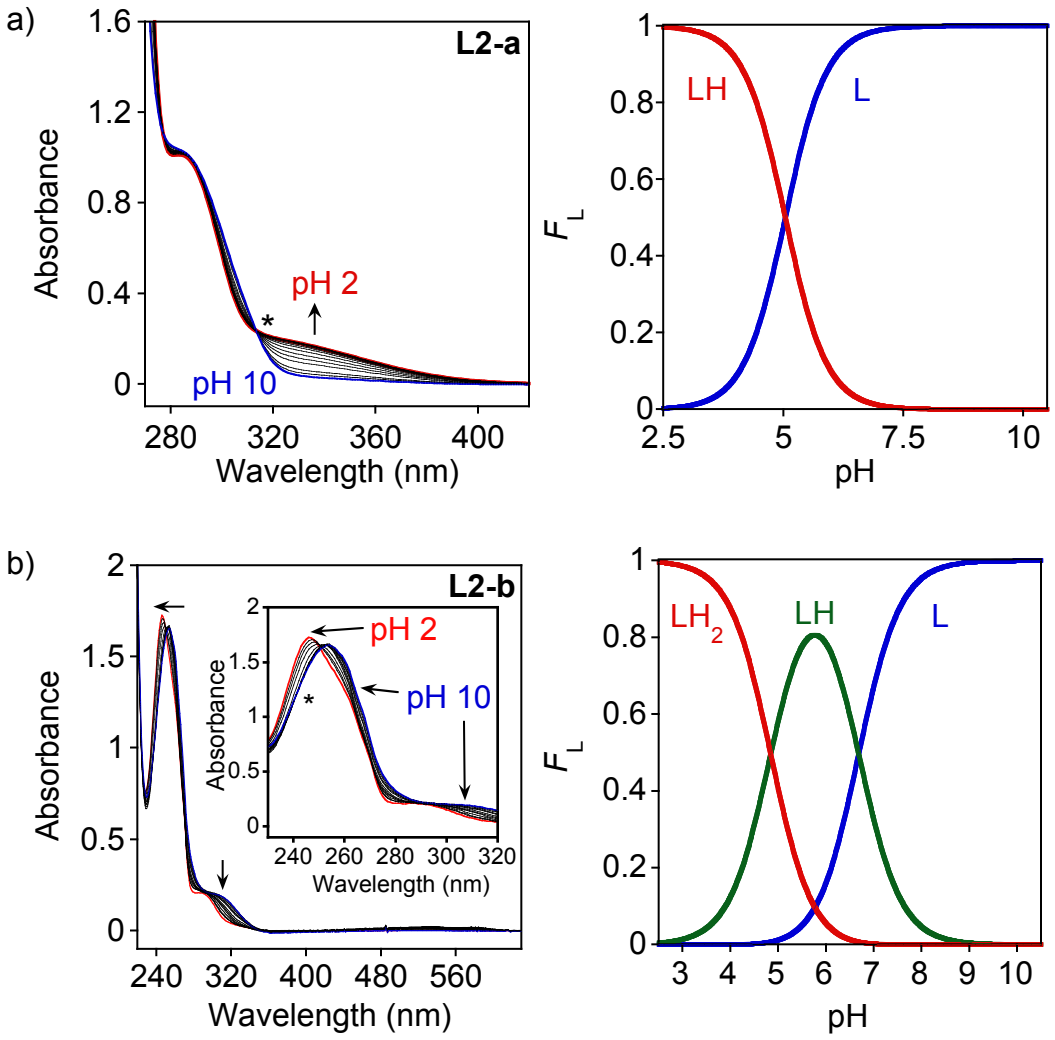


Conditions: Left: Variable pH (pH 2.0—10.0) UV-vis spectra of **L2-a** (500 μM) and **L2-b** (100 μM) at rt and I = 0.10 M NaCl. Right: Solution speciation diagram for **L2-a** (500 μM) and **L2-b** (100 μM) where FL = fraction of compound with given protonation. Charges are omitted for clarity. * indicate isosbestic points.

**Table 3.5. p$K_a$ summary for K0 and L2 series.**

| Species | p$K_a$ | | |
|---|---|---|---|
| | **K1** | **L2-a** | **L2-b** |
| **$H_2L$ ⇆ HL + H** (p$K_a$ 1) | 2.41(1) | 5.037(2) | 4.844(4) |
| **HL ⇆ HL + H** (p$K_a$ 2) | 5.989(2) | - | 6.684(5) |

In order for the rationally designed bifunctional molecules to interact with and/or to compete for metal ions from metal-Aβ species, they must have comparable metal binding affinities. Using similar spectrophotometric pH titrations to ligand speciation, various metal species of the **L** series and their binding affinities in aqueous solution were determined in the presence of $CuCl_2$ and/or $ZnCl_2$. It is noted here that titration attempts with **K1** in the presence of $CuCl_2$ did not yield substantial enough changes in the absorption spectra and metal speciation data could not be determined *via* this method.

The incubation of compounds with $CuCl_2$ for 10 min at *ca*. pH 7.5 – 8.0 ([$CuCl_2$]/[L] = 1:2, [**L2-a**] = 500 $\mu$M and [**L2-b**] = 100 $\mu$M, room temperature, $I$ = 0.10 M NaCl), resulted in absorption bands at 388 nm for **L2-a** and 450 nm for **L2-b** (Figure 3.18).[112,114] With the addition of small aliquots of HCl, significant shifts in the spectra were observed (Figure 3.23), which allowed for the determination of stability constants of metal complexes (log $\beta$; p$K_a$ values of the ligands and hydrolysis of free metal ions were considered in the calculations).[127,128] For **L2-a**, a first species conversion was observed with an isosbestic point at 295 nm corresponding to the equilibrium Cu + L ⇆ CuL (log $\beta_1$ = 5.857(2), Figure 3.23a). A second transformation with four isosbestic points at 279, 316, 337, and 362 nm was assigned to Cu + 2L ⇆ $CuL_2$ (log $\beta_2$ = 10.151(5)). Two species conversions were also observed for **L2-b**, a first with two isosbestic points at 226 and 245 nm [Cu + L ⇆ CuL (log $\beta_1$ = 10.20(7))] and a second indicated by five isosbestic points at 248, 308, 339, 539, and 581 nm [Cu + 2L ⇆ $CuL_2$ (log $\beta_2$ = 15.30(9)), Figure 3.23b]. From these stability constants (Table 3.6), the distribution of metal species as a function of pH was plotted and indicated that at

physiological pH (*e.g.,* 7.4), both CuL and $CuL_2$ species are present (*ca.* 35:65 for both **L2-a** and **L2-b**; Figure 3.23a-b). According to these solution speciation diagrams, free $Cu^{2+}$ could be observed up to pH 6.0 for **L2-a** and up to pH 4.0 for **L2-b**. Using the results from solution speciation studies, concentrations of unbound $Cu^{2+}$ at specific pHs can be calculated from equation 1 (see section 3.6, pCu = 5.86 and 5.87 at pH 6.6 and 7.0 for **L2-a**; pCu = 9.93 and 10.21 at pH 6.6 and 7.4 for **L2-b**). The values of pCu for the **L** series reflect approximate dissociation constants ($K_d$) of the ligands ranging from high picomolar to low micromolar.

Determination of stability constants for Zn complexes was conducted in a similar manner for **L2-b**.[114] **L1-a** could not be studied with $Zn^{2+}$ under these conditions because of the lack of significant spectral changes (Figure 3.18). Upon lowering the pH of an **L2-b** (500 μM) and $ZnCl_2$ (2:1) solution and monitoring the UV-Vis spectral features, the absorption band at 430 nm initially red-shifted with a decrease in intensity and an isosbestic point at 519 nm (Figure 3.23c). The intensity of this absorption feature continued to decrease as the pH dropped, with a small band growing in at *ca.* 590 nm with a second isosbestic point at 540 nm. These conversions were fitted and assigned to the corresponding equilibria: Zn + L ⇆ ZnL (log $\beta_1$ = 6.167(5) and Zn + 2L ⇆ $ZnL_2$ (log $\beta_2$ = 10.727(8), Table 3.6). A speciation diagram based on the fitted data showed that, like $Cu^{2+}$, both ZnL and $ZnL_2$ are present at physiological pH with $ZnL_2$ having the higher abundance (Figure 3.23c). Furthermore, at pH 7.4 the concentration of unbound $Zn^{2+}$ was calculated as pZn = 6.1 corresponding to micromolar binding affinity of **L2-b** for $Zn^{2+}$.

From the speciation and log$\beta$ data, it is clear that **L2-b** binds $Cu^{2+}$ stronger than **L2-a** and also chelates $Cu^{2+}$ more effectively than $Zn^{2+}$ (Table 3.6). The values of pCu and pZn, in particular for **L2-b,** reflect approximate $K_d$ values suitable for competing with metal-Aβ species ($K_d$ for Cu-Aβ and Zn-Aβ ≈ picomolar to micromolar and micromolar, respectively).[36,64] These data provide insight into the ability of our compounds to interact with and modulate the reactivity of metal-Aβ species (refer to section 3.4).

**Figure 3.23. Metal speciation studies of L2 series.**

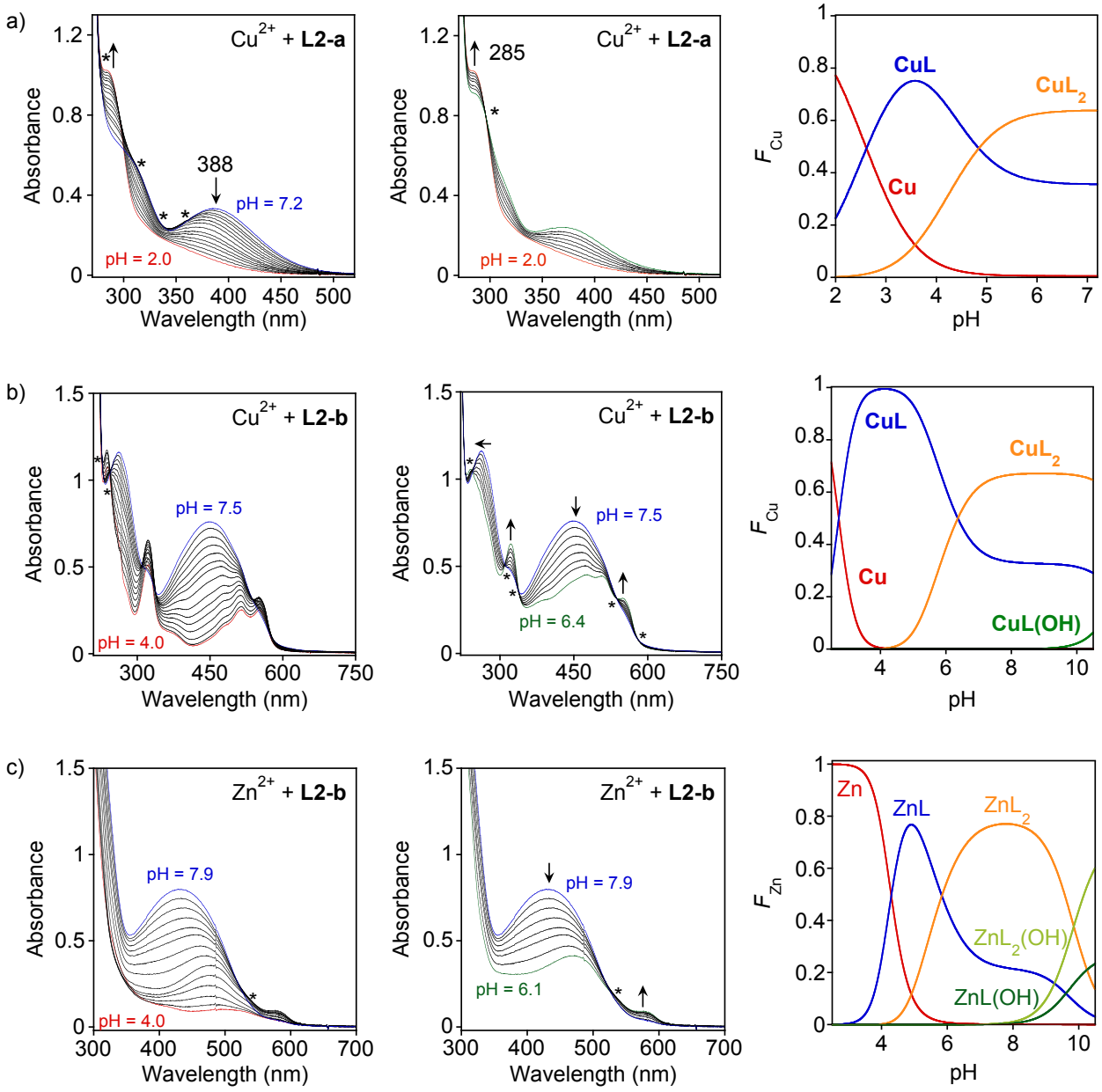


Conditions: Left: UV-Vis pH titration with **L2-a** and **L2-b** with either $Cu^{2+}$ or $Zn^{2+}$ from *ca.* pH 4.0 to 8.0. Center: spectra indicating species conversions with isosbestic points indicated by * in specified pH ranges. Right: Solution speciation diagrams for **L2-a** and **L2-b** (cited as L in the figures) in the presence of either $Cu^{2+}$ or $Zn^{2+}$. a) [**L2-a**] = 500 μM, [$CuCl_2$] = 250 μM; b) [**L2-b**] = 100 μM, [$CuCl_2$] = 50 μM; c) [**L2-b**] = 500 μM, [$ZnCl_2$] = 250 μM; rt, I = 0.10 M NaCl. Charges are omitted for clarity.

**Table 3.6. Stability constants for complexes of the L series.**

| Species[d] | $\log\beta^{a,b,c}$ | | |
|---|---|---|---|
| | **L2-a + $Cu^{2+}$** | **L2-b + $Cu^{2+}$** | **L2-b + $Zn^{2+}$** |
| **M + L ⇆ ML** | 5.857(2) | 10.20(7) | 6.167(5) |
| **M + 2L ⇆ $ML_2$** | 10.151(5) | 15.30(9) | 10.727(8) |
| **ML + $H_2O$ ⇆ ML(OH) + H** | - | -0.96(1) | 0.851(8) |
| **$ML_2$ + $H_2O$ ⇆ $ML_2$(OH) + H** | - | - | -3.435(9) |

[a] Conditions: [M]/[L] = 1:2, $[Cu^{2+}]_{total}$ = 50 and 500 μM for **L2-a** and **L2-b**, respectively (10 min incubation), $[Zn^{2+}]_{total}$ = 1 mM (3 h incubation), rt, *I* = 0.10 M NaCl. [b] Error is shown in the last digit. [c] Charges are omitted for clarity. [d] The species containing $OH^-$ (M(OH) and $ML_2$(OH)) were introduced into the calculation model yielding a good fit to the data.

*X-ray crystallographic characterization of **L2** Series.* Characterization of the **L2** complexes was also accomplished in the solid state.[112] Crystals were isolated by slow vapor diffusion with $Et_2O$ into a $CH_3OH$ solution of 1:1 ligand to metal chloride salt ($CuCl_2$ or $ZnCl_2$). Selected bond lengths and angles of [Cu(**L2-a**)$Cl_2$] and [Zn(**L2-b**)$Cl_2$] are summarized in Table 3.7. It is important to note that the crystals were grown with chloride salts because chloride is the most abundant biologically relevant anion, occurring at millimolar concentrations.[129,] As depicted in Figure 3.25, the structures show that 1:1 metal to ligand complexes are formed (both metal complexes crystallized in the monoclinic space group, P21/c, Z = 4). In both structures, the secondary amino group of **L2-a** and **L2-b** remains protonated when $CuCl_2$ or $ZnCl_2$ is bound to the ligand, which was also found in the $Ru^{2+}$ complex [Ru(**L2-a**)($L^1$)Cl] ($L^1$ = $\eta^6$-$C_6H_4MeCHMe_2$, Figure 3.24).[130] Different from our observation, some $Zn^{2+}$ complexes containing napthalimide-based fluorescent chemosensors ([Zn($L^2$)], $L^2$ = *N*-butyl-4-[di-(2-picolyl)amino-5-(2-picolyl)amino-1,8-napthalimide) composed of the pyridinylmethylamine moiety show deprotonation of the secondary amine group.[131] The

relatively stronger electron withdrawing ability of the napthalimide group as compared to **L2-a** and **L2-b** may lead to the deprotonation of the secondary amino group upon metal chelation.

**Figure 3.24. Complexes of L2-a and a related structure showing both protonated and deprotonated secondary amines.**

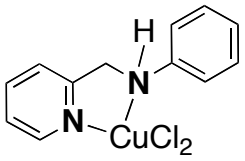


[Cu(**L2-a**)$Cl_2$]

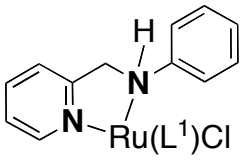


[Ru(**L2-a**)($L^1$)Cl]

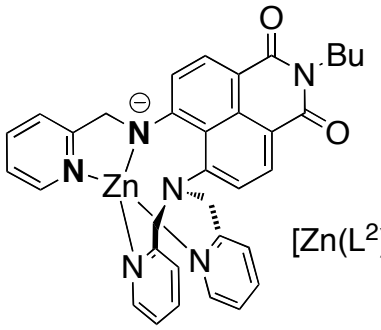


[Zn($L^2$)]

For [Cu(**L2-a**)$Cl_2$], nearly square planar geometry was observed, showing a dihedral angle (Θ) of 7.4°, measured between the planes of the three- and five-membered rings on the metal center (Figure 3.25). Bond lengths between $Cu^{2+}$ and the N donor atoms of the pyridyl and secondary amino group were 2.0744(18) Å and 2.0052(18) Å (Table 3.7), respectively, (N1) and (N2). These are comparable to similar tridentate ligands containing the aryl substituted 2-(methylamino)pyridine moiety bound to a $CuCl_2$ center (C–N, 1.984–2.334).[132,133,134] Comparing the molecular structure of [Cu(**L2-a**)$Cl_2$] to that of [Zn(**L2-b**)$Cl_2$], a similar twisting of the amine-based ligand framework with respect to the aromatic rings was observed, with the aromatic planes intersecting at 80° and 73° for the two complexes, respectively (Figure 3.25). This twisting clearly differentiates the second-generation **L** compounds from the first-generation and may influence how the compounds and their metal complexes interact with Aβ species (Figure 3.13), which will be discussed in section 3.4.

The structure of [Zn(**L2-b**)$Cl_2$] exhibits a bite angle (81.79(4)°) of the two N donor atoms (N1 and N2) to the $Zn^{2+}$ center and a distorted tetrahedral geometry at the metal center (Figure 3.25 and Table 3.7). The observed Zn–N and Zn–Cl bond lengths for [Zn(**L2-b**)$Cl_2$] are comparable to the reported values from the structures of $Zn^{2+}$ complexes of similar ligand frameworks in the literature.[135] Similar bond distances are observed in the first generation $Zn^{2+}$ complex [Zn(**L1-b**)$Cl_2$] and second generation complex [Zn(**L2-b**)$Cl_2$]. In contrast, the bond angles in [Zn(**L2-b**)$Cl_2$] were significantly different than those in the first generation complexes (i.e., [Zn(**L1-a**)$Cl_2$], [Zn(**L2-b**)$Cl_2$], and [Zn(**L1-b**)$Cl_2$]; N2–Zn1–Cl2, 117.10(6)°, 114.30(3)°, and 120.03(6)°, respectively, Table 3.3 and Table 3.7). These results suggest subtle changes in Zn–N and Zn–Cl bond lengths and angles depending on the C–N hybridization and presence of the dimethylamino group. Overall, the X-ray crystal structures of the metal complexes demonstrate metal chelation by our compounds (**L2-a** and **L2-b**) displaying different ligand conformations of the metal complexes associated with C–N bond order (Figure 3.13 and Figure 3.25).

**Figure 3.25. ORTEP diagrams showing 50% thermal ellipsoids for a) [Cu(L2-a)$Cl_2$] and b) [Zn(L2-b)$Cl_2$].**

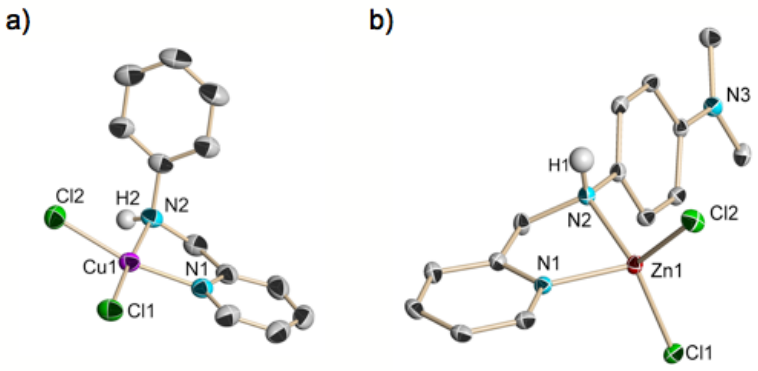

**Table 3.7. Selected Bond Lengths (Å) and Angles (deg) of L2 complexes.**

| | [Cu(**L2-a**)$Cl_2$] | [Zn(**L2-b**)$Cl_2$] |
|---|---|---|
| Zn1/Cu1-N1 | 2.0052(18) | 2.0451(10) |
| Zn1/Cu1-N2 | 2.0744(18) | 2.0922(10) |
| Zn1/Cu1-Cl1 | 2.2701(7) | 2.2366(3) |
| Zn1/Cu1-Cl2 | 2.2442(7) | 2.2070(3) |
| N1-Zn1/Cu1-N2 | 82.11(7) | 81.79(4) |
| N1-Zn1/Cu1-Cl1 | 94.77(6) | 108.34(3) |
| N1-Zn1/Cu1-Cl2 | 168.44(5) | 112.21(3) |
| N2-Zn1/Cu1-Cl1 | 176.28(6) | 116.25(3) |
| N2-Zn1/Cu1-Cl2 | 89.53(6) | 114.30(3) |
| Cl1-Zn1/Cu1-Cl2 | 93.27(3) | 117.979(14) |

*1D NMR of **L2** Series.* Analogous to the $^1$H NMR observations for the first-generation molecules, changes in chemical shifts of aromatic protons due to the imine versus amine functionality were first examined (Figure 3.14 and Figure 3.26). With reduction of the Schiff base to the secondary amine, upfield shifting of aromatic $^1$H signals was observed, which is expected due to increased shielding from the addition of electron density to the framework. The proximity of $H_d$ to the C–N bond varies depending on whether a single or double bond is present, leading to $\Delta\delta$ shifts of 0.83 and 0.78 ppm for the **L1** and **L2** series, respectively. Further differentiating the imine and amine functionalities was the upfield shifting of the phenyl protons ($\Delta\delta$ ($H_e$, **L1-a** versus **L2-a**) = 0.69 ppm; $\Delta\delta$ ($H_e$, **L1-b** versus **L2-b**) = 0.68 ppm), a result of the electron donating nature of the secondary amine.

In addition to the C–N functionality, the presence of the dimethylamino group affected the proton chemical shifts of the ligands. Comparing **L2-a** to **L2-b** (without and

with the dimethylamino group), an increase in shielding throughout the aromatic rings was observed (Figure 3.26). Based on the addition of this electron-donating moiety, the $H_f$ protons shifted to lower frequencies with $\Delta\delta$ of 0.53 ppm for **L2-a** versus **L2-b**, respectively. The presence of the tertiary amino group did not lead to any significant changes of the chemical shifts of the methine or methylene protons, although a more observable influence on the secondary amine proton was seen with an upfield shift of 0.39 ppm. Overall, the environment of the protons throughout the scaffold showed sensitivity to both C–N hybridization as well as the presence of the dimethylamino substituent.

Further effects of $Zn^{2+}$ binding to the **L2** ligands were analyzed by $^1$H NMR spectroscopic analysis of [Zn(**L2-a**)$Cl_2$] (generated *in situ*) as well as of isolated crystals of [Zn(**L2-b**)$Cl_2$] (Figure 3.26). Similar changes of resonances compared to the **L1** series were observed for the **L2** series (*i.e.*, overall downfield shifting of resonances). Furthermore, the signals at 5.99 and 5.64 ppm for the secondary amine proton of [Zn(**L2-a**)$Cl_2$] and [Zn(**L2-b**)$Cl_2$], respectively, indicate that the ligands are not deprotonated upon $Zn^{2+}$ binding, in agreement with the characterization in the solid state (X-ray structural determination, *vide supra* and FT-IR, *vide infra*) and in previous literature for metal polyamine complexes.[136] The downfield shifting along with the sharpening of the N–H signal due to an increased exchange between the proton and solvent suggest that $Zn^{2+}$ is coordinated to the secondary amine of both ligands.[137] Overall, $^1$H NMR studies of the ligands and their corresponding $Zn^{2+}$ complexes indicate that the electronic environment of the compounds is affected by $Zn^{2+}$ coordination in solution and that the N–H bonds remained intact, suggesting availability for hydrogen

bonding in the $Zn^{2+}$ complexes of the pyridinylmethylamine derivatives.

**Figure 3.26. $^1$H NMR of L2 series and their $Zn^{2+}$ complexes.**

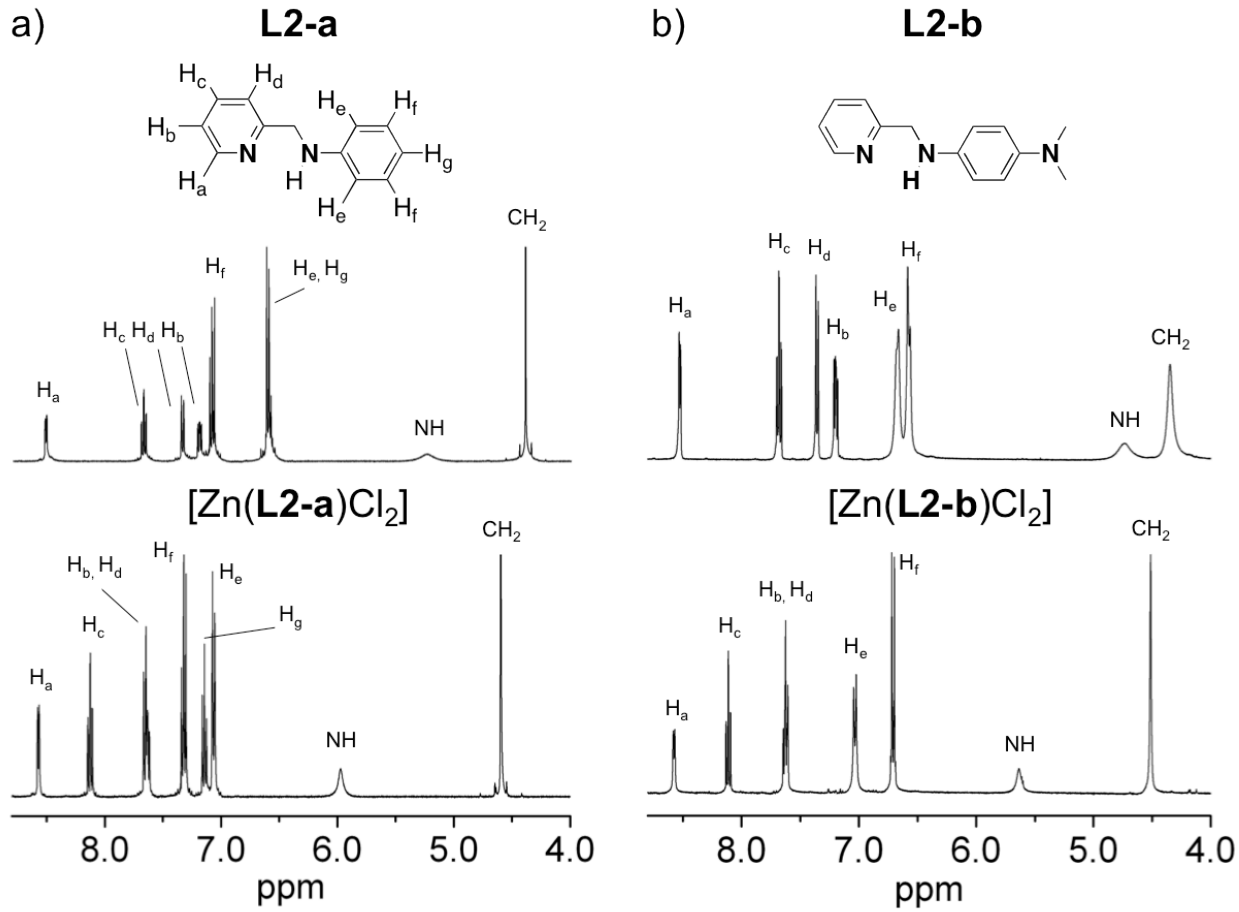


Conditions: Spectra acquired in $CD_3CN$ at rt (400 MHz). [Zn(**L2-a**)$Cl_2$] was formed *in situ* with the addition of 1 equiv of $ZnCl_2$ to a 4.0 mM solution of **L2-a** and incubated for 1 h.

*IR of **L2** Series.* Differentiating the ligands and complexes by IR spectroscopy provided additional insight into the effects of imine versus amine, presence and absence of dimethylamino group, and metal coordination. Reduction from the imine to amine affected the C–N, C=N, and C=C stretching frequencies between 1100 and 1700 $cm^{-1}$ as well as the N–H bending mode $\rho$(N−H) in this region. The Schiff base stretching bands (Figure 3.15a) at 1580 $cm^{-1}$ (**L1-a**) and 1572 $cm^{-1}$ (**L1-b**) were absent in both **L2-a** and **L2-b**, as expected with reduction of the C=N bond (Figure 3.27a). The presence

of the secondary amine was evident due to asymmetric and symmetric $\nu$(N–H) stretching bands located between 3300 to 3400 $cm^{-1}$ as well as the $\rho$(N–H) bending mode near 1600 $cm^{-1}$. In agreement with the **L1-b** spectrum (Figure 3.15), the appearance of the C–N stretching frequency at 1528 $cm^{-1}$ is indicative of the dimethylamino moiety (Figure 3.27). In addition, the broad $\nu$(N–H) stretching peak of 3299 $cm^{-1}$ for **L2-a** resolved into two peaks and shift to 3369 and 3394 $cm^{-1}$ for **L2-b**, suggesting a stronger N–H bond in the presence of the dimethylamino group in the structure, consistent with NMR solution studies.

Additional metal binding effects in the solid state for the **L2** series were observed by changes in the IR spectra of the isolated metal complexes [Cu(**L2-a**)$Cl_2$] and [Zn(**L2-b**)$Cl_2$], Figure 3.27b). For [Cu(**L2-a**)$Cl_2$], the C–N stretching frequency seen for the free ligand was not observed at 1529 $cm^{-1}$, suggesting that metal binding changed the character of the C–N bond of the secondary amine. The clear appearance of both $\nu$(N–H) and $\rho$(N–H) bands for both [Cu(**L2-a**)$Cl_2$] and [Zn(**L2-b**)$Cl_2$] excluded the deprotonation process in the metal complexes as expected from the crystal structural and $^1$H NMR studies. For both complexes, the $\nu$(N–H) bands of the free ligands (3299 / 3394 $cm^{-1}$ and 3369 $cm^{-1}$ for **L2-a** and **L2-b**, respectively) were found to shift to a lower wavenumber (3189 $cm^{-1}$ and 3223 $cm^{-1}$ for [Cu(**L2-a**)$Cl_2$] and [Zn(**L2-b**)$Cl_2$], respectively) corresponding to weakening of the N–H bond (Figure 3.27), in agreement with the $^1$H NMR experiment (Figure 3.26). The appearance of mainly one peak for $\nu$(N–H) vibrations suggested the preference of one vibrational mode due to metal binding. In summary, changes in the bond frequencies indicative of metal chelation presented an overall effect on the ligand frameworks in the metal bound form.

**Figure 3.27. IR study of L2 series and their metal complexes.**

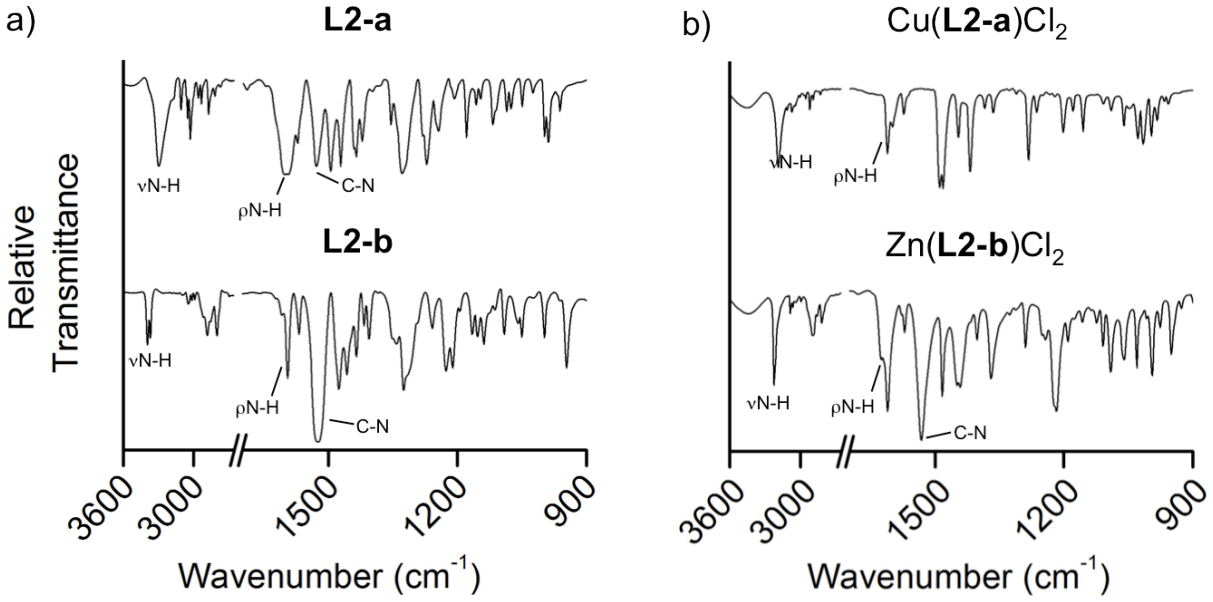


Conditions: FT-IR spectra of ligands (a) **L2-a** / **L2-b** and their $Zn^{2+}$ or $Cu^{2+}$ complexes (b) [Cu(**L2-a**)$Cl_2$] / [Zn(**L2-b**)$Cl_2$] in KBr.

From the above studies (UV-vis, $^1$H NMR, IR, and X-ray structures), both the **K** and **L** series of molecules exhibited properties as metal chelators. The second-generation of bifunctional molecules showed improved stability under aqueous conditions allowing for speciation of the **K1, L2-a**, and **L2-b** ligands, which indicated predominantly neutral compounds at physiological pH. This is an important consideration for BBB permeability and for understanding the species that can interact with the amino acid residues of Aβ (described in Section 3.3.3). With the success of the **L** series (*vide infra*), more detailed metal binding studies were conducted showing that both **L1-b** and **L2-b** were relatively selective for $Cu^{2+}$, a requirement for the desired targeting of metal-Aβ species. Further determination of stability constants indicated that the **L2** series may be capable of competing for $Cu^{2+}$ and $Zn^{2+}$ from Aβ.

### 3.3.3 Aβ Interaction of First Generations

To establish the extent of interaction of the designed molecules with Aβ in the absence of metal ions, which along with metal chelation affords bifunctionality, high-resolution 2D $^{1}H–^{15}N$ TROSY-HSQC NMR experiments were performed. Sodium dodecylsulfate-$d_{25}$ (SDS-$d_{25}$) was employed in NMR studies of $^{15}N$-labeled $A\beta_{1-40}$ in order to solubilize and prevent aggregation of the peptide.[138,139] When bound to SDS micelles, the Aβ monomer adopts two α-helical segments involving residues Q15 − V24 and G29 − M35 (Figure 3.1).[139,140] Helicity has also been observed in solution and when in contact with other biological molecules and has been suggested to precede the aggregation pathways of Aβ leading to proposed neurotoxic oligomers.[21,22,49,141,142] Although the *in vivo* conformation of Aβ remains elusive, this model system can provide an environment for determining the ability of our compounds to interact with and target a potentially biologically relevant Aβ conformation. All 2D NMR experiments were carried out at 25 °C on a 900 MHz instrument with general conditions of SDS-$d_{25}$ (200 mM), sodium phosphate buffer (20 mM, pH 7.3), and $D_2O$ (7%, v/v). Spectra of $^{15}N$-labeled $A\beta_{1-40}$ were in agreement with previous studies.[140, 143] The magnitude of $^{1}H–^{15}N$ crosspeak shifting was quantified using equation 2. The shifts caused by compound were compared to Aβ only (signals for Aβ only are displayed in black for all spectra). Residues D1 and A2 do not appear in the 2D spectra due to being located at the flexible N-terminal of the peptide. These residues, along with others that overlap with one another in the spectra are indicated by an asterisk (*) in the chemical shift plots.

While the residue-specific influence of our compounds on the Aβ monomer can be determined by 2D NMR spectroscopy, visualization of the structural details of their contact modes with the peptide backbone or residue side chains was conducted by docking studies. To consider possible conformations of our compounds with Aβ, docking studies were performed using AutoDock4 for modeling peptide-ligand interactions using a Lamarckian genetic algorithm over the entire peptide.[144,145,146] A previously determined solution NMR structure of $A\beta_{1-40}$ in SDS micelles (PDB 1BA4) was utilized, and the molecules were evaluated with 10 conformations of Aβ in an attempt to account for the dynamic nature of Aβ in solution.[139] Ligand conformations with Aβ were selected from clusters with the highest occurrence and the lowest energy. As a comparison of the interaction of the bifunctional compounds (**L1** and **L2** series) with Aβ, **S0** and **S1** that do not contain metal binding site as well as 8-HQ, a traditional metal chelator, were also investigated by NMR and/or docking studies (Figure 3.28).

**Figure 3.28. Control molecules used in Aβ interaction studies.**

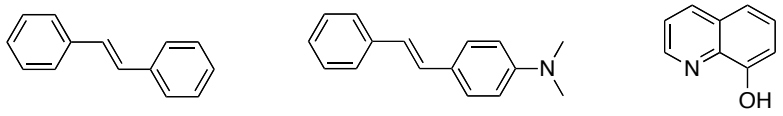


**S0** **S1** **8-HQ**

*2D NMR of **K0***. Upon the addition of 8 equiv of **K0** to a solution of Aβ, various amino acid residues were observed to shift with E11 and H13 shifting the most significantly (Figure 3.29). A less intense but observable periodic trend occurred along the peptide backbone at residues Q15, V18, and E22 (Figure 3.29) suggesting that

these residues may lie on a similar face of the inner helix (Q15–N27 depicted in Figure 3.34) and shift because of direct interaction with the small molecule or a change in conformation upon ligand binding. These results show that **K0** can interact with the Aβ monomer and cause residues near the proposed metal binding site of Aβ (involving H6, H13, and H14) to shift, which is desirable for targeting metal ions associated with Aβ.

**Figure 3.29. 2D $^{1}$H–$^{15}$N NMR spectra (left) and chemical shifts (right) of K0.**

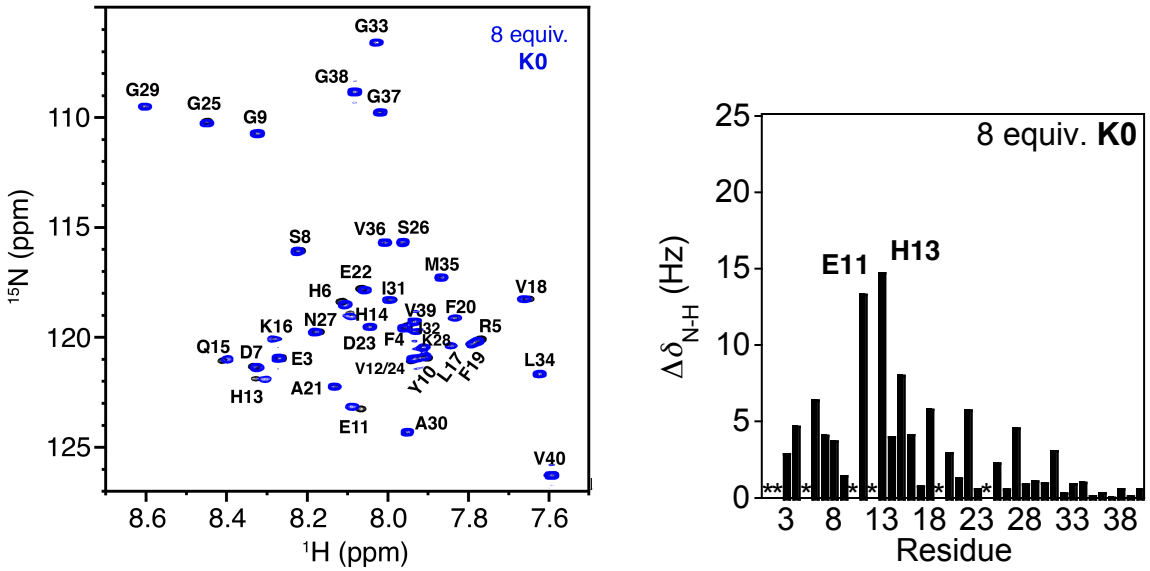


*2D NMR of **L1** Series*. For the **L1** series, changes in chemical shifts of Aβ were also observed upon the addition of the small molecules (Figure 3.30), suggesting direct Aβ interaction.[113] Both **L1-a** and **L1-b** (10 equiv) exerted an influence mainly on the N−terminal portion of the peptide (E3–Q15), with the largest shifts at residues E11 and H13. The chemical shift patterns can be compared to understand the effect of the dimethylamino functionality on Aβ interaction (**L1-a** versus **L1-b**, Figure 3.30). While **L1-b** interacted more broadly through the N-terminal region and also with the inner helix of the peptide (Q15–N27), **L1-a** had fewer contacts in these portions of the peptide and did

not show as strong of an interaction (Figure 3.31). The absence of the dimethylamino structural moiety in **L1-a**, which has been proposed to be important in Aβ interaction[109,115,116] may explain why its degree of perturbance of the Aβ spectra is less than that of **L1-b**. For **L1-b**, similar shifting intensities and the periodic trend seen at residues Q15, V18, and E22 for the interaction of **K0** with Aβ was also observed (Figure 3.29 andFigure 3.31). Like the IMPY framework, the stilbene derivatives also show an ability to interact with the Aβ peptide, highlighting their bifunctional properties.

**Figure 3.30. 2D $^{1}$H–$^{15}$N NMR spectra of L1 series.**

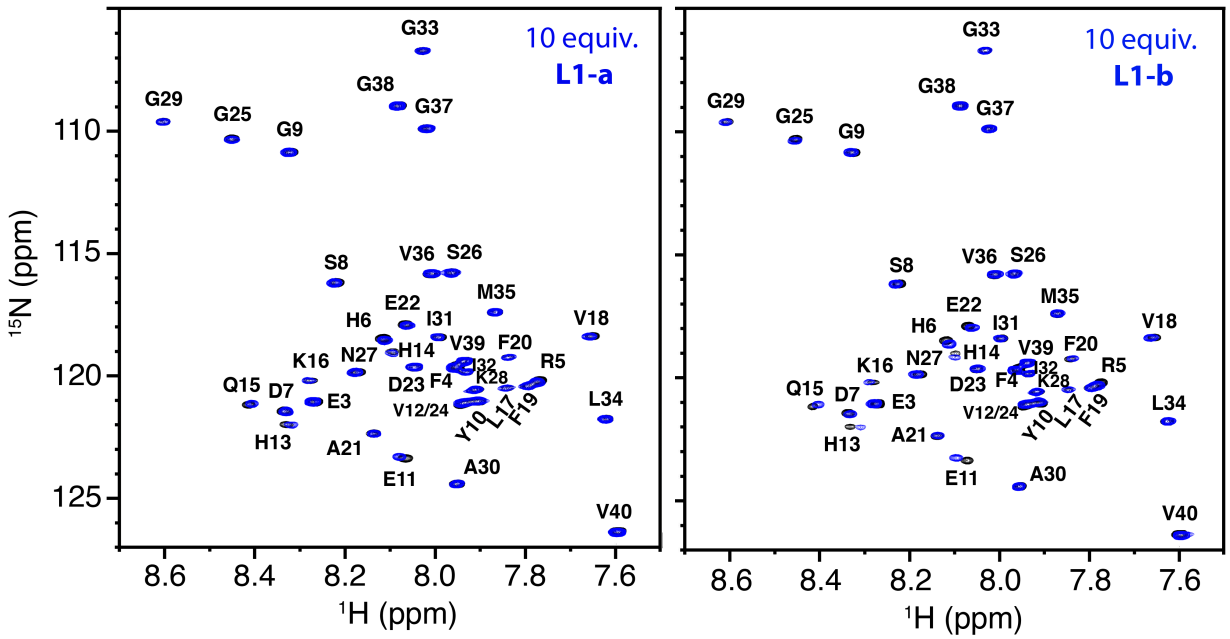

**Figure 3.31. 2D $^{1}H–^{15}N$ NMR chemical shifts of L1 series.**

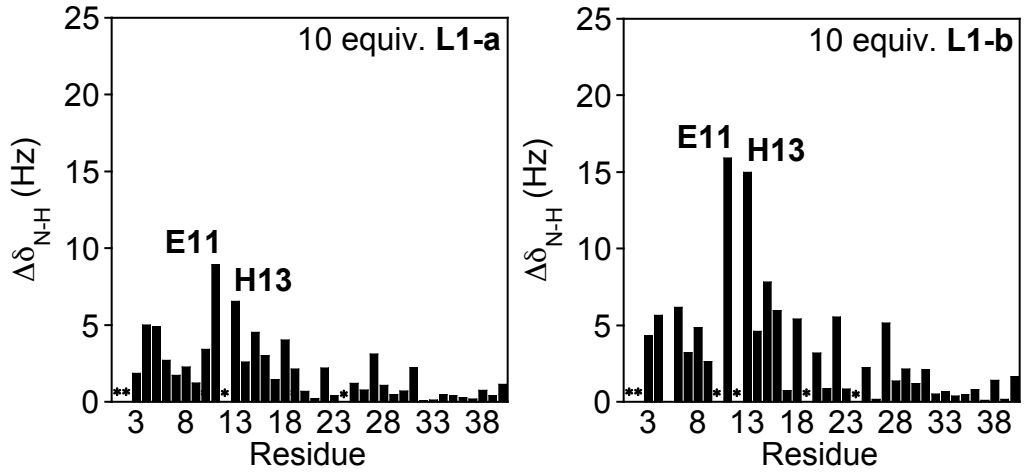


To further compare the effect of both the addition of two nitrogen atoms and the presence of the dimethylamino group in our molecules, compounds without a metal binding site (**S0** and **S1**) were also studied by NMR (Figure 3.28).[113] Because of the low solubility of **S0** and **S1** in the buffered conditions (SDS-$d_{25}$ (200 mM), sodium phosphate buffer (20 mM, pH 7.3), and $D_2O$ (7%, v/v)), DMSO was employed to deliver the compounds to the Aβ solution. Both compounds and DMSO alone (*ca.* 2 equiv of compound in 2.28 μL of DMSO) appeared to have an influence on the shifting of residues but shifting trends were different from **L1-a** and **L1-b** (Figure 3.31 and Figure 3.33). Upon addition of both **S0** and **S1** to the solution of Aβ, residues E11 and H13 did not shift as much as with DMSO alone, suggesting these compounds may compete for contacts with the peptide. However, direct comparison is difficult to discern because of the possibility of compounds interacting both with the peptide and/or counteracting the DMSO effect. With the consideration of the DMSO effect on the Aβ monomer, **S0** and **S1** showed a different ability to recognize Aβ under these conditions compared to the bifunctional compounds **L1-a** and **L1-b**. Contrasting **L1-a** and **L1-b** from **S0** and **S1**, the

dimethylamino functionality may not be solely responsible for interaction within this molecular scaffold. The combination of placing two nitrogen atoms into the stilbene framework with the dimethylamino group revealed that minor changes in chemical structure might better control Aβ interaction *via* hydrogen bonding and hydrophobic contacts.

**Figure 3.32. 2D $^{1}H–^{15}N$ NMR of control molecules and DMSO.**

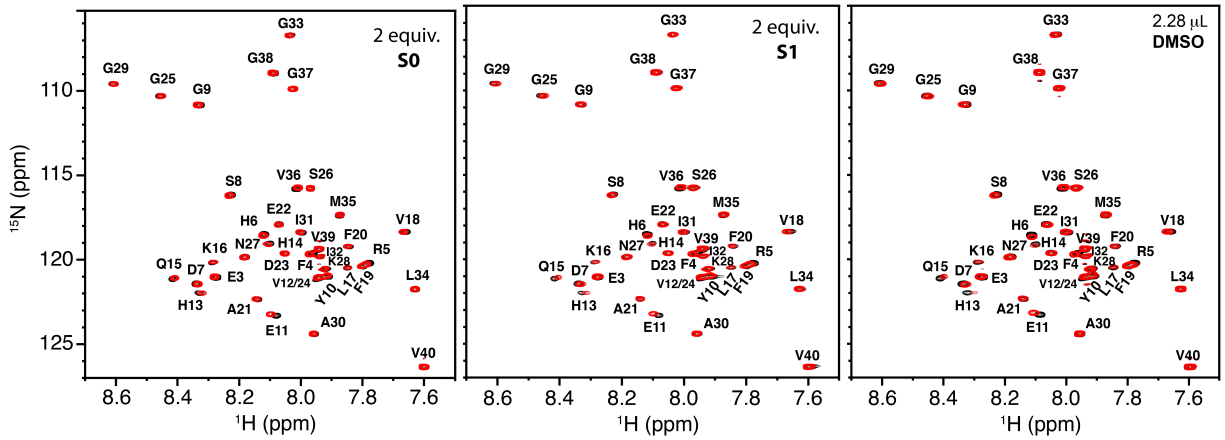


**Figure 3.33. 2D $^{1}H–^{15}N$ NMR chemical shifts for control molecules and DMSO.**

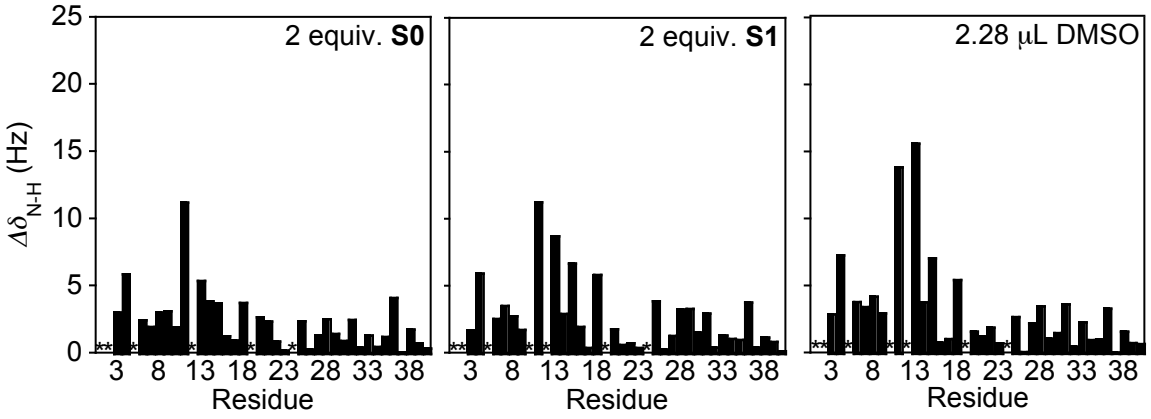

*Docking Studies of **L1** Series.* Of the 10 NMR conformations tested by our docking studies, five conformations of Aβ docked with **L1-a** and **L1-b** were consistent with our NMR results.[113] Based on the lowest energy clusters with highest occurrence, the conformations of compounds with Aβ were selected (Table 3.8). In agreement with NMR observations discussed above, the overall docking results suggested that our bifunctional small molecules may contact the N−terminal region and inner helix of the peptide near the proposed metal binding site (Figure 3.34). Most of the Aβ conformations showed the compounds oriented closer to the hydrophilic metal binding region, while one conformation showed ligands docked near the hydrophobic inner helix (conformation C, Figure 3.34). The docking results for **L1-a** and **L1-b** illustrate similar binding in three of the conformations analyzed, suggesting that these molecules may behave similarly with common hydrogen bonding contacts with the peptide backbone and side chain residues. Along with hydrogen bonding interaction, positioning of the dimethylamino group of **L1-b** either toward the hydrophilic N-terminal region or the hydrophobic helical region revealed various amphiphilic contacts with the peptide, potentially accounting for the greater chemical shift changes exhibited in the NMR experiments. For **S0** and **S1**, interactions were indicated in the hydrophilic turn and along the inner helix of the peptide as well. More variation between these two molecules (**S0**/**S1**) was observed in the different conformations tested, although some conformations showed similar binding modes of these compounds as were seen for **L1-a** and **L1-b** (Figure 3.34). Different orientations of **L1-a**, **L1-b**, **S0**, and **S1** were visible in the docking investigations, with general interaction near the turn of the peptide (near the metal binding site and inner helix) indicating the utility of the stilbene framework for

recognizing the Aβ peptide. The individual differences between the ligands docked to the Aβ conformations displayed several possible contacts that may exist in solution, such as hydrogen bonding and hydrophobic contacts that along with NMR imply more favorable interaction of **L1-a** and **L1-b** over **S0** and **S1** with the Aβ peptide. Therefore, these docking results give further support for direct Aβ interaction of the bifunctional small molecules.

**Figure 3.34. Aβ confirmations A-E from docking studies (surface left and cartoon right) indicating contacts of L1-a (light blue), L1-b (yellow), S0 (orange), and S1 (purple) with the Aβ peptide.**

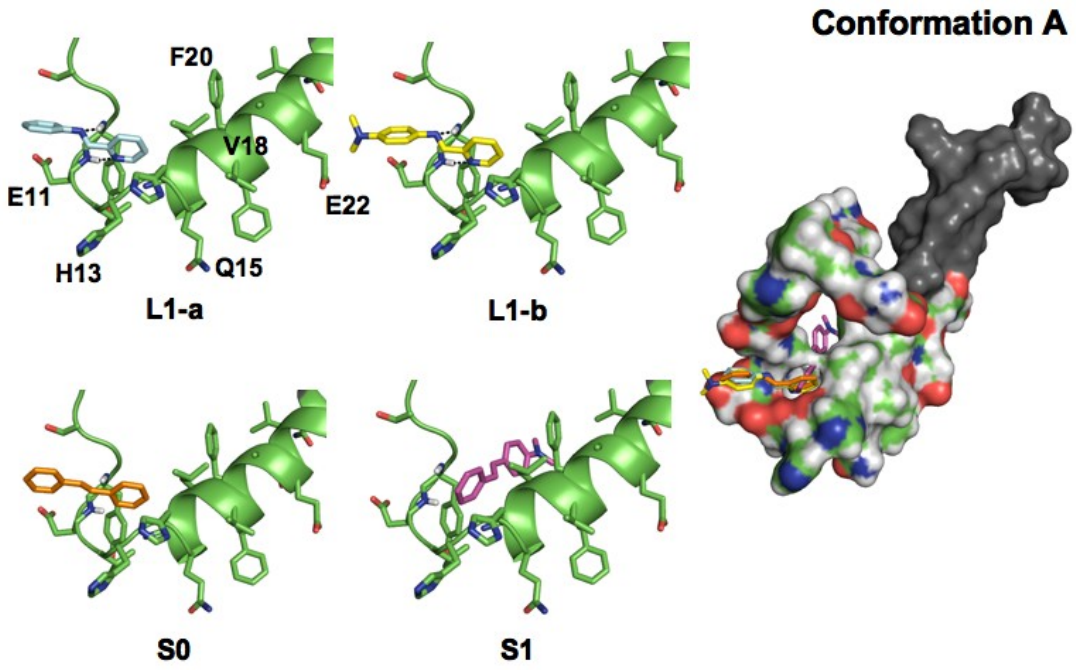

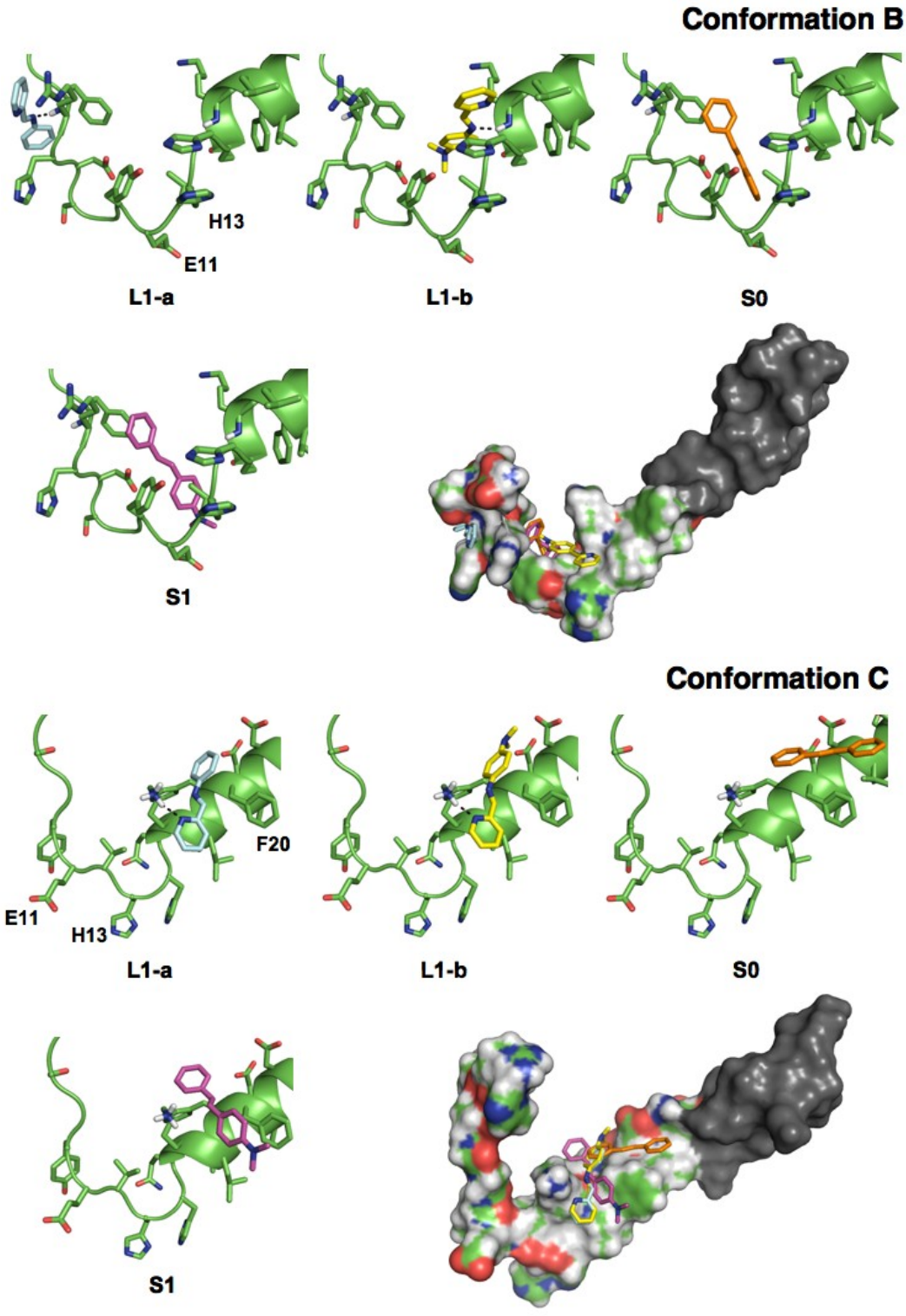
Conformation B
H13
E11
L1-a
L1-b
S0
S1
Conformation C
F20
E11
H13
L1-a
L1-b
S0
S1

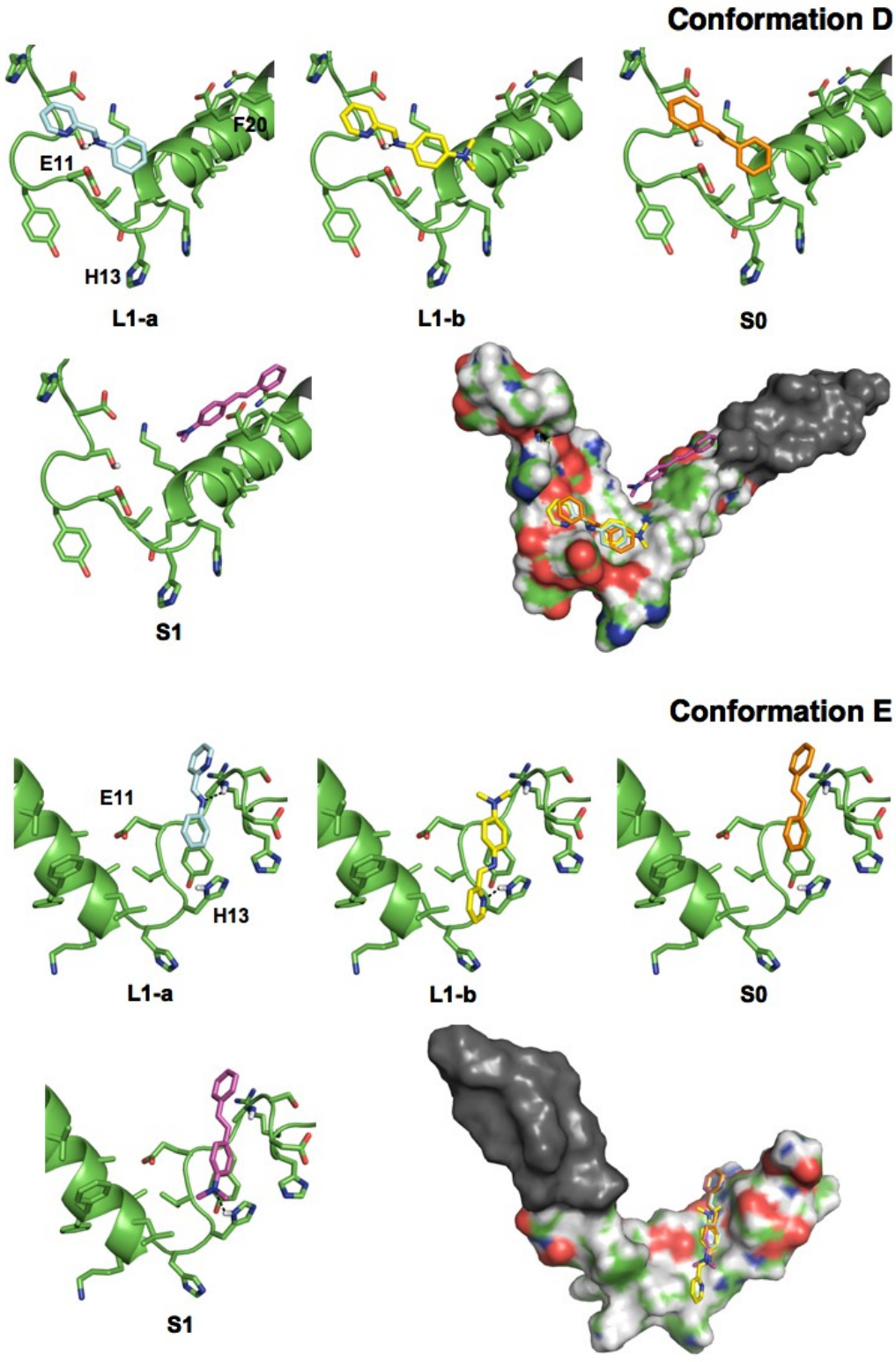
Conformation D
F20
E11
H13
L1-a
L1-b
S0
S1
Conformation E
E11
H13
L1-a
L1-b
S0
S1

**Table 3.8. Calculated energies for clusters with highest occurrence of ligands binding to Aβ based on AutoDock4 results for L and S series of molecules.**

| Conformation (PDB 1BA4) | L1-a (kcal/mol) | L1-b (kcal/mol) | S0 (kcal/mol) | S1 (kcal/mol) |
|---|---|---|---|---|
| **A** | -5.83 | -5.55 | -5.07 | -5.35 |
| **B** | -4.57 | -4.84 | -4.24 | -4.28 |
| **C** | -4.11 | -3.18 | -4.11 | -2.85 |
| **D** | -4.40 | -4.77 | -4.36 | -4.28 |
| **E** | -4.04 | -4.56 | -4.34 | -4.63 |

### 3.3.4. Aβ Interaction of Second Generations

*2D NMR of **K1**.* Upon the addition of four equiv of **K1** to a solution of Aβ, the N–terminus of the peptide was perturbed with E11 and H13 shifting most significantly similar to **K0** (Figure 3.35).[111] With a total amount of eight equiv of compound introduced to the peptide solution, the residues E11, H13, and Q15 showed the greatest amount of $^{1}H–^{15}N$ shifting. Compared to **K0** (Figure 3.29), **K1** indicated greater interaction of these residues, which were shifted at least 5 Hz greater (Figure 3.35). Additionally, periodic portions (in particular, Q15, V18, and E22) of the α-helical region (Q15–V36) experienced a change in chemical shift, similar to observations of **K0** and **L1-b**.

The 2D NMR results for **K0**, **K1**, and **L1-b** suggest similar interactions with the peptide and potential contact with the metal binding site of Aβ (H6, H13, and H14). The chemical shifts observed in the presence of these molecules could be due to direct contact with the peptide, indirect contact at one site causing a change in confirmation at another site, interrupting interactions of the peptide with the SDS micelles, and/or multiple binding sites. For example, with 4 equiv of **K1**, the N–terminus and, in

particular, E11 and H13, were most affected while at 8 equiv, portions of the inner helix underwent shifting.[111] Overall, these qualitative NMR studies suggest that **K0**, **K1**, **L1-a**, and **L1-b** have the capability to interact with $A\beta_{1\text{-}40}$ to varying degrees.

**Figure 3.35. 2D $^{1}H$–$^{15}N$ NMR spectra of K1 (left) and chemical shifts (right).**

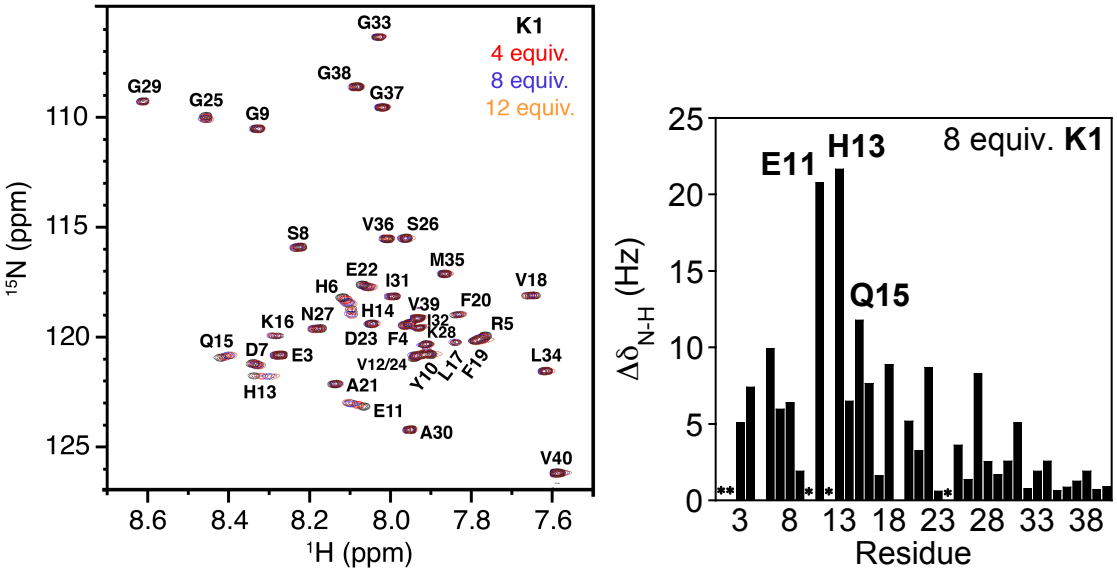


*2D NMR of **L2** Series.* With the addition of **L2-b** to $^{15}N$-labeled $A\beta_{1\text{-}40}$ in SDS-$d_{25}$ micelles, a significant effect on portions of the peptide was observed upon increasing the ligand concentration from 5 to 15 equiv (Figure 3.36), while **L2-a** showed more modest effects (Figure 3.37).[114] Additionally, the traditional metal chelator, 8-hydroxyquinoline (8-HQ) afforded a smaller effect in $\Delta\delta_{(N\text{-}H)}$ shifts than **L2-a** and **L2-b** (Figure 3.37), indicating that our bifunctional scaffold has greater interaction ability with the Aβ monomer. Additionally, the significance of the dimethylamino group was exemplified by comparing spectra of **L2-a** and **L2-b** (Figure 3.36) and Figure 3.37). Adding 10 equiv of **L2-a** to the Aβ monomer resulted in similar shifting of residues as **L2-b** but to a much lesser extent (Figure 3.38). Overall, the NMR studies suggest more

direct interaction of **L2-b** with Aβ than **L2-a** and **8-HQ**, which clearly displays greater bifunctionality.

Different from the rigid molecules already discussed (**K** and **L1** series), **L2-b** showed a more dispersed effect on the N-terminus and inner helix of Aβ (Figure 3.38). This observation indicates that **L2-b** has a different and more influential effect over the peptide structure. Comparing residue shifting of the relatively planar imine molecules (Figure 3.31) versus the more flexible amines (**L1** versus **L2**), the **L2** series shows greater interaction over the entire N-terminal portion of the peptide (E3–E22). While **L2-b** interacts broadly through the E3 – E22 region, **L1-b** has fewer contacts, with more of a periodic trend on the inner helix segment. The NMR studies of **L1-b** and **L2-b** do show commonality in that they both exert greater influence (notably on residues E11 and H13) over **L1-a** and **L2-a**, demonstrating the importance of the dimethylamino groups in interacting with the peptide. These results imply not only that the stilbene derivatives interact with the Aβ monomer but also that planar and non-planar molecules may interact in different modes based on the chemical environment.

**Figure 3.36. 2D $^{1}H-^{15}N$ NMR for L2-b with zoomed area of interest in the red box.**

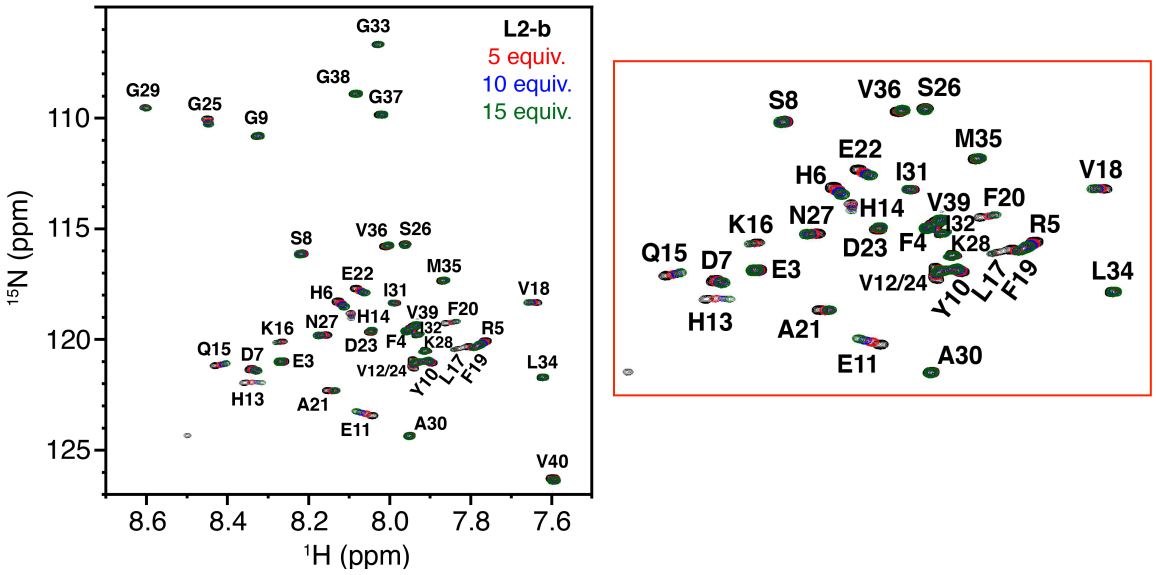


**Figure 3.37. 2D $^{1}H-^{15}N$ NMR of L2-a and 8-HQ.**

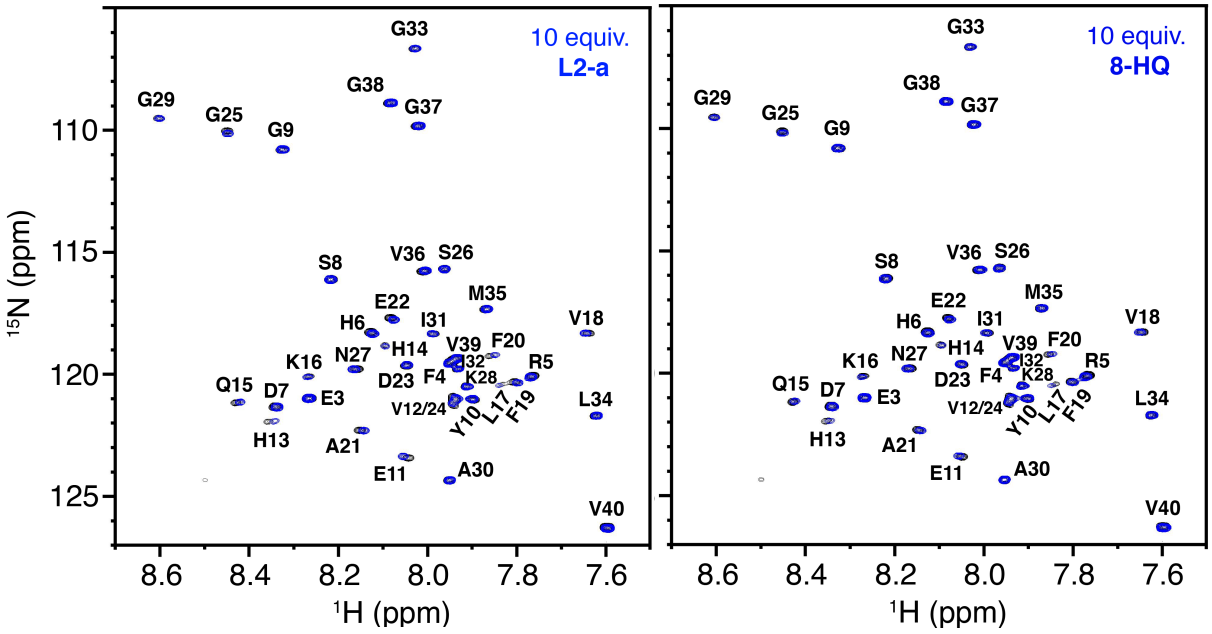

**Figure 3.38. 2D $^{1}H-^{15}N$ NMR chemical shifts of L2 series and 8-HQ.**

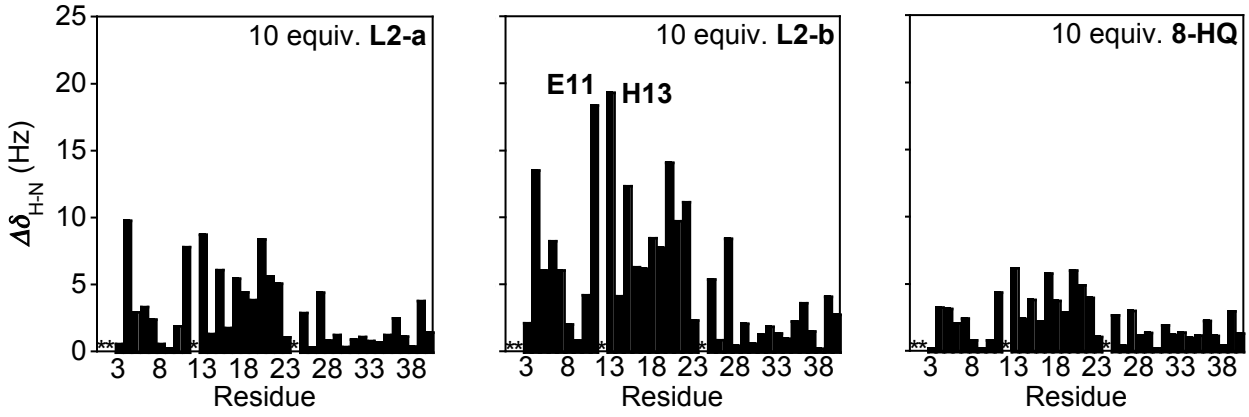


*Docking Studies of **L2** Series.* Similar to the results for the **L1** series, five of the Aβ conformations with the docked **L2** series agreed with the NMR results where the region from E11 to E22 was most affected (Figure 3.39).[114] Binding energies ranged from −3.49 to −3.78 and −2.61 to −5.68 kcal/mol for **L2-a** and **L2-b**, respectively (Table 3.9). Interaction of **L2-a** with Aβ as determined by docking studies was also in agreement with the NMR spectroscopic data, where the hydrophobic region from L17 to A21 was preferred. The dimethylamino functionality appears to act in an amphiphilic manner, with two conformations positioning the head group toward the hydrophilic E11 and H13 residues, while the other three conformations suggest interaction with the hydrophobic region from L17 to A21 (Figure 3.39). These two orientations hint at multiple binding modes in which the dimethylamino group can act as an anchor through either hydrophobic or hydrophilic contacts, which is in accordance with previous results studying the significance of this functionality. Inclusion of two N donor atoms for metal coordination in the structure of the stilbene derivative could facilitate hydrogen bonding with the amino acid residues or the peptide backbone affording better Aβ interaction. As expected, possible hydrogen bonding interactions of **L2-a** and **L2-b**, using N donor

atoms and amine functionality (N−H), with Aβ were detected (dotted lines, Figure 3.39). Taken with NMR investigations, our docking studies demonstrate direct Aβ interaction of **L2-a** and **L2-b** with different contacts due to the dimethylamino functionality.

**Figure 3.39. Aβ confirmations A-E from docking studies (surface left and cartoon right) indicating contacts of L2-a (yellow) and L2-b (orange) with the Aβ peptide.**

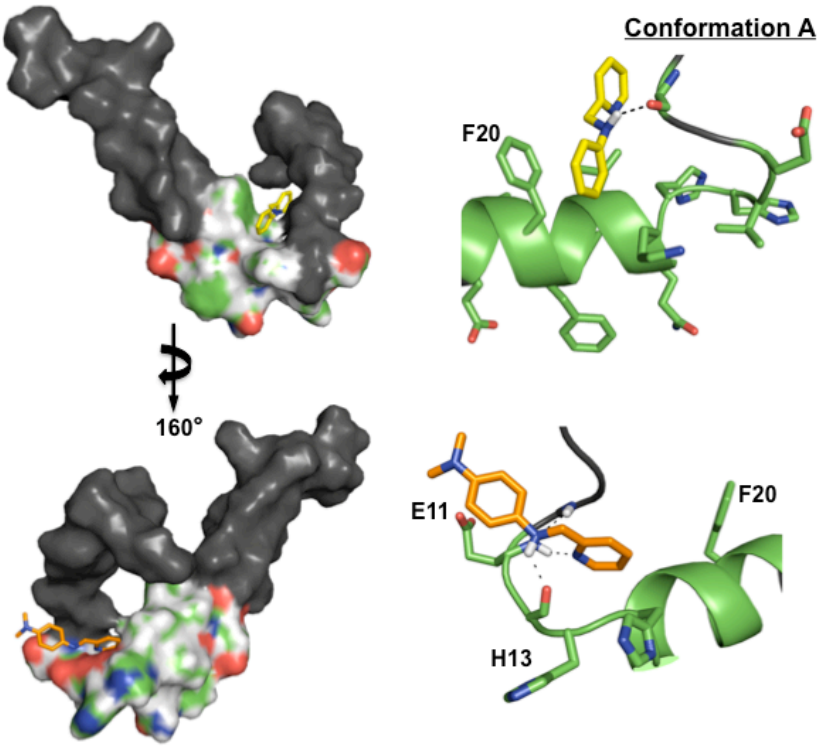

**Conformation B**

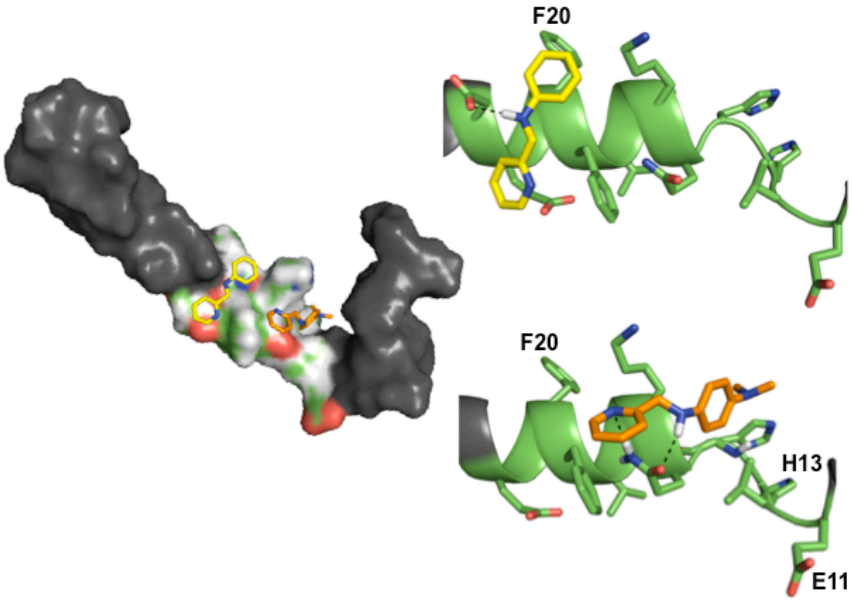


**Conformation C**

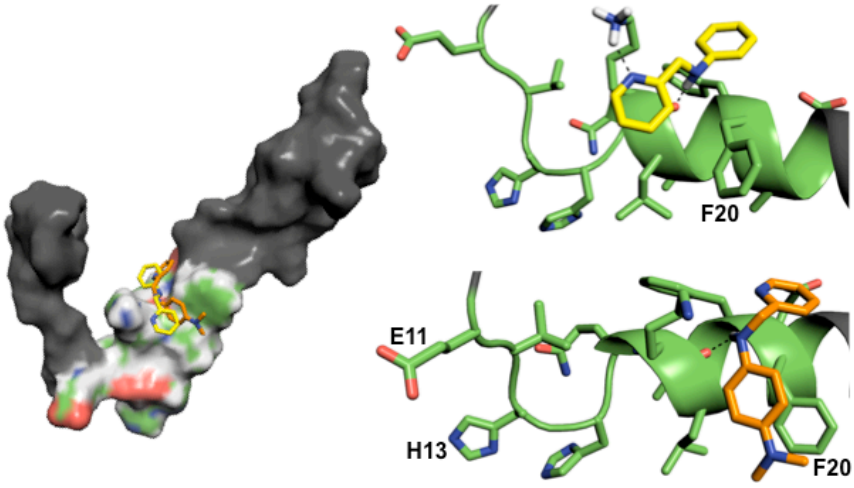

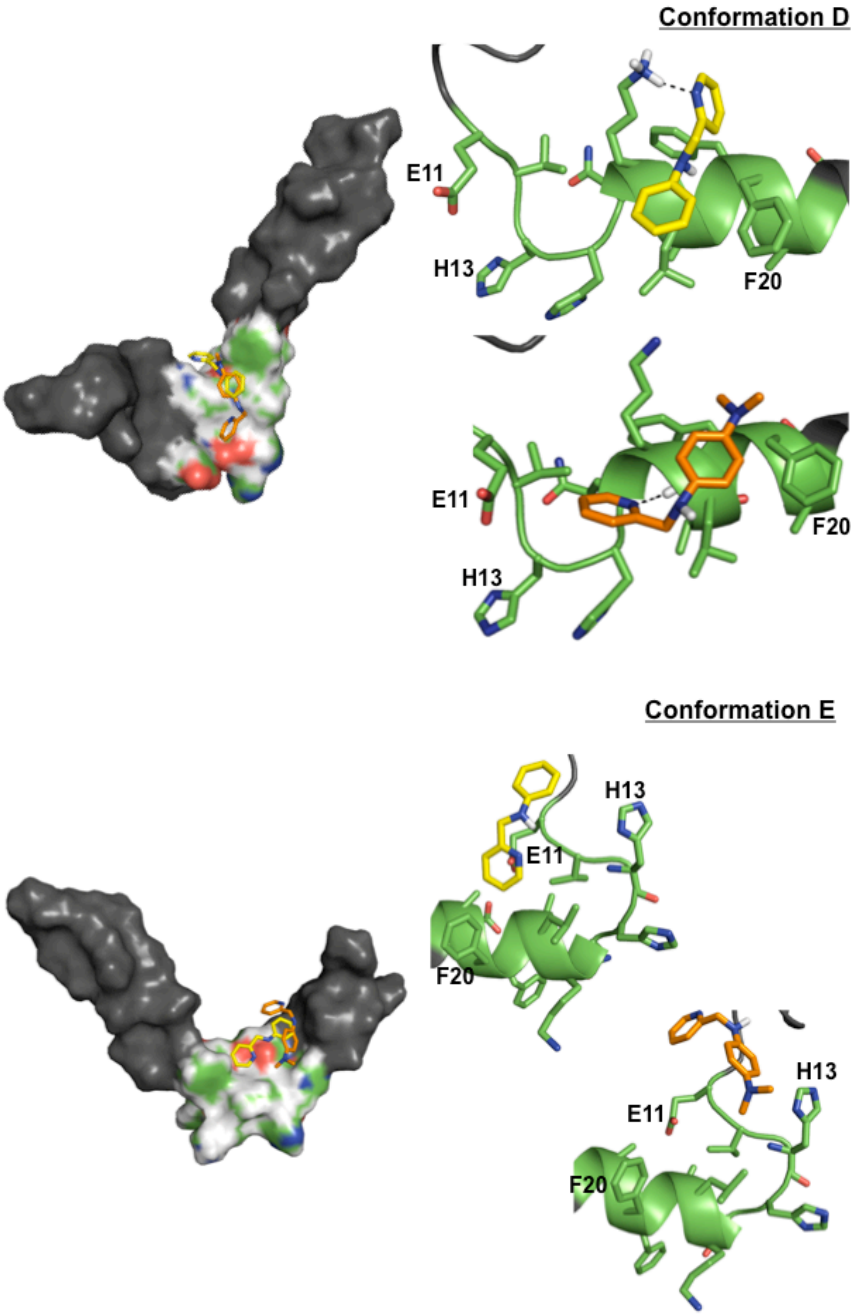
Conformation D
E11
H13
F20
E11
H13
F20
Conformation E
H13
E11
F20
H13
E11
F20

**Table 3.9. Calculated energies for clusters with highest occurrence of ligands binding to Aβ based on AutoDock4 results for the L2 series.**

| Conformation (PDB 1BA4) | L2-a (kcal/mol) | L2-b (kcal/mol) |
|---|---|---|
| **A** | -3.60 | -5.68 |
| **B** | -3.78 | -4.23 |
| **C** | -3.76 | -2.61 |
| **D** | -3.52 | -4.19 |
| **E** | -3.49 | -4.05 |

In summary, the **K** and **L** series of molecules have been demonstrated as both metal chelators and molecules that can interact with the Aβ peptide distinguishing them as bifunctional molecules for targeting metal-Aβ species. From the compounds investigated, the choice of molecular scaffold and functionality are important variables in selecting effective Aβ interacting molecules to be used as a basis for rational structure-based design. As shown in the metal binding and Aβ interaction studies by NMR, the dimethylamino group plays an important role in affecting the ligands structure providing stronger metal chelation and greater contacts with Aβ. It is also an interesting observation that the more flexible **L2-b** ligand interacts with Aβ compared to the more rigid **K** and **L1** molecules. Typically rigid, planar molecules are used to target amyloids (*i.e.*, ThT, IMPY, *p*-I-stilbene). Here it is observed that this is not entirely necessary for metal-Aβ species and that other interactions (*i.e.,* H-bonding) can be effective. Overall, our investigations above indicated that the IMPY and stilbene derivatives could interact with both metal ions and Aβ, making them candidates as chemical tools for exploring metal-Aβ reactivity (Section 3.4)

### 3.4 Testing Reactivity of Bifunctional Molecules Towards Metal-Aβ Species

As stated by the metal ion hypothesis, metal-Aβ species are believed to contribute to the neurotoxicity observed in the AD brain. However, the nature of the metal-Aβ species that contributes to the greatest detrimental effects remains uncertain. It could be, for example, metal-incorporated low MW oligomers, amorphous aggregates, or fibrils. Studies conducted *in vitro* indicate that $Fe^{2+/3+}$, $Cu^{+/2+}$, and $Zn^{2+}$ can increase aggregation rates of Aβ, induce more potentially toxic Aβ oligomeric states, and cause oxidative damage ($Fe^{2+/3+}$ and $Cu^{+/2+}$).[36,42,49,64,78,87] Chemical tools that can manipulate and interfere with the various reactivity modes of metal-Aβ species may be critical for better understanding how these processes could be related to the progression of neuropathology *in vivo*.

Based on Section 3.3, the two families of designed compounds (**K** and **L**, Figure 3.8) are bifunctional compounds that have the potential to serve as chemical tools for studying AD. To verify that the bifunctional abilities of the designed molecules translate to modulating the reactivity of metal-Aβ species, *in vitro* experiments were carried out.[110,111,113,114] Techniques utilized in the Lim Lab to determine the efficacy of bifunctional compounds to regulate metal-Aβ chemistry are transmission electron microscopy (TEM) and native gel electrophoresis with Western blot analysis.[113,114,147] Further determination of the ability of compounds to control ROS production and neurotoxicity imparted by metal-Aβ species were established by both cell-free and cellular biochemical experiments. Compounds that are non-toxic and successful at influencing metal-Aβ species reactivity and toxicity in the above experiments have the

potential to be used as chemical tools for investigating the relationship of metal-Aβ species to AD.

In sections 3.4.1 and 3.4.2 below, summaries of the **L** compounds are provided to display the applicability of our compounds *in vitro* and in living cell experiments. It is noted here that the **K** family of molecules are toxic as indicated by cellular studies, which limits their utility to the study of metal-Aβ reactivity under *in vitro* conditions.[110,111] The **L** series is presented here along with more in depth discussion on mechanisms based on 2D NMR investigations (Section 3.4.3).

### 3.4.1 Summary of Reactivity Studies by TEM and Western Blotting

In order to understand the reactivity of metal-Aβ species leading to various aggregated states and their relationship to toxicity, molecules that have the ability to disrupt aggregation processes are desired. There are two perspectives to consider when probing the amyloid cascade (Figure 3.2 and Figure 3.40). From the preventative viewpoint, molecules can be screened for how effective they are at impeding the interaction of Aβ monomers and inhibiting oligomer and fibril formation. Secondly, the ability of compounds to breakdown or disassemble preexisting aggregates can be explored.

Effective compounds at both inhibition and disaggregation will produce more soluble, smaller Aβ species. The resulting lower MW species can be viewed by native gel electrophoresis with Western blotting using a 6E10 antibody. This antibody is capable of recognizing Aβ species by the first 10 residues of the N–terminal region of the peptide.[148] The smaller-sized peptide aggregates have the ability to penetrate and be separated on the gel matrix based on their MW. On the other hand, large Aβ

aggregates (*i.e.*, mature fibrils) are restricted at the entrance of the gel where the sample is loaded.[149,150] If a compound disassembles preformed Aβ aggregates, a wide MW range of Aβ species can be generated. In the native gel, the amount of smearing from top to bottom (high to low MW) is indicative of the utility of the molecule for disaggregation. In conjunction with native gel analysis, TEM can be used to visualize morphological features of the larger Aβ species that are generated. Under our experimental conditions that employ these methods together, monitoring the degree of Aβ aggregation (*i.e.*, changes in MW distribution of Aβ species) and/or morphologies of the Aβ aggregates can reveal how effective a small molecule is at regulating Aβ aggregation and/or disaggregation in the presence or absence of metal ions.

For all inhibition experiments, fresh $A\beta_{1\text{-}40}$ (25 μM) and $CuCl_2$ or $ZnCl_2$ (25 μM) were treated with the small molecules (50 μM) for 24 h. In the disaggregation experiments, the samples containing Aβ and metal chloride salts were incubated for 24 h to allow Aβ aggregates to form. The resultant samples were then agitated with each small molecule for 24 h.

**Figure 3.40. General schematic illustrating the concept of using bifunctional small compounds to a) inhibit and b) disaggregate metal-Aβ species.**

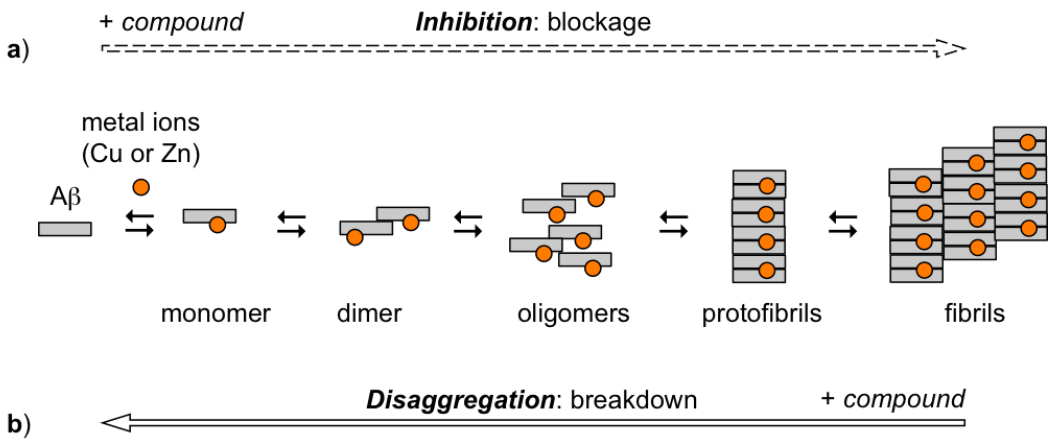


*Inhibition by **L** Series.* Inhibition studies with the **L** series of bifunctional molecules indicated a noticeable effect on metal-induced Aβ aggregation by TEM.[110,113,114] As compared to the large, structured Aβ aggregates formed in the presence of only $Cu^{2+}$ or $Zn^{2+}$, smaller metal-Aβ aggregates with different morphology were formed with both the **L1** and **L2** series of bifunctional small molecules in the inhibition experiments for both metal ions (Figure 3.41a). Partially structured aggregates were observed in the $Cu^{2+}$ samples, whereas samples with $Zn^{2+}$ produced amorphous, unstructured aggregates. The control molecule **S1** was unable to prevent the formation of the large metal-induced aggregated species, although morphological changes were observed. These observations show that the inclusion of a metal binding site into the stilbene scaffold is critical for inhibiting the formation of metal-Aβ aggregates.

Consistent with the TEM results, native gel analysis followed by western blotting (6E10) also showed the influence of the **L** compounds on aggregation states of metal-Aβ (Figure 3.41b). Both the **L1** and **L2** series caused smearing in the gels, indicating

the production of a wide range of Aβ species, including a greater distribution below 32 kDa compared to the compound-free samples. The presence of the dimethylamino group for **L1-b** and **L2-b** provided distinguishable results compared to compounds without it (**L1-a** and **L2-a**). More smearing of $Cu^{2+}$- and $Zn^{2+}$-Aβ species was observed suggesting that the dimethylamino group imparts greater interaction of the stilbene derivative framework resulting in greater inhibition of Aβ aggregation in the presence of metal ions. These inhibition studies demonstrate the effectiveness of the **L** series of compounds as modulators of metal-induced Aβ aggregation.

**Figure 3.41. $Cu^{2+}$ (top) and $Zn^{2+}$-Aβ (bottom) inhibition studies by a) TEM and b) Western blotting of L series.**

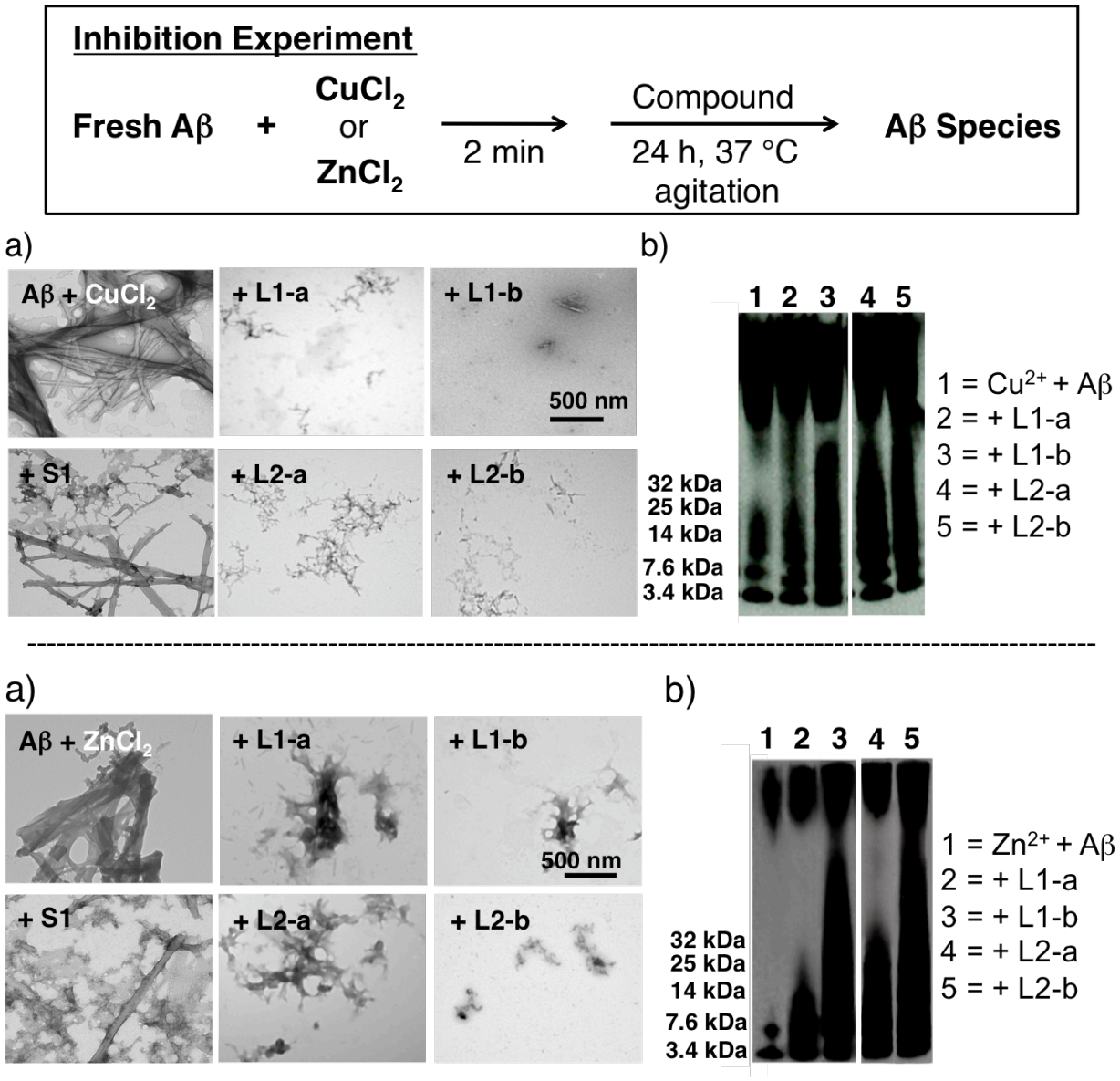


*Disaggregation by **L** Series.* The bifunctional compounds **L1-a**, **L1-b**, **L2-a**, and **L2-b** were also able to alter the structure of pre-formed metal-Aβ aggregates, resulting in their partial disaggregation (Figure 3.42). The samples with bifunctional molecules were absent of the large aggregated species that were indicated in the samples containing only Cu/Zn and Aβ. When the bifunctional small molecules were present, all of the samples showed amorphous aggregates, except $Cu^{2+}$-Aβ treated with **L1-a**,

which showed smaller ordered structures. Like in the inhibition experiment, the control molecule **S1** did not show an effect on the size of metal-Aβ aggregates although observable changes in the structure of the aggregates were observed, indicating the ability of the stilbene derivative framework to recognize metal-Aβ species but not induce their breakdown.

**Figure 3.42. TEM disaggregation studies of a) $Cu^{2+}$- and b) $Zn^{2+}$-Aβ species by L series.**

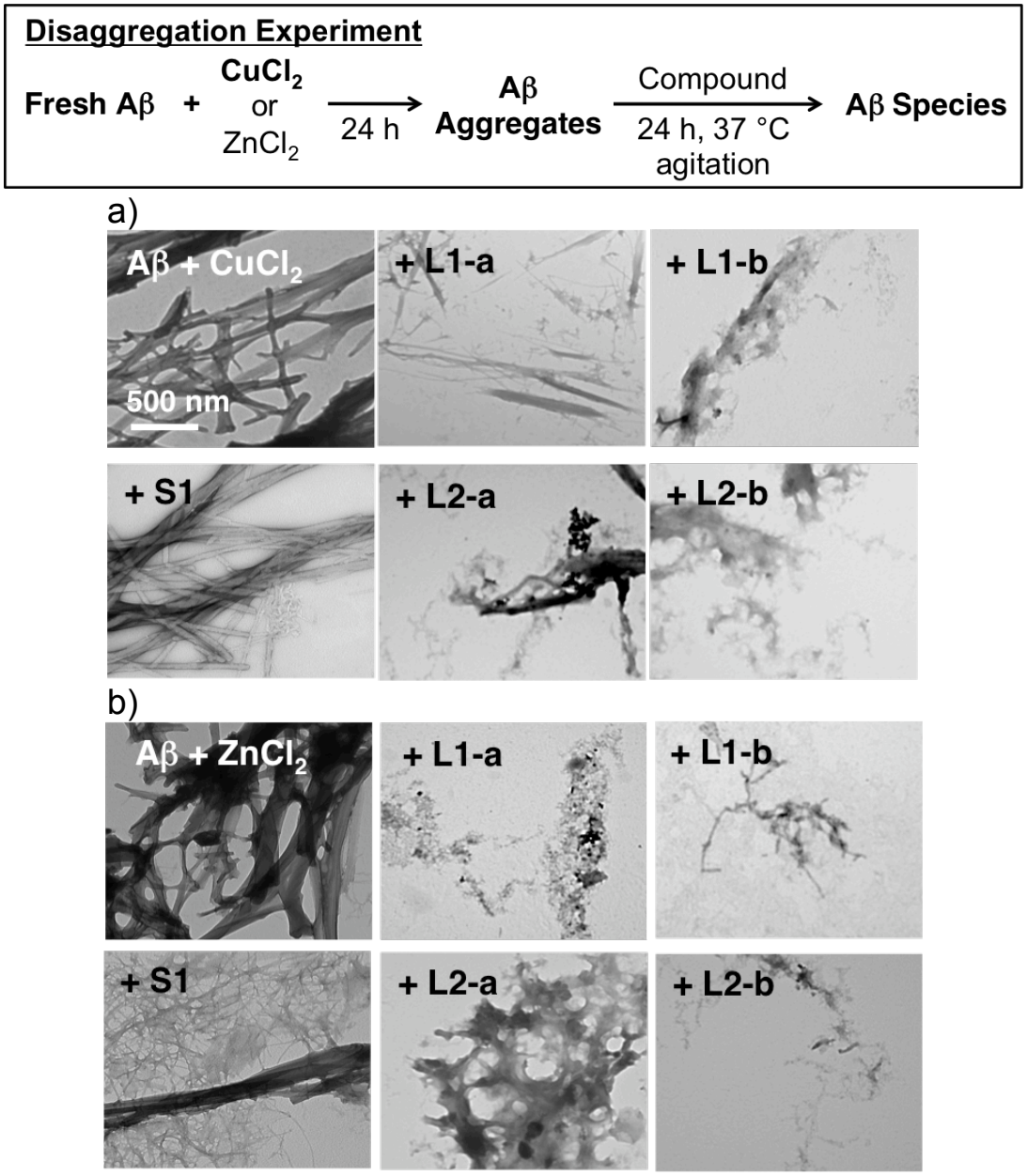

*Metal-free Reactivity Studies of **L2** Series.* To determine the ability of the bifunctional small molecules to disassemble metal-free Aβ species, the disaggregation experiments were repeated without $Cu^{2+}$ or $Zn^{2+}$. When metal ions were not involved in the formation of Aβ aggregates, TEM results showed structured Aβ aggregates that remained after 24 h incubation with either **L2-a** or **L2-b** (Figure 3.43). This observation suggests that the compounds are capable of selectively interacting with metal-triggered Aβ aggregates over metal-free Aβ species. Selectivity for metal-Aβ species over metal-free Aβ could be useful in future experiments where distinguishing toxicity between the two systems is important. It is of interest to note that **L2-b** has the ability to recognize the aggregated form of Aβ under metal-free conditions as previously detected by a modified enzyme-linked immunosorbent assay (ELISA). **L2-b** cannot, however, facilitate the breakdown of preformed metal-free Aβ aggregates (Figure 3.43). These results clearly show that not only can the influence of metal ions on aggregation effects be regulated but also that compounds can be selectively designed to target metal-Aβ species.

**Figure 3.43. Metal-free disaggregation studies of L series by TEM.**

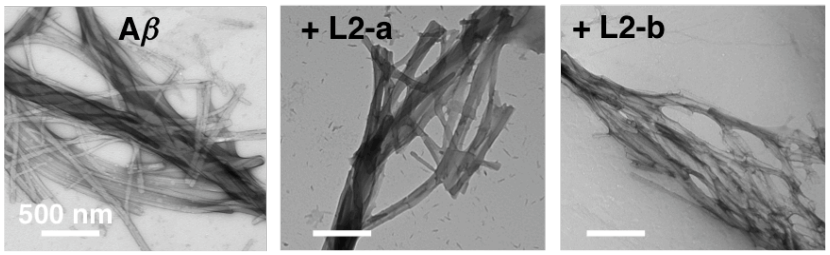


The TEM and Western blotting results from both inhibition and disaggregation experiments demonstrate the requirement of bifunctionality (metal chelation and Aβ

interaction) for molecules that are desired for interfering with metal-mediated Aβ aggregation processes (formation of metal-induced Aβ aggregates as well as their disaggregation). These observations imply that the bifunctionality of our compounds leads to enhanced reactivity with metal-Aβ species. Furthermore, the presence of a dimethylamino group results in an enhanced effect, providing preliminary clues into the structure-interaction-reactivity relationship. Overall, these reactivity studies demonstrate that the designed bifunctional small molecules can function as modulators of metal-Aβ species.

*Testing of **L2** series in AD Brain Tissue Homogenate.* The inhibition and disaggregation studies above were all carried out with synthetic $A\beta_{1-40}$. In order to determine if our compounds are capable of targeting Aβ and/or metal-Aβ in a biological environment, **L2-a** and **L2-b** were further explored for their interaction with Aβ species from human AD brain tissue (Figure 3.44).[114] The frontal cortex section of the human brain was selected because it contains high amounts of Aβ aggregates. The metal contents (Cu and Zn) of the supernatants of the human brain homogenates were first determined by inductively coupled plasma mass spectrometry (ICP-MS). The concentrations of Cu and Zn found in 100 mg/mL of brain tissue were *ca.* 6 μM and *ca.* 9 μM, respectively (Figure 3.44a), which may be sufficient to influence the pathways of Aβ aggregation based on the metal binding affinities of Aβ. Secondly, the distribution of Aβ species in the supernatants of the human brain tissue samples was illustrated by native gel electrophoresis followed by Western blotting using the anti-Aβ antibody 6E10.[151] Along with the protein content visualized by silver staining as a control (Figure 3.44b, lane 1), distributions of high MW Aβ species were imaged as major components

in the homogenate (Figure 3.44b, lane 2). Noticeably, as depicted in lane 4, upon 24 h treatment of the supernatants of homogenates from the human AD brain tissue with **L2-b** (10 μM), more gel-permeable and lower MW Aβ species were visualized by native gel electrophoresis followed by Western blotting with 6E10. As expected, **L2-b** showed stronger ability to disassemble Aβ aggregates obtained from the human AD brain than **L2-a**. These results imply that **L2-b** may target and fragment existing Aβ aggregates that may be associated with metal ions in heterogeneous *in vivo* contexts.

**Figure 3.44. ICP-MS and Western blot results from AD brain homogenate.**

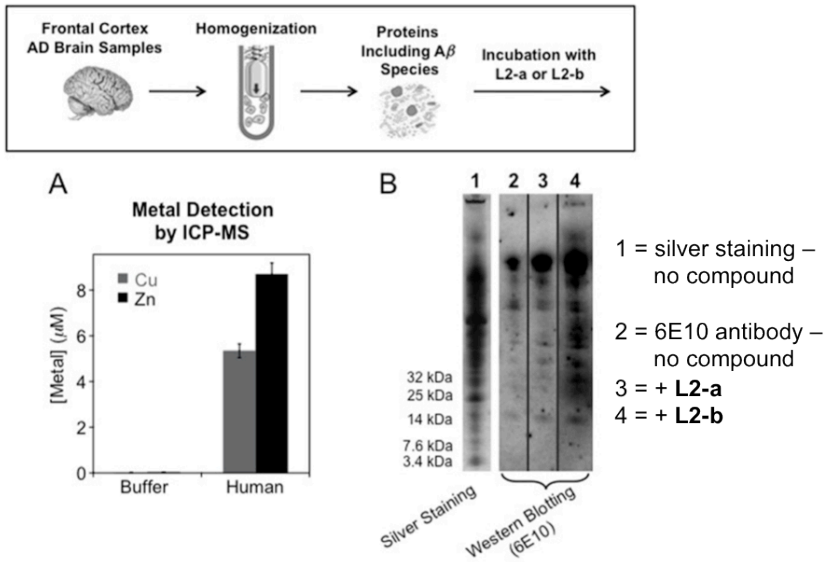


### 3.4.2 Summary of Reactivity and Toxicity Studies by Cell-free and Cellular Assays

As discussed in the introduction, ROS production within the AD brain may be a leading contributor to the neurotoxicity in AD due to oxidative damage. Metal chelators have the ability to not only sequester metal ions from Aβ species, but they can also prevent the generation of ROS by controlling the coordination sphere around the metal ion. Our compounds (**L1-a**, **L1-b**, **L2-a**, and **L2-b**)[110,112,114] demonstrate the ability to

reduce ROS production (in the form of $H_2O_2$) by 60 to 80% in the presence of Cu-Aβ in cell free experiments. Along with the potential to reduce damaging ROS, the **L** series was able to counteract the cellular toxicity imparted by Cu-Aβ and Zn-Aβ species and recover cell survival in human neuroblastoma cells. In agreement with all previous data, **L2-b** showed the greatest recovery of cell viability confirming its superior bifunctionality to the other **L** compounds.[114] These results, in addition to the compounds being relatively nontoxic, suggest the further use of the **L2** family (compounds with higher stability) as chemical tools for understanding metal-Aβ species in more sophisticated AD models systems (*i.e.,* AD mouse models).

Overall, the compounds showed the ability to modulate not only metal-Aβ reactivity (inhibition/disaggregation and ROS production) but also to mitigate toxic effects from these species in a cellular environment. Our results agree with previous reports detailing the reactivity and toxicity of metal-Aβ species that support the metal ion hypothesis of AD and our compounds are some of the first examples of bifunctional molecules designed by the incorporation approach that can counteract these damaging effects.

### 3.4.2 Metal-Aβ Reactivity Studies by 2D NMR

Based on the biochemical experiments in Sections 3.4.1 and 3.4.2, our compounds have an effect on inhibition and disaggregation of metal-Aβ species along with modulating ROS and neurotoxicity in cells. The nature of how our compounds provide these effects is not yet well understood, and I was particularly interested in asking the question, *how do bifunctional small molecules control metal-induced Aβ aggregation*? To understand possible mechanisms underlying the modulation of metal-

triggered Aβ events by our small molecules, spectroscopic investigations were conducted using high-resolution 2D NMR and UV-Vis on $Zn^{2+}$-treated Aβ solutions in the absence and presence of the bifunctional small molecules. Preliminary studies were done with similar experimental conditions to our Aβ interaction screening by 2D NMR (200 mM SDS, 20 mM sodium phosphate buffer, pH 7.3, 7% $D_2O$ (v/v), 25 °C, Section 3.3.2).

*$Zn^{2+}$-Aβ with **L1** Series.* To first determine the ability of **L1-b** to compete for $Zn^{2+}$ binding from Aβ, this molecule (40 μM) was added to a solution containing equal concentrations of $ZnCl_2$ and Aβ (20 μM) in the presence of SDS.[113] The resulting UV-Vis spectrum showed the generation of $Zn^{2+}$-**L1-b** species with an optical band near 400 nm (Figure 3.45), which is comparable to the metal-ligand complex only (Figure 3.11 and Figure 3.45inset). Because of the small optical change upon addition of $Zn^{2+}$ into the solution of **L1-a** (Figure 3.11), the UV-Vis study of Aβ, $Zn^{2+}$, and **L1-a** was not performed.

**Figure 3.45. UV-Vis studies of $Zn^{2+}$-Aβ and L1-b.**

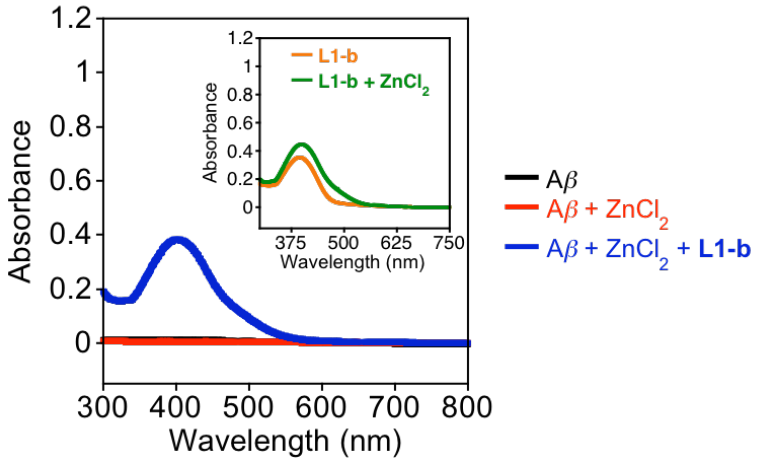


Conditions: UV-vis spectra of Aβ [20 μM, black], [Aβ + $ZnCl_2$] (1:1, red), and [Aβ + $ZnCl_2$ + **L1-b]** (1:1:2, blue) in the NMR buffered condition (200 mM SDS, 20 mM sodium phosphate, pH 7.3). Inset indicates the optical spectra of **L1-b** (40 μM) and solution of $ZnCl_2$ (20 μM) treated with two equivalents of **L1-b**.

Carrying out 2D TROSY-HSQC experiments under similar conditions suggested that more than just metal chelation by our small molecules from the peptide is occurring. As expected from previous reports, the addition of 1 equiv of $ZnCl_2$ to an NMR solution of Aβ (308 μM) resulted in the disappearance of a large portion of the 2D NMR spectrum because of line broadening as a result of $Zn^{2+}$ binding (Figure 3.46, red spectrum).[65,143,152] With the treatment of 10 equiv of the bifunctional small molecules **L1-a** and **L1-b**, the $^{1}H$ and $^{15}N$ cross peaks absent upon introduction of $Zn^{2+}$ were recovered within 30 min of incubation time (Figure 3.46, purple and blue spectra, respectively). Additionally, cross peak shifts were observed for both **L1-a** and **L1-b** that indicate small variations from the metal-free samples in the N−terminal and inner helix portions of the peptide (Figure 3.47). These observations indicate that metal chelation by these bifunctional molecules from $Zn^{2+}$-Aβ occurs leading to signal recovery. Metal removal from the peptide is followed by either interaction of the free compound and/or

the metal complex with Aβ causing shifting of peptide residues indicating the bifunctionality of the **L1** series in the presence of metal ions and Aβ.

**Figure 3.46. 2D $^{1}$H-$^{15}$N NMR experiments of $Zn^{2+}$-Aβ and L1 series.**

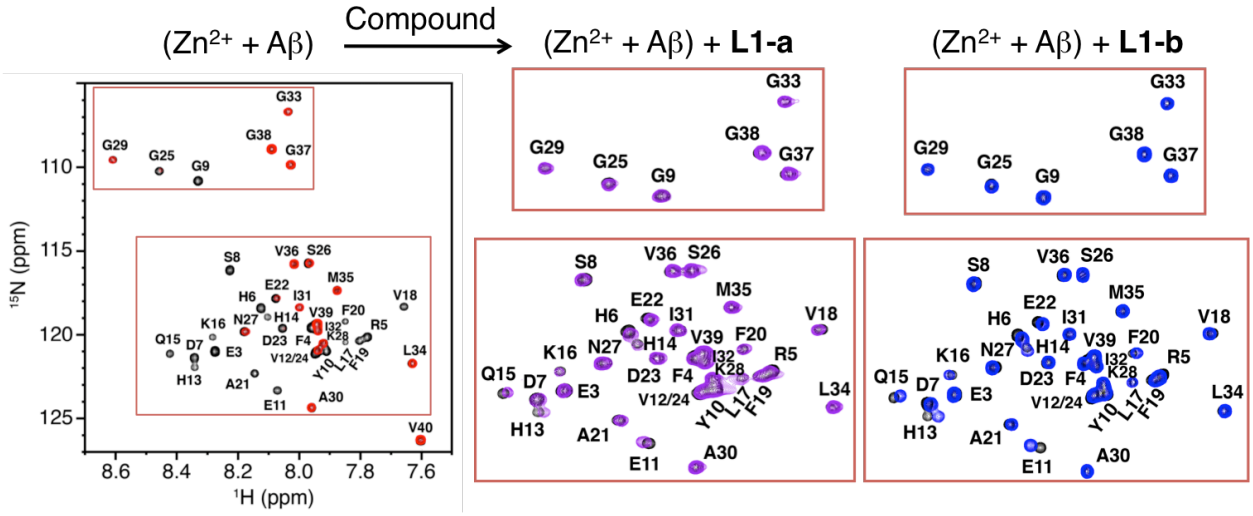


**Figure 3.47. 2D $^{1}$H-$^{15}$N chemical shifts for $Zn^{2+}$-Aβ treated with the L1 series.**

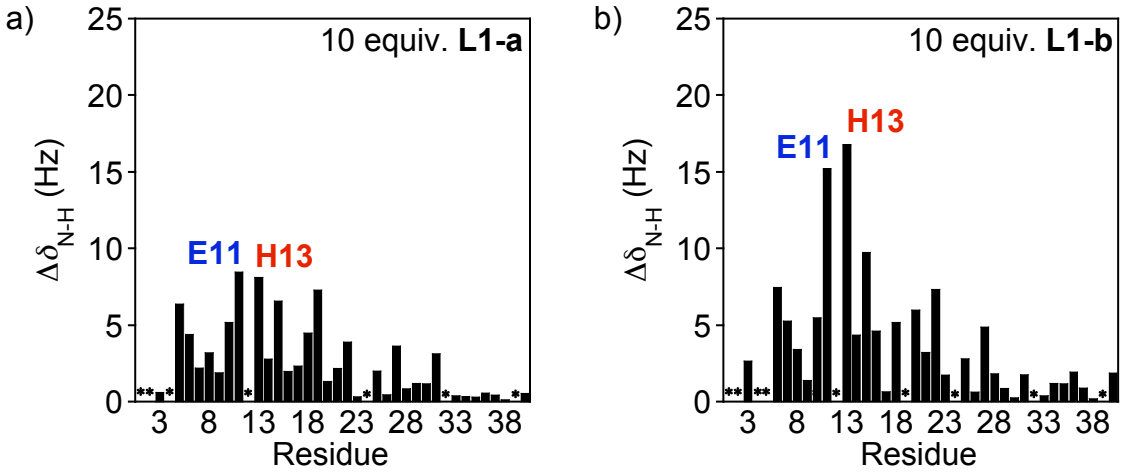

*$Zn^{2+}$-Aβ with **L2-b**.* The same experiments were carried out with **L2-b** to determine any differences between the **L1** and **L2** series.[114] Like its imine precursor, **L2-b** (400 μM) was able to interact with $Zn^{2+}$ bound to Aβ (40 μM) in the presence of SDS. This interaction was identified based on the characteristic UV-Vis absorption feature at *ca.* 500 nm of the **L2-b**-Zn adduct (Figure 3.48).

**Figure 3.48. UV-Vis studies of $Zn^{2+}$-Aβ and L2-b.**

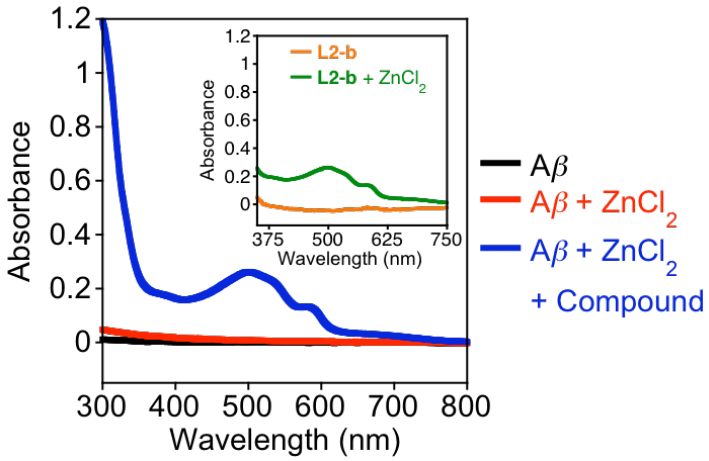


Conditions: UV-vis spectra of Aβ [40 μM, black]; [Aβ + $ZnCl_2$] (1:1, red) and [Aβ + $ZnCl_2$ + **L2-b**] (1:1:10, blue). Inset indicates **L2-b** (40 μM, orange) and [**L2-b** + $ZnCl_2$] (10:1, green). 200 mM SDS, 20 mM sodium phosphate, pH 7.3, 4 h incubation.

Interestingly, 2D NMR studies of **L2-b** provided different results than the **L1** series. Upon incubation of **L2-b** (10 equiv) with $Zn^{2+}$ treated Aβ under our NMR conditions for 4 h, most $^{1}H-^{15}N$ crosspeaks reappeared. However, this was not true for all residues. In particular, residues H6, H13, and H14 did not show any signal return (Figure 3.49). This suggests that while **L2-b** can interact with $Zn^{2+}$ (as determined by UV-Vis spectroscopy), the peptide still has $Zn^{2+}$ bound as well, indicating that ternary type structures could be forming under these conditions.

Further details suggesting the possibility of ternary structures are differences in the magnitudes of $^{1}H-^{15}N$ shifts for the metal-free and $Zn^{2+}$ samples. Although several residues cannot be observed, the central region of the peptide (E11−E22) appears to be affected the most (Figure 3.38 and Figure 3.50). Furthermore, the addition of 1 equiv of the isolated complex, [Zn(**L2-b**)$Cl_2$], resulted in the disappearance of the N-terminal residues, similar to the addition of only $Zn^{2+}$. With the sample composed of stoichiometric amounts of Aβ, $Zn^{2+}$, and **L2-b**, the peptide appears to compete for $Zn^{2+}$ from **L2-b**, although small differences can be observed compared to $Zn^{2+}$-Aβ only. For example, residues V18 and F19 are present and shifted in the $Zn^{2+}$-Aβ-**L2-b** spectrum and absent in $Zn^{2+}$-Aβ. Residues E22, S26, N27, and G38 are not present for the $Zn^{2+}$-Aβ-**L2-b** sample. These differences suggest that while the peptide binds the metal ion, $Zn^{2+}$-**L2-b** interactions remain intact and still influence the structure of the peptide.

**Figure 3.49. 2D $^{1}H$-$^{15}N$ NMR experiments of $Zn^{2+}$-Aβ and L2-b.**

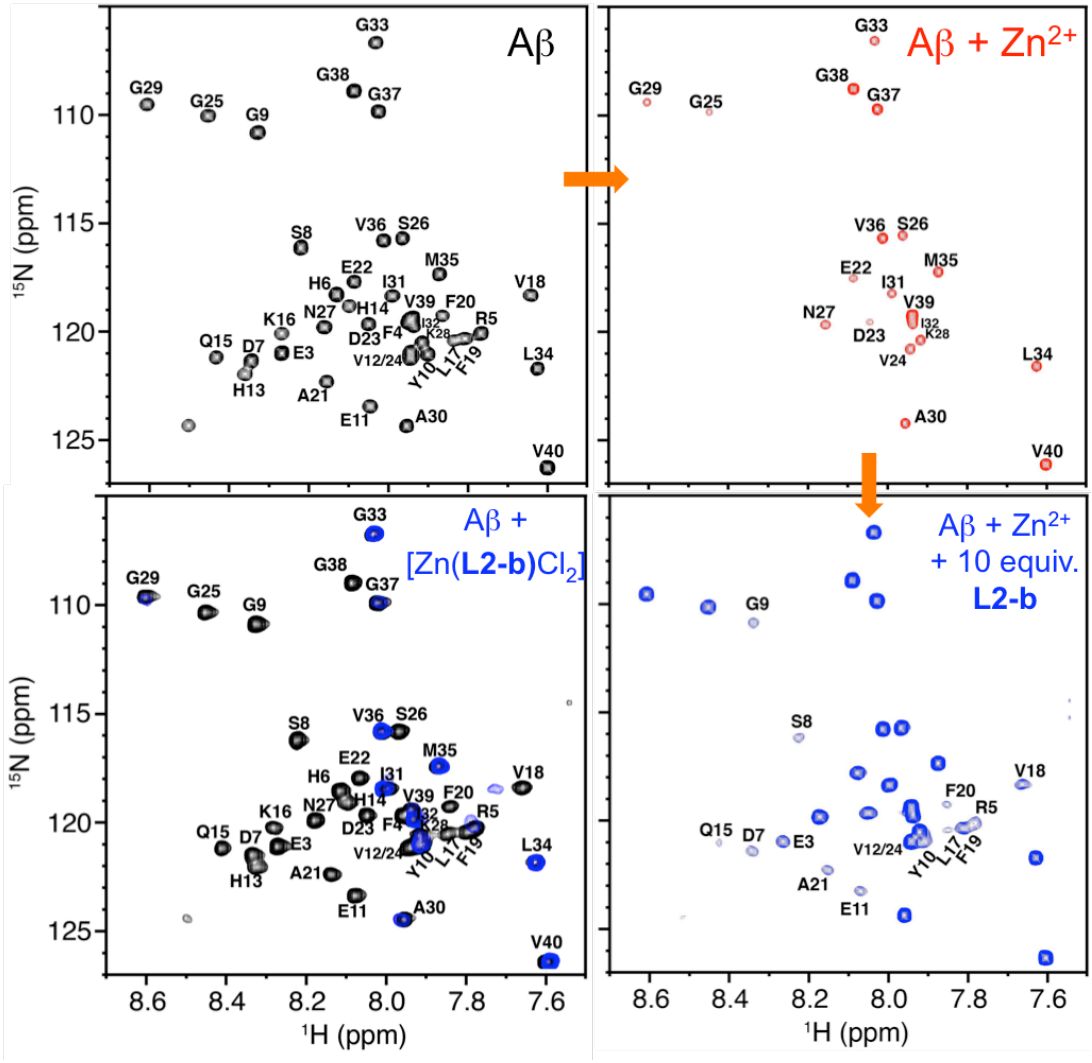


**Figure 3.50. 2D $^{1}H$-$^{15}N$ chemical shifts for $Zn^{2+}$-Aβ treated with L2-b.**

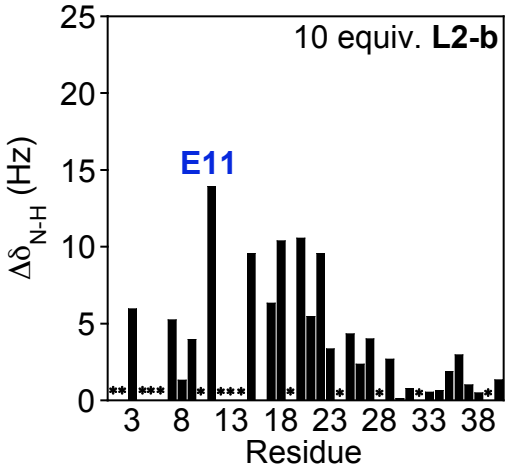

Based on reactivity studies of compounds with metal-Aβ species by TEM (*vide supra*), disruption of metal-peptide interactions is a driving force for preventing metal-induced Aβ aggregation. From previously reported NMR observations, the traditional metal chelators CQ and EDTA were shown to remove $Cu^{2+}$ and/or $Zn^{2+}$ from Aβ. However, our reported TEM results (not shown here) show that EDTA and other orthodox metal chelators do not deter the formation of the large, structured aggregates in metal-induced Aβ aggregation experiments.[85,143,153] This may be the result of full removal of metal ions from Aβ but no additional metal complex interaction with the peptide to prevent aggregation of the metal-free peptides (Figure 3.51a). Since our compounds appear to interfere with metal-Aβ species in a different manner than CQ, our bifunctional molecules may exhibit desirable effects *in vivo*.

Our NMR and optical results involving $Zn^{2+}$-Aβ species and **L1-a**, **L1-b**, and **L2-b** indicate that the observed interference on metal-Aβ reactivity in the inhibition and disaggregation experiments could be due to several possible mechanisms. Either the removal of the metal ion from metal-Aβ species (through metal chelation by the ligand or ligand-induced metal-Aβ conformational changes) and/or the potential formation of ternary type complexes involving Aβ, $Zn^{2+}$, and ligand (through the interaction of ligand with metal-Aβ species or ligand-metal complexes with the peptide, Figure 3.51) could be responsible.[113,114] It is unlikely that excess **L1**/**L2** molecules have a strong enough binding affinity to inhibit Aβ aggregation after metal removal by ligand based on metal-free inhibition and disaggregation experiments (Figure 3.51b). Most likely, Aβ interaction by metal complexes formed upon removal of metal ions from Aβ (type 1) or direct

interaction of ligands with the metal and the metal remaining bound to the peptide (type 2) are mechanisms for ternary type complexes that may be responsible for influencing metal-associated reactivity (Figure 3.51c).

We also observed that this influence could be tuned by the ligand used, where results for **L1-b** suggest the former mechanism while **L2-b** may act *via* the latter mechanism. A combination of these mechanisms could also be at play for the NMR experiments due to the use of excess ligand. Thus, small variations in the stilbene scaffold (**L1** *versus* **L2** and presence of dimethylamino group) could not only affect ligand binding to Aβ (Section 3.3.3) but also indicate the ability to tune interactions with metal-Aβ species.

**Figure 3.51. General scheme depicting possible interactions of metal chelators with metal-Aβ species.**

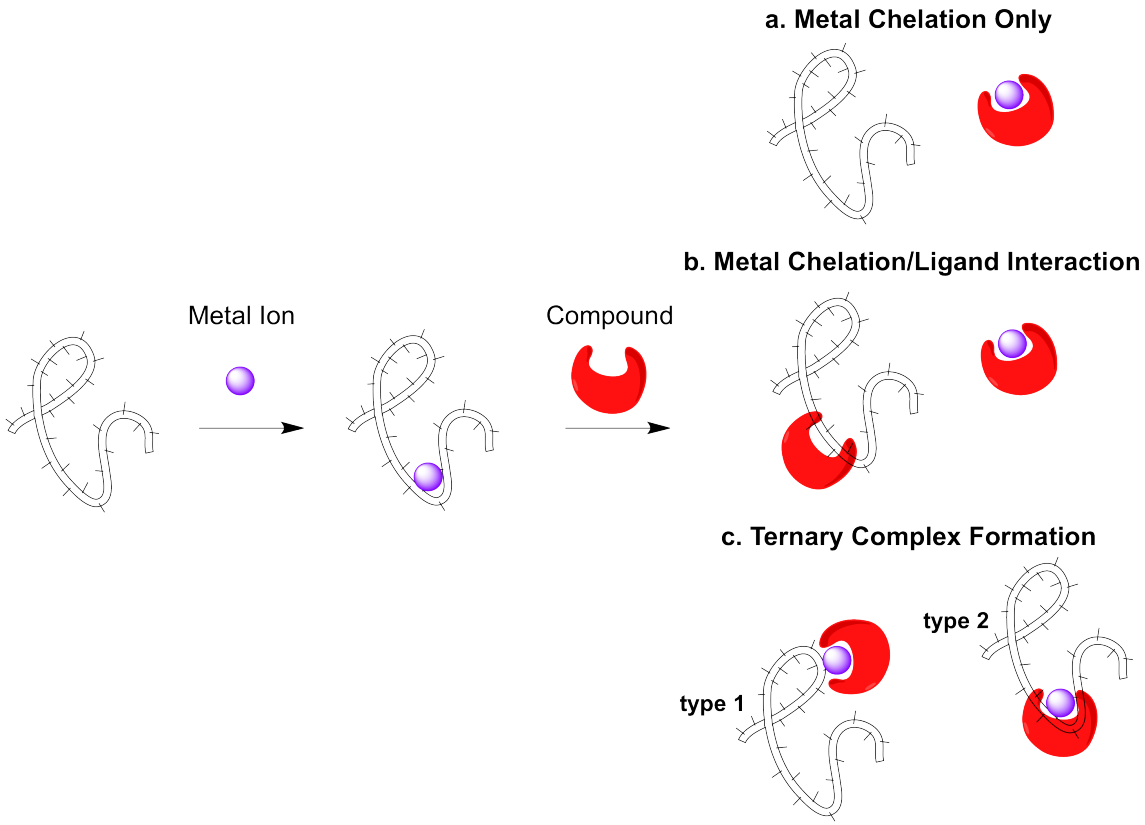

### 3.4.4 Comments on New Bifunctional and Multifunctional Molecules

Stemming from our work and others, new bifunctional molecules have been presented in the literature that, like the **K** and **L** series, are able to modulate the reactivity of metal-Aβ species (Figure 3.53).[88] Several of the molecules utilize the benzothiazole ring that is reminiscent of ThT.[154,155,156] These molecules represent a slightly different approach to bifunctional molecules. Instead of linkage or incorporation, the design of these compounds follows more from a functionalization approach (Figure 3.52).[88] While ThT-d1 (Thioflavin T derivative 1) retains both the benzothiazole and phenyl ring similar to ThT, ThT-d2 and Tht-d3 retain only the benzothiazole ring.

**Figure 3.52. Revised approaches to bifunctional molecules that target metal-Aβ.**

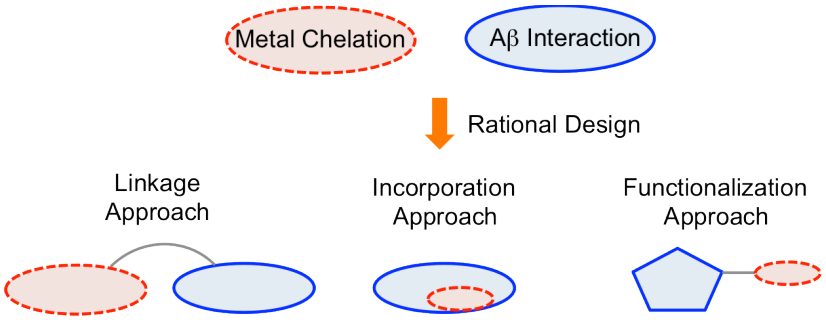


Contrary to our results, ThT-d1 and ThT-d2 can influence metal-Aβ reactivity, but they induce the formation of proposed toxic metal-associated Aβ oligomers.[154,156] This type of result is not completely unexpected, as it is known that certain amyloid modulators can accelerate or inhibit aggregation of metal-free Aβ oligomers or amorphous aggregates.[157,158] Conversely, ThT-d3 has the ability to reverse cellular toxicity imparted by metal-Aβ species similar to **L2-b**.[114,155]

The functionalization approach has also been implemented by attempting to improve the metal chelation and Aβ interaction of the natural product myricetin.[147] However, derivatization proved to be detrimental to the bifunctional design in this

case.[159] The expansion of bifunctional molecules that are able to target and/or produce a variety of toxic and nontoxic metal-Aβ species is exciting due to the fact that an arsenal of compounds could be used to test both toxic and nontoxic conditions. This new duality of bifunctional molecules could further facilitate insight into how metal-Aβ species are related to the progression and neuropathology of AD.

**Figure 3.53. Representative examples of new bifunctional molecules separated by their influence on metal-Aβ species in cellular studies.**

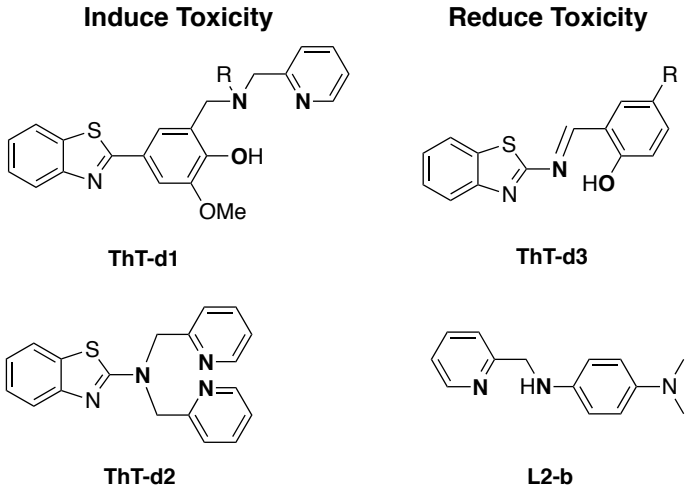


Furthermore, the field of rationally designed compounds has been expanding to incorporate more than just Aβ interaction and metal chelation. Multifunctional molecules containing combinations of Aβ interaction, metal chelation, enzyme/reagent specific cleavable masking groups, antioxidant properties, BBB permeability functionality, acetylcholine esterase targeting, BACE1 targeting and others have been developed.[97] Figure 3.54 exhibits a few examples of these approaches with their properties defined in color. Detailed discussion of these compounds can be found in recent reviews.[160,161] Whether increased functionality will provide additional insight into the complex interplay of Aβ, metal ions, ROS, and other contributors to AD has yet to be determined, but this approach provides a multitude of possible frameworks for future design and exploration.

**Figure 3.54. Multifunctional compounds for study in AD.**

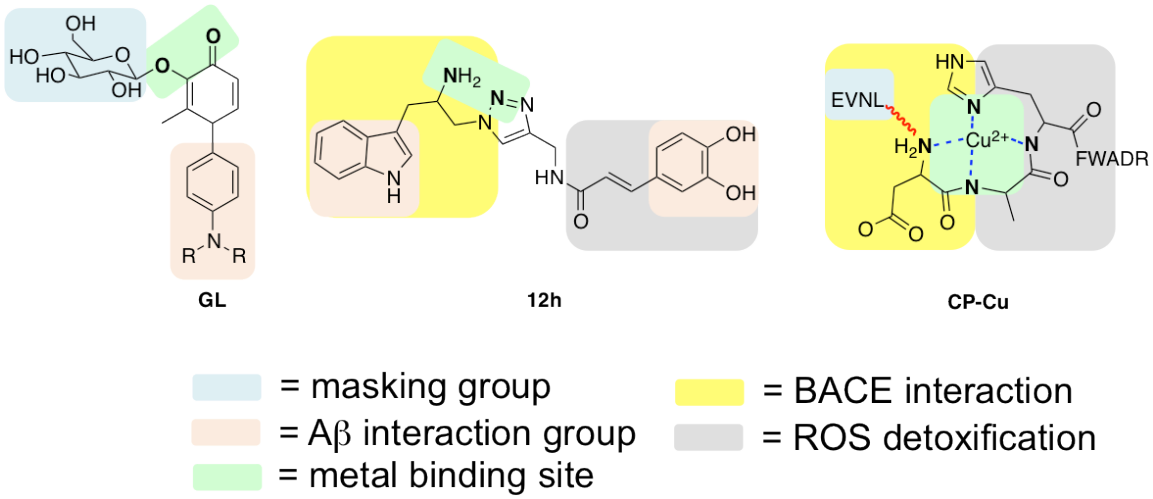


### 3.5 Conclusions and Future Directions

As was discussed in Sections 3.2 and 3.3, our first attempts at rationally designing bifunctional small molecules (**K** and **L**, Figure 3.8) for targeting metal-Aβ species were successful using IMPY and stilbene derivative frameworks. Experiments discussed in Section 3.4 showed the utility of the **L** series in interfering with the reactivity and toxicity of metal-induced Aβ species *in vitro* and in cellular studies. The studies here exemplify the ability of small, simple molecules for modulating metal-Aβ species and validate the need for continued study of metal-involved systems in order to better understand the pathology of AD.

Like the Aβ imaging probes that our compounds were originally derived from, the importance of the dimethylamino functionality was demonstrated through structure-function-reactivity relationships of our molecules. Compounds including this moiety show improved characteristics as bifunctional molecules (better metal chelation and

increased interaction with Aβ). This also translated to a greater ability to modulate reactivity and neurotoxicity of metal-Aβ species. This effect is apparent in the most promising bifunctional molecule, **L2-b**. Pertaining to metal binding of **L2-b**, the dimethylamino moiety most likely donates electron density into the metal center, which provides higher stability constants of its metal complexes. This is significant because the binding affinity of **L2-b** for $Cu^{2+}$ and $Zn^{2+}$ are in the range of metal-Aβ species. Greater contacts of the dimethylamino group through H-bonding and/or hydrophobic contacts may explain why **L2-b** has enhanced Aβ interaction ability and hence greater influence on controlling metal-Aβ reactivity modes. These factors are crucial for directing the metal chelating abilities of bifunctional molecules to the correct location in the brain, Aβ aggregates and/or Aβ deposits. Additionally for **L2-b**, the molecule is predominately neutral at physiological pH, making it a potential BBB penetrable chemical tool for further studying of metal-Aβ species in *in vivo* contexts and as a potential therapeutic. These properties show **L2-b** as a promising molecule that appears to be ideal for targeting metal-Aβ species and will provide an excellent framework for devising further generations of bifunctional molecules with enhanced reactivity.

It is necessary to point out that the progress with our bifunctional molecules has been put into perspective by comparing their effects to control compounds that lack metal binding sites and traditional metal chelators (Figure 3.8 and Figure 3.28). Even though IMPY or *p*-I-stilbene can bind to metal-free Aβ plaques, they do not prevent metal-Aβ induced aggregation events or are able to dissemble metal-Aβ aggregates like their modified metal chelating counterparts (**K** and **L** series, Figure 3.8). By simple installation of heteroatoms for metal binding, these compounds can be rendered as

bifunctional molecules with minimal structural modification. Our studies have shown that the consideration of having Aβ interaction capabilities along with metal chelation is crucial for targeting and manipulating metal-Aβ species. Traditional metal chelators may remove metal ions from metal-Aβ; however, they are not able to inhibit the formation of large aggregates or able to disassemble preformed aggregates.[110,113,153] This suggests that upon metal removal by metal chelators that lack Aβ specificity, the remaining amyloids can continue to aggregate through typical metal-free aggregation events.

With the intent of decreasing plaque burden and metal-associated toxicity, ligands that interact with metal-associated Aβ and prevent aggregation or breakdown of large aggregates may be the most beneficial as therapeutic targets for determining if clearance of metal-Aβ species reduces AD symptoms. Based on our experiments and preliminary mechanistic investigations, the formation of ternary type structures may be a target to aim for in combating these species in the AD brain. Overall, we have demonstrated that both metal chelation and Aβ interaction are required for modulating metal-Aβ species aggregation events. With the potential of Aβ to bind metal ions (Cu and Zn) under physiological conditions, our experiments provide further support that metal ions may be an important consideration for *in vivo* studies and in the design of future therapeutics.

Further investigations into these families of compounds are ongoing in the Lim lab. It will be interesting to see how additional studies give insight into the reactivity of the bifunctional molecules (*i.e.,* studies within AD mouse models, reactivity with metal-$A\beta_{1-42}$ species, mechanistic studies into potential ternary complexes, and susceptibility of metal-compound-Aβ aggregates to be processed by metalloproteases and their

clearance from the AD brain). Additionally, it will be exciting to see the field of rationally designed compounds continue to expand. The past few years have seen an explosion in this field with new avenues to bifunctional compounds (incorporation, linkage, and functionalization approaches) being pursued and additionally, the development of multifunctional compounds. Furthermore, the outcome of clinical trials for PBT2 may continue to confirm the case for metal ion dyshomeostasis and metal-Aβ involvement in AD. Continued endeavors in the field of rational structure-based design may be essential to uncovering the roles of metal ions and Aβ in AD and lead to new, life saving therapeutics for this devastating disease.

### 3.6 Methods and Procedures

*General Materials*. All reagents were purchased from commercial suppliers and used as received unless stated otherwise. The **L1**, **L2**, and **K** series of molecules were synthesized according to literature procedures.[110,111,114] $^{15}$N-labeled $A\beta_{1\text{-}40}$ peptide (free acid terminal) was purchased from rPeptide (>97% purity, Athens, GA) and stored at −80 °C.

*General Methods.* NMR spectra of small molecules were recorded on a Varian 400 MHz spectrometer. NMR experiments with Aβ peptide were carried out on a Bruker Avance 900 MHz spectrometer (Michigan State University). Optical spectra were collected on an Agilent 8453 UV-visible spectrophotometer. Mass spectrometric measurements were performed using a Micromass LCT Electrospray Time-of-Flight mass spectrometer.

#### 3.6.1 X-ray Crystallography

Single crystals suitable for data collection were mounted on a Bruker SMART

APEX CCD-based X-ray diffractometer equipped with a low temperature device and fine focus Mo-target X-ray tube (λ = 0.71073 Å) operated at 1500 W power (50 kV, 30 mA). The X- ray intensities were measured at 85(2) K. Empirical absorption corrections were calculated with the SADABS or TWINABS program.[162] Structures were solved and refined with the SAINTPLUS and SHELXTL software packages.[163,164] All non-hydrogen atoms were refined anisotropically. Hydrogen atoms were assigned in idealized positions and each was given a thermal parameter equivalent to 1.2 times the thermal parameter of the atom to which it was attached. The structure solution was checked for higher symmetry with PLATON.[165]

*[Zn(**L1-a**)$Cl_2$]*. Colorless plate crystals were grown by vapor diffusion of diethyl ether ($Et_2O$) into an acetonitrile ($CH_3CN$) solution of commercially available **L1-a** (5.0 mg, 27 μmol) and $ZnCl_2$ (3.7 mg, 27 μmol) at room temperature over 2 days. The crystals were isolated, washed with $Et_2O$ three times, and dried in vacuo (7.1 mg, 22 μmol, 81%). FTIR (KBr, $cm^{-1}$): 3445 (w, br), 3086 (vw, sh), 3085 (vw), 3064 (w), 3024 (w), 1620 (vw, sh), 1594 (s), 1563 (w), 1494 (s), 1476 (m, sh), 1456 (m, sh), 1445 (s), 1421 (vw, sh), 1385 (vw, sh), 1368 (m), 1339 (vw), 1303 (w), 1280 (w), 1236 (w), 1195 (w), 1186 (vw, sh), 1158 (w), 1111 (m), 1076 (vw), 1050 (w), 1024 (s), 1000 (vw, sh), 976 (w), 959 (w), 916 (m), 840 (vw), 778 (vs), 740 (s), 684 (s), 650 (m), 616 (vw, sh), 567 (w), 535 (m), 481 (vw), 462 (vw, sh), 413 (w). $^1H$ NMR (400 MHz, $CD_3CN$): δ =7.54 (t, *J* = 8 Hz, 1H), 7.61 (t, *J* = 8 Hz, 2H), 7.80 (d, *J* = 8 Hz, 2H), 7.94 (t, *J* = 8 Hz, 1H), 8.16(d, *J* = 8 Hz, 1H), 8.36 (t, *J* = 8 Hz, 1H), 8.85 (d, *J* = 8 Hz, 1H), 9.03 (s, 1H). ESI(+)MS (m/z): $[M-Cl]^+$ calcd for $C_{12}H_{10}ClN_2Zn$, 281.0, found 280.9. Anal. Calcd for $C_{12}H_{10}Cl_2N_2Zn$: C, 45.25; H, 3.16; N, 8.80. Found: C, 45.24; H, 3.17; N, 8.70. UV-vis

[$CH_3CN$; λ nm (ε × $10^4$, $M^{-1}$ $cm^{-1}$)]: 235 (1.1), 241 (1.2), 328 (1.9), 341 (1.8).

*[Zn(**L1-b**)$Cl_2$]*. Orange needle crystals were grown by vapor diffusion of $Et_2O$ into a $CH_3CN$ solution of **L1-b** (5.0 mg, 22 μmol) and $ZnCl_2$ (3.0 mg, 22 μmol) at room temperature overnight. The crystals were isolated, washed with $Et_2O$ three times, and dried in vacuo (6.8 mg, 19 μmol, 86%). FTIR (KBr, $cm^{-1}$): 3440 (w, br), 3077 (vw), 3027 (vw), 3008 (vw), 2974 (vw), 2902 (w), 2863 (vw, sh), 2822 (vw), 1622 (s), 1599 (vs), 1583 (s, sh), 1546 (vs), 1471 (s), 1447 (s), 1415 (vw, sh), 1371 (s), 1328 (vw), 1321 (vw), 1300 (w), 1284 (w), 1250 (w), 1231 (w), 1215 (vw, sh), 1188 (s), 1173 (s), 1159 (s, sh), 1123 (vw, sh), 1105 (vw), 1067 (w), 1050 (vw), 1024 (vw), 1000 (vw), 946 (w), 923 (vw, sh), 842 (vw, sh), 810 (s), 771 (m), 744 (w), 644 (vw, sh), 642 (w), 551 (vw), 529 (m), 430 (vw), 411 (w). $^1H$ NMR (400 MHz, $CD_3CN$): δ = 3.06 (s, 6H), 6.86 (d, *J* = 8 Hz, 2H), 7.71 (d, *J* = 8 Hz, 2H), 7.80 (t, *J* = 4 Hz, 1H), 8.00 (d, *J* = 8 Hz, 1H), 8.27 (t, *J* = 8 Hz, 1H), 8.75 (d, *J* = 4 Hz, 1H), 8.86 (s, 1H). ESI(+)MS (m/z): $[M+H]^+$ Calcd for $C_{14}H_{16}Cl_2N_3Zn$, 360.0, found 360.0. Anal. Calcd for $C_{14}H_{15}Cl_2N_3Zn$: C, 46.50; H, 4.18; N, 11.62. Found: C, 46.44; H, 4.14; N, 11.57. UV-Vis [$CH_3CN$; λ nm (ε × $10^4$, $M^{-1}$ $cm^{-1}$)]: 277 (2.0), 477 (3.3).

*[Cu(**L2-a**)$Cl_2$].* Green needle crystals were grown by vapor diffusion of $Et_2O$ into a $CH_3OH$ solution of **L2-a** (5.0 mg, 27 μmol) and $CuCl_2$ (3.7 mg, 27 μmol) at room temperature overnight. The crystals were isolated, washed with $Et_2O$ three times, and dried in vacuo (6.2 mg, 19 μmol, 72%). FTIR (KBr, $cm^{-1}$): 3445 (w, br), 3189 (s), 3113 (vw, sh), 3073 (w), 3043 (vw, sh), 2956 (vw), 2921 (w), 2893 (vw, sh), 2832 (vw), 1612 (m), 1600 (w, sh), 1573 (w), 1490 (s), 1482 (s), 1447 (m), 1419 (s), 1384 (w), 1365 (w), 1312 (vw), 1283 (m), 1264 (w), 1222 (vw), 1202 (m), 1180 (w), 1156 (m), 1107 (w),

1090 (w), 1061 (w), 1049 (w, sh), 1028 (m), 1016 (m), 996 (m), 984 (w), 967 (vw), 956 (vw), 891 (vw), 820 (w), 787 (s), 765 (vs), 719 (w), 694 (s), 652 (m), 614 (vw), 572 (w), 525 (m), 464 (w), 418 (w). ESI(+)MS (m/z): $[M-Cl]^+$ Calcd for $C_{12}H_{12}ClCuN_2$, 282.0, found 282.0. Anal. Calc. for $C_{12}H_{12}Cl_2CuN_2$: C, 45.23; H, 3.80; N, 8.79. Found: C, 45.27; H, 3.74; N, 8.74. UV–Vis [$CH_3CN$; $\lambda$ nm ($\varepsilon \times 10^3$, $M^{-1}$ $cm^{-1}$)]: 310 (3.3), 400 (1.8).

*[Zn(**L2-b**)$Cl_2$]*. Pink crystals were grown by vapor diffusion of $Et_2O$ into a $CH_3OH$ solution of **L2-b** (5.0 mg, 22 μmol) and $ZnCl_2$ (3.0 mg, 22 μmol) at room temperature overnight. The crystals were isolated, washed with $Et_2O$ three times, and dried in vacuo (6.3 mg, 17 μmol, 79%). FTIR (KBr, $cm^{-1}$): 3440 (w, br), 3224 (s), 3087 (w), 3066 (w), 3038 (vw, sh), 2996 (vw), 2891 (m), 2860 (vw, sh), 2818 (w), 1866 (w), 1760 (vw), 1737 (vw), 1680 (vw), 1627 (m, sh), 1612 (s), 1572 (m), 1533 (vs), 1484 (s), 1450 (s), 1442 (s), 1403 (m), 1369 (s), 1290 (m), 1253 (w, sh), 1244 (m), 1217 (s), 1191 (s), 1175 (w, sh), 1157 (w), 1124 (w), 1109 (m), 1091 (s), 1059 (s), 1030 (s), 1008 (w, sh), 995 (s), 976 (w), 949 (m), 926 (vw), 898 (vw), 863 (w), 807 (s), 776 (s), 729 (w), 710 (vw), 651 (w), 615 (vw), 539 (m), 526 (w, sh), 510 (vw, sh), 480 (w), 454 (vw), 442 (vw), 426 (w), 417 (vw, sh). $^1$H NMR (400 MHz, $CD_3CN$): $\delta$ = 2.88 (s, 6H, N(CH3)2), 4.51 (s, 2H, $CH_2$), 5.64 (s, 1H, NH), 6.71 (d, 2H, Ph-H), 7.04 (d, *J* = 12 Hz, 2H, Ph-H), 7.62 (d, *J* = 4 Hz, 1H, Py-H), 7.63 (t, *J* = 4 Hz, 1H, Py-H), 8.11 (t, *J* = 8, 4 Hz, 1H, Py-H), 8.58 (d, *J* = 4 Hz, 1H, Py-H). ESI(+)MS (m/z): $[M-Cl]^+$ Calcd for $C_{14}H_{15}ClN_3Zn$, 326.0. Found 326.0. Anal. Calc. for $C_{14}H_{17}Cl_2N_3Zn$: C, 46.25; H, 4.71; N, 11.56. Found: C, 46.14; H, 4.62; N, 11.41. UV–Vis [$CH_3CN$; $\lambda$ nm ($\varepsilon \times 10^3$, $M^{-1}$ $cm^{-1}$)]: 310 (2.9), 473 (0.3).

### 3.6.2 UV-Vis Studies

*Metal Selectivity of **L1-b**.* The metal ion selectivity of **L1-b** was determined in

EtOH with metal chloride salts ($MgCl_2$, $CaCl_2$, $MnCl_2$, $FeCl_2$, $FeCl_3$, $CoCl_2$, $NiCl_2$, and $ZnCl_2$) using UV-Vis. All stock solutions of metal salts were prepared in EtOH. Studies employing $FeCl_2$ were conducted anaerobically (all solvents were thoroughly purged with $N_2$). The selectivity values ($A_M/A_{Cu}$) were obtained by comparing the absorbance of the solution at 525 nm before and after the addition of $CuCl_2$. Absorption values were normalized relative to that of **L1-b** and $CuCl_2$ at this wavelength (525 nm) to provide minimal interference between absorption bands.

*Metal Selectivity of **L2-b**.* To investigate the metal binding ability of **L2-b**, a solution of the ligand (40 μM or 1 mM in 20 mM HEPES, pH 7.4, 150 mM NaCl) was prepared and treated with 1 equivalent of $MgCl_2$, $CaCl_2$, $MnCl_2$, $FeCl_2$, $CoCl_2$, $NiCl_2$, $CuCl_2$, or $ZnCl_2$. The $Fe^{2+}$ samples were prepared anaerobically (all solvents were thoroughly purged with $N_2$). Spectra were recorded after 5 or 30 min incubation at room temperature. The metal ion selectivity of **L2-b** for $Cu^{2+}$ over other metal ions was determined by UV-Vis. To a solution of **L2-b** (40 μM in 20 mM HEPES, pH 7.4, 150 mM NaCl), 40 μM or 1 mM of metal salt ($MgCl_2$, $CaCl_2$, $MnCl_2$, $FeCl_2$, $CoCl_2$, $NiCl_2$, or $ZnCl_2$) was added. The solution was incubated at room temperature for 5 min, the spectrum was recorded, and then 40 μM $CuCl_2$ was added. The resulting solution was mixed well and the spectrum was recorded after additional 5 min incubation at room temperature. Selectivity was quantified by comparing and normalizing the absorbance values of the metal-ligand complex at λ = 450 nm to the absorbance of the solution at this wavelength after the addition of $CuCl_2$.

*$pK_a$ Determination.* Spectrophotometric pH titrations were conducted to determine acidity constants ($K_a$) of **K1**, **L2-a**, and **L2-b**. The pKa value ($pK_a = -\log [K_a]$)

was measured at room temperature in a solution of 100 mM NaCl and 10 mM NaOH starting from pH 12.5. At least 30 spectra were acquired from pH 2–10 after adding small aliquots of HCl to the solution containing compound ([**K1**] = 50 μM, [**L2-a**] = 500 μM, [**L2-b**] = 100 μM).

*Metal Speciation Studies.* Under similar conditions as the p$K_a$ determinations, titrations were conducted with **L2-a** (500 μM) and **L2-b** (100 μM) in the presence of $CuCl_2$ ([$CuCl_2$]/ [compound] = 1:2). A titration with $ZnCl_2$ (500 μM) and **L2-b** (1 mM) was also carried out. At least 30 spectra were acquired from pH ranges of 2.0–8.0. Acidity and stability constants were calculated using the HypSpec program (Protonic Software, UK).[166] Speciation diagrams of compounds and their corresponding metal complexes were modeled using the HySS2009 program (Protonic Software).[167] pM values were calculated using equation 1 using concentrations of unchelated metal at specific pHs from the HypSpec software.

$$pM = -\log[M_{unchelated}] \qquad (1)$$

### 3.6.3 Two-Dimensional $^{1}H-^{15}N$ Transverse Relaxation Optimized Spectroscopy (TROSY)-Heteronuclear Single Quantum Correlation (HSQC) NMR Measurements.

$^{15}$N-labled A$\beta_{1\text{-}40}$ (*ca.* 0.25 mg) was dissolved into 185 μL of a buffer solution containing SDS-$d_{25}$ (200 mM), sodium phosphate buffer (20 mM, pH 7.3), $D_2O$ (7%, v/v) and briefly vortexed. The peptide solution (*ca.* 308 μM) was transferred to a Shigemi NMR tube. After acquiring spectra of the peptide, 5, 10, or 15 equiv of a 5 mM stock solution of **L1-a**, **L1-b**, **L2-a**, **L2-b**, or **8-HQ** in the NMR buffer solution were added to the NMR samples. For **K0** and **K1**, 4, 8, or 12 equiv of 4 mM stock solution in NMR buffer was added.

Control samples were conducted under similar conditions with the addition of 2.28 μL of either neat dimethyl sulfoxide-d6 (DMSO-$d_6$) or a 50 mM DMSO-$d_6$ stock solution of **S0** or **S1** to a 300 μL solution containing 190 μM Aβ.

For the study with $Zn^{2+}$, ca. 1.0 equivalent of $ZnCl_2$ (100 mM stock solution in $D_2O$) was added into the peptide solution followed by treatment with 10 equiv of either **L1-a**, **L1-b**, or **L2-b**. Spectra were obtained after 30 min and 1 h for **L1-a** and **L1-b** (no further change after 1 h) and after 1, 2, and 4 h incubation for **L2-b** (no spectral change was observed after 2 h).

For NMR studies, the TROSY version of 2D $^{1}H-^{15}N$ HSQC spectra were recorded on the 900 MHz Bruker Avance NMR spectrometer (equipped with a TCI cryoprobe accessory) with 14.3 kHz and 1.7 kHz spectral width and 2,048 and 128 complex data points in the $^{1}H$ an $^{15}N$ dimension, respectively, 4 scans for each $t_1$ experiment and 1.5 s recycle delay; each spectrum took 10 min for completion. Water peak was referenced to 4.78 ppm at 25 °C. $^{1}H-^{15}N$ HSQC peaks were assigned by comparison of the observed chemical shift values with those reported in the literature.[140] Combined $^{1}H$ and $^{15}N$ 2D chemicals shifts ($\Delta\delta_{N-H}$) were calculated from equation 2.[168,169,170] The 2D results were processed using Topspin software (version 2.1 from Bruker) and analyzed with Sparky (version 3.112).

$$\Delta\delta_{N-H} = \sqrt{\frac{(\Delta\delta_H{}^2 + (0.2(\Delta\delta_N))^2}{2}} \qquad (2)$$

### 3.6.4 Docking with AutoDock4 and AutoDockTools4

Docking studies of the **L1**, **L2,** and **S** series were performed using AutoDock4 with general protocols.[146] Minimized structures of compounds were generated by

Chem3D Ultra 12.0 using MMFF94 minimization with default parameters and were transferred into AutoDockTools4. Peptide files were prepared from the previously determined NMR solution structure of monomeric Aβ in SDS-$d_{25}$ micelles (PDB 1BA4).[139] For AutoGrid4, grid volumes were set to cover the entire peptide conformation with 0.375 Å spacing: [Conformation: box size (Å): center (x,y,z)] A: 126 × 84 × 56: 7.663, 7.889, −8.371; B: 126 × 72 × 66: 0.194, −6.01, −7.711; C: 126 × 72 × 58: 5.665, −5.79, −8.124; D: 126 × 72 × 76: 5.432, −4.614, −12.983; E: 118 × 88 × 54: 10.202, 9.338, −4.058. Compounds were run with 256 Lamarckian genetic algorithm local searches (GALS) with docking calculations consisting of a population size of 150 and 2.5 million energy evaluations. The rest of the calculation parameters were left on default values for AutoDockTools4. Using the default cluster option in AutoDockTools4, the lowest energy conformation of the highest populated cluster was selected and figures of ligands docked with Aβ were depicted using Pymol.

## 3.7 References


[1] Alzheimers Association *Alzheimers Dementia* **2011**, *7*, 208.
[2] Robertson, E. D.; Mucke, L. *Science* **2006**, *781*, 781.
[3] Gravitz, L. *Nature* **2011**, *475*, S9.
[4] Jakob-Roetne, R.; Jacobsen, H. *Angew. Chem. Int. Ed.* **2009**, *48*, 3030.
[5] Anand, R.; Kaushal, A.; Wani, W. Y.; Gill, K. D. *Pathobiology* **2012**, *79*, 55.
[6] Mucke, L. *Nature* **2009**, *461*, 895.
[7] Abbott, A. *Nature* **2011**, *475*, S2.
[8] Hamley, I. W. *Chem. Rev.* **2012**, *112*, 5147.
[9] Gaggelli, E.; Kozlowski, H.; Valensin, D.; Valensin, G. *Chem. Rev.* **2006**, *106*, 1995.
[10] Kepp, K. P. *Chem. Rev.* **2012**, *112*, 5193.
[11] Selkoe, D. J. *Nat. Med.* **2011**, *9*, 1060.
[12] Hardy, J.; Selkoe, D. J. *Science* **2002**, *297*, 353.
[13] Selkoe, D. J. *Neuron* **1991**, *6*, 487.
[14] Hardy, J. A.; Higgins, G. A. *Science* **1992**, *256*, 184.
[15] Selkoe, D. J. *Physiol. Rev.* **2001**, *81*, 741.
[16] Mawuenyega, K. G.; Sigurdson, W.; Ovod, V.; Munsell, L.; Kasten, T.; Morris, J. C.; Yarasheski, K. E.; Bateman, R. J. *Science* **2011**, *330*, 1774.
[17] Zhang, Y.; McLaughlin, R.; Goodyer, C.; LeBlank, A. *J. Cell Biol.* **2002**, *156*, 519.
[18] Miller, Y.; Ma, B.; Nussinov, R. *Chem. Rev.* **2010**, *110*, 4820.
[19] Rauk, A. *Chem. Soc. Rev.* **2009**, *38*, 2698.
[20] Benilova, I.; Karran, E.; De Strooper, B. *Nat. Neurosci* **2012**, *15*, 349.
[21] Haass, C.; Selkoe, D. J. *Nat. Rev. Mol. Cell. Biol.* **2007**, *8*, 101.
[22] Roychaudhuri, R.; Yang, M.; Hoshi, M.; Teplow, D. B. *J. Biol. Chem.* **2009**, *284*, 4749.
[23] Bernhardi, R. v.; Eugenín, J. *Antioxid. Redox Signaling* **2012**, *16*, 974.
[24] Golde, T. E.; Schneider, L. S.; Koo, E. H. *Neuron* **2011**, *69*, 203.
[25] Bush, A. I. *Trends Neurosci*. **2003**, *26*, 207.
[26] Roberts, B. R.; Ryan, T. M.; Bush, A. I.; Masters, C. L.; Duce, J. A. *J. Neurochem*. **2012**, *120*, 149.
[27] Zatta, P.; Drago, D.; Bolognin, S.; Sensi, S. L. *Trends Pharm. Sci.* **2009**, *30*, 346.
[28] DeToma, A. S.; Salamekh, S.; Ramamoorthy, A.; Lim, M. H. *Chem. Soc. Rev.* **2012**, *41*, 608.
[29] Pithadia, A. S.; Lim, M. H. *Curr. Opin. Chem. Biol.* **2012**, *16*, 67.
[30] Hureau, C.; Sasaki, I.; Gras, E.; Faller, P. *ChemBioChem* **2010**, *11*, 950.
[31] Braymer, J. J.; DeToma, A. S.; Choi, J.-S.; Ko, K. S.; Lim, M. H. *Int. J. Alzheimers Dis.* **2011**, *2011*, 623051.
[32] Tomski, S. J.; Murphy, R. M. *Arch. Biochem. Biophys.* **1992**, *294*, 630.
[33] Bush, A. I.; Pettingell, W. H. Jr.; Paradis, M. d.; Tanzi, R. E. *J. Biol. Chem.* **1994**, *269*, 12152.
[34] Bush, A. I.; Pettingell, W. H.; Multhaup, G.; Paradis, M. d.; Vonsattel, J.-P.; Gusella, J. F.; Beyreuther, K.; Masters, C. L.; Tanzi, R. E. *Science* **1994**, *265*, 1464.

[35] Atwood, C. S.; Moir, R. D.; Huang, X.; Scarpa, R. C.; Bacarra, N. M. E.; Romano, D. M.; Hartshorn, M. A.; Tanzi, R. E.; Bush, A. I. *J. Biol. Chem.* **1998**, *273*, 12817.
[36] Faller, P.; Hureau, C. *Dalton Trans*. **2009**, 1080.
[37] Smith, M. A.; Harris, P. L. R.; Sayre, L. M.; Perry, G. *Proc. Natl. Acad. Sci. USA* **1997**, *94*, 9866.
[38] Nunez, M. T.; Urrutia, P.; Mena, N.; Aguirre, P.; Tapia, V.; Salazar, J. *BioMetals* **2012**, *25*, 761.
[39] Smith, M.; Zhu, X.; Tabaton, M.; Liu, G.; McKeel, D. W.; Cohen, M. L.; Wang, X.; Siedlak, S.; Dwyer, B. E.; Hayashi, T.; Nakamura, M.; Nunomura, M.; Perry, G. *J. Alzheimers Dis.* **2010**, *19*, 363.
[40] Scott, L. E.; Orvig, C. *Chem. Rev.* **2009**, *109*, 4885.
[41] Bush, A. I. *Curr. Opin. Chem. Biol.* **2000**, *4*, 184.
[42] Viles, J. H. *Coord. Chem. Rev.* **2012**, *256*, 2271.
[43] Chen, W.-T.; Liao, Y.-H.; Yu, H.-M.; Cheng, I. H.; Chen, Y.-R. *J. Biol. Chem.* **2011**, *286*, 9646.
[44] Noy, D.; Solomonov, I.; Sinkevich, O.; Arad, T.; Kjaer, K.; Sagi, I. *J. Am. Chem. Soc.* **2008**, *130*, 1376.
[45] Sarell, C. J.; Wilkinson, S. R.; Viles, J. H. *J. Biol. Chem.* **2010**, *285*, 41533.
[46] Solomonov, I.; Korkotian, E.; Born, B.; Feldman, Y.; Bitler, A.; Rahimi, F.; Li H.; Bitan, G.; Sagi, I. *J. Biol. Chem.* **2012**, *287*, 20555.
[47] Liu, B.; Moloney, A.; Meehan, S.; Morris, K.; Thomas, S. E.; Serpell, L. C.; Hider, R.; Marciniak, S. J.; Lomas, D. A.; Crowther, D. C. *J. Biol. Chem.* **2011**, *286*, 4248.
[48] Tabner, B. J.; Mayes, J.; Allsop, D. *Int. J. Alzheimers Dis.* **2010**, *2011*, 546380.
[49] Butterfield, S. M.; Lashuel, H. A. *Angew. Chem. Int. Ed.* **2010**, *49*, 2.
[50] Tamano, H.; Takeda, A. *Metallomics* **2012**, *3*, 656.
[51] Lame, M. E.; Chambers, E. E.; Blatnik, M. *Anal. Biochem.* **2011**, *419*, 133.
[52] Deshpande, A.; Kawai, H.; Metherate, R.; Glabe, C. G.; Busciglio, J. *J. Neurosci.* **2009**, *29*, 4004.
[53] Goodman, L. *J. Nerv. Men. Dis.* **1953**, *117*, 97.
[54] Schrag, M.; Mueller, Oyoyo, U.; Smith, M. A.; Kirsh, W. M. *Prog. Neurobiol.* **2011**, *94*, 296.
[55] House, E.; Esiri, M.; Forster, G.; Ince, P. G.; Exley, C. *Metallomics* **2012**, *4*, 56.
[56] Wang, H.; Wang, M.; Wang, B.; Li, M.; Chen, H.; Yu, X.; Zhao, Y.; Feng, W.; Chai, Z. *Metallomics* **2012**, *4*, 289.
[57] Leskovjan, A. c.; Kretlow, A.; Lanzirotti, A.; Barrea, R.; Vogt, S.; Miller, L. M. *NeuroImage* **2011**, *55*, 32.
[58] Leskovjan, A. C.; Lanzirotti, A.; Miller, L. M. *NeuroImage* **2009**, *47*, 1215.
[59] Hare, D. J.; Lee, J. K.; Beavis, A. D.; Gramberg, A. v.; George, J.; Adlard, P. A.; Finkelstein, D. I.; Doble, P. A. *Anal. Chem.* **2012**, *84*, 3990.
[60] Bourassa, M. W.; Miller, L. M. *Metallomics* **2012**, *4*, 721.
[61] Lovell, M. A.; Roberston, J. D.; Teesdale, W. J.; Campbell, J. L.; Markesbery, W. R. *J. Neurol. Sci.* **1998**, *158*, 47.
[62] Miller, L. M.; Wang, Q.; Telivala, T. P.; Smith, R. J.; Lanzirotti, A.; Miklossy, J. *J. Mol. Biol.* **2006**, *155*, 30.

[63] Dong, J.; Atwood, C. S.; Anderson, V. E.; Siedlak, S. L.; Smith. M. A.; Perry, G.; Carey, P. R. *Biochemistry* **2003**, *42*, 2768.
[64] Tougu, V.; Tiiman, A.; Palumaa, P. *Metallomics* **2011**, *3*, 250.
[65] Danielsson, J.; Pierattelli, R.; Banci, L.; Gräslund, A. *FEBS J.* **2007**, *274*, 46.
[66] Drew, S. C.; Barnham, K. J. *Acc. Chem. Res.* **2011**, *44*, 1146.
[67] Hureau, C.; Balland, V.; Coppel, Y.; Solari, P. L.; Fonda, D.; Faller, P. *J. Biol. Inorg. Chem.* **2009**, *14*, 995.
[68] Shearer, J.; Szalai, V. A. *J. Am. Chem. Soc.* **2008**, *130*, 17826.
[69] Valensin, D.; Migliorini, C.; Valensin, G.; Gaggelli, E.; La Penna, G.; Kozlowski, H.; Gabbiani, C.; Messori, L. *Inorg. Chem.* **2011**, *50*, 6865.
[70] Bousejra-ElGarah, F.; Bijani, C.; Coppel, Y.; Faller, P.; Hureau, C. *Inorg. Chem.* **2011**, *50*, 9024.
[71] Ali-Torres, J.; Rodriguez-Santiago, L.; Sodupe, M.; Rauk, A. *J. Phys. Chem. A* **2011**, *115*, 12523.
[72] Jomova, K.; Vondrakova, D.; Lawson, M.; Valko, M. *Mol. Cell. Biochem.* **2010**, *345*, 91.
[73] Smith, M. A.; Perry, G.; Richey, P. L.; Sayre, L. M.; Anderson, V. E.; Beal, M. F.; Kowall, N. *Nature* **1996**, *382*, 120.
[74] Nunomura, A.; Perry, G.; Aliev, G.; Hirai, K.; Takeda, A.; Balraj, E. K.; Jones, P. K.; Ghanbari, H.; Wataya, T. Shimohama, S.; Chiba, S.; Atwood, C. S.; Petersen, R. B.; Smith, M. A. *J. Neuropathol. Exp. Neurol*. **2001**, *60*, 759.
[75] Pappolla, M. A.; Chyan, Y.-J.; Omar, R. A.; Hsiao, K.; Perry, G.; Smith, M. A.; Bozner, P. *Am. J. Pathol.* **1998**, *152*, 872.
[76] James, S. A.; Volitakis, I.; Adlard, P. A.; Duce, J. A.; Masters, C. L.; Cherny, R. A.; Bush, A. I. *Free Radical Biol. Med.* **2012**, *52*, 298.
[77] Opazo, C.; Huang, X.; Cherny, R. A.; Moir, F. D.; Roher, A. E.; White, A. R.; Cappai, R.; Masters, C. L.; Tanzi, R. E.; Inestrosa, N. C.; Bush, A. I. *J. Biol. Chem.* **2002**, *277*, 40302.
[78] Eskici, G.; Axelsen, P. H. *Biochemistry* **2012**, *51*, 6289.
[79] Behl, C.; Davis, J. B.; Lesley, R.; Schubert, D. *Cell* **1994**, *77*, 817.
[80] Hureau, C.; Faller, P. *Biochimie* **2009**, *91*, 1212.
[81] Shearer, J.; Callan, P. E.; Tran, T.; Szalai, V. A. *Chem. Commun.* **2010**, *46*, 9137.
[82] Huang, X.; Atwood, C. S.; Moir, R. D.; Hartshorn, M. A.; Vonsattel, J.-P.; Tanzi, R. E.; Bush, A. I. *J. Biol. Chem.* **1997**, *272*, 26464.
[83] Cherny, R. A.; Legg, J. T.; McLean, C. A.; Fairlie, D. P.; Huang, X.; Atwood, C. S.; Beyreuther, K.; Tanzi, R. E.; Masters, C. L.; Bush, A. I. *J. Biol. Chem.* **1999**, *274*, 23223.
[84] McLachlan, D. R. C.; Dalton, A. J.; Kruck, T. P. A.; Bell, M. Y.; Smith, W. L.; Kalow, W.; Andrews, D. F. *Lancet* **1991**, *337*, 1305.
[85] Cherny, R. A.; Atwood, C. S.; Xilinas, M. E.; Gray, D. N.; Jones, W. D.; McLean, C. A.; Barnham, K. J.; Volitakis, I.; Fraser, F. W.; Kim, Y.-S.; Huang, X.; Goldstein, L. E.; Moir, R. D.; Lim, J. T.; Beyreuther, K.; Zheng, H.; Tanzi, R. E.; Masters, C. L.; Bush, A. I. *Neuron* **2001**, *30*, 665.

[86] White, A. R.; Du, T.; Laughton, K. M.; Volitakis, I.; Sharples, R. A.; Xilinas, M. E.; Hoke, D. E.; Holsinger, R. M. D.; Evin, G.; Cherny, R. A.; Hill, A. F.; Barnham, K. J.; Li, Q.-X.; Bush, A. I.; Masters, C. L. *J. Biol. Chem.* **2006**, *281*, 17670.
[87] Bush, A. I.; Tanzi, R. E. *Neurotherapeutics* **2008**, *5*, 421.
[88] Rodriguez-Rodriguez, C.; Telpoukhovskaia, M.; Orvig, C. *Coord. Chem. Rev.* **2012**, *256*, 2308.
[89] Cahoon, L. *Nat. Med.* **2009**, *15*, 356.
[90] Adlard, P. A.; Cherny, R. A.; Finkelstein, D. I.; Gauthier, E.; Robb, E.; Cortes, M.; Volitakis, I.; Liu, X.; Smith, J. P.; Perez, K.; Laughton, K.; Li, Q.-X.; Charman, S. A.; Nicolazzo, J. A.; Wilkins, S.; Deleva, K.; Lynch, T.; Kok, G.; Ritchie, C. W.; Tanzi, R. E.; Cappai, R.; Masters, C. L.; Barnham, K. J.; Bush, A. I. *Neuron* **2008**, *59*, 43.
[91] Crouch, P. J.; Barnham, K. J. *Acc. Chem. Res.* **2012**, DOI: 10.1021/ar200074t.
[92] Donnelly, P. S.; Mot, I. A.; Parker, S. J.; Greenough, M. A.; Volitakis, I.; Adlard, P. A.; Cherny, R. A.; Masters, C. L.; Bush, A. I.; Barnham, K. J.; White, A. R. *J. Neurochem.* **2011**, *119*, 220.
[93] Dedeoglu, A.; Cormier, K.; Payton, S.; Tseitlin, K. A.; Kremsky, J. N.; Lai, L.; Li, X.; Moir, R. D.; Tanzi, R. E.; Bush, A. I.; Kowall, N. W.; Rogers, J. T.; Huang, X. *Exp. Gerontol.* **2004**, *39*, 1641.
[94] Vassar, P. S.; Culling, C. F. A. *Arch. Pathol.* **1959**, *68*, 487.
[95] Levine, H., III. *Protein Sci*. **1993**, *2*, 404.
[96] Wu, W.-h.; Lei, P.; Liu, Q.; Hu, J.; Gunn, A. P.; Chen, M.-s.; Rui, Y.-f.; Su, X.-y.; Xie, Z.-p.; Zhao, Y.-F.; Bush, A. I.; Li, Y.-m. *J. Biol. Chem.* **2008**, *283*, 31657.
[97] Rodriguez-Rodriquez, C.; Sanchez de Groot, N.; Rimola, A.; Alvarez-Larena, A.; Lloveras, V.; Vidal-Gancedo, J.; Ventura, S.; Vendrell, J.; Sodupe, M.; Gonzalez-Duarte, P. *J. Am. Chem. Soc.* **2008**, *131*, 1436.
[98] Kung, H. F.; Lee, C.-W.; Zhuang, Z.-P.; Kung, M.-P.; Hou, C.; Plössl, K. *J. Am. Chem. Soc.* **2001**, *123*, 12740.
[99] Kung, H. F.; Kung, M.-P.; Zhuang, Z.-P.; Hou, C.; Lee, C.-W.; Plössl, K.; Zhuang, B.; Skovronsky, D. M.; Lee, V. M.; Trojanowski, J. Q. *Mol. Imaging. Biol.* **2003**, *5*, 418.
[100] Zhuang, Z.-P.; Kung, M.-P.; Wilson, A.; Lee, G.-W.; Plössl, K.; Hou, G.; Holtzman, D. M.; Kung, H. F. *J. Med. Chem.* **2003**, *46*, 237.
[101] Kung, M.-P.; Hou, C.; Zhuang, Z.-P.; Zhang, B.; Skovronsky, D.; Trojanowski, J. Q.; Lee, V. M.; Kung, H. F. *Brain Res.* **2002**, *956*, 202.
[102] Kung, M.-P.; Hou, C.; Zhuang, Z.-P.; Skovronsky, D.; Kung, H. F. *Brain Res.* **2004**, *1025*, 98.
[103] Newberg, A. B.; Wintering, N. A.; Plössl, K.; Hochold, J.; Stabin, M. G.; Watson, M.; Skovronsky, D.; Clark, C. M.; Kung, M.-P.; Kung, H. F. *J. Nucl. Med.* **2006**, *47*, 748.
[104] Zhang, W.; Oya, S.; Kung, M.-P.; Hou, C.; Maier, D. L.; Kung, H. F. *J. Med. Chem.* **2005**, *48*, 5980.
[105] Kung, H. F.; Choi, S. R.; Qu, W.; Zhang, W.; Skovronsky, D. *J. Med. Chem.* **2010**, *53*, 933.
[106] Vassar, P. S.; Culling, C. F. A. *Arch. Pathol.* **1959**, *68*, 487.
[107] Levine, H., III. *Protein Sci.* **1993,** *2*, 404.
[108] Wolk, D. A.; Klunk, W. E. *Curr. Neurol. Neurosci. Rep.* **2009**, *9*, 345.

[109] Klunk, W. E.; Wang, Y.; Huang, G.-f.; Debnath, M. L.; Holt, D. P.; Mathis, C. A. *Life Sci*. **2001**, *69*, 1471.
[110] Hindo, S. S.; Mancino, A. M.; Braymer, J. J.; Liu, Y.; Vivekanandan, S.; Ramamoorthy, A.; Lim, M. H. *J. Am. Chem. Soc.* **2009**, *131*, 16663.
[111] Choi, J.-S.; Braymer, J. J.; Park, S. K.; Mustafa, S.; Chae, J.; Lim, M. H. *Metallomics*, **2011**, *3*, 284.
[112] Braymer, J. J.; Merrill, N. M.; Lim, M. H. *Inorg. Chim. Acta* **2011**, *380*, 261.
[113] Braymer, J. J.; Choi, J.-S.; DeToma, A. S.; Wang, C.; Nam, K.; Kampf, J. W.; Ramamoorthy, A.; Lim, M. H. *Inorg. Chem.* **2011**, *50*, 10724.
[114] Choi, J.-S.; Braymer, J. J.; Nanga, R. P. R.; Ramamoorthy, A.; Lim, M. H. *Proc. Natl. Acad. Sci, USA* **2010**, *107*, 21990.
[115] Leuma Yona, R; Mazéres, S. Faller, P.; Gras, E. *ChemBioChem* **2008**, *3*, 63.
[116] Ono, M.; Yoshida, N.; Ishibashi, K.; Haratake, M.; Arano, Y.; Mori, H.; Nakayama, M. *J. Med. Chem.* **2005**, *48*, 7253.
[117] Lipinski, C. A.; Lombardo, F.; Dominy, B. W.; Feeney, P. J. *Adv. Drug Del. Rev.* **2001**, *46*, 3.
[118] Clark, D. E.; Pickett, S. D. *Drug Discov. Today* **2000**, *5*, 49.
[119] Di, L.; Kerns, E. H.; Fan, K.; McConnell, O. J.; Carter, G. T. *Eur. J. Med. Chem.* **2003**, *38*, 223.
[120] *p*ION Inc. (2009) BBB protocol and test compounds. *Report* (*p*ION Inc., Woburn, MA).
[121] Grabowski, Z. R.; Rotkiewicz, K.; Rettig, W. *Chem. Rev.* **2003**, *103*, 3899.
[122] Dehghanpour, S.; Mahmoudi, A.; Khalaj, M.; Salmanpour, S.; Adib, M. *Acta. Crystallogr., Sect. E: Struct. Rep. Online* **2007**, *63*, m2841.
[123] Bell, C. F.; Mortimore, G. R.; Reed, G. L. *Org. Magn. Reson.* **1976**, *8*, 45.
[124] Lopez-Garriga, J. J.; Babcock, G. T.; Harrison, J. F.; *J. Am. Chem. Soc.* **1986**, *108*, 7241.
[125] Gourbatsis, S.; Perlepes, S. P.; Butler, I. S.; Hadjiliadis, N. *Polyhedron* **1999**, *18*, 2369.
[126] Perrin, D. D. Dissociation Constants of Organic Bases in Aqueous Solution, IUPAC, Butterworths, London, **1965**.
[127] Martell, A. E.; Smith, R. M. Critial Stability Constants, Plenum Press, New York, **1974**.
[128] Baes, C. F.; Mesmer, R. E. The Hydrolysis of Cations, Wiley, New York, **1976**.
[129] Markova, O.; Mukhtarov, M.; Real, E.; Jacob, Y.; Bregestovski, P. *J. Neurosci. Methods* **2008**, *170*, 67.
[130] Dickson, S. J.; Paterson, M. J. Willans, C. E.; Anderson, K. M.; Steed, J. W. *Chem. Eur. J.* **2008**, *14*, 7296.
[131] Xu, Z.; Qian, X.; Cui, J.; Zhang, R. *Tetrahedron* **2006**, *62*, 10117.
[132] Ugozzoli, F.; Massera, C.; Manotti Lanfredi, A. M.; Marisch, N.; Camus, A. *Inorg. Chim. Acta.* **2002**, *340*, 97.
[133] Tsai, W.; Liu, Y.-H.; Peng, S.-M.; Liu, S.-T. *J. Organomet. Chem*. **2005**, *690*, 415.
[134] Almesåker, A.; Bourne, S. A.; Ramon, G.; Scott, J. L.; Strauss, C. R. *CrystEngComm* **2007**, *9*, 997.

[135] Canovese, L.; Visentin, F.; Chessa, G.; Levi, C.; Dolmella, A. *Eur. J. Inorg. Chem.* **2007**, *2007*, 3669.
[136] Perera, T.; Marzilli, P. A.; Fronczek, F. R.; Marzilli, L. G. *Inorg. Chem*. **2010**, *49*, 5560.
[137] Silverstein, R. M.; Webster, F. X. Spectrometric Identification of Organic Compounds, Wiley, New York, **1998**.
[138] Wahlstrom, A.; Hugonin, L.; Peralvarez-Marin, A.; Jarvet, J.; Gräslund, A. *FEBS J.* **2008**, *275*, 5117.
[139] Coles, M.; Bicknell, W.; Watson, A. A.; Fairlie, D. P.; Craik, D. J. *Biochemistry* **1998**, *37*, 11064.
[140] Jarvet, J.; Danielsson, J.; Damberg, P.; Oleszcuk, M.; Gräslund, A. *J. Biomol. NMR*. **2007**, *39*, 63.
[141] Jarvet, J.; Damberg, P.; Danielsson, J.; Johansson, I.; Erikkson, L. E. G.; Graslund, A. *FEBS Lett.* **2003**, *555*, 371.
[142] Walsh, D. M.; Hartley, D. M.; Kusumoto, Y.; Fezoui, Y.; Condron, M. M.; Lomakin, A.; Benedek, G. B.; Selkoe, D. J.; Teplow, D. B. *J. Biol. Chem.* **1999**, *274*, 25945.
[143] Hou, L.; Zagorksi, M. G. *J. Am. Chem. Soc*. **2006**, *128*, 9260.
[144] Morris, G. M.; Goodsell, D. S.; Halliday, R. S.; Huey, R.; Hart, W. E.; Delew, R. K.; Olson, A. J. *J. Comput. Chem.* **1998**, *19*, 1639.
[145] Morris, G. M.; Huey, R.; Lindstrom, W.; Sanner, M. F.; Belew, R. K.; Goodsell, D. S.; Olson, A. J. *J. Comput. Chem.* **2009**, *30*, 2785.
[146] Morris, G. M.; Huey, R.; Olson, A. I. *Curr. Protoc. Bioinf*. **2008**, *Chapter 8*, 8.14.11-18.14.40.
[147] DeToma, A. J.; Choi, J.-S.; Braymer, J. J.; Lim, M. H. *ChemBioChem* **2011**, *12*, 1198.
[148] Venezia, V.; Russo, C.; Repetto, E.; Salis, S.; Dolcini, V.; Genova, F.; Nizzari, M.; Mueller, U.; Schettini, G. *J. Neurochem*. **2004**, *90*, 1359.
[149] Hartley, D. M.; Walsh, D. M.; Ye, C. P.; Diehl, T.; Vasquez, S.; Vassilev, P. M.; Teplow, D. B.; Selkoe, D. J. *J. Neurosci.* **1999**, *19*, 8876.
[150] Klug, G. M. J. A.; Losic, D.; Subasinghe, S. S.; Aguilar, M.-I.; Martin, L. L.; Small, D. H. *Eur. J. Biochem*. **2003**, *270*, 4282.
[151] Bolmont, T.; Clavaguera, F.; Meyer-Luehmann, M.; Herzig, M. C.; Radde, R.; Staufenbiel, M.; Lewis, J.; Hutton, M.; Tolnay, M.; Jucker, M. *Am. J. Pathol.* **2007**, *171*, 2012.
[152] Ghalebani, L.; Wahlstrom, A.; Danielsson, J.; Warmlander, S. K. T. S.; Gräslund, A. *Biochem. Biophys. Res. Comm.* **2012**, *421*, 554.
[153] Mancino, A. M.; Hindo, S. S.; Kocki, A.; Lim, M. H. *Inorg. Chem.* **2009**, *48*, 9596.
[154] Zhang, Y.; Chen, L.-Y.; Yin, W.-X.; Yin, J.; Zhang, S.-B.; Liu, C.-L. *Dalton Trans.* **2011**, *40*, 4830.
[155] Geng, J.; Li, M.; Wu, L.; Ren, J.; Qu, X. *J. Med. Chem.* **2012**, DOI: 10.1021/jm3003813.
[156] Sharma, A. K.; Pavlova, S. T.; Kim, J.; Finkelstein, D.; Hawco, N. J.; Rath, N. P.: Kim, J.; Mirica, L. M. *J. Am. Chem. Soc.* **2012**, *134*, 6625.

[157] Ryan, T. M.; Friedhuber, A.; Lind, M.; Howlett, G. J.; Masters, C.; Roberts, B. R. *J. Biol. Chem.* **2012**, *287*, 16947.
[158] Bieschke, J.; Herbst, M.; Wiglenda, T.; Friedrich, R. P.; Boeddrich, A.; Schiele, F.; Kleckers, D.; Lopez del Amo, J. M.; Grüning, B. A.; Wang, Q.; Schmidt, M. R.; Lurz, R.; Anwyl, R.; Schnoegl, S.; Fändrich, M.; Frank, R. F.; Reif, B.; Günther, S.; Walsh, D. M.; Wanker, E. E. *Nat. Chem. Biol.* **2011**, *8*, 93.
[159] He, X.; Park, H. M.; Hyung, S.-J.; DeToma, A. S.; Kim, C.; Ruotolo, B. T.; Lim, M. H. *Dalton Trans.* **2012**, *41*, 6558.
[160] Telpoukhovskaia, M. A.; Orvig, C. *Chem. Soc. Rev.* **2012**, DOI: 10.1039/c2cs35236b.
[161] Jiaranaikulwanitch, J.; Govitrapong, P.; Fokin, V. V.; Vajragupta, O. *Molecules* **2012**, *17*, 8312.
[162] Sheldrick, G. M. SADABS or TWINABS, Version 2008/1, Program for Emperical Absorption Correction of Area Detector Data, University of Göttingen, Göttingen, German, **2008**.
[163] SAINTPLUS, Version 7.60a, Software for the CCD Detector System, Bruker AXA, Madison, WI, 2009.
[164] Sheldrick, G. M. SHELXTL, Version 2008/3, Program Library for Structure Solution and Molecular Graphics, Bruker AXA, Madison, WI, USA, 2008.
[165] Spek, A. L. PLATON, A Multipurpose Crystallographic Tool, Utrecht University, Utrecht, The Netherlands, 2010.
[166] Gans, P.; Sabatini, A.; Vacca, A. *Ann. Chim.* **1999**, *89*, 45.
[167] Alderighi, L.; Gans, P.; Ienco, A.; Peters, D.; Sabatini, A.; Vacca, A. *Coord. Chem. Rev.* **1999**, *184*, 311.
[168] Grzesiek, S.; Bax, A.; Clore, G. M.; Gronenborn, A. M.; Hu, J. S.; Kaufman, J.; Palmer, I.; Stahl, S. J.; Wingfield, P. T. *Nat. Struct. Biol.* **1996**, *3*, 340.
[169] Garrett, D. S.; Seok, Y. J.; Peterkofsky, A.; Clore, G. M.; Gronenborn, A. M. *Biochemistry* **1997**, *36*, 4393.
[170] Foster, M. P.; Wuttke, D. S.; Clemens, K. R.; Jahnke, W.; Radhakrishnan, I.; Tennant, L.; Reymond, M.; Chung, J.; Wright, P. E. *J. Biomol. NMR* **1998**, *12*, 51.